Multiple Nucleon Emission from ^{232}Th Following High Energy Photo-Excitation

by

Gary John Miller, B.Sc.

Presented as a Thesis for the Degree of Doctor of Philosophy

Department of Physics and Astronomy,

University of Glasgow,

July 1987.

Abstract

New results are presented on the multiple emission of nucleons from ^{232}Th following photo-excitation in the energy range 40–150 MeV. Using activation techniques, the cross-sections for 11 separate $(\gamma, xnyp)$ photoreactions have been determined from the residual α-activity of their reaction products. In the course of this investigation, improved half-lives have also been measured for several of the actinide nuclides studied.

Photoreaction cross-sections, obtained from the electron and bremsstrahlung yield curves, have been compared with the predictions of the intranuclear cascade and hybrid exciton models for precompound nuclear decay. The photodisintegration models in their present form, while reproducing the general trends of the measured cross-sections, appear to underestimate the importance of precompound fast particle emission during the nuclear de-excitation sequence which follows photon absorption. Necessary improvements to these models, regarding their application to photonuclear interactions, are discussed.

The importance of fission competition in the nuclear disintegration process has also been demonstrated and present estimations of the parameters governing fission decay in this energy domain, are shown to be reasonably valid.

Comparisons of the real and virtual photon data gathered in this experiment suggest that present calculations of the virtual photon spectra, made in second order Born approximation, underestimate the E1 intensity for nuclei in this mass and energy range. The need for a virtual photon formalism which incorporates a full treatment of both nuclear size and charge effects is emphasised.

This new data greatly extends the information available on photodisintegration in heavy nuclei and provides a useful testing ground for theoretical treatments of the final-state interactions and absorption mechanism associated with photonuclear processes at these energies.

Declaration

The data presented in this thesis was obtained by the Nuclear Structure group at the University of Glasgow, in which I undertook the principal role. The analysis and interpretation of this data is entirely my own work. This thesis was composed by myself.

Gary J. Miller

Acknowledgements

I wish to thank, above all, my supervisor Dr. Robert Owens for his patience, guidance and expert advice during the period of this work. I would also like to thank Dr. Cameron McGeorge for his assistance with the experimental activations and without whose tireless effort and youthful enthusiasm, the collection of this data would have been a much greater burden. I am equally indebted to Dr. Ian Anthony, principally for his work on the implementation and modification of the complex computer codes used in this project but also for many informative discussions on the topic of photon activation measurements. I am indebted to Professor Dirk Ryckbosch at the Laboratorium Voor Kernfysica, Rijksuniversiteit, Gent, who performed some of the theoretical calculations presented here and with whom our Laboratory has developed a fruitful collaboration. Also to Professor David Onley at the University of Ohio for providing us with calculations from his distorted wave virtual photon code.

I am grateful to Professor Jack Reid, who as Director of the Kelvin Laboratory, afforded me use of his experimental facilities and to Maurice Kelliher who, as Project Manager, resolved the multitude of problems associated with an ageing accelerator, allowing the successful completion of our experimental programme.

Our systems staff, Arrick Wilkinson and Andy Sibbald, deserve special thanks for their frequent assistance with computing problems all of which were resolved, I must say, swiftly and with user-friendliness. Dr. George Clelland deserves a special mention for his work on the mini-computer system and acquisition codes used for data collection in this experiment. His services have been invaluable.

I express my thanks to the technical staff of the Kelvin Laboratory's elec-

tronic and mechanical workshops for their craftsmanship and advice regarding the design and manufacture of components used in this project.

I am extremely grateful to Eileen Taylor who prepared many of the diagrams which appear in this thesis. Her work has proved to be of the highest standard.

I would like to thank Professors Laing and Hughes, who as successive heads of department, have funded my attendance at various schools and conferences. I am indebted to the Science and Engineering Research Council and the Institute of Physics in the same respect and gratefully acknowledge the receipt of an S.E.R.C. postgraduate studentship for the period of this research.

May I thank everyone at the Kelvin Laboratory, staff and students, for their enthusiasm and humour all of which have provided a most enjoyable working environment.

Finally, my sincerest thanks go to my parents who, with love and encouragement, have helped my studies reach a successful conclusion.

Contents

Chapter 1

Introduction

1.1 Introduction

The use of photons and electrons as probes of the nuclear system is known to yield valuable information on the structure of the nucleus and on the correlations which occur between individual nucleons. Since photo and electronuclear reactions proceed via the simple electromagnetic interaction, their effects upon the nuclear charges and currents are well understood. Unlike hadron probes, the weak nature of their interaction causes minimal perturbation of the nuclear system under investigation, and the associated nuclear transparancy allows the entire nuclear volume to be examined. In addition, the observed enhancement of the total photon absorption cross-section, with respect to the simplest sum-rules, can be used to assess the importance of meson exchange contributions to the nuclear force without recourse to a detailed model of the nucleus.

However, to extract information on the structure of the nucleus and the nature of the nuclear force, the interaction mechanism between the photon and the nucleus must firstly be understood. This mechanism is known, from experiment, to be highly energy dependent and, despite being investigated for more than 40 years, has yet to be established over the full range of photon energies obtainable from modern sources. This is principally due to the weak nature of the interaction and the unavailability of a high-flux mono-energetic photon

source, both of which have hindered the collection of experimental data in regions of low cross-section. The present work examines photonuclear processes in the energy range 40–150 MeV where experimental data are particularly scarce and where the reaction mechanism is consequently still uncertain. However, it is in precisely this region, where the photon wavelength becomes smaller than the average nuclear radius, that photonuclear reactions are expected to be most sensitive to the effects of the nucleon-nucleon correlations.

Present knowledge of the photon absorption mechanism at other energies can best be summarised as follows. At very low energies (< 10 MeV) photon absorption leads to the excitation of isolated states (bound or unbound) which are attributed to the shell model structure of the nucleus. Photodisintegration of the nucleus at such energies can be interpreted as the direct photo-ejection of a nucleon from some well defined orbit. At energies between 10 and 40 MeV nuclear excitations occur via collective vibrational modes, dominated by the giant dipole resonance (GDR). This region has received most attention over the past 40 years [1] due to the low energies and large cross-section associated with the resonance. The GDR can be interpreted, within the framework of the hydrodynamical model [2], as the oscillation of the nuclear proton fluid against the neutron fluid or, alternatively, as a superposition of shell-model particle-hole states [3]. Nuclear photo-excitation at these energies is essentially a two-step process in which all nucleons participate, the available energy becoming statistically distributed to form a 'high-temperature' nuclear state or 'compound nucleus'. The decay of the compound nucleus proceeds via particle evaporation, which in medium and heavy nuclei is restricted to neutrons only, due to the large Coulomb barrier which inhibits proton emission. Above the pion threshold at $\sim$ 140 MeV, photon absorption is dominated by the formation of nucleon resonances, such as the $\Delta(1236)$, on quasi-free nucleons [4].

In the energy range (40–150 MeV), the photon absorption cross-section is very much lower than in the bordering regions and the mechanism for absorption is not so well understood [5,6,7]. The few photodisintegration experiments which have been made in this region imply that non-resonant direct processes are important although the exact nature of the interaction has yet to be established. The outgoing momentum of emitted nucleons has been observed to substantially exceed that supplied by the absorbed photon and this momentum mismatch, which reflects the internal momentum distribution of the nucleons in the nucleus, appears to be inexplicable on the basis of single particle absorption [3]. It is thought that the strong short-range correlations [8] between nucleons play an important role in the photon absorption process and are necessary to explain the high momentum components in the data. Whether the photon couples to correlations between only two nucleons, as in the quasi-deuteron model [9], or whether even more complex cluster models are required [10,11], has yet to be determined. The interaction mechanism determines the resulting nuclear state and the nucleons which emerge directly from its decay are a good guide to the nature of this state. Unfortunately final-state interactions within the nucleus generally lead to scattering processes which result in more complex decay channels.

The present experiment examines the photodisintegration of the heavy nucleus ^{232}Th in an attempt to learn more about the photon absorption mechanism and about the final state interactions which often mask the nature of the excited state that is initially produced.

The next section of this chapter reviews some of the historical developments in the investigation of photonuclear reactions which have led to the present level of understanding. Theoretical topics and previous experiments, which are of particular relevance to the present work, are also discussed. As both electron

and photon induced reactions are investigated in this work, Section 1.3 discusses the relationship between the electronuclear and the photonuclear process and reviews the development of the virtual photon formalism. In heavy nuclei, the final state interactions which affect the initially excited nucleons are particularly important and must be properly accounted for if the final decay channels of the nucleus are to be properly interpreted. Nuclear models which attempt to incorporate these effects are described in Section 1.4. The final section outlines the principal aims of the present investigation.

1.2 Photonuclear Interactions

1.2.1 Review of Photonuclear Experiments

The photodisintegration process was first observed by Chadwick and Goldhaber in 1934 [12], when they discovered protons in a deuterium gas ionisation chamber bombarded with 2.61 MeV γ-rays from ^{208}Tl. A similar process was found to occur on ^{9}Be when irradiated with photons [13] or with electrons [14] and this led to investigations of the 'nuclear photo-effect' in a wide range of nuclei. However these early photonuclear experiments were restricted to the use of γ-rays from naturally occuring radioactive isotopes or from the decay of the highly excited nuclear states formed in reactions induced by protons from low-energy accelerators. They could therefore be studied at only a limited number of photon energies until the invention of the betatron in 1940 [15]. Larger photon fluxes and hence higher reaction yields could then be obtained by using the bremsstrahlung radiation produced by high energy electrons in thick radiators, and it became possible to make detailed studies of the reactions as a function of photon energy. With bremsstrahlung beams of up to 35 MeV, evidence was found of a photonuclear giant resonance by Baldwin and Klaiber [16] in 1947. At these energies, the photo-excited nuclei were found to decay

principally by the emission of one or possibly two nucleons (mainly neutrons) and so, by detecting these particles directly [17] or by measuring the residual activity of the (γ, n) and $(\gamma, 2\mathrm{n})$ reaction products [18], it was possible to investigate the nuclear photo-effect in a large number of elements. Improvements in accelerator and detector technology throughout the 1950's, as well as refined analysis techniques, led to extensive studies in this low energy region and it was soon realised that *all* nuclei exhibit a strong resonance in the photon absorption cross-section between 10 and 30 MeV. The neutron counting method had the advantage that it did not depend upon the reaction products being unstable and did not rely upon knowledge of the radioactive decay schemes, many of which had yet to be determined. However as only the *total* neutron yield was measured in these experiments, and this included contributions from $(\gamma, 2\mathrm{n})$ as well as from (γ, n) reactions, some energy dependent model of the neutron multiplicity was required to transform the measured yields into photonuclear cross-sections. Since photon absorption, via the giant resonance, was thought to lead to the formation of a highly excited compound nucleus without prior particle emission, the corrections for multiple nucleon emission were generally based on statistical model calculations [19].

The total neutron counting method was extended beyond the giant resonance in 1953 by Jones and Terwilliger [20] who measured the total photonuclear absorption cross-section for eleven elements up to 320 MeV. However, the neutron multiplicity corrections, which were again evaluated on a statistical basis, were shown in other experiments to be of limited validity at such high energies. The statistical model predicted that the individual $(\gamma, x\mathrm{n})$ photoreactions, now of much higher multiplicity due to the increased nuclear excitation, would have strength over only a narrow range of photon energies, each cross-section falling rapidly to zero as a new channel became energetically possible. It was

also predicted that the nuclear de-excitation would involve the evaporation of only low energy ($\sim$ 2 MeV) nucleons but such effects were not observed experimentally. With bremsstrahlung radiation at an end-point of 86 MeV, Sugarman and Peters [21] used activation methods to measure the integral yields of several $(\gamma, xnyp)$ reactions from ^{209}Bi, which involved the emission of 0, 1 or 2 protons as well as up to 8 neutrons. Their observation of strong charged-particle decay channels, especially in a heavy nucleus where the Coulomb barrier was thought to suppress proton evaporation, suggested that these particles were being emitted with energies much greater than could be explained by a statistical mode of decay. The detection of high energy neutrons and protons from a range of photo-excited nuclei [22] merely confirmed the existance of a 'direct' photonuclear process above the GDR. Consequently, photon absorption mechanisms were suggested by which the excitation energy would be shared initially between a relatively small number of nucleons. Of these, the 'quasi-deuteron' model of Levinger [9] has had perhaps the most success in describing photonuclear reactions above the GDR. In this model, photon absorption is assumed to occur on a 2-nucleon cluster and, since the interaction is known to be predominantly dipole in character, it is further assumed that only neutron-proton pairs contribute to the process. The closely correlated n-p pair, responsible for the absorption, were considered by Levinger to have a wave function resembling that of the free deuteron and this considerably simplified the theoretical calculations.

In the early 1960's, the development of solid-state detectors, which offered excellent energy resolution, allowed the cross-sections for many more $(\gamma, xnyp)$ reactions to be determined from the complex γ-ray activity of β-unstable reaction products [23]–[28]. However, due to the unfavourable nature of the residual nuclide decay schemes and the lower cross-sections associated with those reactions which involved charged particle emission, nearly all of these mea-

surements were focussed on the $(\gamma, x\mathrm{n})$ photoneutron channels. The individual cross-sections were found to have finite strength even to quite large energies and this was again inconsistent with a statistical evaporation hypothesis. In an attempt to understand this behaviour, calculations were performed which extended the quasi-deuteron model to include the effects of final-state interactions upon the initially excited particles. Although the possibility of fast particle emission was recognised, it was predicted that, in complex nuclei, the strength of the final-state interactions would markedly reduce the probability of such processes and would predominantly lead to the formation of a compound nucleus without prior particle emission. The subsequent decay was therefore predicted to occur via channels of relatively high multiplicity which were not altogether representative of the initial energy distributions. These calculations were a marginal improvement over those obtained from the statistical model alone but were again found to underestimate the measured cross-sections at high energies, probably due to an incorrect treatment of the final state interactions. Despite being overemphasised in the calculations, it was clear that compound nucleus evaporation did indeed dominate the measured $(\gamma, x\mathrm{n})$ channels and although these photoneutron reactions showed some evidence of a direct interaction mechanism, they were relatively insensitive to the details of that process. As a result, little could be deduced from the $(\gamma, x\mathrm{n})$ measurements regarding the nature of the initial photon absorption. The $(\gamma, x\mathrm{n}y\mathrm{p})$ charged particle channels which, in medium and heavy nuclei, necessarily involve the emission of high energy protons, would have been more sensitive to the initial energy distributions and hence to the photon absorption mechanism, but were not measured in any of the previous investigations.

During the past twenty years the development of electron accelerators with energies of several GeV has allowed activation experiments of this type to be

continued to photon energies well above the pion threshold. At these energies, the effects of pion production on quasi-free nucleons are found to dominate the interaction and to cause a substantial rise in the photon absorption cross-section. As a result this region has been relatively well studied, with major experimental contributions coming from the group at Lund [29].

In all of the experiments described above, the photonuclear reactions were studied using continuous bremsstrahlung or virtual photon radiation, usually by incrementing the end-point energy to obtain the integral reaction yield as a function of electron energy. To determine the cross-section as a function of photon energy, the radiation spectrum had to be unfolded from the measured data. However, uncertainties associated with the deconvolution procedure often reduced the reliability of the final cross-section measurements and, in the past, bremsstrahlung experiments have not always led to unambiguous results. For this reason, mono-energetic photon sources were sought, which would in principle avoid all of the difficulties associated with continuous energy beams.

From the mid 1960's onwards, an increasing number of experiments were performed, at Saclay [30] and at Livermore [31], using quasi-monochromatic photon beams obtained from the in-flight annihilation of positrons. The photon spectrum from these sources comprised a narrow peak of $e^+ - e^-$ annihilation photons on a continuous background of e^+-bremsstrahlung. By assuming charge equivalence, the positron bremsstrahlung contribution to the reaction yield could, in principle, be subtracted from the measurement by repeating the experiment under identical conditions with e^--bremsstrahlung. In association with high-efficiency 4π neutron detectors, capable of distinguishing between neutron events of different multiplicity, these photon sources have been used extensively during the past 20 years to measure photoneutron cross-sections for many elements in the GDR region [1]. In general, the results of these experi-

ments confirmed the findings of the earlier bremsstrahlung measurements but despite the use of similar systems, the Saclay and Livermore results were often found to be in substantial disagreement. These disparities have recently been attributed [32] to differences in the multiplicity sorting at the two facilities, although it is not yet clear which of the measurements are in error.

Saclay have recently extended their measurements of partial photoneutron cross-sections to energies beyond the GDR [33]–[37] and thus to reactions of even greater multiplicity. The latest Saclay neutron detection system, associates each $(\gamma, x\mathrm{n})$ partial photoneutron channel with a *measured* neutron multiplicity, although the cross-sections are *inclusive* of any number of undetected charged particles i.e.

$$\sigma_{\mathrm{inc}}(\gamma, x\mathrm{n}) = \sigma(\gamma, x\mathrm{n}) + \sigma(\gamma, x\mathrm{n1p}) + \sigma(\gamma, x\mathrm{n2p}) + ...$$

Due to the low fluxes ($\sim 10^4$/s) obtainable with annihilation sources, reaction yields from these experiments have generally been small and it is difficult to determine the individual $\sigma_{\mathrm{inc}}(\gamma, x\mathrm{n})$ excitation functions. More fundamentally, it is impossible with such a system to separate those reactions which do and do not involve charged particle emission. The Saclay results do provide a valuable measurement of the total photon absorption cross-section above the GDR, since the experimental uncertainties associated with the *sum* of the partial cross-sections are generally quite low. However, the classification of events by 'neutron multiplicity sorting', which was shown to have uncertainties even for the lowest multiplicity reactions, must at present be treated with some caution. This is especially true for the measurement of photonuclear processes in very heavy nuclei where the multiplicity is further complicated by the presence of fission neutrons. Unfortunately, there are also differences between the e^+ and e^- bremsstrahlung spectra which increase with photon energy and consequently lead to a reduction in the mono-energetic part of the photon spectrum. In ad-

dition, systematic errors arise due to atomic interactions of the annihilation photons in the photonuclear target, which form e^+- e^- pairs and give rise to low energy bremsstrahlung and therefore to spurious events. Since this process depends upon the thickness of the target material, the measurements have to be repeated with targets of different thickness in order to evaluate a suitable correction. These effects, coupled with the low photon intensities achievable from annihilation sources, mean that conventional bremsstrahlung experiments, for the investigation of partial photoreaction cross-sections above the GDR, are significant even today.

1.2.2 Total Photonuclear Absorption

The total cross-section for photon absorption is an important quantity in nuclear physics since it can, in comparison to the simplest sum rules, yield valuable information on the nucleon-nucleon force. Various techniques have been used to measure this quantity but experimental data, especially for heavy nuclei and high photon energies, are still unacceptably few.

The Mainz group have determined the total photonuclear cross-section for various light nuclei using a direct absorption method [38] in which the attenuation of a collimated bremsstrahlung beam is measured as it passes through the absorbing material. However, atomic effects account for up to 97 % of the measured attenuation and have to be calculated and subtracted to obtain the nuclear absorption cross-section. This technique requires precise measurements and detailed knowledge of the atomic cross-sections and since these become unreliable above A $\sim$ 40, the method is unsuitable for all but the lightest nuclei.

For medium and heavy nuclei the sum of the partial photonucleon cross-sections obtained from activation experiments provides a useful estimate of the

total absorption cross-section,

$$\sigma_{\rm tot}(\mathrm{E}_\gamma) \approx \sum_{xy} \sigma_{x\mathrm{n}y\mathrm{p}}(\mathrm{E}_\gamma)$$

but rarely do all of the reaction products have half-lives and decay schemes favourable to the residual activity method and in previous experiments of this type [24,28] most measurements have been restricted to the photoneutron channels only. Intranuclear cascade models (Section 1.4) are commonly used to evaluate the missing (predominantly charged particle) channels but, until the validity of these calculations can be checked experimentally, such results must also be treated with some caution. In addition, the above summation neglects those reactions which terminate in fission, even though this is known to be an important mode of decay in heavy nuclei (Section 1.2.3).

Perhaps the most useful method for determining total photonuclear absorption cross-sections is the neutron counting technique used at Saclay [39] since it can, in principle, be applied to a much wider range of nuclei. For a given photon energy, the total cross-section is approximately equal to the sum of the partial photoneutron cross-sections (inclusive of charged particles) i.e.

$$\sigma_{\rm tot}(\mathrm{E}_\gamma) \approx \sum_{x} \sigma_{\rm inc}^{\mathrm{E}_\gamma}(\gamma, x\mathrm{n})$$

Those reactions (γ,p), $(\gamma,2\mathrm{p})$, (γ,α) etc., involving charged particles only, are undetected by this method and are consequently missing from the above summation. However, calculations [33] show these contributions to be less than ~ 5 % of the total cross-section. An advantage of the Saclay method is that the photofission contribution to the total cross-section can, in principle, be evaluated if the fission neutrons are also detected. The major difficulties associated with this technique are the determination of absolute neutron detection efficiencies and the removal of target-dependent and target-independent background. Until some of the individual photoreaction cross-sections can be checked against

independent activation measurements, the multiplicity sorting process must also be treated with some caution.

Examples of the total photon absorption cross-section for two heavy nuclei are shown in Figures 1.1 and 1.2. Such results, which are similar for all nuclei, clearly show the differing behaviour of the photonuclear absorption cross-section at different photon energies.

Giant Resonances (E_γ < 40 MeV)

It is now well known that the E1 giant resonance in the low-energy photon absorption cross-section is a phenomenon exhibited by all nuclei which can be explained on the basis of collective or independent-particle models. In spherical nuclei the resonance is relatively narrow and can be fitted by a single Lorentzian curve, while in non-spherical nuclei it is seen to be somewhat broader. In deformed nuclei, such as ^{232}Th (Figure 1.3), the GDR is actually split into two resonances, each associated with vibrations along an axis of symmetry of the nucleus [41]. In heavy nuclei, the large Coulomb barrier inhibits proton evaporation and the GDR decays predominantly via the (γ, n) and $(\gamma, 2n)$ channels. In fissile nuclei, the (γ, F) photofission reaction also contributes to the nuclear de-excitation process and can, in some cases, exhaust a substantial fraction of the absorption cross-section.

Multipole resonances other than E1 were predicted by collective model and many-body calculations [41] but experimental evidence for these has only recently been obtained. Inelastic scattering measurements show evidence of several multipole resonances below the GDR [42] as well as an E2 quadrupole resonance [43] higher in energy at $\sim 120.A^{-\frac{1}{3}}$ MeV. These higher order collective effects may therefore account for *some* of the strength above the giant dipole resonance but are almost certainly confined to energies below the present

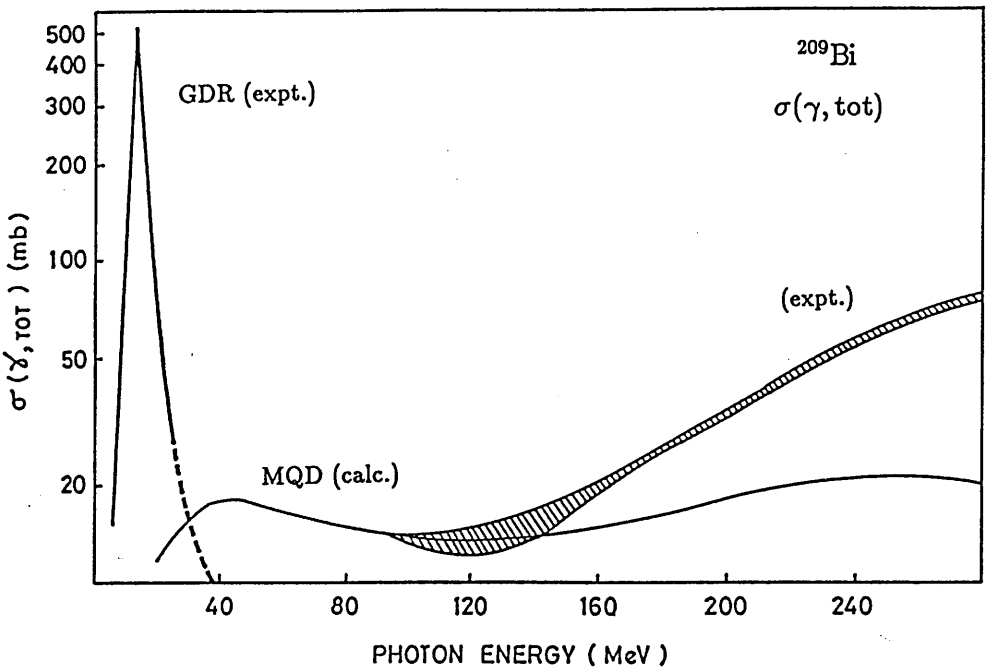

Figure 1.1: Total photon absorption cross-section for ^{209}Bi. The cross-section in the GDR region was measured by a neutron counting method at Livermore. The shaded area above the pion threshold is experimental data taken from Reference [40]. No data exists for the region between the GDR and the meson threshold and only an estimated cross-section, based on the modified quasi-deuteron model, is shown (L = 8, D = 60 MeV).

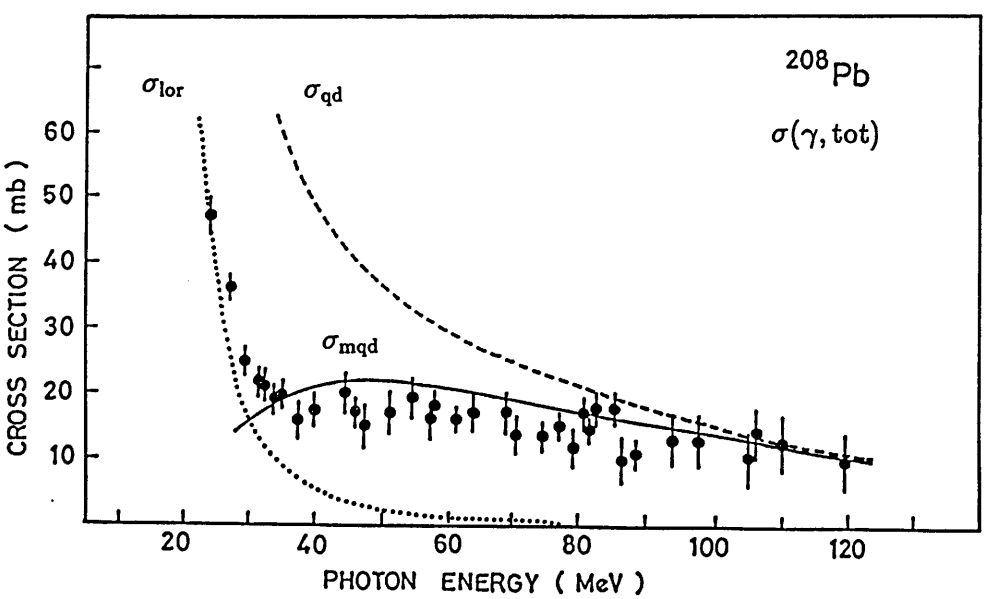

Figure 1.2: Total photon absorption cross-section for ^{208}Pb measured by the Saclay method [37]. The dotted line is an extrapolation of the Lorentz curve fit to GDR data. The dashed line is the simple quasi-deuteron formula with L = 4.6. An improved fit (solid line) is obtained using the modified quasi-deuteron model (L = 8, D = 60 MeV).

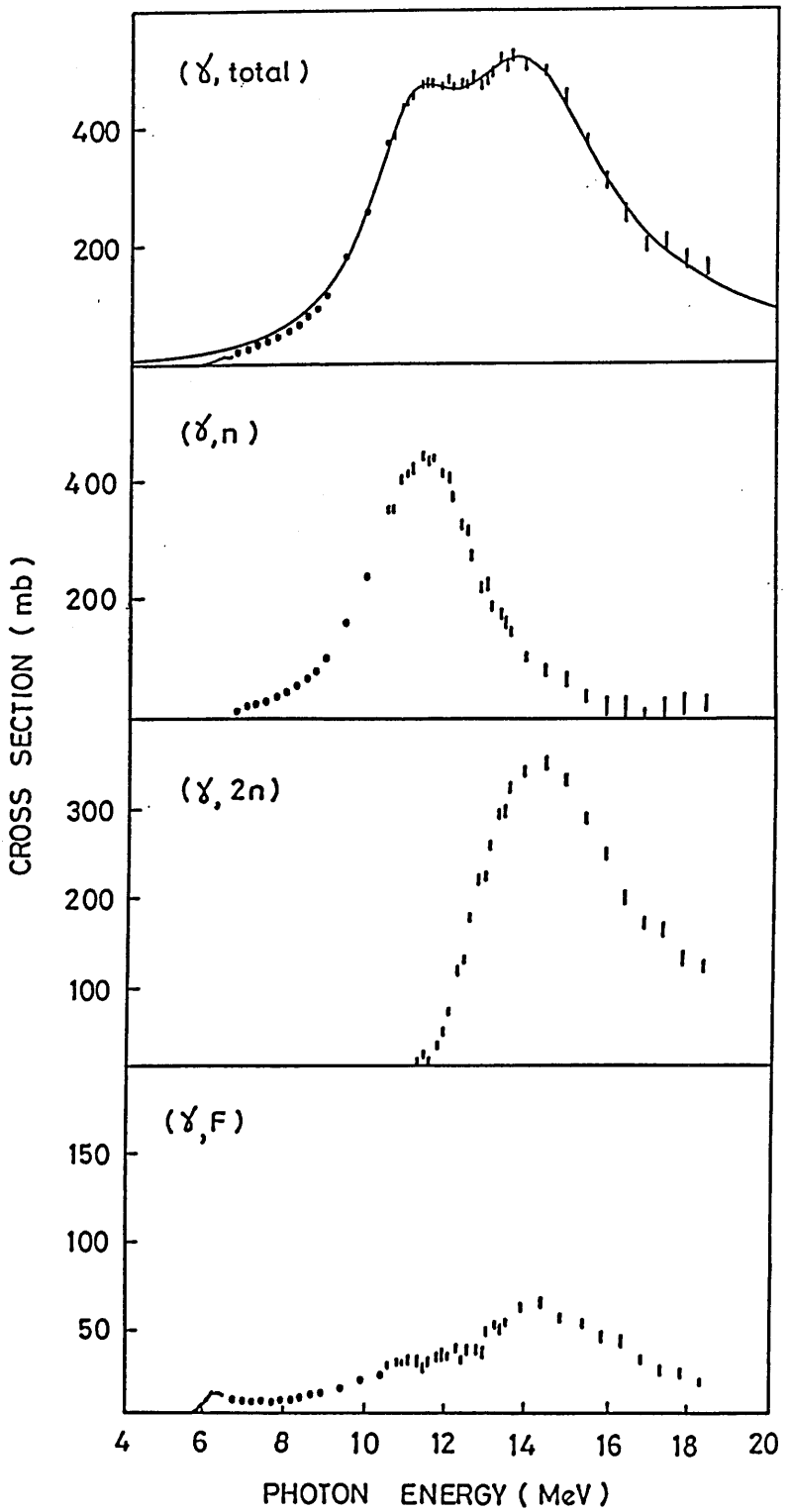

Figure 1.3: Total photonuclear cross-section for ^{232}Th in the resonance region (data from Ref. [56] - Livermore). The upper figure shows the total absorption cross-section with double-Lorentz curve fit. The partial photoneutron and photofission decay channels are shown below.

region of interest (40–150 MeV).

The Quasi-Deuteron Model (30–140 MeV)

As shown in Figure 1.2, an extrapolation of the Lorentzian curve from the GDR region fails to account for the small but finite cross-section observed at photon energies above $\sim$ 30 MeV, and experimental observations in this region are no longer found to be consistent with a statistical mode of decay. Indeed the observed equivalence of (γ,n) to (γ,p) reactions, the high energies and forward peaking of photoprotons [22] and the existence of high energy tails on the excitation functions of individual photoreactions [23,44], all point to some form of direct process in the photon-nucleus interaction. A direct knockout mechanism has been suggested, but, contrary to observation, it predicts that the $(\gamma,\mathrm{p_o})$ reaction for ground state transitions should be substantially greater than the $(\gamma,\mathrm{n_o})$ process. In reality these reactions are found to be of comparable magnitude. In addition, $(\gamma$,p) measurements, which show the outgoing proton momentum to often greatly exceed that supplied by the photon, imply that the proton can in some cases have a very large momentum inside the nucleus. In general, the high momentum components observed in the data are much too large to be explained on the basis of a normal shell-model knockout and this suggests that the short-range correlations between nucleons play an important role in balancing the momentum mismatch.

These ideas are contained phenomenologically in the quasi-deuteron model of Levinger [9] which assumes that photonuclear interactions above $\sim$ 100 MeV can be explained on the basis of a 2-body process. Since the interaction is known to be predominantly dipole in character, it is assumed that only neutron-proton pairs contribute to the absorption, and since the two nucleons are required to be close together in a high relative momentum state, it is further assumed that the

wavefunction of this 'quasi-deuteron' pair is similar to that of the free deuteron. The quasi-deuteron photon absorption cross-section at energy E_γ can therefore be written as

$$\sigma_{qd} = L \frac{NZ}{A} \sigma_d \tag{1.1}$$

The quantity NZ/A is the number of n-p pairs per unit volume, σ_d is the real deuteron cross-section and L, the so called Levinger parameter, corresponds to the relative probability that the two nucleons, in nuclear matter and in the deuteron, are close enough for photon absorption to occur.

The quasi-deuteron model therefore provides a simple phenomonological interpretation of the photon absorption process above the GDR which has proved to be successful in several respects. In light nuclei for example, the final-state interactions are less important than elsewhere and the photo-excited nucleus decays via simple channels which, in principle, directly reflect the initially excited state. As suggested by the quasi-deuteron model, the two-nucleon (γ, np) reactions are found [38] to account for a much larger fraction of the total photon absorption cross-section above the GDR than do the (γ, n) or (γ, p) single-nucleon channels. In addition, the total cross-sections measured for light nuclei at Mainz can be fitted, reasonably well, by the simple quasi-deuteron formula using an L value of $\sim$ 4.6. Evidence has also been found for the direct emission of correlated n-p pairs from nuclei such as ^{12}C [46], which can again be attributed to a quasi-deuteron process. However, even in nuclei as light as carbon, the final-state interactions are noted [47] to have a substantial influence upon the energy spectra and angular distributions of the emitted particles and so evidence such as this requires further confirmation.

The simple quasi-deuteron formula does however have a limit to its success and when applied to the Saclay total cross-section data for medium and heavy nuclei [36], is clearly seen to diverge at low (< 100 MeV) photon energies (Fig-

ure 1.2). Levinger [48] suggested that, due to Pauli blocking of some of the states reached by the initially excited n-p pair, there would be a damping of the cross-section at photon energies comparable to the nuclear Fermi energy. He chose to represent this blocking by a quenching factor in the absorption cross-section, writing the 'modified' quasi-deuteron cross-section as

$$\sigma_{mqd} = L \frac{NZ}{A} \exp\left(-\frac{D}{E_\gamma}\right) \sigma_d \qquad (1.2)$$

No theoretical evaluation of D has yet been made although the Saclay data suggest a value of $D \approx 60$ MeV when $L = 8$. The modified quasi-deuteron formula has been relatively successful in explaining much of the total cross-section data [36] for medium and heavy nuclei between 30 and 140 MeV (Figure 1.2).

More rigorous quantum-mechanical treatments of the photon-nucleus interaction, which start from a shell-model description of the absorption process and introduce N-N correlations to account for the high momentum components in the proton wavefunction, essentially reproduce the quasi-deuteron model which was derived phenomenologically. Its success is primarily due to the importance of charge exchange terms in the N-N potential, which imply that the photon couples predominantly to n-p pairs rather than n-n or p-p.

Pion Photoproduction (E_γ > 140 MeV)

As can be seen from the modified quasi-deuteron calculation of Figure 1.1, the two-nucleon absorption process is predicted to remain finite even to quite high energies but, beyond the pion production threshold, new degrees of freedom enter into the photon absorption cross-section. The rise in the cross-section above $\sim$ 140 MeV [24] is thought to be due to the excitation of the Δ-resonance on quasi-free nucleons. However, since these isobaric resonances lead to the formation of real pions (Figure 1.4), such reactions are energetically forbidden in the present region of interest.

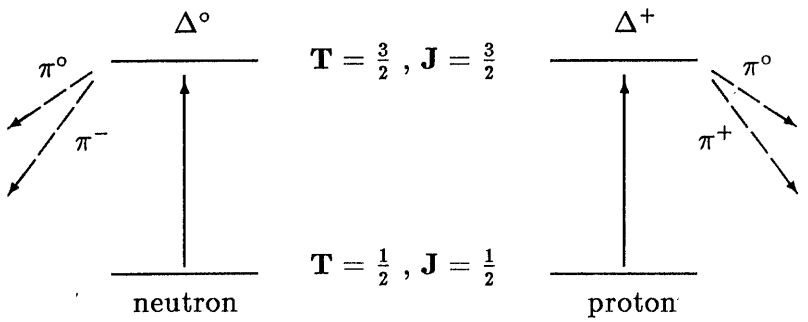

Figure 1.4: Schematic representation of the excitation and decay of the Δ-resonance.

Sum Rules

Sum rules provide a model-independent theoretical prediction of the total photon absorption strength, integrated over some well defined energy range. In heavy nuclei only electric transitions contribute significantly to the absorption process [49] and even then only ~ 6 % of the integrated cross-section corresponds to transitions other than E1 [50].

The classical dipole sum rule [51] for a nucleus, $^{Z}_{N}A$, is essentially a sum of the individual absorption strengths of the Z coupled oscillators (independent of their coupling) and gives the following value for the integrated cross-section

$$\Sigma_o^{E1} = \int_o^\infty \sigma(E_\gamma) dE_\gamma \approx 60 \frac{NZ}{A} \quad \text{mb.MeV} \tag{1.3}$$

Although experimental results are not in complete agreement, total absorption cross-sections integrated up to the pion threshold are generally found to exceed the classical dipole sum rule by a factor of $1.4 \rightarrow 2$. This can not be attributed to contributions from multipoles other than E1 since these are firstly known to be small and secondly shown to cancel with dipole retardation effects [52] in such a way that the measured integral cross-section remains a reasonable estimate of the E1 sum rule. The anomalously large values obtained experimentally, have therefore prompted new calculations of the electric dipole sum-rule which

also take into account the exchange of mesons between the nucleons. Levinger and Bethe [53] derived a modified sum rule, inclusive of charge exchange terms, which shows the absorption cross-section to be enhanced by a factor κ

$$\Sigma^{\mathrm{E1}} = \Sigma_{\circ}^{\mathrm{E1}} (1 + \kappa) \tag{1.4}$$

In effect, this enhancement results from the increased number of charges available for photon absorption. In the dipole approximation, κ is therefore a global measure of the charge exchange component of the nuclear force and as such merits further investigation by more detailed total absorption measurements.

1.2.3 Photofission

To understand the behaviour of the $(\gamma, xnyp)$ photoreactions in heavy nuclei or to evaluate the total absorption cross-section from such quantities, proper account must be taken of the competition between particle emission and fission decay.

In the GDR region, the (γ, F) photofission cross-section for ^{232}Th has been measured at both Saclay [55] and Livermore [56], using monochromatic photons and a fission neutron counting method. The Livermore results exceed the Saclay values by ~ 80 % but agree with the bremsstrahlung measurements of Arruda Neto *et al.* [57] and therefore appear to be the more acceptable of the two values. Figure 1.3 shows that the competition between photoneutron emission and photofission in ^{232}Th is non-negligible even at low excitation energies and increases with the number of neutrons evaporated. The reason for this is that the (γ, n) reaction competes only with the (γ, f) 'first-chance' fission process while the $(\gamma, 2\mathrm{n})$ reaction is further depleted by the additional possibility of (γ, nf) 'second-chance' fission.

The ^{232}Th photofission cross-section above the GDR, has recently been measured at Saclay using monochromatic 'tagged' photons and a fission fragment

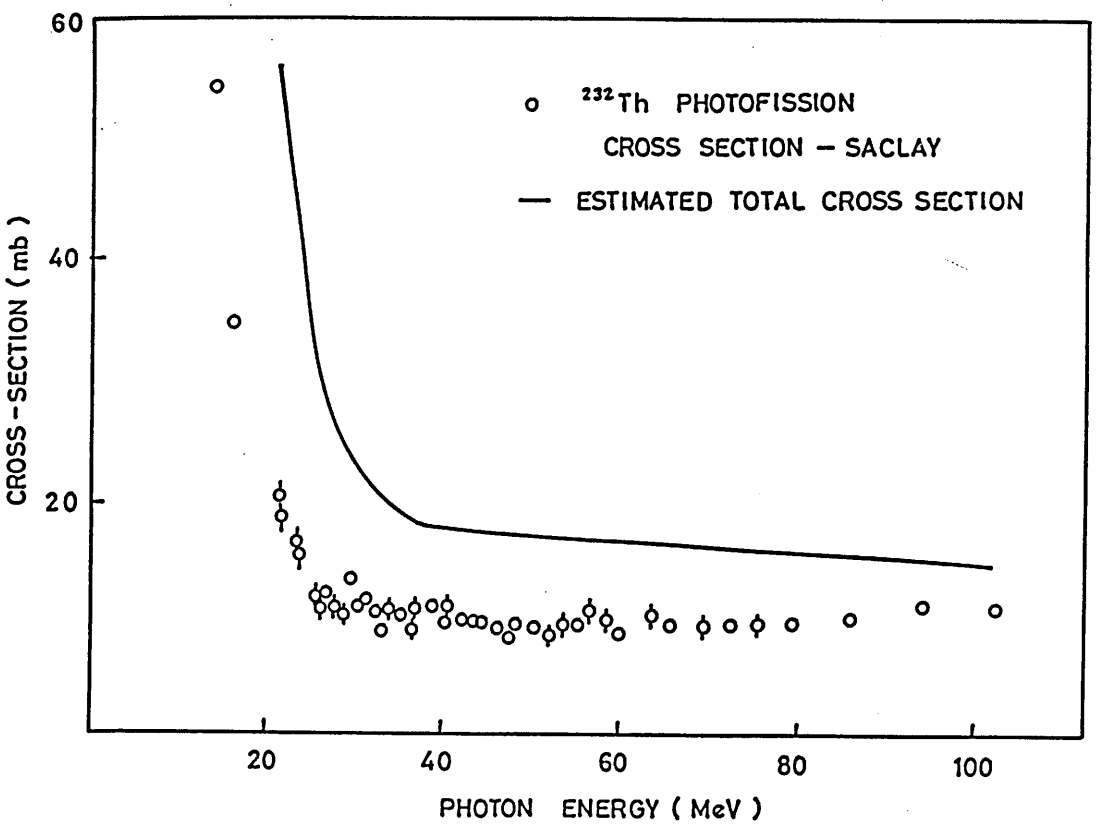

Figure 1.5: The absolute photofission cross-section for ^{232}Th measured at Saclay [54] which exhausts a substantial fraction of the total photon absorption cross-section above 30 MeV. The total cross-section was estimated from giant resonance data and the modified quasi-deuteron model (L = 20.9, D = 111.2 MeV). These parameters were taken from best-fits to the measured cross-sections of similar mass nuclei [36].

detection method. These results (Figure 1.5), which are free from the systematic errors of the $e^+ - e^-$ annihilation method and from the uncertainties associated with neutron multiplicity evaluation, agree with the Livermore GDR data in the region where the two measurements overlap. No measurement of the total cross-section for ^{232}Th has yet been made above the GDR, but the following expression provides a convenient estimate

$$\sigma_{\rm tot}(E_\gamma) \approx \sigma_{\rm lor}(E_\gamma) + \sigma_{\rm mqd}(E_\gamma) \tag{1.5}$$

Here, $\sigma_{\rm lor}$ is a Lorentz curve fit to the giant resonance data measured at Livermore (Figure 1.3) and $\sigma_{\rm mqd}$ is a modified quasi-deuteron calculation for ^{232}Th using parameters L and D obtained from the best fits to other heavy nuclei [36]. These results (Figure 1.5) predict that the (γ, F) photofission reaction exhausts a substantial fraction of the total cross-section above the GDR as well as below.

If it can be assumed that, following any precompound fast particle emission, the decay of a heavy compound nucleus proceeds only via neutron evaporation or fission decay, then for the $i^{\rm th}$ daughter reached in the neutron evaporation chain (Figure 1.6), the fission probability is given [58] by

$$P_f^{(i)} = \frac{\Gamma_f^{(i)}}{\Gamma_n^{(i)} + \Gamma_f^{(i)}} \tag{1.6}$$

The fissility of the daughter nuclei varies approximately as Z^2/A [58] and therefore increases with the number of neutrons emitted. The probability that the nucleus will fission at *some* point during its de-excitation, i.e. the total fission probability, is just

$$P_f^{\rm tot} = 1 - \prod_i \left(1 - P_f^{(i)}\right) \tag{1.7}$$

For the nucleus to de-excite through a $(\gamma, xnyp)$ channel which does *not* end in fission, it must survive the possibility of fission at each stage of the neutron evaporation chain. The multi-chance nature of the fission process should therefore lead to a depletion in the yield of those reaction products which result

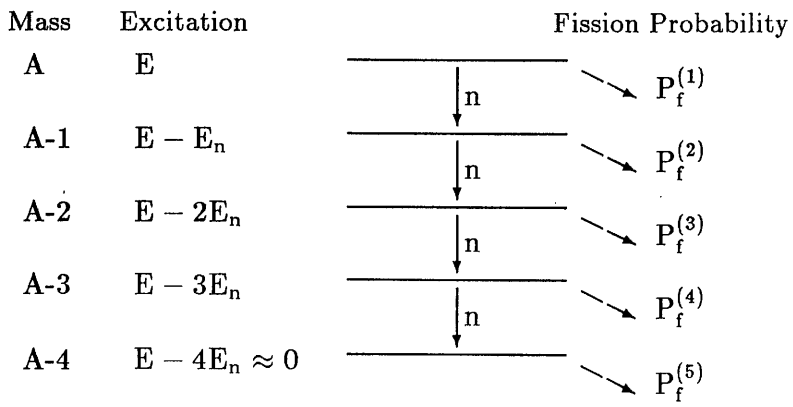

Figure 1.6: Schematic representation of fission competition in the neutron evaporation chain of a compound nucleus ; mass A, excitation energy E. Each daughter nucleus which is reached in the chain may decay via further neutron evaporation (requiring energy E_n) or may undergo fission with a probability $P_f^{(i)}$.

from high multiplicity reactions. At present, the individual fission probabilities $P_f^{(i)}$ have been measured only in the giant resonance region and therefore for first and second chance processes only. No experimental information exists on the fission parameters of those nuclei which are reached after multiple nucleon emission and so there is clearly a need to obtain $(\gamma, xnyp)$ excitation functions for photoreactions above the GDR as a test of the multi-chance fission process. However, not all nuclei are conducive to such investigations. For the less fissile pre-actinide nuclei, such as ^{197}Au, the $(\gamma, xnyp)$ channels appear to dominate the nuclear de-excitation process at all energies, while for the Uranium isotopes, the fission probability approaches unity above $\sim$ 50 MeV and the (γ, F) reaction then exhausts the total photon absorption cross-section. The ^{232}Th nucleus, being of intermediate fissility, provides a useful testing ground for photofission calculations at high energies since neither the fission nor the non-fission decay channels completely dominate the nuclear disintegration process.

1.3 Nuclear Electrodisintegration

1.3.1 The Electron–Nucleus Interaction

The electro-magnetic field of an incident electron interacts with nuclear charges and currents in a manner similar to that of a real photon. In fact the close resemblance between electron and photon induced nuclear reactions was noted as long ago as 1939 [14]. It is clear from the kinematics of the electron–nucleus interaction that the nuclear excitation is determined by the scattering angle of the electron and may therefore take any value up to the incident electron energy, E_e. Unlike photo-absorption however, where the momentum transfer to the nucleus, q , is completely determined by the photon energy, the momentum transfer from a scattered electron has a continuous distribution for any given excitation.

In virtual photon theory [59,60] the effect of the electron's electro-magnetic field upon the target nucleus is considered to be equivalent to an incident burst of radiation. In this treatment the electro-magnetic field is decomposed into its various multipoles (λL) and a 'virtual' radiation spectrum defined for each. These virtual spectra can then be used to relate electrodisintegration processes to the corresponding photodisintegration reaction.

When an electromagnetic interaction occurs, the nucleus samples those multipole components in the radiation field (usually only one or two) which excite allowable transitions. The total photonuclear reaction cross-section σ_γ can in general be written as a sum over all multipoles ; this is just

$$\sigma_\gamma(E_\gamma) = \sum_{\lambda L} \sigma_\gamma^{\lambda L}(E_\gamma) \tag{1.8}$$

where

λ = E for electric ; M for magnetic

L = multipole order

E_γ = photon energy

$\sigma_\gamma^{\lambda L}(E_\gamma)$ = photo-absorption cross section for photons of energy E_γ and multipolarity λL

Since the virtual photon spectra (like bremsstrahlung) have a continuous energy distribution, the electrodisintegration cross-section for electrons of energy E_e is an integral quantity

$$\sigma_e(E_e) = \sum_{\lambda L} \int_0^{E_e - m_o} \sigma_\gamma^{\lambda L}(E_\gamma)\, N_e^{\lambda L}(E_e, E_\gamma)\, \frac{dE_\gamma}{E_\gamma} \tag{1.9}$$

$N_e^{\lambda L}(E_e, E_\gamma)$ represents the virtual photon spectrum for multipole λL at endpoint E_e and m_o is the electron rest mass. The equivalent cross-section obtained with bremsstrahlung radiation σ_{br} has a similar form

$$\sigma_{br}(E_e) = \sum_{\lambda L} \int_0^{E_e - m_o} \sigma_\gamma^{\lambda L}(E_\gamma)\, N_{br}^{\lambda L}(E_e, E_\gamma)\, \frac{dE_\gamma}{E_\gamma} \tag{1.10}$$

Due to the plane-wave nature of real radiation all multipole components are present in equal amounts, that is to say the bremsstrahlung spectra are identical for all multipolarities and the decomposition of Equation 1.10 is redundant. i.e.

$$\sigma_{br}(E_e) = \int_0^{E_e - m_o} \sigma_\gamma(E_\gamma)\, N_{br}(E_e, E_\gamma)\, \frac{dE_\gamma}{E_\gamma} \tag{1.11}$$

The virtual spectra are, on the other hand, markedly different for each of the multipole orders and the decomposition of Equation 1.9 is highly significant. When more than one order contributes to the absorption cross-section, a clear distinction arises between real and virtual radiation fields which differ then, not only in their energy distribution, but also in their mixture of multipoles orders. Due mainly to mathematical difficulties in the computation, 'exact' calculations of the virtual photon spectra remain at a fairly preliminary stage. In the past various approximations have been used to estimate the virtual photon intensities but with varying degrees of success. These approximate spectra and their regions of validity are discussed in the following section.

1.3.2 Virtual Photon Approximations

The original concept of the virtual photon spectrum comes from Weizsäcker [59] and Williams [60] who performed a Fourier analysis of the rapidly changing electromagnetic field of the passing electron to obtain the relative multipole strengths. The Coulomb interaction between the electron and nuclear charge was found to add a longitudinal component into the interaction mechanism which is not present in the purely transverse field of the real photon. The components of this longitudinal field are similar to those of the transverse field but with the addition of an $L = 0$ multipole. Electrons, unlike photons, may thus induce nuclear excitations which involve zero angular momentum transfer.

An accurate calculation of the virtual photon intensities must correct for influences of the nuclear charge upon the incident electron (commonly called the Z-correction) and also allow for effects of the variation of the electron's electromagnetic field over the finite size of the nucleus (the A-correction). Such computations are however complex and generally require many approximations. The development and validity of the most common formalisms is outlined below.

PWBA + point nucleus

The earliest calculations of virtual photon intensities used the plane wave Born approximation (PWBA) and long wavelength limit [61]. In this approach the incident and scattered electron are represented by plane waves and distortions of the incoming and outgoing waves, due to the nuclear Coulomb field, are omitted. In addition, the nucleus is considered to be of negligible extent ; an assumption which holds only when the electron wave function has constant amplitude in that vicinity. The approximation is valid in the long wavelength limit, $qR_{nuc} \ll L$, where R_{nuc} represents the nuclear radius and q is the electron momentum. Only then can the electron be reasonably assumed to move in the

field of a point charge.

The main advantage of this approach lies in the simplicity of the expressions which result for the multipole intensities. These depend upon kinematic factors only and can be evaluated without detailed knowledge of the nuclear wavefunction. In comparison with measured electrodisintegration cross-sections in the giant resonance region [62]–[68], the plane wave approximation has had mixed success. In light nuclei, good agreement was found with measured cross-sections by assuming $\sim$ 10% E2 contribution to an otherwise dominant E1 mode of absorption. In heavy nuclei however, the required E2 contribution of up to 50% proved far in excess of that expected for an excitation process which was thought to be predominantly dipole in nature. (Theoretically, the ratio between E1 and E2 integrated photo-absorption cross-sections can be obtained from sum rules [69,70]). However, the inclusion of finite size effects into the virtual photon formulation served only to *increase* the discrepancy and therefore indicated some other source of error for the heavier nuclei. It became apparent that for high Z nuclei the Coulomb distortion of the electron wavefunction could no longer be neglected. A subsequent re-analysis using a 'distorted wave' treatment [71,72] proved that the data could, in fact, be fitted on the assumption of E1 transitions only, if the effects of charge distortion were incorporated.

Due to the approximations involved, virtual photon spectra calculated in the PWBA + 'long wavelength limit' are valid only for low Z, low A nuclei and in an energy domain $E_e < 30$ MeV. An exact PWBA calculation for reactions which involve a 2-body hadronic final-state has recently been released by Tiator and Wright [73]–[75] and is particularly relevant for quasi-deuteron interactions. For larger electron energies and high Z, high A nuclei one must take into account both penetration into the nuclear surface and Coulomb distortion of the electron wave. The methods used to apply such corrections are discussed below.

DWBA + point nucleus

The significance of charge distortion effects became clear in an investigation, performed by Herring *et al.* [76], of electron and positron induced nuclear disintegration. Their results showed that a discrepancy exists between $\sigma(e^-, e^{-\prime}X)$ and $\sigma(e^+, e^{+\prime}X)$ cross-sections due to the electron's closer passage to the positively charged nucleus. When this discrepancy was found to increase with Z it prompted investigations of a 'distorted wave' treatment for the electron–nucleus interaction which would properly correct for the influence of the nuclear charge upon the electron wavefunction. In the distorted wave Born approximation (DWBA) the Z-correction is made by substituting Coulomb waves for plane waves, in which case the spectra must be written as a sum over partial waves. (Coulomb waves are solutions of the Dirac equation with a point charge Coulomb potential and as such are known analytic functions).

The first distorted wave treatment of virtual photon theory was performed by Gargaro and Onley [77] and had immediate success in the low energy domain. Nascimento *et al.* [78] were able to account for the observed ratios of e^- to e^+ induced reaction cross-sections at energies below 50 MeV while Martins [79], Wolynec [71,72,80] and co-workers found that (e,n) and (e,2n) cross-sections for high Z nuclei in the resonance region could now be explained solely on the basis of an E1 transition.

The major difficulty with distorted wave calculations lies in the evaluation of the radial part of the electron matrix element and summation over the outgoing partial waves. It has been noted [81] however that the Coulomb distortions affect only the first few partial waves in the sum and so matrix elements involving higher partial waves may be replaced with their corresponding plane wave values all of which can be summed analytically. Such methods have been incorporated in the computer code VIRTSPEC [82]–[84] to provide fast calculations

of the virtual photon spectra in DWBA.

Such calculations still assume a point nucleus however, and are therefore appplicable only when $E_e < 30$ MeV. In general, nuclear charge effects cause an enhancement of the virtual photon spectra which increases with the atomic number Z and multipolarity L.

PWBA + finite size nucleus

When the wavelength of the electron or photon becomes comparable with the physical radius of the nucleus (e.g. at high E_e or high A), the point nucleus expressions become invalid. The first estimates of finite size effects were obtained from the data of Barber *et al.* [66,67] who investigated the electrodisintegration of ^{12}C at electron energies high enough for such effects to be important but in a low Z nucleus where Coulomb distortions were minimal. They, like Isabelle and Bishop [85], were able to use a PWBA approach to determine the lowest order corrections to the virtual photon spectra resulting from a finite nuclear size. More recently Shotter [86] obtained a finite size correction-factor by incorporating into the PWBA theory a Helm model [87] description of the nuclear transition charge and current densities. This showed that it is the longitudinal components in the virtual photon spectra which are most strongly influenced by finite size considerations and since these tend to dominate the E2 spectra rather than the E1, it is within the E2 intensities that the most notable corrections occur. In general, finite size effects lead to asuppressionof the virtual photon spectra which is most noticeable in the higher multipole orders.

Using the PWBA in first order implies that Coulomb distortion effects are ignored, while for large A, large Z nuclei at high energies, both A *and* Z effects must be taken into account. In an investigation of the electro- and photofission strengths of some heavy elements, Shotter used his nuclear size correction

factors (calculated in PWBA) to modify the DWBA (point nucleus) spectra of Gargaro and Onley [77]. It has since been suggested [88,89] that the sequential application of a Z-correction from one calculation and an A-correction from another is incorrect since the two effects do, in fact, interfere strongly.

DWBA + finite size nucleus

As discussed in the previous sections, virtual photon spectra are subject to two major influences (a) distortion due to the nuclear charge (Z-correction) and (b) effects due to a finite nuclear size (A-correction). Attempts have been made to correct for these effects by (a) replacing the plane waves with distorted waves and (b) by introducing form factors into the plane wave calculation. Since both corrections severely modify the lower partial waves, they are found to exhibit strong interference [88,89]. It becomes clear that a full distorted wave treatment must, in some way, take both effects into account simultaneously. Until recently, the mathematical complexities associated with such a treatment rendered the full calculations impractical. With the advent of modern, faster computers however, Onley has reported [88,89] an accurate determination of the virtual photon spectra which involves very few approximations. In his full DWBA calculation a Z-correction is applied, as before, by replacing Coulomb waves for plane waves in the Born approximation. Since plane and distorted wave solutions vary only in the lowest partial waves, summation over an excessive number of partial waves can be avoided. The A-correction requires the introduction of charge and transition current distributions for the nucleus. (It has been shown that the details of these distributions are unimportant and that only the transition and r.m.s. radii, both of which are functions of A, need be specified accurately). With the A-correction included however, the electron wave functions are no longer precisely known analytic functions and the radial

integrals become vastly more complicated. These integrals, which must now be evaluated numerically, are found to converge very poorly as a function of the radial variable, and the arithmetic operations involved in their solution require large amounts of processing time on high-speed computers.

Onley's calculations represent the most accurate virtual photon spectra yet considered (1987) and are applicable to all nuclei over a wide range of energies. The computations are however, very expensive in terms of computer time and must be carefully monitored for problems of convergence. To date no computer code has been released for general usage.

SOBA

A successful approximation to the full distorted wave analysis, which has a wide range of validity and achieves faster computations, is that due to Durgapal and Onley [90]–[92]. They have corrected for the nuclear finite size and Coulomb distortion by including form factors for both elastic and inelastic scattering and performing calculations in second order Born approximation (SOBA) [93,94]. In such a treatment the effects of A and Z are included simultaneously although charge distortions are taken into account only to first order in Z. (In a full distorted wave treatment the size and charge corrections are, in principle, included to all orders). Although a few limitations arise when Coulomb distortions are very strong (large Z nuclei), the SOBA results are at present thought to be valid without correction for E1, E2 and M1 virtual photon spectra in ^{232}Th at electron energies greater than $\sim$ 80 MeV. Since the mathematical expressions involved in the SOBA calculations contain no singularities, no infinite sums and no infinite integrals, consistent results can be obtained in less than 2 % of the processing time required for a full DWBA analysis. The SOBA calculations employed in the present work were made using the computer code SOVPS [91].

Summary

It is useful to compare results from several of the formalisms described above to determine the ranges of nuclear mass and electron energy over which each calculation is applicable. The formalisms and associated computer codes are summarised in Table 1.1. The calculated spectra are given the generic labels PW (plane wave) or DW (distorted wave) to specify the absence or inclusion of charge corrections, and FN (finite nucleus) or PN (point nucleus) dependent upon whether nuclear size effects are, or are not considered. The E1, E2 and M1 spectra from these calculations are compared at low and high electron energies in Figures 1.7, 1.8 and 1.9 respectively.

It is clear from these comparisons that only a virtual photon analysis which includes both size and charge effects can be applied to a nucleus as heavy as ^{232}Th over the entire energy region of interest here ($40 \leq E_e \leq 150$ MeV), but over most of this range, the calculations made in SOBA show good agreement with the full distorted wave (DWFN) results [95]. Only at the lowest energies are the SOBA calculations outwith the region of validity suggested by the authors [90]. The divergence of the SOBA results from the DWFN calculation is expected to be greatest at low electron energies and in the higher multipole orders. Even so, the difference in the E2 spectrum at 50 MeV is still less than 25%. Since a full distorted wave code is not yet available and since such calculations are anyway very lengthy, the SOBA formalism has been used extensively for virtual photon analysis in the present work.

Spectrum Label	Corrections Included	Computer Code	Comments
PWPN	None	Various	Conventional spectra in PWBA and long wavelength limit.
	None	VPSPEC [73]	Includes kinematic corrections for 2-body hadronic final state.
PWFN	A	SOVPS [91]	PWBA, first order spectrum including finite size effects.
DWPN	Z	VIRTSPEC [82]	Distorted wave, point nucleus
DWFN	A , Z	Not released [88]	Full distorted wave calculation. Includes nuclear size and charge effects.
SOBA	A , Z	SOVPS [91]	Virtual photon spectrum in 2^{nd} order Born approximation. Finite size corrections. Charge distortions to first order in Z.

Table 1.1: Summary of virtual photon codes and formalisms.

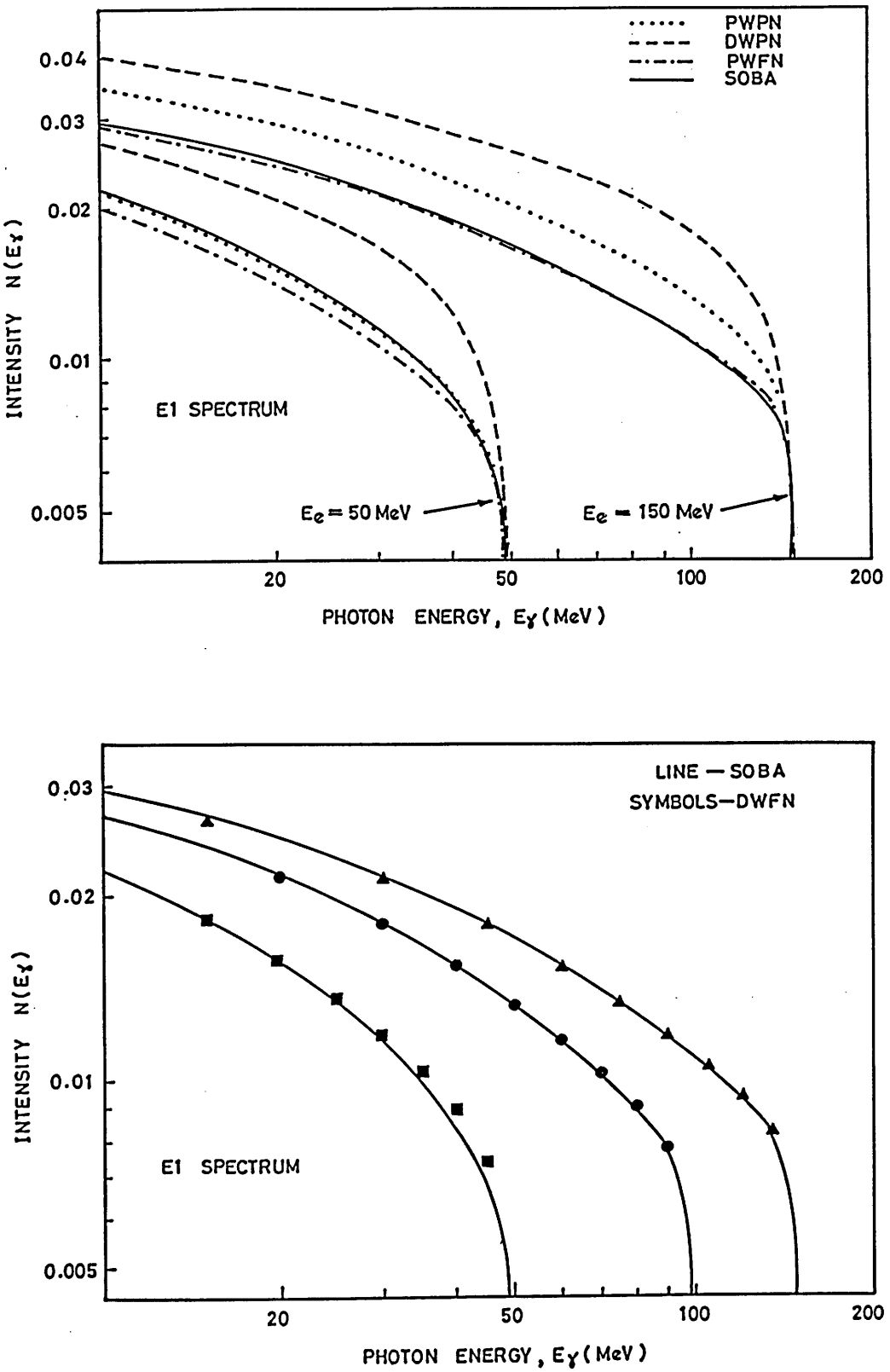

Figure 1.7: (a) E1 virtual photon spectra from electrons of 50 and 150 MeV incident upon ^{232}Th. Plane wave (PW) and distorted wave (DW) treatments of the virtual photon spectrum for point (PN) and finite size (FN) nuclei are compared with the corresponding spectra calculated in 2nd order Born approximation (SOBA). (b) Comparison of SOBA results with a full distorted wave calculation [95] for finite nuclei (DWFN) at 50, 100 and 150 MeV.

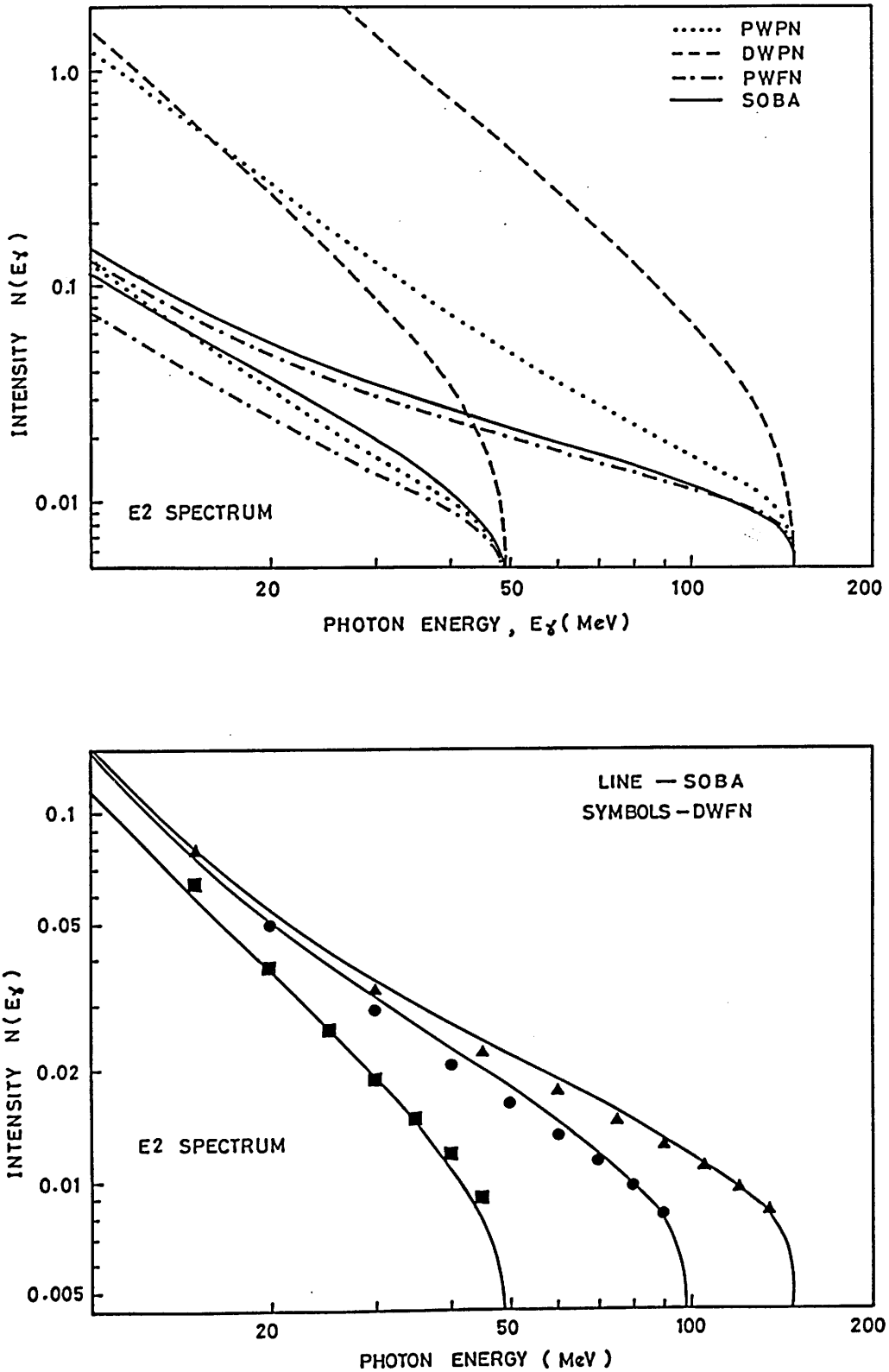

Figure 1.8: (a) E2 virtual photon spectra from electrons of 50 and 150 MeV incident upon ^{232}Th. Plane wave (PW) and distorted wave (DW) treatments of the virtual photon spectrum for point (PN) and finite size (FN) nuclei are compared with the corresponding spectra calculated in 2nd order Born approximation (SOBA). (b) Comparison of SOBA results with a full distorted wave calculation [95] for finite nuclei (DWFN) at 50, 100 and 150 MeV.

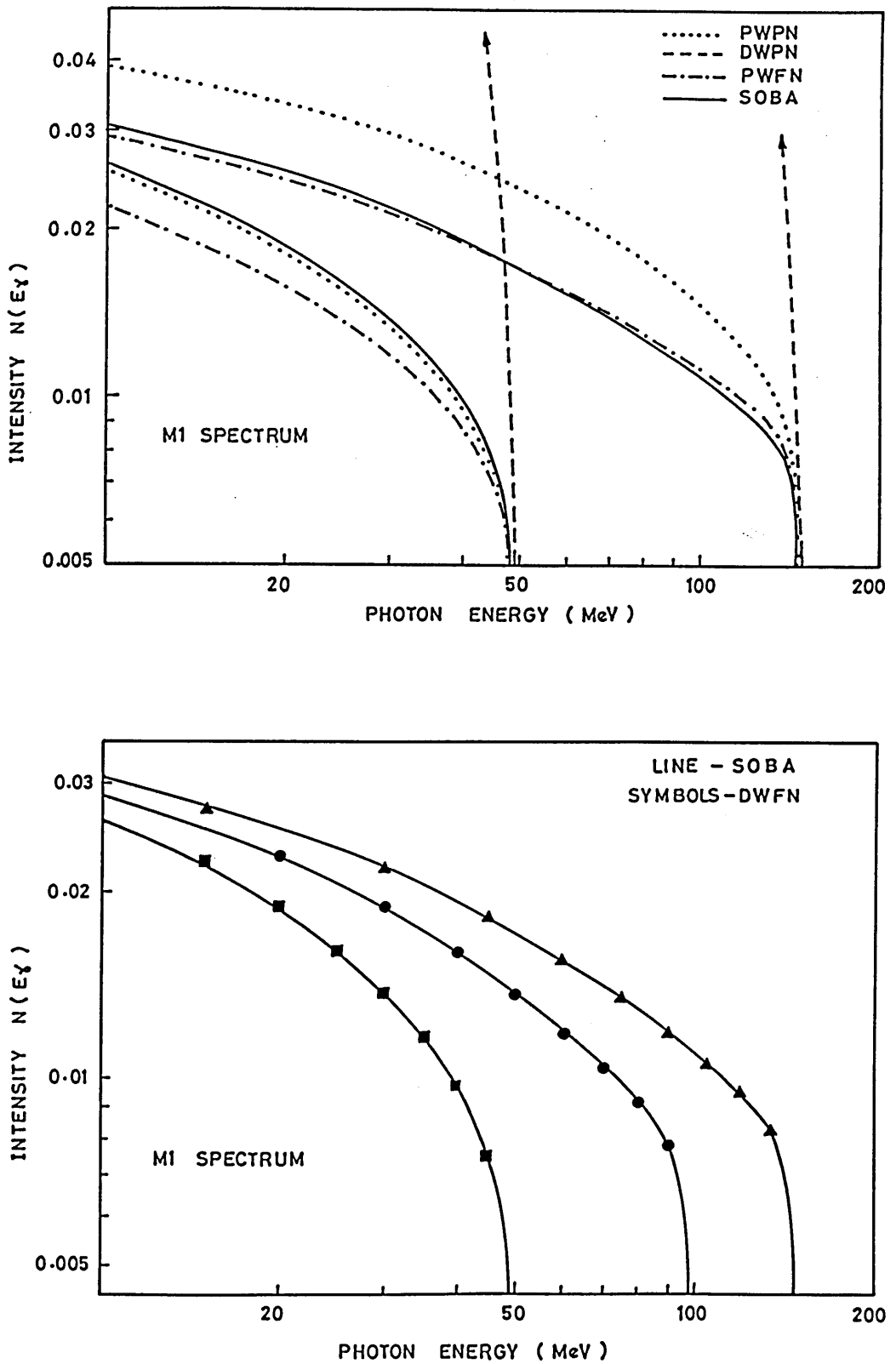

Figure 1.9: (a) M1 virtual photon spectra from electrons of 50 and 150 MeV incident upon ^{232}Th. Plane wave (PW) and distorted wave (DW) treatments of the virtual photon spectrum for point (PN) and finite size (FN) nuclei are compared with the corresponding spectra calculated in 2nd order Born approximation (SOBA). (b) Comparison of SOBA results with a full distorted wave calculation [95] for finite nuclei (DWFN) at 50, 100 and 150 MeV.

1.4 Precompound Nuclear Decay

Theoretical treatments of photonuclear reactions in many body systems are generally based on models, many of which are applicable only to a limited range of atomic mass and excitation energy. In nuclei at low energies for example, photon capture leads to the formation of a compound nucleus which reaches statistical equilibrium without prior particle emission. Its subsequent decay can be satisfactorily treated within the framework of statistical evaporation models [96]. In light nuclei at higher energies, the interaction of the photon with only one or a few nucleons is a direct reaction process since residual interactions affecting the outgoing particles are small. In heavy nuclei at energies from (40 – 150 MeV) photon absorption is again thought to be confined to only a few nucleons but residual interactions of the participating particles with the remainder of the nucleus can no longer be ignored. A situation arises which is intermediate to the former cases. Several models, which are applicable to this intermediate region, were developed for the treatment of nucleon induced reactions and have recently been applied to the photon-nucleus interaction. In these models an initial partition of the excitation energy is assumed to occur between a relatively few degrees of freedom. The details of this partition depend, of course, upon the initial absorption mechanism. In the quasi-deuteron picture for example, the energy of the absorbed photon is shared equally between one neutron and one proton. The system then evolves through a series of increasingly more complicated states, as a result of nucleon-nucleon residual interactions, until an equilibrium distribution of the excitation energy is achieved i.e. a compound nucleus is formed. Particle emission is considered from the "precompound" stage of this equilibration process as well as from the compound nucleus.

Two distinct formulations have been used in the treatment of precompound

particle emission, each with certain advantages over the other. In the first of these, the so called "intranuclear cascade" model, the equilibration process is assumed to occur via a series of N-N collisions and the positions and directions of all participating particles are traced through the nucleus in geometrical space. In the second approach the coordinate system of the cascade model is replaced by a "phase space" where, instead of the positions and velocities of individual nucleons, the partition of energy between excited particles and holes (or "excitons") is followed as a function of time or exciton number. Effects of the model formulation upon the precompound component of the nuclear decay process are discussed in the remainder of this section.

Intranuclear Cascade Method

In this model [97]–[99] a localised initial interaction is considered to result in the excitation of only a few particles. It is assumed that their subsequent interaction with the remainder of the nucleus can be represented by a series of 2-body nucleon-nucleon collisions [100]. The calculations involve a Monte Carlo simulation of the absorption and collision sites and the reaction kinematics which describe the N-N collision sequence. The collision properties are based on free N-N interactions which are modified to include Pauli effects by excluding scattering to states below the nuclear Fermi energy. The vector momenta of all scattered particles are followed until the particle either (i) escapes from the nucleus – it must reach the surface with sufficient energy to overcome some predefined threshold, or (ii) is captured – its kinetic energy having fallen below some chosen cut-off value. The residual energy of the captured particles is assumed to contribute to the net excitation of the compound nucleus which remains.

The nucleus itself is modelled on a zero-temperature Fermi gas with a step-

function density distribution. The diffuse nuclear edge, which may have important consequences for precompound particle emission, is therefore incorporated naturally. The importance of surface effects in photon induced reactions is not yet clear and will be discussed later. Since all of the geometrical information associated with the precompound collision sequence is retained, these models allow angular as well as energy distributions to be determined for emitted particles.

Phase Space Method

One model by which precompound particle emission spectra have been calculated on a phase space basis is that due to Harp, Miller and Berne (HMB-model) [101,102] who use a Boltzmann "master equation" to determine the time evolution of a nuclear Fermi gas system. In this model the state of the nuclear system is described by the occupation numbers of the single particle states which, for computational purposes, are binned into conveniently sized energy intervals. The fractional occupation numbers of these bins are then followed as a function of time. The time evolution is described by a master equation which contains all of the information necessary to determine the scattering into and out of each bin as well as the rate of particle emission from bins above the particle binding energy. Following solution of this master equation at the time of the initial interaction, the bin occupation numbers are appropriately modified and the calculation repeated in units of time short with respect to the average nucleon-nucleon collision period. The internal transition rates , based on the probability that two particles from states i, j say will scatter to states k, l, are obtained from free N-N scattering cross-sections. The emission probabilities for particles in unbound levels are derived from inverse reaction cross-sections.

A method similar to the HMB-model, but involving simpler computations,

is the so called "exciton" model originated by Griffin [103]–[105]. In this model the nuclear states are characterised by the number of excited particles plus holes (or excitons) which are present, where these are defined with respect to the nuclear Fermi energy. The equilibration process proceeds from some initial exciton configuration, determined by the original excitation mechanism, to an equilibrium (or most probable) value, through a series of 2-body collisions, each of which change the exciton number by ± 2. For each of the "intermediate exciton states" it is assumed that all configurations of the particles and holes, which are consistent with the excitation energy and exciton number, are equally probable. As some of the configurations will have particles in unbound levels, there is a finite probability that one or more particles may be emitted before a further N-N scattering event changes the exciton number. It is this competition between internal transition ($\Delta n = \pm 2$) and particle emission ($\Delta n = -1$) which must be evaluated in order to determine the precompound particle emission spectrum. The total precompound emission spectrum is found by summing the contributions from all intermediate exciton states between the initial value and equilibrium. While the particle emission probability is based on the inverse reaction cross-section as before, it is through use of an average state lifetime to describe the internal transition rate that a major simplification is achieved over the detailed 'book-keeping' of the HMB and cascade models. This averaged transition rate for the n-exciton state is however difficult to calculate and allows only relative rather than absolute spectral yields to be evaluated. It has been suggested [106] that the use of such a transition rate may include an incorrect influence of 'spectator' particles and holes upon the transition/emission probability of particles in unbound levels. This, however, is still a debatable subject.

In order to predict absolute spectral yields, a model was developed by Blann

[106]–[111] which retains the exciton description of the excited particle populations but in which the transition/emission probability of a particle depends upon the specific lifetime of the excited particle state instead of the average lifetime of the n-exciton configuration. Intranuclear transition rates of these excited particles were based on the mean free paths of nucleons in nuclear matter. As this model combined the ability of the HMB-model to predict absolute precompound emission with the simplicity of the exciton model it was referred to as the "hybrid" model. Serious questions have, however, been raised [112] regarding the multiple counting of events in this formulation and the matter must presently be considered as unresolved.

Deficiencies in the Models

Although all of these models are semi-classical in nature and include only 2-body interactions to describe the residual interactions within the nucleus, this has not yet been shown to be a serious limitation of their validity. Other deficiencies, which may have important effects upon the precompound calculations, are confined to individual formulations. The cascade model, for example, ignores the effect of all holes once they have been created and the interaction of particles below the Fermi level although the significance of these omissions is presently unclear. In addition, transmission coefficients are often given a rather simplistic treatment in the cascade model and, although this is done for computational convenience and is not an intrinsic deficiency of the method, it is possible that such approximations are insufficient to give a realistic description of precompound particle emission.

In the phase space formulations on the other hand, all geometrical aspects of the nuclear model and emission spectra are neglected. Such geometrical considerations were found to be important in the treatment of nucleon induced

reactions, the problem for which precompound models were originally developed and have most frequently been applied. Miller [113], in a review of precompound models for the treatment of nucleon induced reactions, suggested that all of the phase space calculations showed a tendency to underestimate the magnitude of precompound particle emission. The remedy lay in recognising that, for nucleon projectiles, the first interaction has a high probability of occuring in the nuclear edge and that much of the precompound emission therefore occurs when the excitation is concentrated in that diffuse outer region. Strong evidence for this was seen in the work of Bertrand [114] who showed precompound cross-sections to vary as $A^{\frac{1}{3}}$ in nucleon induced reactions, as would be expected for peripheral interactions. The underestimation of precompound decay was remedied in a refined formulation of the hybrid model [115] which allowed for the longer mean free path of nucleons near the nuclear surface. As this model incorporated effects of the diffuse surface region it was referred to as the "geometry dependent hybrid" (GDH) model. The GDH model has had great success in fitting the experimental results of nucleon induced reactions, but a scarcity of experimental data from photon induced reactions means that precompound models, in their application to the photonuclear problem, have not been so rigorously tested. Whether such geometrical considerations are of importance for photonuclear interactions remains to be investigated.

1.5 Objectives and Structure of Thesis

The need to obtain data on photonuclear processes, in the low cross-section region between the giant dipole resonance and the meson threshold, has been identified. The distribution of strength among the many decay channels open to photo-excited heavy nuclei at these energies, should yield valuable information on the photon absorption mechanism and the influence of final-state interactions upon the nucleons which participate in this process.

Using photon activation techniques to determine the yields of α-unstable reaction products from ^{232}Th, it is possible to measure cross-sections for reactions of the type $(\gamma, xnyp)$ where 0, 1 or 2 protons accompany neutron emission. The charged particle channels, where precompound nucleon emission is ensured, are particularly sensitive to the initial absorption mechanism and are not dominated by the large neutron multiplicities of the evaporation process which follows compound nucleus formation. Such data should therefore provide a rigorous test of the precompound decay models, and their associated parameter sets, which have recently been applied to the photonuclear problem.

Using a thorium target, some of the particle emission chains are expected to end in fission, i.e. $^{232}\mathrm{Th}(\gamma, xnypf)$. The observed depletion of the $(\gamma, xnyp)$ non-fission channels can therefore be used to determine whether nuclear fission parameters, taken from the giant resonance region, are still valid at the present energies.

Chapter 2 describes the experimental system and the techniques employed in the collection of the photon activation data. Chapter 3 describes the analysis of this data and its reduction to the form of electron and bremsstrahlung yield functions. The $(\mathrm{e}, xnyp)$ and $(\gamma_{\mathrm{br}}, xnyp)$ yield functions are presented for each of the photoreactions measured. In Chapter 4, two of the precompound nuclear decay models introduced earlier are described in detail and an outline is

given of the theoretical calculations performed. The unfolding process, used to extract energy-dependent photoreaction cross-sections from the measured yield functions, is discussed in Chapter 5. The measured cross-sections are then compared with the predictions of the photodisintegration models. Limitations of the present models are discussed and various improvements suggested. In Chapter 6, a brief summary is given of the experimental work and theoretical calculations which comprise this thesis and topics are suggested for future study.

Chapter 2

The Experimental System

2.1 Introduction

Several $(\gamma, x\mathrm{n}\, y\mathrm{p})$ and $(\mathrm{e}, \mathrm{e}'\, x\mathrm{n}\, y\mathrm{p})$ cross-sections have been measured for ^{232}Th using activation techniques to determine the yields of $^{232-x-y}_{Z-y}X$ reaction products from their residual α–activity.

The experimental work described in this section was carried out at the University of Glasgow's Kelvin Laboratory. Targets of natural thorium were irradiated at energies between 40 and 150 MeV using the laboratory's 160 MeV electron linear accelerator. A tantalum foil was used as a source of bremsstrahlung radiation for the latter of two targets in a 'radiator sandwich' assembly. Following irradiation, the targets were removed to a low background area where their residual α–activity was monitored for up to 8 months using solid state detectors in a well defined geometry.

Sections (2.2) to (2.7) of this chapter describe the equipment and methods used in the gathering of experimental data. Section (2.8) discusses the experimental programme followed, including the criteria which governed the time scales of irradiation and data collection. Previous experiments, on other heavy nuclei, have used the residual γ–ray activity of irradiation products to determine the individual reaction yields. The final section of this chapter highlights some of the advantages *and* disadvantages of the α–activity measurements over

these previous investigations as well as summarising the key points of the experimental system.

2.2 Electron Accelerator Facility

The general layout of the Electron Accelerator Facility at the University of Glasgow [116] is shown in Figure 2.1. The electron beam from a linear accelerator (LINAC) enters a high resolution energy analysis system in which electrons of a selected momentum are deflected through 90° into a shielded experimental area. The energy-analysed beam strikes the photonuclear target, housed within an evacuated scattering chamber, before entering a shielded concrete beam dump.

The relatively poor energy spectrum from the LINAC stage is, however, rather ill matched to the requirements of the high resolution beam transport system which it precedes. To avoid sacrificing a large fraction of the available current, an energy compression system (E.C.S.), which greatly reduces the momentum spread of the electron bunch, is employed as a matching device.

During experimental irradiations, accelerator operations are monitored remotely from an operator control room. A detailed description of the facility is given in the following sections.

2.2.1 Linear Accelerator

The Glasgow LINAC uses travelling electromagnetic waves at 2.8562 GHz to accelerate electrons up to energies of 160 MeV. The accelerator is divided into three sections, each composed of four lengths of iris-loaded cylindrical waveguide. Radio frequency power, supplied to each section via rectangular air-filled guides, is generated in three 25 MW klystron amplifiers pulsed from a master oscillator at 100 p.p.s.

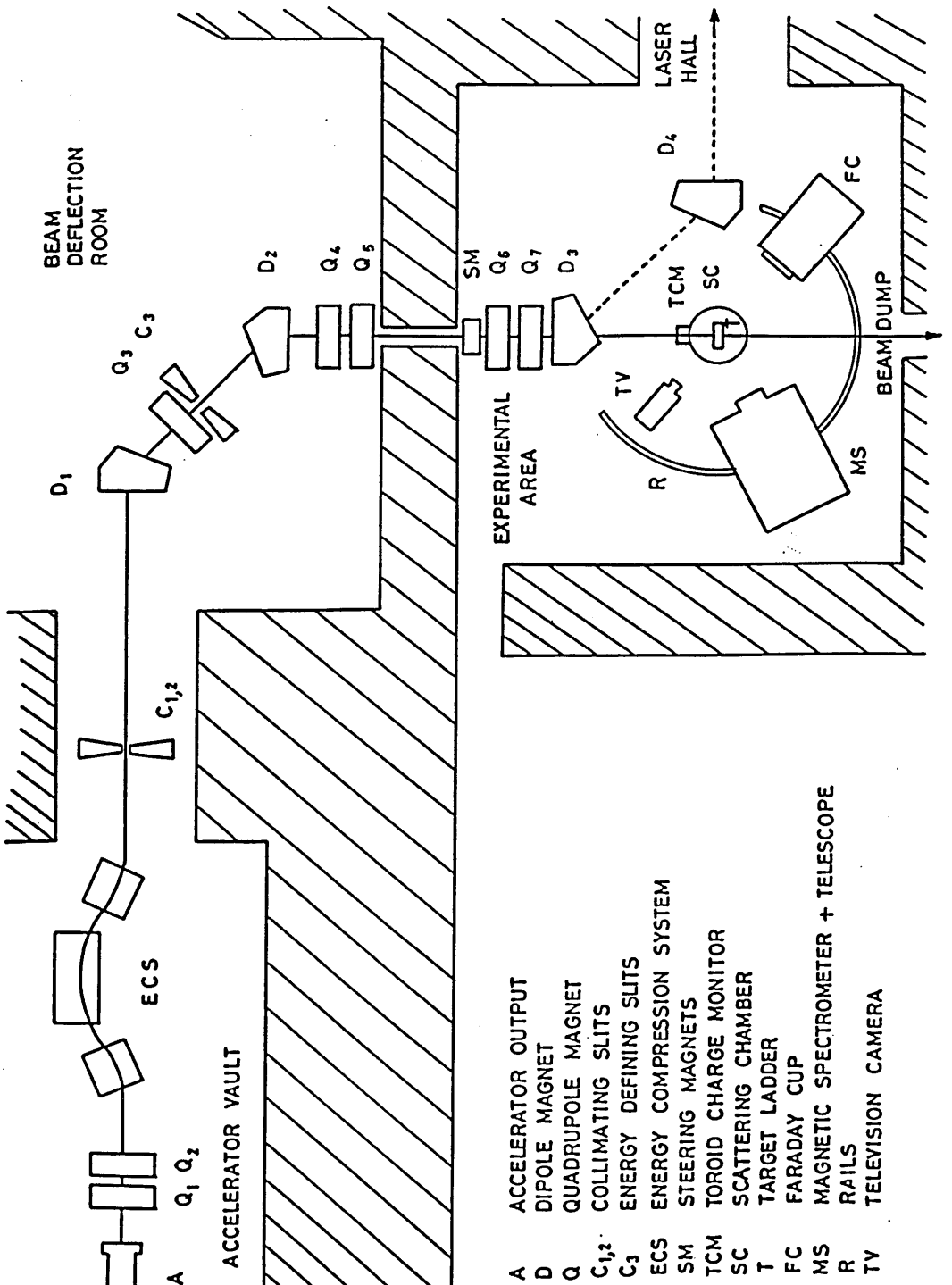

Figure 2.1: General layout of the Electron Accelerator Facility at the University of Glasgow

At maximum operating power, electrons gain approximately 40 MeV in each of sections 1 and 2 and around 80 MeV in section 3. The final electron beam energy may be tuned by reducing the r.f. power in one or more of the waveguide sections or by adjusting the relative phase of the r.f. wave between sections. For energies above 80 MeV, electrons must be accelerated in all three sections with suitable attenuation of the r.f. power. For energies below 80 MeV, electrons are accelerated in sections 1 and 3 but decelerated in section 2 by the process of 'back-phasing'. On occasions, with only two modulators/klystrons operational, acceptable performance was obtained by simply drifting electrons through the unpowered section, albeit with a slight reduction in beam stability.

For the present series of irradiations the accelerator was operated with a pulse length of 3.25 μs which at 100 p.p.s. yields a duty cycle of 3.25×10^{-4}. With an energy resolution of $\sim 0.5\,\%$ (Section 2.2.3) and peak pulsed currents typically in the range 60—100 mA, average beam currents of 5—15 μA were achieved in the experimental area.

2.2.2 Energy Compression System

Situated at the end of the accelerator vault (Figure 2.1) is the 3–magnet system and r.f. correcting cavity (Figure 2.2) which form an 'energy compressor' for the Glasgow LINAC [117]. The function of this device is to reduce the momentum spread, dP, of electrons leaving the accelerator, thus allowing larger beam currents to be transmitted through the beam-handling system which follows.

Figure 2.3 shows schematically the variation in beam emittance through the energy compression system. On exit from the accelerator, electrons are sharply bunched near the peak field of the r.f. wave but have a relatively large momentum distribution, dP_1 (Figure 2.3.a.I). The dipole-triplet carries electrons via an off-axis route, the path-length travelled being momentum-dependent.

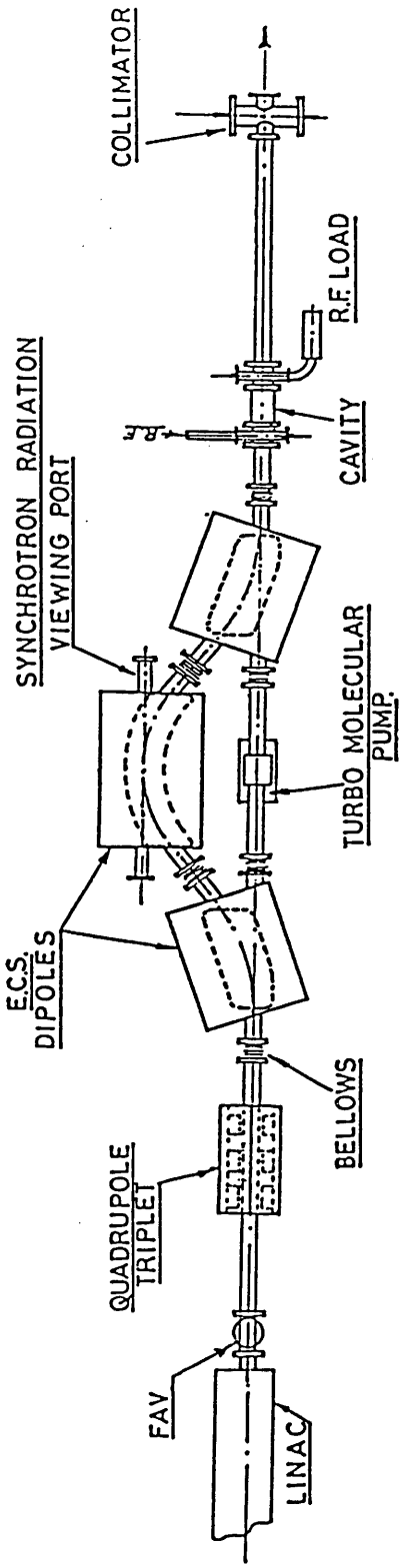

Figure 2.2: The Energy Compression System of the Glasgow LINAC

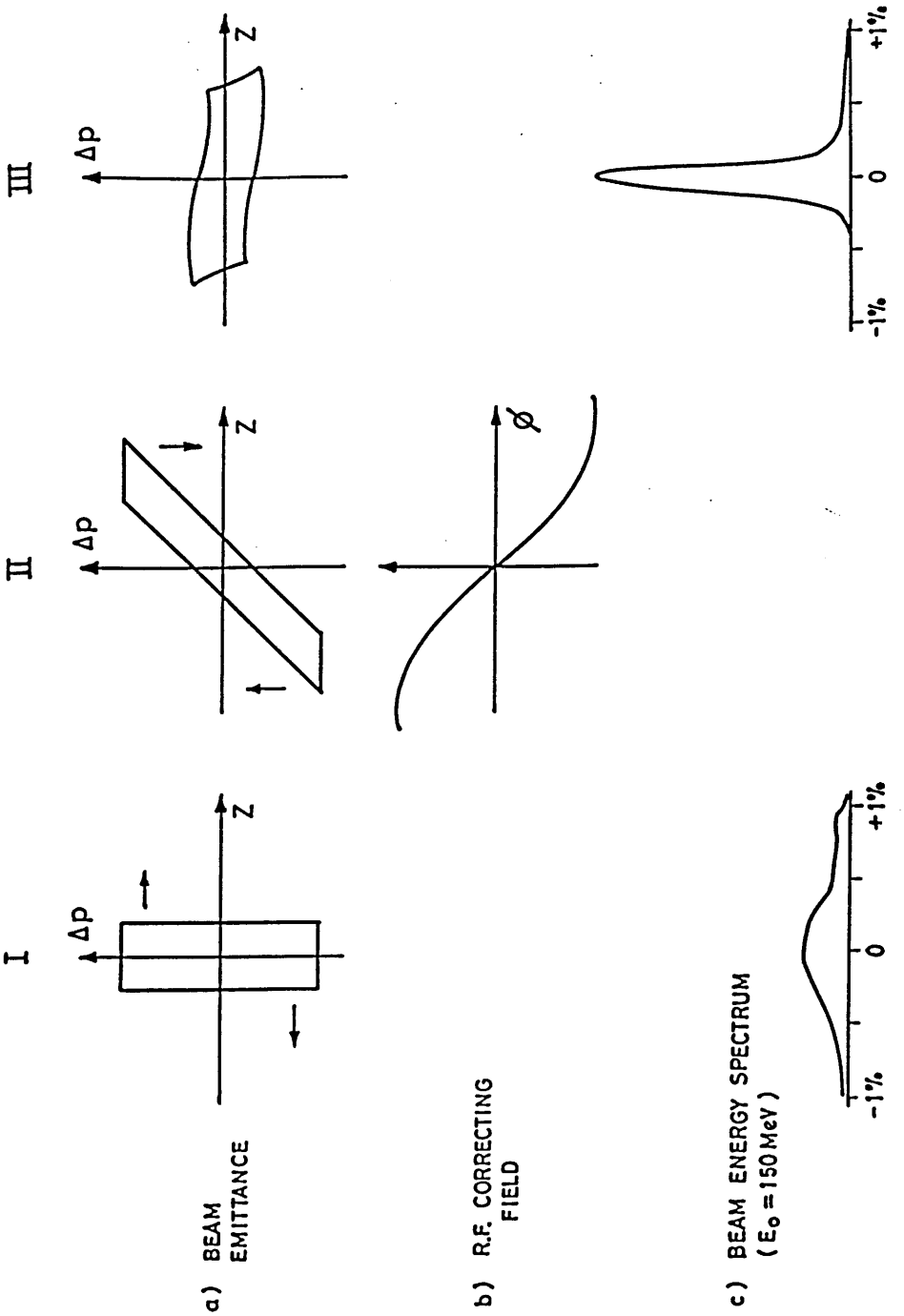

Figure 2.3: Schematic variation of electron bunch parameters through the Energy Compression System. (a) beam emittance (b) applied r.f. field (c) energy spectrum. Region I — on exit from accelerator, Region II — on exit from dipole triplet, Region III — on exit from r.f. correcting cavity.

Figure 2.3.a.II shows that a linear relation is introduced between the energy of a 'debunched' electron and its axial position. The electrons now enter a final section of powered waveguide in which the phase of the r.f. field (Figure 2.3.b.II) is so adjusted as to accelerate the lower energy electrons at the tail of the bunch while retarding those of higher energy near the front. The final electron bunch (Figure 2.3.a.III) has a greatly reduced momentum spread, dP_2. The corresponding loss in bunch structure is of no consequence in experiments of this type.

The compression factor, F_c, defined as the ratio of final to initial spectrum widths,

$$F_c = \frac{dP_1}{dP_2}$$

is energy dependent but lies typically in the range 5 – 15 . Figure 2.3.c shows the effect of energy compression on an electron beam bunch at 150 MeV. In addition to an improved spectrum, the E.C.S. acts as a useful energy stabiliser since it inherently corrects for small drifts in the mean beam energy.

2.2.3 Beam Handling System

Electrons emergent from the E.C.S. are deflected by a series of magnets through 90° and focussed onto a photonuclear target situated within the scattering chamber. The electrons are energy analysed in this transport system by means of dipole magnets D_1 & D_2 and an energy-defining slit C_3.

A pair of adjustable slits, $C_{1,2}$, form a rectangular aperture which acts as a primary object for the energy analysis system. The electron beam is deflected through 45° in each of the bending magnets D_1 & D_2, while the intervening slit C_3 determines the energy bite of the transmitted beam. Quadrupoles Q_4 & Q_5 produce an approximately parallel beam which passes into the experimental area. Chromatic abberations are marginally reduced by the use of a

central quadrupole, Q_3 [118]. The final energy-analysed beam is positioned and focussed onto the target using small steering magnets and the remaining quadrupoles Q_6 & Q_7.

The *mean* energy of the transported beam is defined by the magnetic field strength in D_1, while the size of the aperture C_3 in conjunction with $C_{1,2}$ determines the energy resolution of the system. The field B, which is related to the transmitted electron momentum p by

$$p = kB$$

is measured to high precision with an N.M.R. probe.

The constant of proportionality, k, has been determined previously by elastically scattering beam electrons into a calibrated magnetic spectrometer using an aluminium target. The procedure is described in detail by Gibson [119] and Flowers [120] who present a value of

$$k = (1.8199 \pm .0005) \times 10^{-2} \quad \text{MeV c}^{-1}\,\text{gauss}^{-1} \tag{2.1}$$

An energy analysis system of this type ensures that the size, position and energy of the electron beam where it intercepts the photonuclear target remain unaffected by fluctuations in accelerator performance. For the present series of irradiations an energy bite of 0.5 % was used to give acceptable energy resolution while still maintaining reasonable beam currents in the experimental area.

2.2.4 Scattering Chamber

An evacuated scattering chamber (Figure 2.4) at the end of the beam-line provides a convenient location for the irradiation of photonuclear targets. This cylindrical chamber is 45 cm in diameter by 25 cm high with a thin exit window of 0.25 mm aluminium. Electrons leaving the chamber travel ~ 2.5 m through air before entering a shielded concrete beam dump.

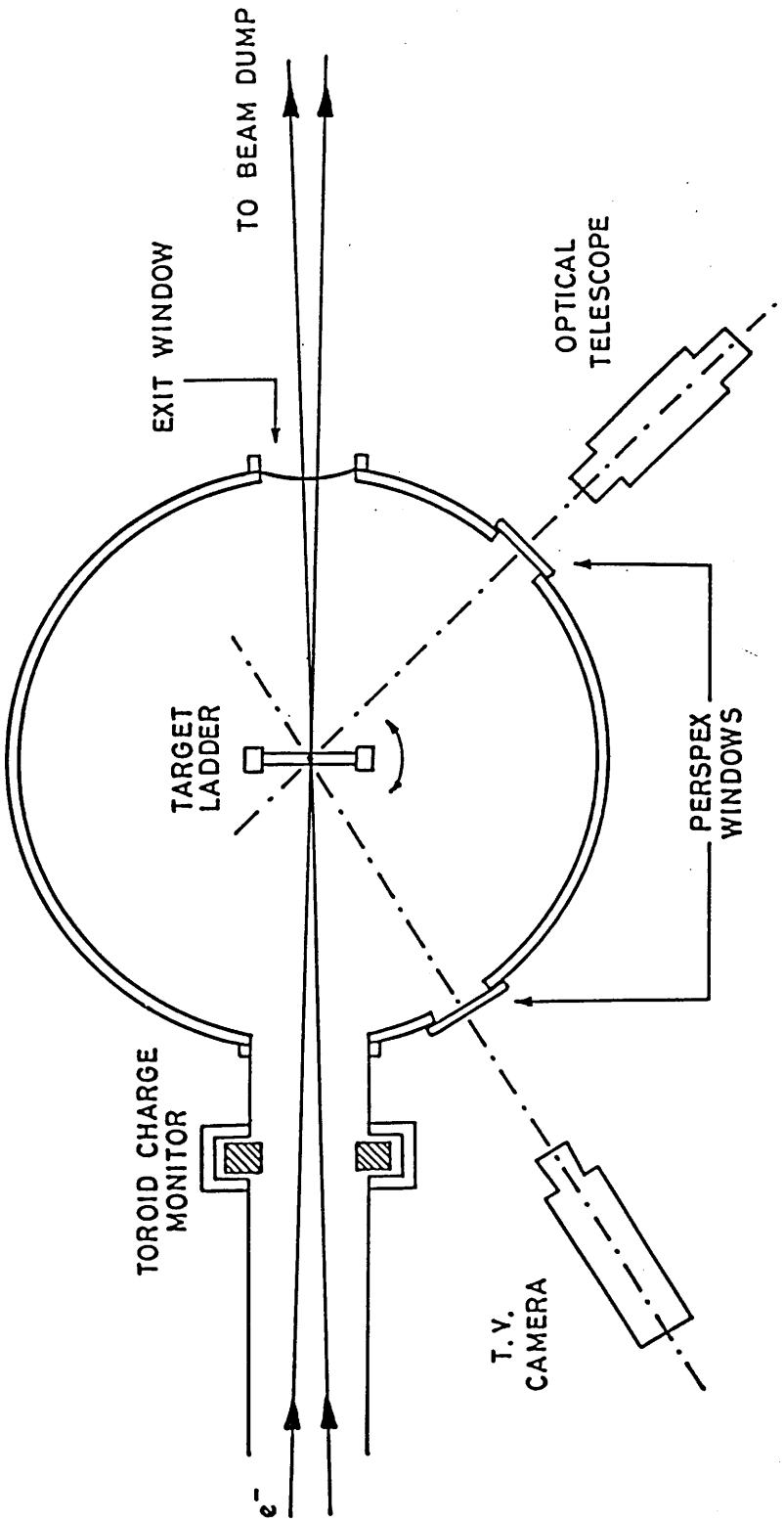

Figure 2.4: Scattering Chamber

Photonuclear targets are mounted on the upper level of a multi-positional ladder which can be lowered or raised remotely to introduce any one of five target locations into the beam-line. A second location is generally reserved for a thin beryllium-oxide (BeO) screen which produces visible scintillations when traversed by the electron beam. Viewed via a t.v. camera, the BeO permits the size and position of the beam spot in the target plane to be correctly adjusted prior to irradiation.

In order to obtain a constant counting efficiency in this experiment, it was required that :

1. The electron beam accurately intercept the *mid-point* of the photonuclear target with an off-centre deviation of no more than 2 mm.

2. The *area* of the target surface activated during irradiation remain as small as possible ($< 30\,\mathrm{mm}^2$).

The latter condition was governed mainly by the quality of the beam optics and could be satisfied with relative ease. A focussed beam spot of the order of 2 mm $\times$ 2 mm was attainable at most energies by suitable tuning of the quadrupole fields. The former requirement was achieved by a careful set-up procedure using a fixed optical telescope whose principal axis lay in the same plane as the beam line.

A pair of intersecting axes scribed on both the BeO screen and the photonuclear target holder (Section 2.4.2) served to locate the centroid of each. With the target ladder rotated into the telescope's field-of-view and the BeO–position selected, the screen was clamped into its housing such that the cross-hairs of the telescope lay exactly upon its centroid. The same routine was followed with the target–position chosen such that the cross-hairs were then superimposed upon the centroid of the target assembly. In this way the centres of both objects took

up the same spatial position in the beam line when the appropriate ladder level was selected.

During a lengthy irradiation the beam position was monitored regularly by moving in the BeO screen and checking, via the remote camera, for any deviation of the beam spot from the defined origin. In practice a positional accuracy of better than $\pm$ 1 mm was maintained throughout.

2.3 Charge Monitors

The amount of charge incident upon the photonuclear target was measured using a non-intercepting beam current integrator [121] whose response was calibrated relative to an evacuated Faraday Cup. The device described in this section is basically a toroidal current transformer whose primary is the electron beam itself. Signals induced in the secondary windings were accumulated by a commercially available current integrator.

The toroidal transformer (Figure 2.5), comprising some 20 turns round a mu-metal core, was situated 30 cm upstream from the target ladder. Current pulses induced by the electron beam were amplified by a low input impedance pre-amp mounted close to the toroid. Due to its close proximity to the beam-line, the pre-amp required heavy shielding to avoid radiation damage in its active components. The boosted signals from the pre-amp output were passed, via low loss cables, to the remainder of the processing electronics situated 60 m away in the accelerator control room. To avoid the serious problems of r.f. pick-up in these lines, principally from the LINAC's high power modulators, the toroid signals were carried along doubly shielded coaxial cables. These were in turn wound round a mu-metal core ($\sim$ 12 turns) forming a high frequency choke to any unwanted signals induced in the outer casing of the cable shielding. The pre-amp was a.c. coupled to both the toroid and the signal processing electronics

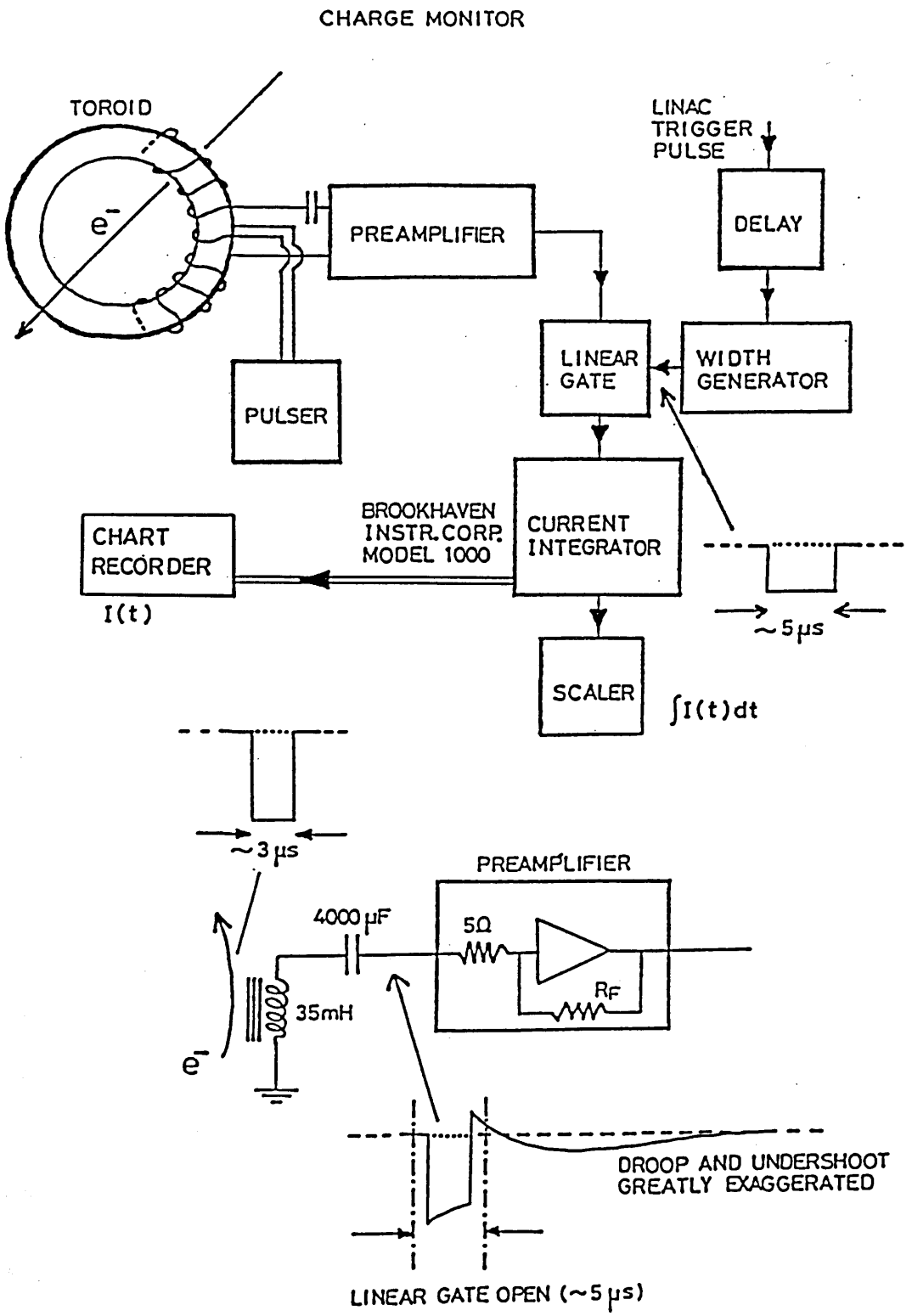

Figure 2.5: Toroid Charge Monitor and associated electronics

in order to minimise d.c. drifts.

A 5 μs linear gate, generated in synchronism with the electron beam pulse, removed both the undershoot from the pre-amp output signal and any spurious pick-up encountered between beam bursts. These amplified and gated toroid signals were finally accumulated by a 'Brookhaven' Current Integrator which fed a logic pulse to a bank of scalers after the collection of a preset quantity of charge. The scaled sum of these logic pulses was then proportional to the total charge incident upon the irradiated target.

The Brookhaven integrator is also equipped with a d.c. output port whose voltage level at time t reflects the 'instantaneous' beam current monitored by the system. Used to drive a moving-pen chart-recorder, this facility allowed the beam current profile $I(t)$, for each irradiation, to be graphically recorded. A typical plot of I against t is shown in Figure 2.6. Due mainly to instabilities in the LINAC and its modulator network, the beam current profiles tend to be far from rectangular. Because the mean current varied so markedly within a single irradiation, it was particularly important that the charge monitoring system operate in a region of linearity. The response of the toroid to different beam currents was measured relative to an evacuated Faraday cup and found to remain constant within $\pm 0.2\,\%$ over the range 0—20 μA. Since the Faraday cup has a known efficiency [122] of 99.6%, this comparison allowed an *absolute* calibration of the charge monitoring system to be made. A calibration constant C_B is defined which relates the *true* electron beam current to the digital output of the Brookhaven integrator :

$$C_B = (2.1617 \pm .0042) \times 10^{-7} \text{ Coulombs per logic pulse} \qquad (2.2)$$

Details of the calibration and linearity measurements can be found in Appendix A.

A *relative* calibration of the system could be made by sending test-signals

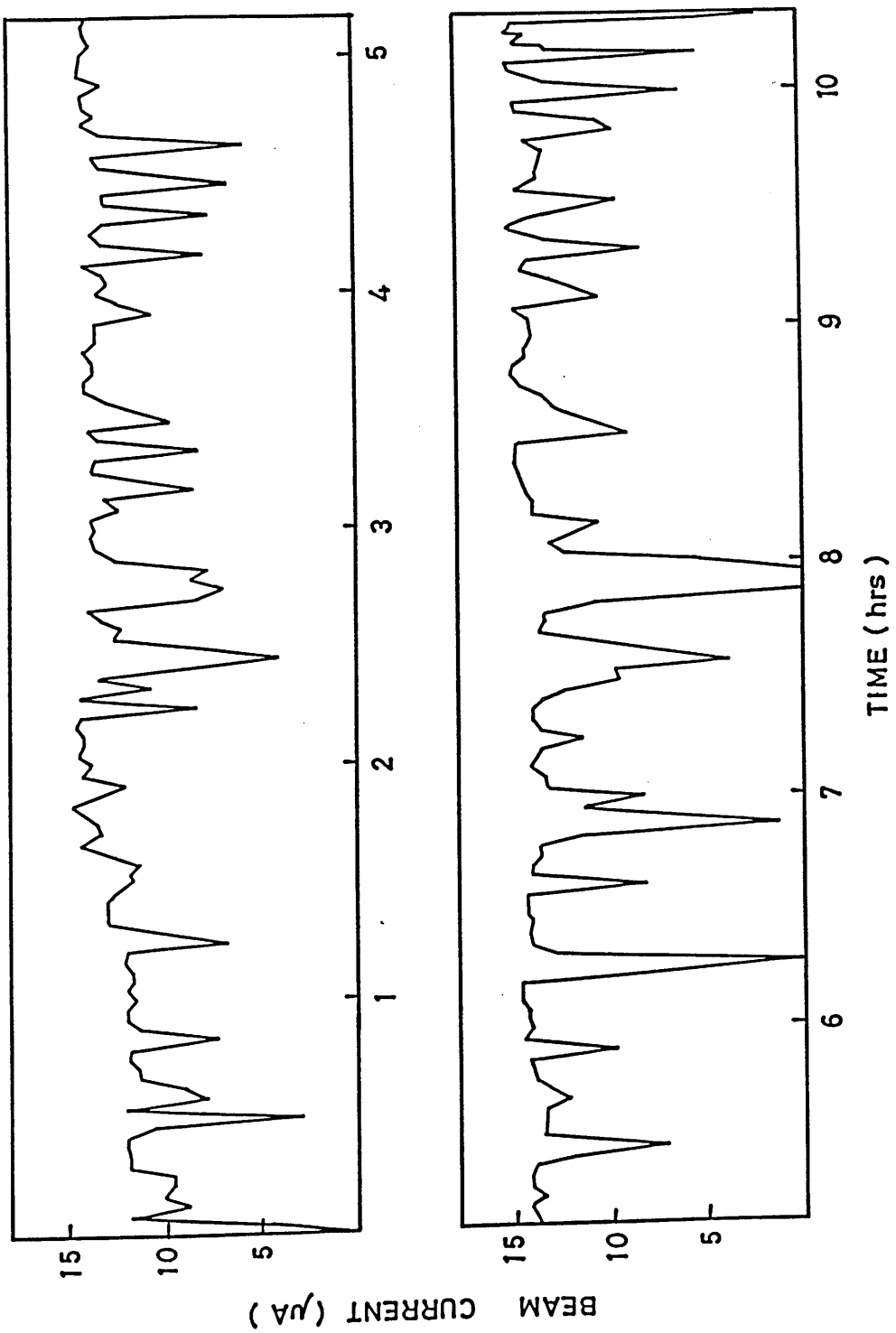

Figure 2.6: Beam Current Profile for a 10 hour irradiation at 90 MeV

from a precision pulser to a single turn test-loop incorporated in the toroid windings. This facility provided a ready check of the general system stability and was used regularly (every 3 or 4 hours) during an irradiation to search for drifts or gain shifts.

2.4 Photonuclear Targets

The photonuclear targets described in this section were manufactured by the Chemistry Division of the Atomic Energy Research Establishment, Harwell. They comprise a thin layer of natural thorium ($\sim 0.05\ \mu$m) on a backing disc of high purity aluminium. The natural radioactivity of the deposit was used to determine absolute target thickness. Due to the observed complexity of measured alpha-spectra, target thicknesses were chosen to provide high α–peak resolution whilst avoiding disproportionate reductions in the overall count-rate.

2.4.1 Target Composition

It is essential to employ very thin targets in α–spectroscopy measurements due to the large ionisation losses incurred by heavy charged particles in matter, which can rapidly deteriorate the energy spectrum of α–particles emitted from a photonuclear target. Selection of target thickness was a compromise between the resolvability of α–lines required in the measured spectra and the amount of induced activity necessary to gather statistically accurate data. To allow satisfatory unfolding of individual spectral components, α–peak widths had to be kept to a tolerable value. Early test irradiations indicated that a FWHM of no more than 40 keV should be maintained for mid-range α's (~ 7 MeV) in order to enable adequate separation of the constituent lines. This limit applied however, to the composite resolution of the entire spectroscopy system and included a contribution of some 20 keV (Section 2.6) from the solid-state

detector and associated electronics. This meant that the energy spread in the photonuclear target had to be restricted to 35 keV FWHM. The relationship between energy spread and target density, which is examined in Appendix B, allowed a permissible target thickness to be defined.

While in theory such a resolution should have been obtained with an uncontaminated deposit of 150 $\mu g\,cm^{-2}$, in practice the first targets which were manufactured by a dry argon "sputtering" technique [123]–[125] were found to exhibit almost double the expected energy spread. While the possibility was recognised [126] that much of the thorium metal may have been deposited in the form of a dioxide, this would have caused an increase of only a 40 % in the width of the energy distribution. The loss in resolution seemed to be a result of the sputtering process itself as metallic deposits prove vulnerable to gas adsorption (argon and other residuals) in the high working pressures of the apparatus.

A second set of targets produced by "vacuum sublimation" [123,127,128] showed much less broadening (due possibly to the higher vacua involved) and this method of preparation was adopted in preference. However this technique also failed to produce the anticipated resolution, perhaps due sample impurities or micro-crystalline formations which can increase the self-absorption of the deposit. Measurements of the natural thorium activity allowed targets of satisfactory resolution to be selected from a larger number of samples and a batch of targets between 40 and 80 $\mu g\,cm^{-2}$ were selected for the irradiations.

The final 'evaporated' deposit formed a sensitive area of 25 mm diameter on a 38 mm diameter backing. Discs of 0.125 mm high-purity aluminium (99.99^{+} %, [129]) were used for this purpose to ensure the following properties in the finished targets :

- *rigidity* : the close geometry of the detection system (Section 2.6) required

minimal distortion of target shapes in order to ensure a constant and reproduceable solid-angle. This was particularly important in the present experiment where the time-scale for data collection was long and frequent target handling was involved.

- *high purity* : impurities giving rise to α–active irradiation products were avoided for obvious reasons, as were chemical contaminants which might have destroyed the cohesion or stability of the evaporated film.

- *low background* : excessively thick target backings can, when irradiated, induce serious background problems. In the present experiment the principal sources of such activity were :

  - β–decay of fission fragments trapped in the backing material.
  - β–decay of the unstable isotope ^{24}Na (half-life = 15 hrs) produced in the aluminium foil by the reaction $^{27}\mathrm{Al}(\gamma, 2\mathrm{pn})$.

  Since the energy deposited by incident β's in the solid-state detectors (< 2 MeV) was well below the α–energies under examination (4 – 10 MeV), no contamination of the α–spectra was observed and, in practice, the electronic pulses from detected β's were rejected by a low-level discriminator in the signal processing network (Section 2.7) in order to reduce the system 'dead-time'. The effect of the β–activity on α–peak resolution was also found to be small for the levels of activity produced.

The ^{232}Th nucleus is itself unstable and decays through α–emission with a half-life of 1.405×10^{10} yrs [130]. Although count-rates were low for such thin layers of material (~ 30 cts hr^{-1} were measured in the present geometry), this natural activity provided an excellent means of determining absolute target thickness. A typical thorium 'background' spectrum is shown in Figure 2.7.b.

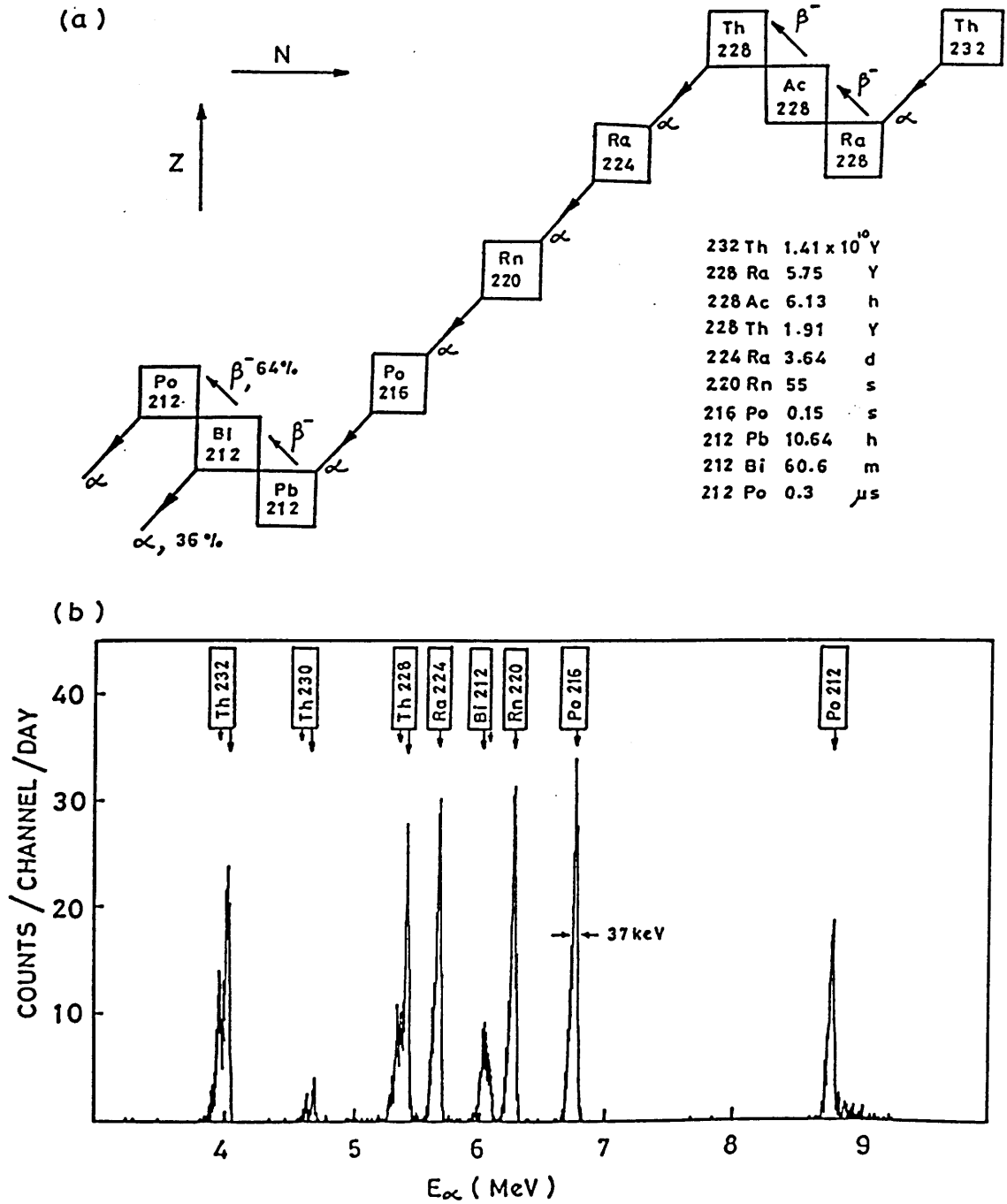

Figure 2.7: Natural radioactivity of ^{232}Th. (a) The thorium [4n] decay scheme. (b) The α–spectrum from a non-irradiated target.

The α–lines from all members of the natural (4n) decay chain (Figure 2.7.a) are clearly resolved. The activities of ^{228}Th $\longrightarrow$ ^{212}Po are in equilibrium while the ratio of ^{232}Th : ^{228}Th is disturbed by a chemical separation of the sample performed some years previously. The ^{230}Th content is independent of the ^{232}Th, originating from a ^{238}U component in the geological mineral. Its activity, which is $\sim 13\%$ of that for ^{232}Th, corresponds to an impurity of less than 1 part per million and is negligible.

2.4.2 Target Holders

Due to the long-lived activity induced through photo-reactions in thorium, a new photonuclear target was in general required for each experimental irradiation. (Cumulative use of the same target was valid only for irradiations at the same beam energy.) Whilst the replication of high quality targets proved a laborious process, the large sensitive area of the individual deposits afforded the possibility of using each target more than once. The small size of the electron beam spot allowed each target disc to be used for up to seven independent irradiations, so in addition to a central spot, six further locations were defined on each target disc at a radius of 8 mm by successive rotation through angles of 60° in an 'off-centre' geometry. The brass target holders of Figure 2.8.a ensured proper alignment of the photonuclear targets in the electron beam line. Targets discs were housed in the matching circular recess where reference marks, at 60° intervals on both target holder and target backing, allowed accurate angular orientation.

A symmetrical target assembly (Figure 2.8.b), comprising two identical target holders fixed back-to-back, provided a facility for photon as well as electron irradiation of the photonuclear targets. A tantalum radiator, sandwiched between the two, acted a source of bremsstrahlung radiation for the rearmost target. (The bremsstrahlung radiator is discussed in detail in the following section.)

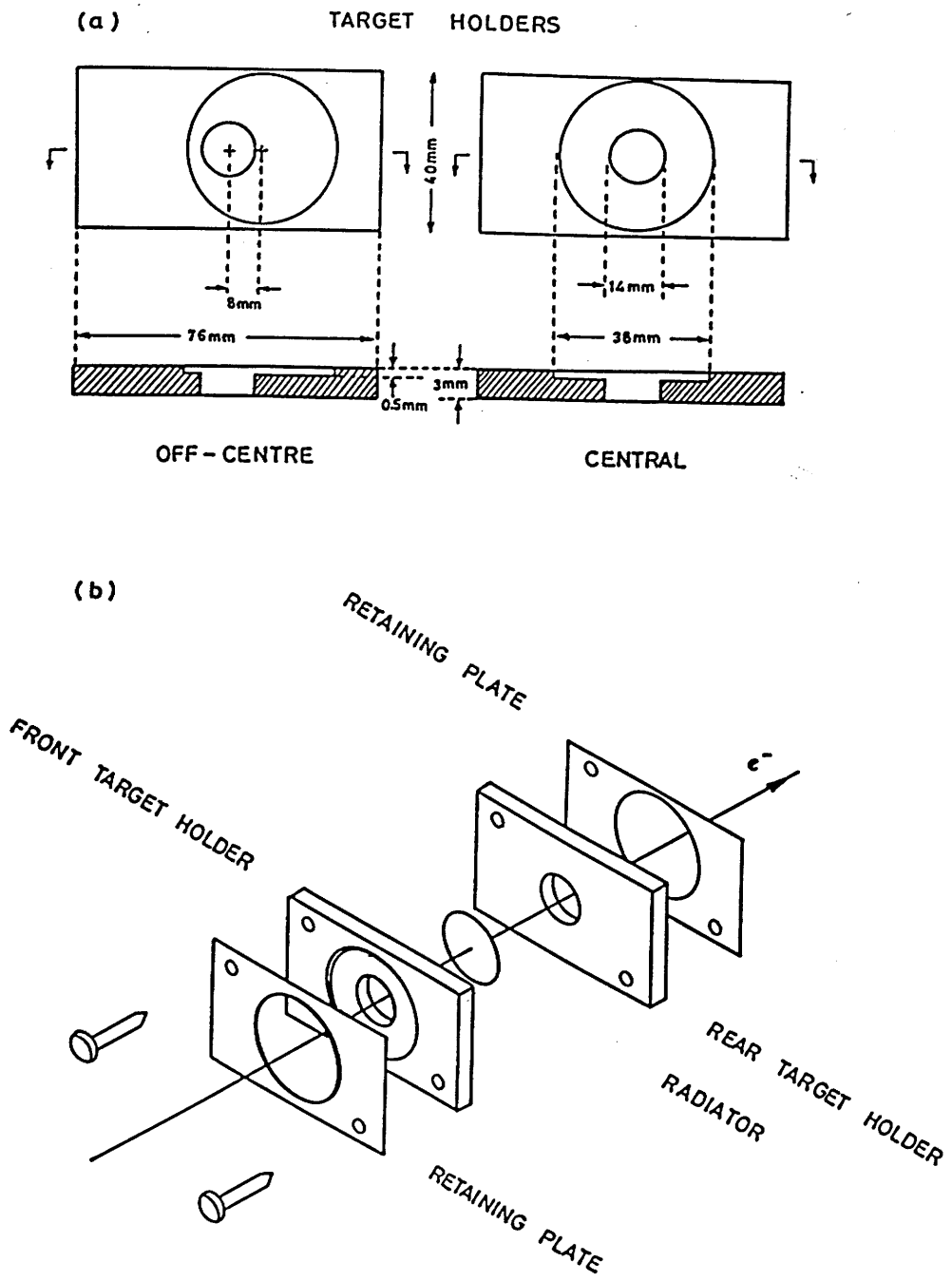

Figure 2.8: Alignment of photonuclear targets in electron beam. (a) Target holders providing off-centre and central alignment. (b) Complete target assembly for electron and bremsstrahlung irradiation (the target holders displayed offer central alignment). Photonuclear targets are not shown.

With its surface deposit facing 'upstream', the disc in the front target holder was activated solely by the electron beam and gave rise to electro-disintegration reaction products only. The rear target on the other hand (facing 'downstream') was subject to both electron *and* bremsstrahlung radiation (generated in the Ta foil and target backings) from which the former contribution was subtracted to obtain the photon-induced yield only. Each photonuclear target was held in place by a thin retaining plate whose aperture was marginally smaller than the target disc diameter.

2.5 Bremsstrahlung Radiator

In the experimental arrangement used to determine the real photodisintegration cross-sections (Section 2.4.2), photons were produced through bremsstrahlung in both of the aluminium target backings as well as in the tantalum radiator foil. The relative contribution from each was proportional to its thickness measured in radiation lengths. The radiation length, l_r , of an element (A,Z) is given by the formula

$$l_r = 716\,\mathrm{A}\left[\mathrm{Z}\left(\mathrm{Z}+1\right)\ln\left(183\,\mathrm{Z}^{-\frac{1}{3}}\right)\right]^{-1} \qquad (2.3)$$

The values for the present experiment are shown in Table 2.1. The tantalum foil produced some 93% of the total photon flux with the remainder being generated in the target backings. The contribution from the thorium deposit was negligible ($< .04\%$).

The radiator had to be thick enough to provide photodisintegration yields of a reasonable statistical accuracy while taking account of the following adverse effects :

1. A degradation of the electron energy spectrum occurs in the downstream target due to collision, ionisation and radiative losses. Corrections are required when subtracting the electrodisintegration contribution from the

Element	Z	Radiation length, l_r [g cm^{-2}]	Foil thickness [μm]	[mg cm^{-2}]	[rad. lengths]
^{27}Al	13	24.4	125	33.7	1.38×10^{-3}
^{181}Ta	73	6.35	138	230.5	3.63×10^{-2}
^{232}Th	90	5.47	0.07	0.08	1.46×10^{-5}

Table 2.1: Radiation lengths and thickness values for target backing, target deposit and radiator materials.

total reaction yield if the two targets see a significantly different spectrum of electron energies.

2. The degradation of the electron spectrum in a radiator of finite thickness will also affect the bremsstrahlung spectrum from the radiator.

3. The multiple scattering of electrons through finite angles can limit the allowable radiator thickness if there are restrictions on the beam spot size at the photonuclear target (Section 2.2.4). In addition, the path length of electrons in the downstream target can be altered, causing an increase in its effective thickness [131].

The actual radiator thickness used (Table 2.1) was chosen to provide photon induced yields of a comparable magnitude and statistical accuracy to those expected for electron induced reactions. The corrections required for finite radiator size, which have been discussed by Barber [66], are summarised below.

(1) At energies above $\sim$ 10 MeV , radiative processes rapidly outweigh collision and ionisation mechanisms as the principal source of energy loss for electrons in matter. The mean energy loss in a material of thickness d_r may then be written [132] as

$$\Delta E_{rad} \approx E_o(1 - e^{-d_r}) \tag{2.4}$$

implying a reduction of $\sim$ 4% in the present case.

(2) The energy losses and straggling of incident electrons can have a significant effect on the bremsstrahlung spectrum when a finite sized radiator is considered [133,134]. The radiator used in the present experiment had however a thickness of less than 0.04 radiation lengths and it was sufficient to employ only the thin target Bethe-Heitler formulation of the bremsstrahlung spectrum.

(3) The mean squared angular deviation of electrons of energy E_o , due to multiple scattering in a foil of thickness d_r (in radiation lengths) is given [135] by

$$\left\langle \theta^2 \right\rangle = \left(\frac{21}{E_o} \right)^2 d_r \tag{2.5}$$

This distribution is highly forward peaked (.1 rads) even at the lowest energies (40 MeV) considered here. By maintaining the close proximity of Figure 2.8 between targets and radiator the spot size was increased by only $\sim$ 0.3 mm and so the entire photon flux was always intercepted within the required area. The effective increase in the thickness of the rear target due to multiple scattering is given by the expression [131]

$$\left(1 - \frac{1}{2} \left\langle \theta^2 \right\rangle \right)^{-1} \tag{2.6}$$

and in this case was negligible.

The radiator thickness was measured accurately in order to make a precise evaluation of the photon spectrum. The tantalum foil was machined to a precise 1″ diameter and the mean thickness $\bar{d}$ found by weighing to be 230.5 $\pm$ 0.3 $\mathrm{mg\,cm^{-2}}$. The thickness uniformity of the tantalum radiator was investigated by monitoring the absorption of low energy x–rays at several points on the foil surface. Details of this measurement are given in Appendix C. The results show that the *local* foil density in the vicinity of the beam spot is the same as the *average* foil density found by weighing.

Since the electron beam travels in a vacuum and is deflected through 45° in the magnetic transport system between the energy-defining slits and the

scattering chamber, it should be free from photon contamination prior to the first target. This was verified by measurements made on areas of the thorium targets 'away from the irradiated spots' which showed the activity produced by 'stray' photons to be negligible.

2.6 Detection System

Following irradiation, the α–activity of the photonuclear targets was measured, under vacuum, using high resolution solid-state detectors in a well defined geometry.

2.6.1 Solid State Detectors

The semi-conductor detectors used here were of the ENERTEC IPE–type with a passivated and ion implanted silicon junction [136]. These low leakage devices ($\sim$ 50 nA) couple high resolution ($<$ 20 keV) with a sensitive detection area of 450 mm^2 and a depletion depth of $\sim$ 100 μm. While α–particles ($\leq$ 12 MeV) deposit *all* of their energy in the sensitive depletion layer of the detector, this region is sufficiently thin that incident β's are transmitted with only a small energy loss and the absorption of γ's is negligible. The detector size used here gave the best compromise between the conflicting requirements of large area and good resolution.

The finite width of an α–peak arises principally from the statistical nature of the charge production processes in the detector, plus a noise contribution from the detector capacity and associated electronics. These effects constitute the 20 keV resolution quoted above. Figure 2.9 shows the α–spectrum from a thin-deposit calibration source illustrating the resolution obtainable with the present system. The real targets had however, a finite thickness which imparted a sizeable energy-loss contribution to the measured peak width (Section 2.4).

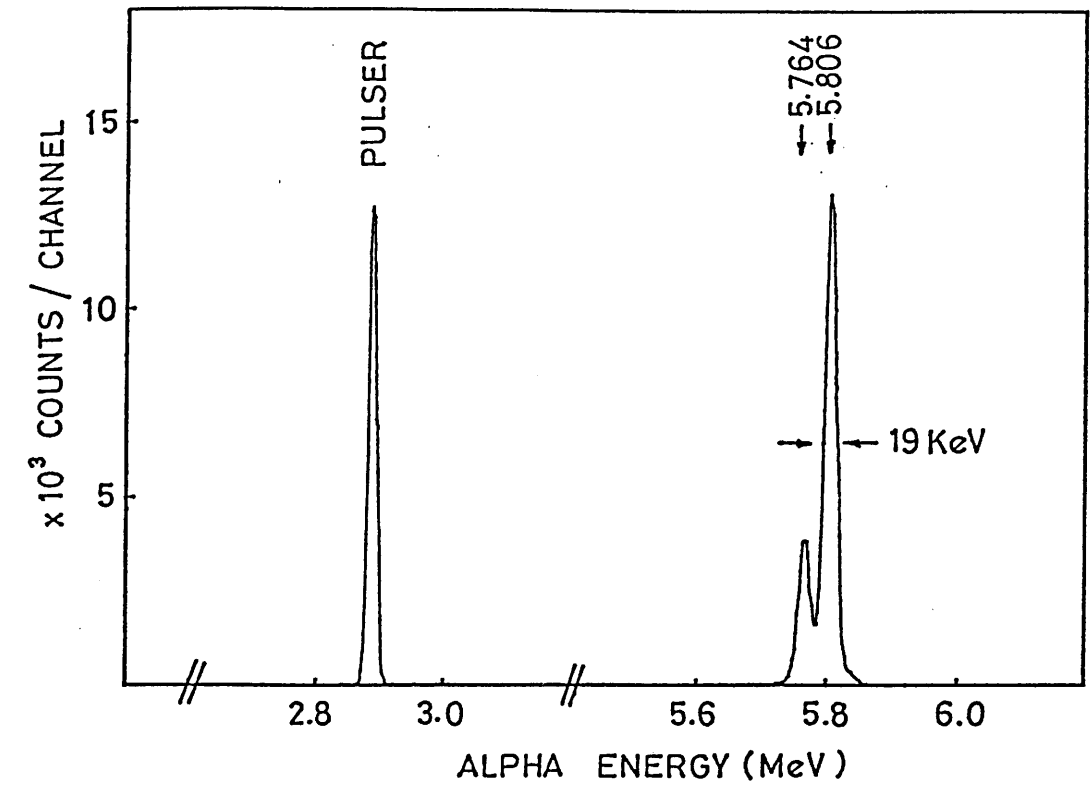

Figure 2.9: The α–spectrum from a ^{244}Cm calibration source showing optimum system resolution. The low energy pulser peak is used for dead-time correction.

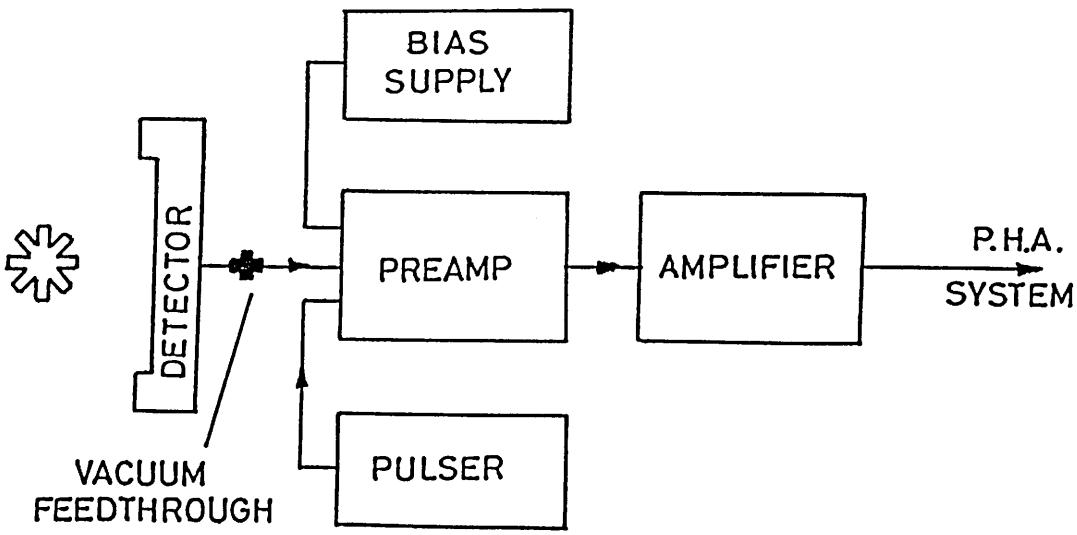

Figure 2.10: Schematic diagram of solid-state detector and analogue electronics.

2.6.2 Counting Geometry

The α–activity of the irradiated targets was measured in the apparatus of Figure 2.11. A close geometry between the source and detector was necessary to maintain a reasonably large solid angle. In this configuration the detector subtended a solid angle of $\sim$ 1.79 sr from a point source 10.25 mm away. This separation was a compromise between the solid angle and the energy resolution, which is broadened at large solid angles (Eqn. B.1) due to additional energy losses in the target material .

The acceptance area of the solid-state detector was defined by an external collimator and *not* by the physical edge of the silicon wafer. The poorer charge collection properties exhibited near the extremes of the detector can otherwise create finite low energy tails on the spectrum peaks.

In this geometry, the irradiated part of the photonuclear target ($\sim$ 2mm in diameter) lay on the central axis of the counting chamber at a distance of 10.25 mm from the detector collimator. A 7 mm collimator masked the activity from other active spots on the target as well as defining the area over which the natural activity was monitored for thickness evaluation. Since the natural and induced activities were measured in the same geometry, the solid angle factor was essentially eliminated from the cross-section evaluation. A small correction did arise due to the extended nature of the two sources, as each had a different 'effective' solid angle as explained in Appendix D.

As targets were removed from the chamber between counting periods and later replaced, a reproduceable solid-angle was essential to avoid discontinuities in the reaction-product 'decay curves'. In such a close geometry, the solid angle Ω varies rapidly with source to detector distance z (Figure 2.12) and targets had to be replaced with great positional accuracy. With low target distortions ensured through the use of a stiff backing material, and precise collima-

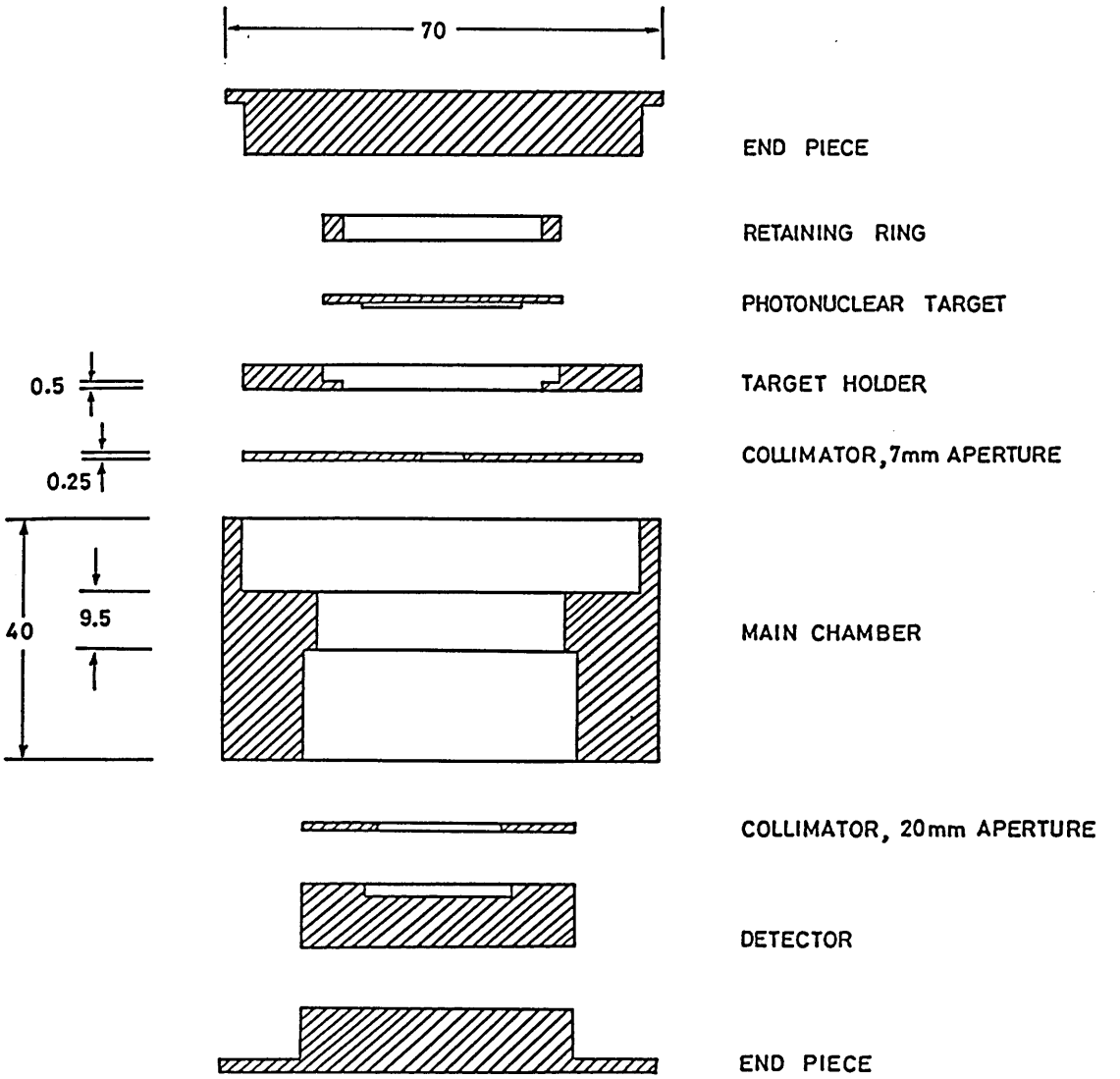

Figure 2.11: Expanded view of the cylindrical chamber used for α–particle counting. Important dimensions are shown in mm. A target holder with an off-axis recess was substituted for the counting of off-central active areas.

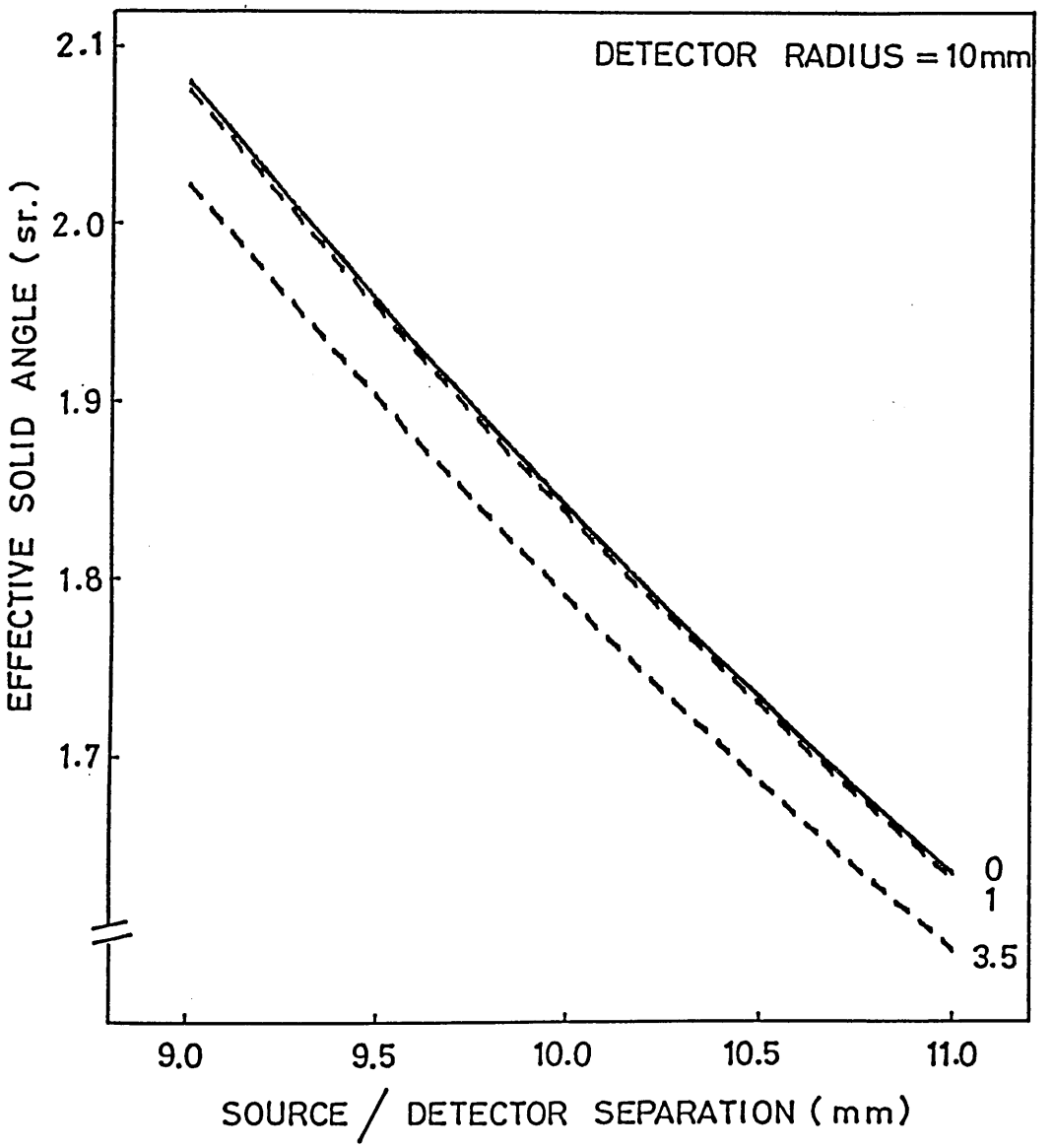

Figure 2.12: Effective solid angle Ω_{eff} vs. z for source radii of 3.5 mm, 1 mm and 0 mm (point source).

tion/separation provided by the counting chambers, a solid-angle reproducibilty of better than 2% has been verified.

2.6.3 Vacuum System

Counting was performed with the chambers under vacuum ($\sim 10^{-6}$ torr) to avoid the energy losses and straggling suffered by α–particles in air. The 'bell-jar' assembly of Figure 2.13 was used to establish the vacuum rapidly, as required for measurement of the short half-life species. The total access and evacuation time for these vessels was $\sim$ 40 seconds and short compared to the total elapsed time from irradiation-end to count start. (The removal of targets from the scattering chamber to the counting room took approximately 4 minutes.)

Four such vacuum 'stations' were available, with independent access, on the same base plate. These were served by single 'diffusion' and 'rotary' pumps via common manifolds (Figure 2.13) to attain the working pressures. Since the diffusion pump required regular filling with liquid nitrogen coolant, high vacuum conditions were maintained by means of an ion pump when the system was left unattended. Electronic connections between the detectors and preamps (Figure 2.10) were made via vacuum feedthroughs (Figure 2.13).

2.7 Signal Processing

Analogue signals from the solid-state detectors were shaped and amplified by the circuit of Figure 2.10 prior to digital conversion in the pulse height analysis system of Figure 2.14.

The current signal from the detector, on the interaction of an incident particle, was first collected by a charge sensitive pre-amplifier. (The connecting cables were kept short ($\sim$ 25 cm) in order to reduce the stray capacity of the

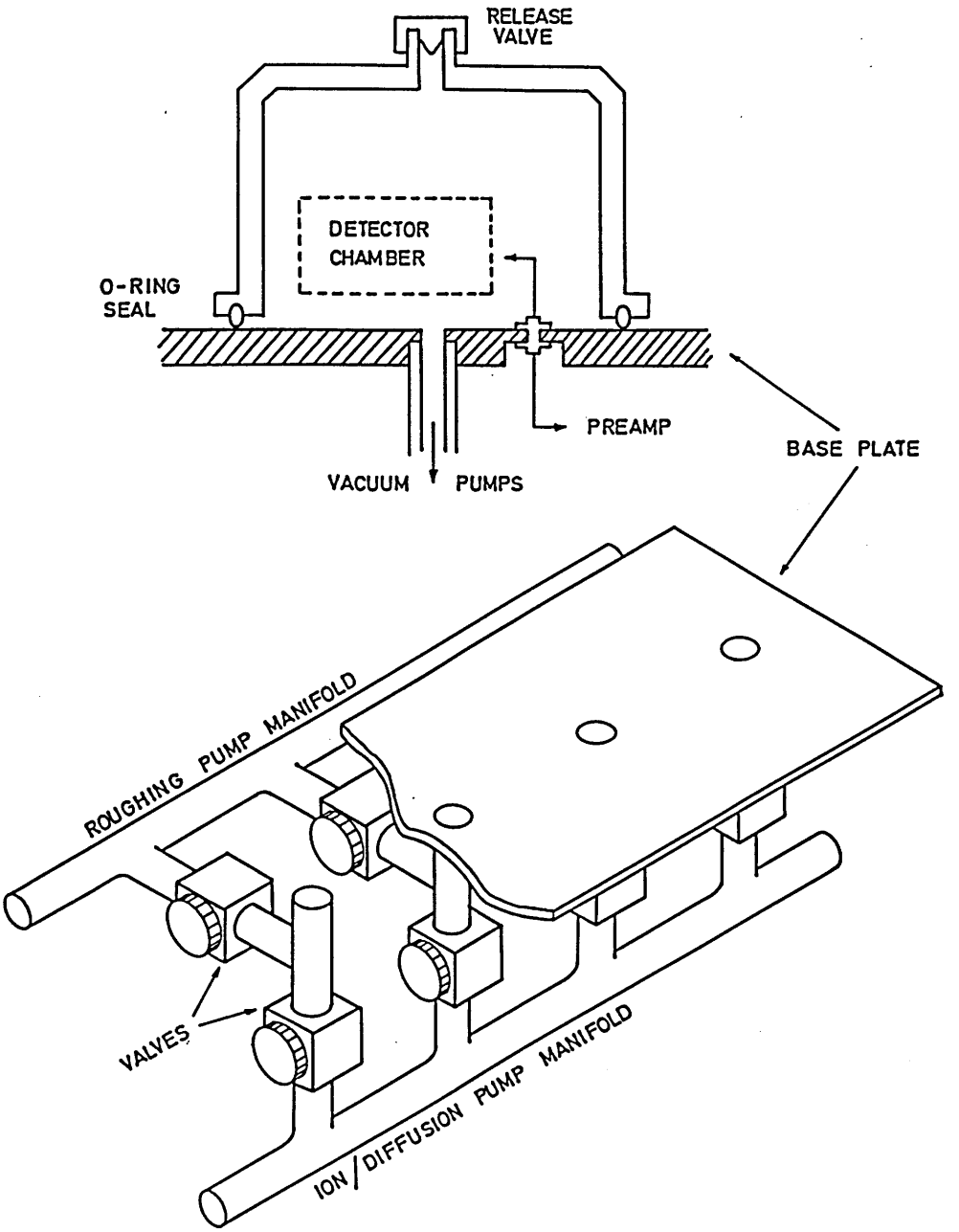

Figure 2.13: Vacuum System

pre-amplifier system). The output pulses from the pre-amplifier were then amplified ($\times 50$) and shaped in a main amplifier whose output range of 0 to 8 volts corresponded to α–energies between 0 and 10 MeV. Four such networks were multiplexed through a single ADC to form a multi-detector spectroscopy system which could be computer controlled. Specifications for the amplifier and pre-amplifier modules are given in Table 2.2.

A single mains-locked pulser was used to send a shaped pulse, of $\sim$ 3 MeV equivalent, sequentially to each of the four pre-amplifiers with a frequency of 12.5 hz in each channel. These test pulses allowed the system 'dead-time', at the time of data collection, to be evaluated by a simple integration of the 'pulser peak' in the α–spectrum. Since a single ADC was used to handle all pulse height conversions, the pulses into each channel had to be 'staggered' in this way to avoid rejection.

The pulse height analysis system (Figure 2.14) consisted basically of a CAMAC interfaced analogue to digital converter (ADC) running under software control from an LSI–11/44 microcomputer. The Le Croy 3511 ADC was sufficiently fast to process the pulses from all four detectors which were mixed and routed via a Le Croy 3542 multiplexer. The digitised pulse heights (4096 channels) and routing signals were transferred to the LSI–11 via the CAMAC dataway. A hardware link between the CAMAC modules and the computer was provided by the crate controller.

Low level discriminators at the multiplexer inputs were used to reject incoming signals with amplitudes below a preset voltage threshold (usually $\sim$ 2 MeV equivalent). This markedly reduced the system dead-time caused through ADC conversion of low energy β signals.

A data acquisition code running under an RT–11 operating system allowed computer control of the entire spectroscopy system. The digitised pulse heights

Pre-amp	type	: Ortec 142A
	load resistance	: 100 MΩ
	conversion gain	: 45 mV MeV^{-1}
	detector bias	: ~ 100 V
	signal rise time	: ≤ 12 ns
Amplifier	type	: Ortec 572
	gain	: ~ 50
	shaping constant	: 1 μs
	output range	: 0 – 8 V
	optimisations	: baseline restorer, pole-zero cancellation, output baseline d.c. level adjustment.

Table 2.2: Amplifier and pre-amplifier specifications.

from each of the 4 inputs were routed to a separate quarter of the LSI-11 16k memory. With independent control of each input, these 4096 channel spectra could be accumulated for a preset interval before being stored on a high capacity Winchester disk. The code controlled the cycling and dumping of spectra, recording the spectrum filenames and accumulation times on a hard-copy lineprinter. Spectra could be visually displayed, during accumulation, on a t.v. display monitor driven from a CAMAC display module. Mass data storage was not possible on this system however, and the collected spectra were transferred frequently, via floppy disk, to the mainframe VAX–11/780 for subsequent analysis.

The microcomputer was powered from a stabilised voltage source to help reduce the number of c.p.u. 'crashes' caused by the voltage 'spikes' which tend to pervade the mains supply of the laboratory. At each restart of the computer operating system, the internal clock (from which the spectrum dump times were taken) was synchronised to a battery powered quartz clock which provided a standard time for the whole experiment.

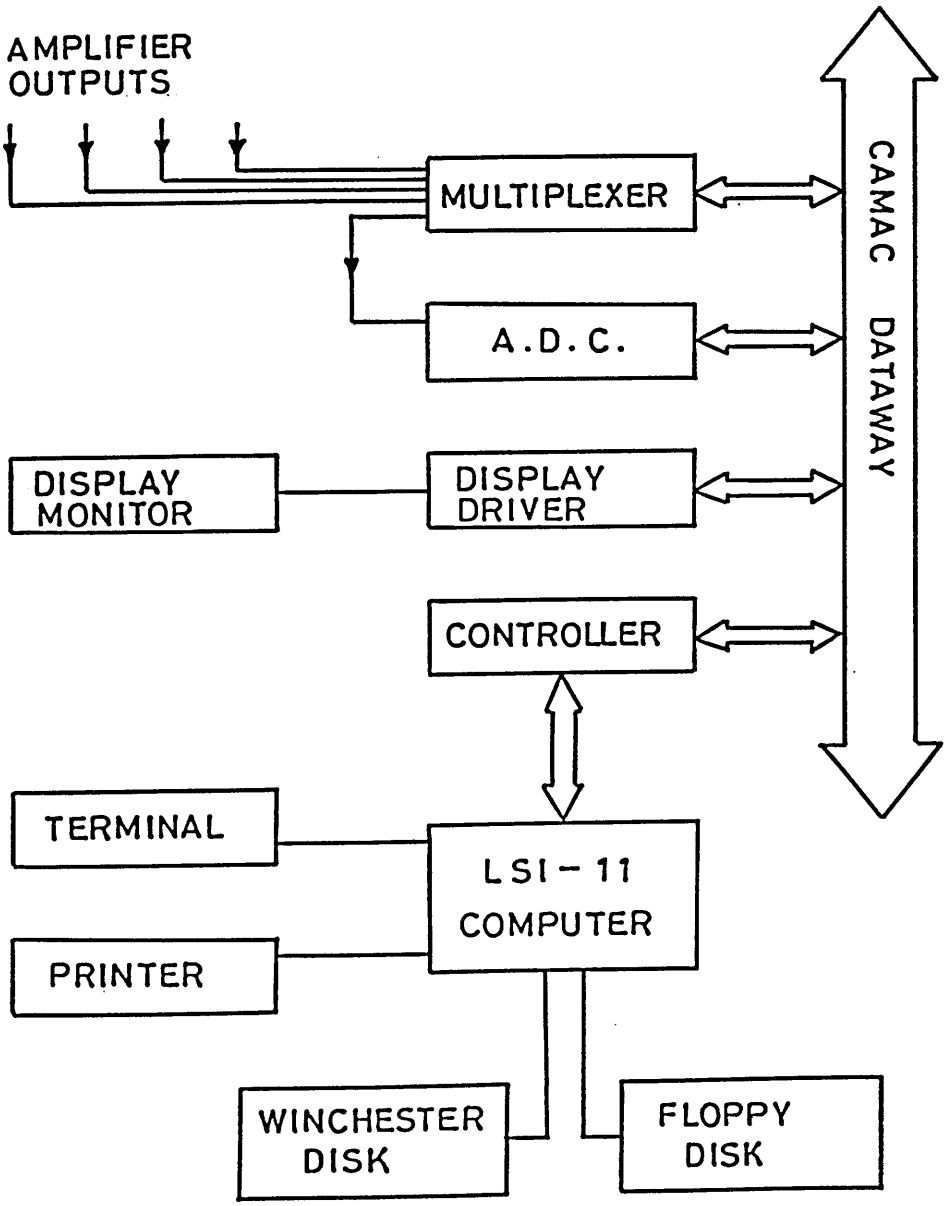

Figure 2.14: Signal processing electronics for the multi-detector spectroscopy system.

2.8 Experimental Programme

Electron irradiations were performed at 40, 50, ..., 150 MeV, spanning the entire energy range achievable with the Glasgow LINAC, and suitably covering the present region of interest. Bremsstrahlung activations were made at 60, 100 and 140 MeV to investigate the relative magnitude of the 'real photon' yields.

Because the reaction products of interest spanned such a wide range of half-lives (2 mins to 2 yrs), the experimental irradiations were divided into two categories in order to enhance the activities of the short-lived over long-lived species, and vice-versa. A series of short irradiations was performed, aimed principally at measuring the reaction yields of ^{226}Th,^{225}Th and ^{223}Ac, which have half-lives of 31, 8 and 2 minutes respectively [137]. Since the population of an unstable reaction product does not increase linearly with irradiation time, as a result of decay loss, those with short lived activities become rapidly 'swamped' due to the build up of longer lived species. It was not worth prolonging any individual irradiation beyond $\sim$ 8 minutes for the shorter half-life measurements and instead repeated irradiations were performed at the same energy in order to build up statistically accurate data. This approach had the added advantage of checking the reproducibility of the measurements and thus the experimental procedures. For example, similar cross-section measurements made on *different* targets provided a check on the target thickness measurements and their assumed uniformity over the exposed area (Section 2.6).

Reaction products with half-lives of several hours or more, suffer less from the effects of decay loss and could be accumulated through longer irradiations of the order of 10 hours. A second set of irradiations was made which produced even the longest lived nuclides in sufficient quantity that they could be counted within a tolerable time scale ($\sim$ 6 months). These irradiations were of such a length that they provided yields of good statistical accuracy ($\sim$ 1 %) before

Electron Energy	Incident Radiation	Experimental Irradiations
40 MeV	e^-	1 × 14 hrs
	e^-	1 × 8 mins
50 MeV	e^-	1 × 14 hrs
	e^-	4 × 8 mins
60 MeV	e^-	1 × 12 hrs
	e^-	3 × 8 mins
	$e^- + \gamma$	1 × 12 hrs
	$e^- + \gamma$	2 × 8 mins
70 MeV	e^-	1 × 8 hrs
	e^-	3 × 8 mins
80 MeV	e^-	1 × 13 hrs
	e^-	4 × 8 mins
90 MeV	e^-	1 × 10 hrs
	e^-	6 × 8 mins
100 MeV	e^-	1 × 8 hrs
	e^-	3 × 8 mins
	$e^- + \gamma$	1 × 8 hrs
	$e^- + \gamma$	2 × 8 mins
110 MeV	e^-	1 × 10 hrs
	e^-	3 × 8 mins
120 MeV	e^-	1 × 9 hrs
	e^-	4 × 8 mins
130 MeV	e^-	1 × 10 hrs
	e^-	4 × 8 mins
140 MeV	e^-	1 × 14 hrs
	e^-	4 × 8 mins
	$e^- + \gamma$	1 × 14 hrs
	$e^- + \gamma$	2 × 8 mins
150 MeV	e^-	1 × 9 hrs
	e^-	4 × 8 mins

Table 2.3: Programme of Irradiations.

Time from Irradiation End			Count Interval
$\sim$ 4 mins	$\longrightarrow$	40 mins	2 mins
40 mins	$\longrightarrow$	2 hrs	6 mins
2 hrs	$\longrightarrow$	4 hrs	12 mins
4 hrs	$\longrightarrow$	12 hrs	20 mins
12 hrs	$\longrightarrow$	2 days	1 hr
2 days	$\longrightarrow$	4 days	12 hrs
4 days	$\longrightarrow$	8 months	12 – 24 hrs

Table 2.4: Count intervals for data collection.

background effects (e.g. ^{24}Na activity) became so intolerably large that further activation would have proved counterproductive. The entire programme of irradiations is listed in Table 2.3.

Following irradiation, the α–spectra from the activated targets were automatically gathered and stored in cycles of preset duration. The counting intervals were incremented, as shown in Table 2.4, as the time from irradiation-end increased. This provided individual spectra with well defined peak structure as well as preserving, with adequate resolution, the time evolution of the decaying activities. Reaction products could then be identified from their radio-active half-lives as well as through their characteristic alpha energy.

For 'short' irradiations, counting was halted after approximately 4 hours in favour of re-irradiation, while for 'long' irradiations, targets were monitored periodically for up to 8 months. Counting intervals of 24 hours were never exceeded during the collection periods, in order to reduce the data loss suffered in the event of a computer processor 'crash' (Section 2.7). In total, more than 6500 spectra were collected in the course of the experimental programme.

While target activities were monitored *constantly* for the first 2 weeks after irradiation, it was not possible, with only 4 detection systems, to measure a large number of activated targets in a continuous fashion beyond this period. To

overcome this restriction, irradiations were staggered in time and targets were interchanged on a daily basis until counting was complete. In order to compare the relative efficiencies of the individual detector systems, arising through small differences in their geometries, some of the targets were replaced in *different* chambers over part of the data collection period. The ratios of natural to induced activity remained constant in each chamber, as expected, while the absolute efficiences differed by only a few per cent.

The maximum count rates encountered during data collection were of the order of several thousand per second and easily handled by the ADC. The mean 'dead-time' of the system, determined from the number of unprocessed test pulses, was in the worst case $\sim 0.2\%$.

2.9 Summary

Previous investigations of multiple photonucleon emission using activation methods, relied upon measurement of the residual γ–ray activity of irradiated targets to determine the yields of β–decaying reaction products. A comparison is made here between the α–spectroscopy methods employed in the present experiment and those used in the γ–ray activation analyses. This will outline the relative merits of the two approaches as well as highlighting some of the key features of the experimental system.

- *Target thickness* : In previous experiments, target thickness measurements were often suspect since they were evaluated from the weight and area of a target whose overall size was much larger than its activated region. An averaged value such as this may of course be quite different from the local thickness in the vicinity of the beam spot and includes a contribution from any impurites which might exist in the sample. Considerably thicker targets could, however, be tolerated due the high penetrability of the γ–rays, but the effects of in-target

bremsstrahlung had then to be considered.

In the present experiment, the natural radioactivity from the target provided an excellent means of determining target thickness and by nature specified the density of *target* nuclei only. Since the natural activity and the induced activity (from reaction products) were measured simultaneously, the solid-angle effect in the detector efficiency was, to first order, removed. While thin targets had to be tolerated for resolution purposes, the α–spectra tended to be free from background contamination and even products of very low yield became discernible. Despite the thickness constraint, adequate count-rates were obtained for most of the reactions under investigation while the problem of in-target bremsstrahlung was avoided.

• *Spectral background* : The large Compton background associated with each 'full-energy' peak in a γ–ray spectrum can swamp the activity of smaller peaks which one might wish to investigate. In addition, these Compton photons substantially increase the total flux incident upon the γ–ray detector, resulting in longer signal processing and larger dead-times in the pulse height analysis system. Despite large amounts of shielding, a finite external background has normally to be subtracted from the spectra.

In α–spectra, the intrinsic background due β and γ–radiation is very small since they deposit very little energy in the depletion layer of the detector and the background from external sources is negligible. As a result, the total count rates are lower in α–spectroscopy measurements for the same yield of data, since none of the processed signals represented 'unwanted' activity.

• *Branching ratios* : In the analysis of γ–ray spectra, the absolute branching-ratios, which determine the intensity of individual lines, are often poorly determined. For each residual nuclide several decay modes are usually possible and this can lead to a vast number of lines in the γ-ray spectrum. Often, only

relative intensities can be established and this gives rise to uncertainties in the evaluated cross-sections.

Alpha transitions, on the other hand, occur predominantly to levels near the ground state with α–branches of 100%. Where other transitions do occur, the branching ratios have usually been well determined by high-precision magnetic spectroscopy measurements on isolated samples. As a result, α–spectra prove less complex than γ–spectra, since fewer lines originate from each unstable nuclide, and absolute cross-section measurements are generally more reliable.

• *Reaction Products* : The cross sections for $(\gamma, x\mathrm{n})$ reactions can, in principal, be measured for a wide range of heavy nuclei ${}^{N}_{Z}X$ using γ–ray methods, since most residual nuclei ${}^{N-x}_{Z}X$ decay via β^{+}–emission or electron capture, coupled with the release of a γ–ray. However the first daughter product of such a decay scheme is a nuclide of the type ${}^{N-x}_{Z-1}X$ which can also arise through the initial $(\gamma, x\mathrm{n}\,1\mathrm{p})$ reaction. This 'feeding' into the ${}^{N-x}_{Z-1}X$ population makes the latter reaction yield very difficult to measure. The situation is worsened due to the higher cross-sections expected for $(\gamma, x\mathrm{n})$ over $(\gamma, x\mathrm{n}\,1\mathrm{p})$ reactions and the fact that nuclide half-lives are frequently quite short.

When the residual nuclides following $(\gamma, x\mathrm{n})$ or $(\gamma, x\mathrm{n}\,1\mathrm{p})$ reactions are α-unstable, the decay schemes do not interfere in the same way and the latter reaction cross-section can be more easily determined. The main disadvantage of this method is that only a small range of nuclides exhibit α–emission as their principal source of decay. This confines investigations to a rather limited region of the nuclide chart and to a limited range of x and y for each target.

• *Detection Efficiency* : While the geometric efficiency of a γ–ray detector is given by the source to detector solid-angle, its intrinsic detection efficiency is an energy-dependent function which must be measured using calibration sources of assumed activity. However, since larger detectors are available, a greater

source to detector separation can be tolerated without substantially reducing the solid-angle. The advantage of a large separation is that the solid angle then depends less critically upon the exact positioning of the source with respect to the detector.

The much thinner α–detectors are limited in size due to capacitive effects which rapidly reduce their energy resolution. A much closer geometry is required to achieve the same solid-angle and the tolerance in the source to detector distance is vastly reduced. With reasonable care however, a reproduceable geometry has been maintained throughout the course of the data acquisition. Due to their low penetrability, α–particles are easily collimated, allowing better evaluation of the absolute solid-angle. Provided that the detector's depletion layer is of adequate depth, the intrinsic detection efficiency for α's is essentially 100% and is independent of the α–particle energy.

• *Vacuum requirement* : While an air gap between source and detector has a negligible effect upon the transmission of γ–rays, it seriously reduces the energy resolution of α–particles due to the large energy losses and straggling incurred. For high resolution α–spectroscopy, the source/detector system must therefore be kept under vacuum. The time taken to establish such conditions at the end of an irradition has been reduced to less than 1 minute, and has not inhibited measurements of the shorter half-life species.

• *Absorption losses* : It has usually to be assumed that any collimating device will totally block the passage of radiation incident upon the detection system, with complete transmission elsewhere. The existance of regions where partial absorption occurs (collimator edges, detector dead-layers, finite air gaps or in the target material itself) can have an uncertain effect on the incident flux. For γ–rays, such partial absorption results in a net loss of flux with no energy degradation and can be difficult to recognise. When the same situation arises in

an α measurement, there is immediate indication through the energy straggling of the individual lines. Greater confidence can then be placed on solid-angles which are calculated solely on a geometrical basis.

Chapter 3

Data Analysis

3.1 Introduction

This chapter describes the data reduction process used to evaluate the reaction yields for electron and bremsstrahlung induced multiple nucleon emission. Since both radiation sources exhibit a continuous spectrum (up to the electron beam energy), mono-energetic cross-sections for these reactions were not obtained directly and instead an *integral* yield was measured as a function of the electron end-point energy. The resultant curve will be referred to as a 'yield function' or, when expressed as the reaction yield per target nucleus per incident electron (or equivalent quantum), as a 'reduced yield function'. The mono-energetic reaction cross-sections were later extracted from these functions by unfolding the appropriate radiation spectrum (Chapter 5).

The reduced yield y, defining the basic probability of a nuclear reaction process at electron energy E_j, is related to the total number of reaction products as follows :

$$y(E_j) = \frac{Y}{N_o n_i} \tag{3.1}$$

where Y is the total reaction-product yield, N_o is the number of target nuclei per cm^2 and n_i is the total number of incident electrons. The total yield Y for each reaction was deduced from the α–activity of the reaction product, measured under well defined geometrical conditions and for a known flux of

incident radiation. Here, the α–decay curves of the residual nuclide activities were fitted in order to determine the contents of reaction products at some reference time, $t = t_o$, just after the end of irradiation. These measured yields Y_m, when corrected for the effects of decay loss and feeding during irradiation (Section 3.4), are related to the total reaction yield through the solid-angle efficiency of the detection system :

$$Y_m = Y \frac{\Omega_{eff}(a)}{4\pi} = Y \frac{\nu_a \Omega_{ps}}{4\pi} \tag{3.2}$$

The quantity ν_a is the correction to the point source solid angle Ω_{ps} for the 'activated' part of the target extending to radius a. The total number of incident electrons depends upon the charge delivered by the electron beam

$$n_i = \frac{Q_{tot}}{e} = \frac{C_B P_{tot}}{e} \tag{3.3}$$

The 'Brookhaven constant' C_B relates the scaled integrator pulses P to the integrated beam current as defined in Section 2.3.

The density of target nuclei N_o (nuclei/cm^2), was deduced from the natural thorium background activity (Figure 3.4) over an area πb^2 with effective solid angle

$$\Omega_{eff}(b) = \nu_b \Omega_{ps} \tag{3.4}$$

If D decays per minute are observed from the exposed ^{232}Th then

$$N_o = \left[\frac{D}{\pi b^2}\right] \left[\frac{4\pi}{\nu_b \Omega_{ps}}\right] \left[\frac{T_{\frac{1}{2}}}{\ln 2}\right] \tag{3.5}$$

where $T_{\frac{1}{2}}$ is the thorium half-life in minutes. Combining equations (3.1) to (3.5) gives

$$y(E_j) = Y_m \left[\frac{\pi b^2}{D}\right] \left[\frac{\ln 2}{T_{\frac{1}{2}}}\right] \left[\frac{e}{C_B P_{tot}}\right] \left[\frac{\nu_b}{\nu_a}\right] \tag{3.6}$$

Except for the lower order corrections, the solid angle efficiency of the detection system cancels out in this evaluation. The symbols are summarised in Table 3.1.

Y_m	:	Total measured yield for a reaction product at $t = t_o$ (corrected for any feeding from a parent nuclide during irradiation and for decay losses during the same period).
t_o	:	A reference time defined for each irradiation which corresponds to the end of the irradiation and the start ($t = 0$) of data collection.
D	:	Measured activity of ^{232}Th in counts/min.
πb^2	:	Area of target measured for thickness evaluation.
Ω_{ps}	:	Point source solid angle subtended by detector.
ν_a	:	Correction to point source solid angle for an extended source of radius a (activated area). The value of a was typically less than 1.5 mm at which radius $\nu_a = 0.995$.
ν_b	:	Correction to point source solid angle for an extended source of radius b (^{232}Th background area). The quantity $\nu_b = 0.973$ for $b = 3.5$ mm.
$\Omega_{eff}(r)$	:	Effective solid angle subtended by detector for an extended source of radius r.
$T_{\frac{1}{2}}$	:	Radioactive half-life of ^{232}Th $= 1.405 \pm .006 \times 10^{10}$ yrs [138].
P_{tot}	:	Time integrated toroid pulses for irradiation up to $t = 0$.
C_B	:	'Brookhaven' constant. Calibration of current integrator equal to $(2.1617 \pm .0042) \times 10^{-7}$ Coulombs/pulse.
e	:	Electronic charge.

Table 3.1: Symbol Definitions

3.2 Alpha Spectrum Analysis

The spectra of Figure 3.1, collected at various time intervals after the end of irradiation, illustrate the typical complexity and time evolution of the induced α–activity.

In order to identify unambiguously the many observed lines in these spectra, some form of energy calibration was required. Fortunately a few strongly active reaction products (namely ^{228}Th and ^{226}Th) were in evidence, along with their daughter products, in a majority of the gathered spectra and their peaks provided a convenient *internal* energy calibration without recourse to the use of separate calibration sources.

The extraction of individual α–peak areas followed one of two paths. In several regions where the peaks are strongly overlapping, the individual areas were extracted by line-shape fitting. The computer code SAMPO [139]–[141], developed for the analysis of γ-ray spectra, was adapted and used here to fit reference functions of predefined shape to the measured α–particle data. The fitted function took the form of a modified Gaussian with low and high energy exponential tailing. The Gaussian was allowed to have different half-widths above and below its centroid to simulate the low energy broadening found in real alpha peaks due to energy losses and straggling. Typical results are shown in Figure 3.2. Details of the functional form and fitting procedures are given in Appendix F.

For the simpler case of well isolated peaks, it was sufficient merely to sum the number of counts within a preset window, outwith which the background activity was measured to be zero. A portion of an α–spectrum where such an approach is appropriate is shown in Figure 3.3. This method was also used in the case of ^{212}Po, where an abnormal peak shape arose due to its fast decay time (300 ns) which frequently caused the α–signals to overlap in time with

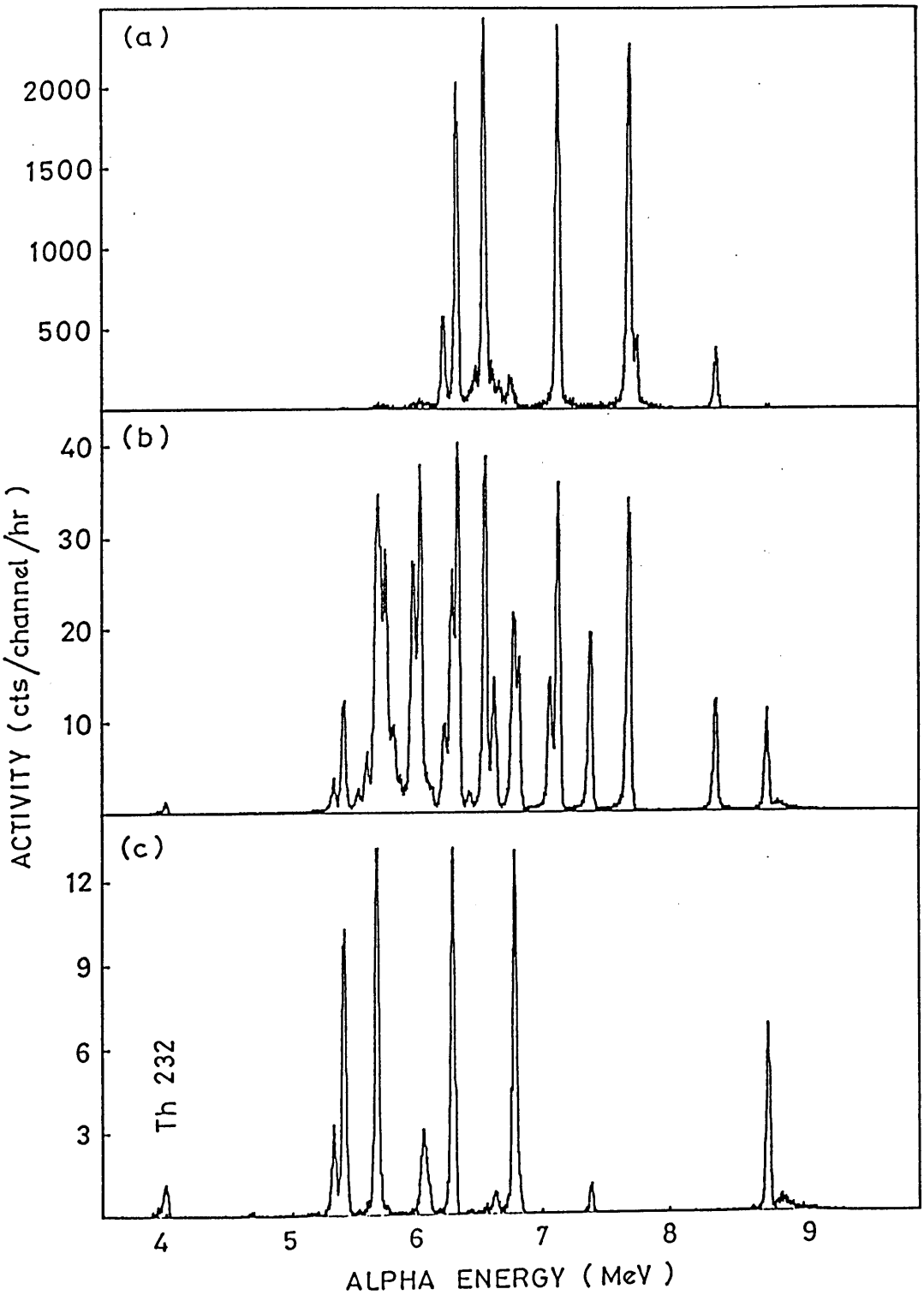

Figure 3.1: Alpha spectra from an 8 hour irradiation at 100 MeV collected at (a) 13 mins. (b) 54 hrs. (c) 157 days.

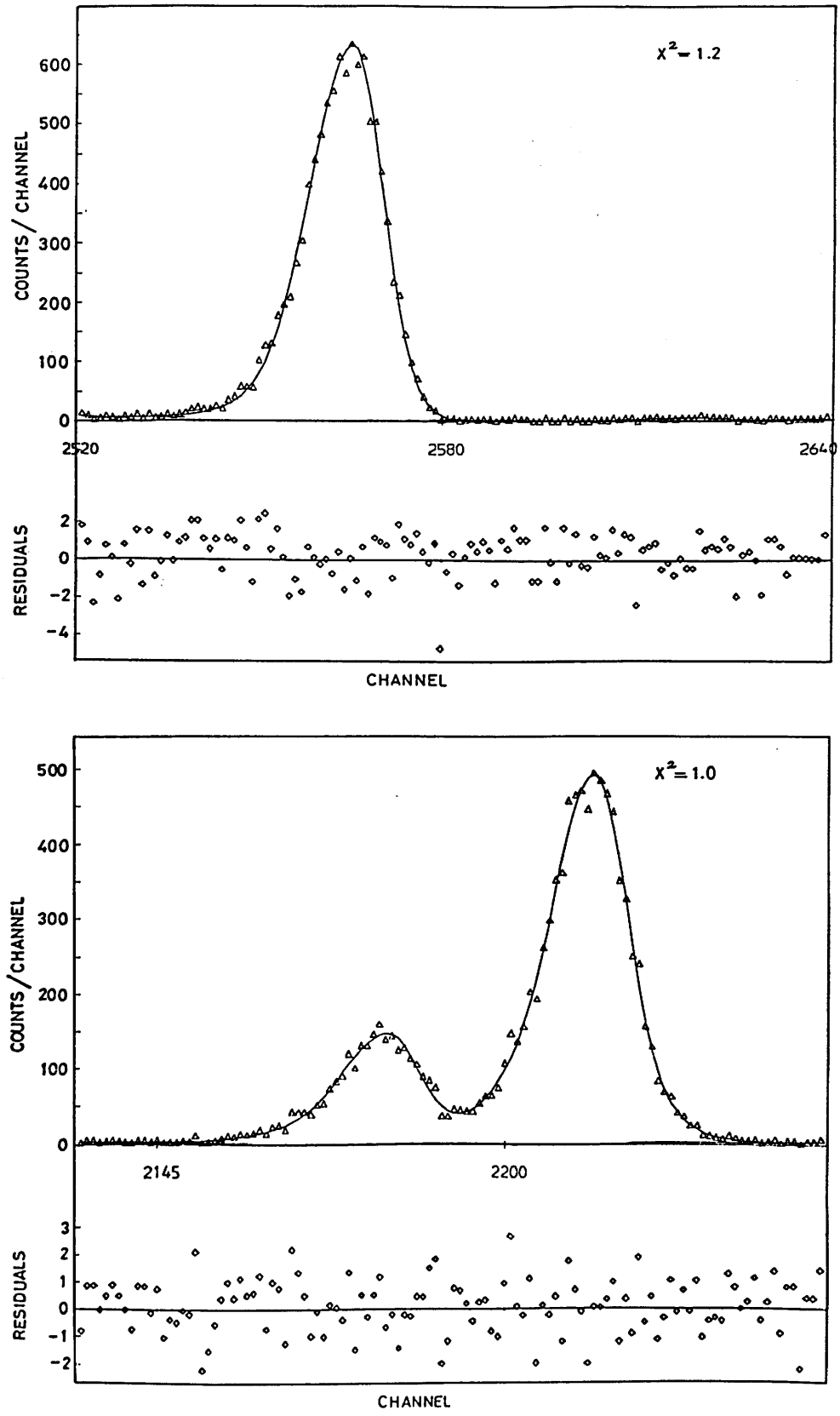

Figure 3.2: The extraction of α-peak areas from measured spectra by line shape fitting. (a) Fitting to a single peak. (b) Fitting to a peak doublet.

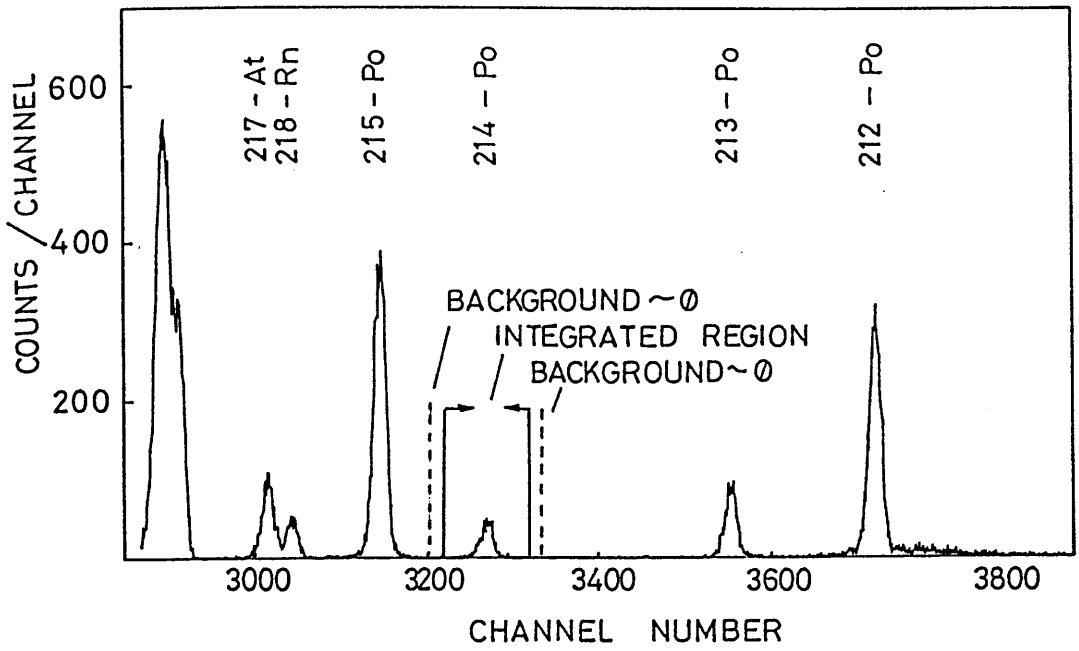

Figure 3.3: The extraction of α–peak areas by a simple integration procedure over preset regions. The method is applicable to isolated peaks (or multiplets) for which the external backgrounds are zero.

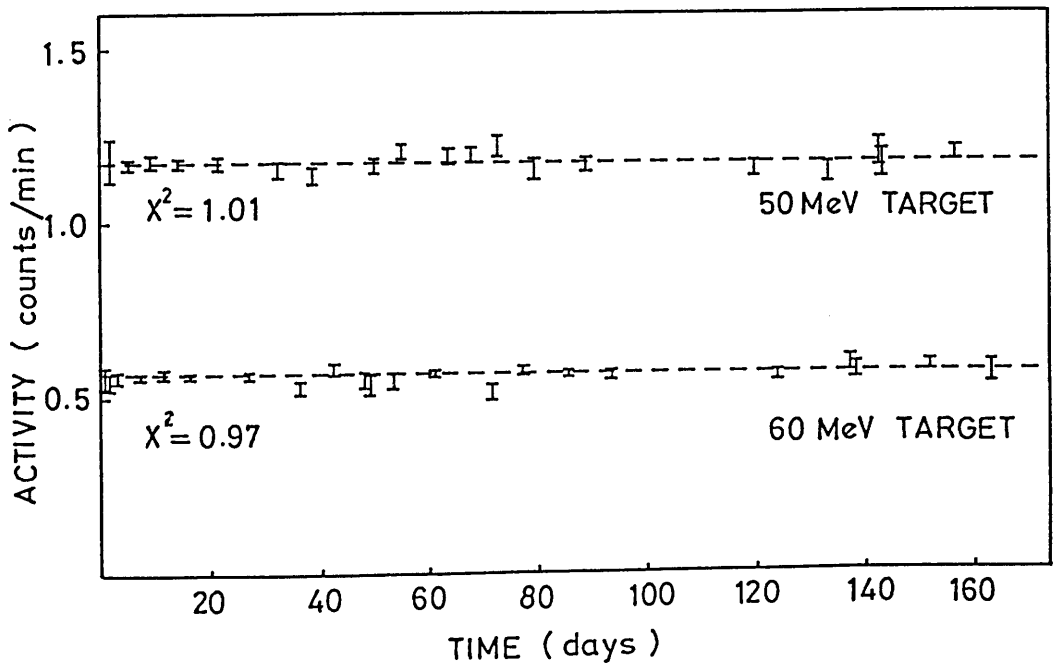

Figure 3.4: Natural ^{232}Th activity from spectra gathered after irradiations at 50 and 60 MeV. The constant activities were fitted to determine target thickness.

those from preceding emissions in the decay chain.

In cases where strongly overlapping peaks were not satisfactorily resolved, the total area was measured for the peak multiplet and, provided that the half-lives were sufficiently different, the individual activities inferred from the behaviour of the composite decay curve (Section 3.3 and Figures 3.6 and 3.7).

A variety of photonuclear reactions were identified from (a) the characteristic α–activity of the *primary* reaction products or (b) the activity of daughter nuclides in their subsequent decay schemes. The major decay chains together with α–particle energies, branching ratios and half-lives are described in Appendix H. Reaction products which emitted alphas in the energy range from approximately 5 to 7 MeV tended to decay through a series of small α–branches, and create many small and overlapping α–peaks which could not be satisfactorily separated with the present system resolution. In order to determine the yields of these primary reaction products, the stronger lines of their shorter lived daughter nuclides, which lay higher in energy and had α–branches closer to 100 % , were analysed instead.

3.3 Decay Curve Analysis

The extracted peak areas were combined with the accumulation and live-time information to produce decay curves for the reaction products identified. A convenient start-time, denoted t_o, between the irradiation-end and the commencement of data collection was chosen as a reference time for each irradiation. Dead time effects were found to be less than 0.2 % in all of the spectra analysed (Section 2.8) and no corrections were applied.

Initial reaction yields were determined by the least-squares fitting (Appendix E) of an appropriate function to each of the decay curves. Appendix G describes the general form of the decay functions which were applied here. In many of the decay curves investigated, nuclides with extremely short half-lives were seen to have a sustained activity which could be attributed to feeding from a longer lived parent. In these decay chains a state of secular equilibrium was rapidly established between the parent and daughter species and the resultant activity allowed the initial content of the parent nuclide to be extracted. Some typical decay curves of varying complexity are shown, together with the fitted values, in Figure 3.5. For unresolved peak multiplets, a linear combination of functions was incorporated to separate the component activities. Examples of the composite decay curve for a peak doublet and peak triplet are shown in Figures 3.6 and 3.7 respectively.

For most of the active nuclei studied here, the radioactive half-lives were well determined. For a few of the shorter lived actinides however, this was not so and large uncertainties were introduced into the yield calculations through the poor precision of the published values. In such cases the present data was used to establish better half-life values using the non-linear fitting procedures described in Appendix E. The individual results from each of the 'short' irradiations are shown in Figure 3.8. The measurements are evenly dispersed around

their weighted means (Table 3.2) with no obvious dependence upon irradiation conditions. Half-lives for some of the longer lived species were determined in a similar fashion from the 'long' irradiation data. Whilst offering little improvement over existing values these results provided a good test of the fitting method, which was shown to be satisfactory.

Nuclide	Fitted Half-life	Previous Measurement	Reference
226–Th	30.57 ± 0.10 m	30.9 m	(1948) [142]
225–Th	8.72 ± 0.04 m	8.0 ± 0.5 m	(1951) [143]
223–Ac	2.10 ± 0.05 m	2.2 ± 0.1 m	(1951) [143]
227–Th	18.738 ± 0.054 d	18.7176 ± 0.0052 d	(1967) [144]
		18.169 ± 0.084 d	(1954) [145]
		18.6 ± 0.1 d	(1949) [146]
223–Ra	11.444 ± 0.046 d	11.4346 ± 0.0011 d	(1965) [147]
		11.22 ± 0.05 d	(1959) [148]
		11.685 ± 0.056 d	(1954) [145]
226–Ac	29.37 ± 0.12 h	29 h	(1950) [149]
224–Ac	2.55 ± 0.28 h	2.9 ± 0.2 h	(1951) [143]
225–Ra	15.02 ± 0.56 d	14.8 ± 0.2 d	(1950) [150]

Table 3.2: Half-lives evaluated from non-linear fits to the measured decay curves. The values quoted are the weighted means of all measurements. The results in the upper half of the table were obtained from the 'short' irradiation data set while those in the lower half are from 'long' irradiations.

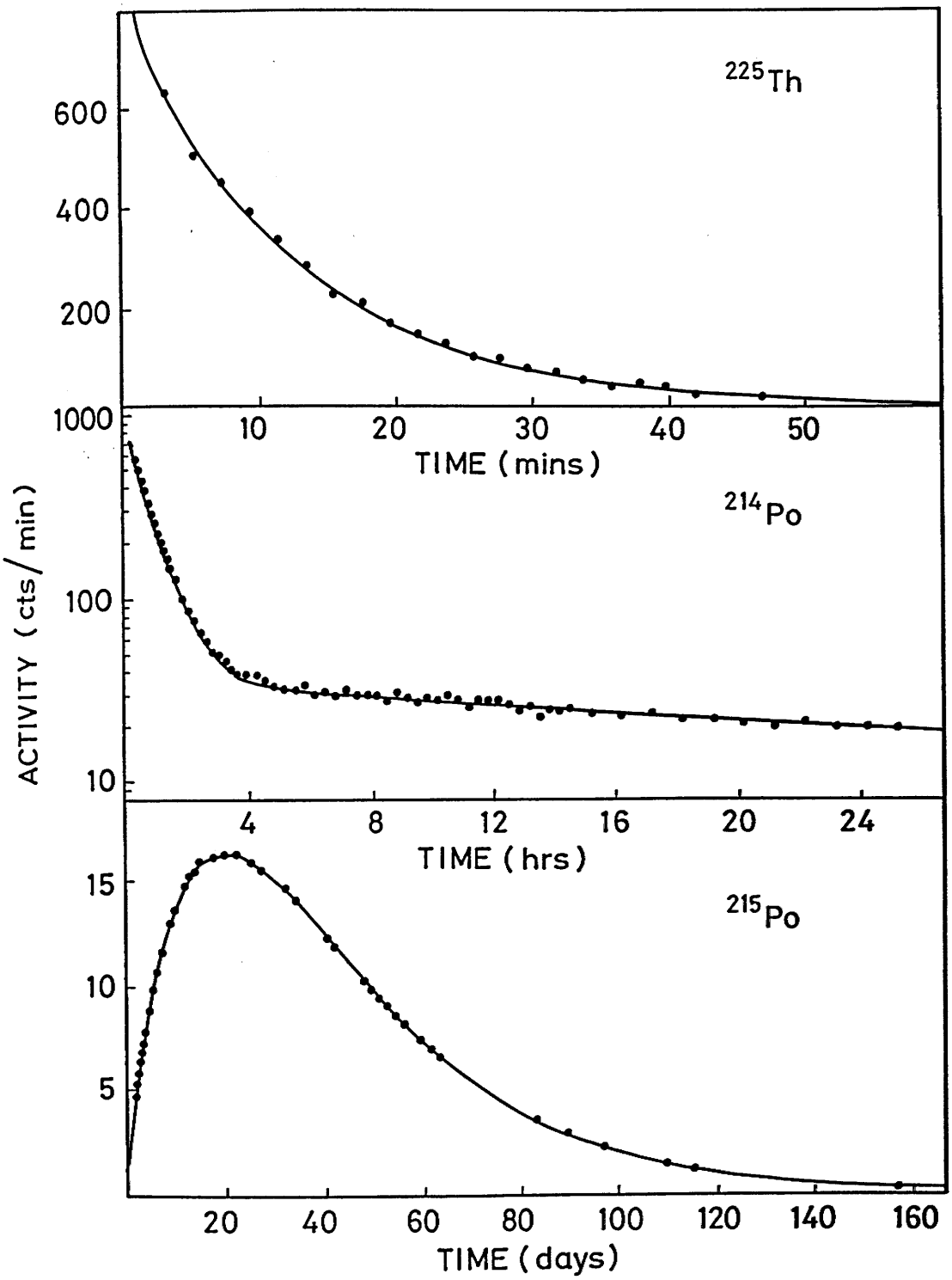

Figure 3.5: The decay of the ^{225}Th, ^{214}Po and ^{215}Po activities following irradiation at 100 MeV. The time dependence of the ^{214}Po activity reflects the half-lives of its longer lived parents ^{226}Ac(29 hrs) $\longrightarrow$ ^{226}Th(31 min) whose initial activities can be deduced from the decay curve. Similarly the ^{215}Po curve enables the initial activities of ^{227}Th(18.7 days) $\longrightarrow$ ^{223}Ra(11.4 days) to be determined.

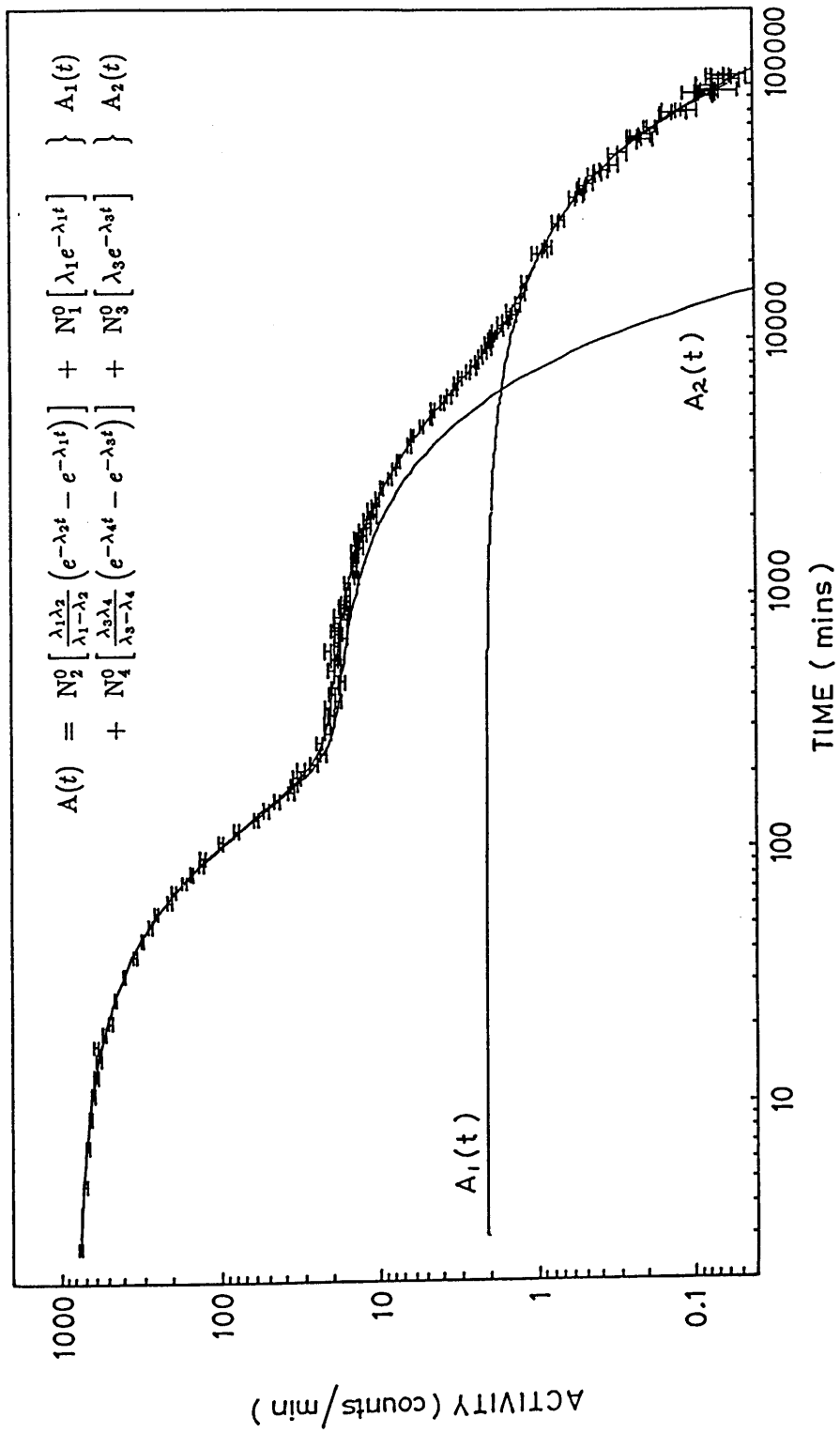

Figure 3.6: Composite decay curve for the peak doublet comprising ^{217}At and ^{218}Rn at 80 MeV with activities A_1 and A_2 respectively.
$A_1(t)$ reflects the parent activities $N_2(^{225}\text{Ra}, 14.8 \text{ days}) \longrightarrow N_1(^{225}\text{Ac}, 10.0 \text{ days})$.
$A_2(t)$ reflects the parent activities $N_4(^{226}\text{Ac}, 29 \text{ hrs}) \longrightarrow N_3(^{226}\text{Th}, 30.6 \text{ min})$.

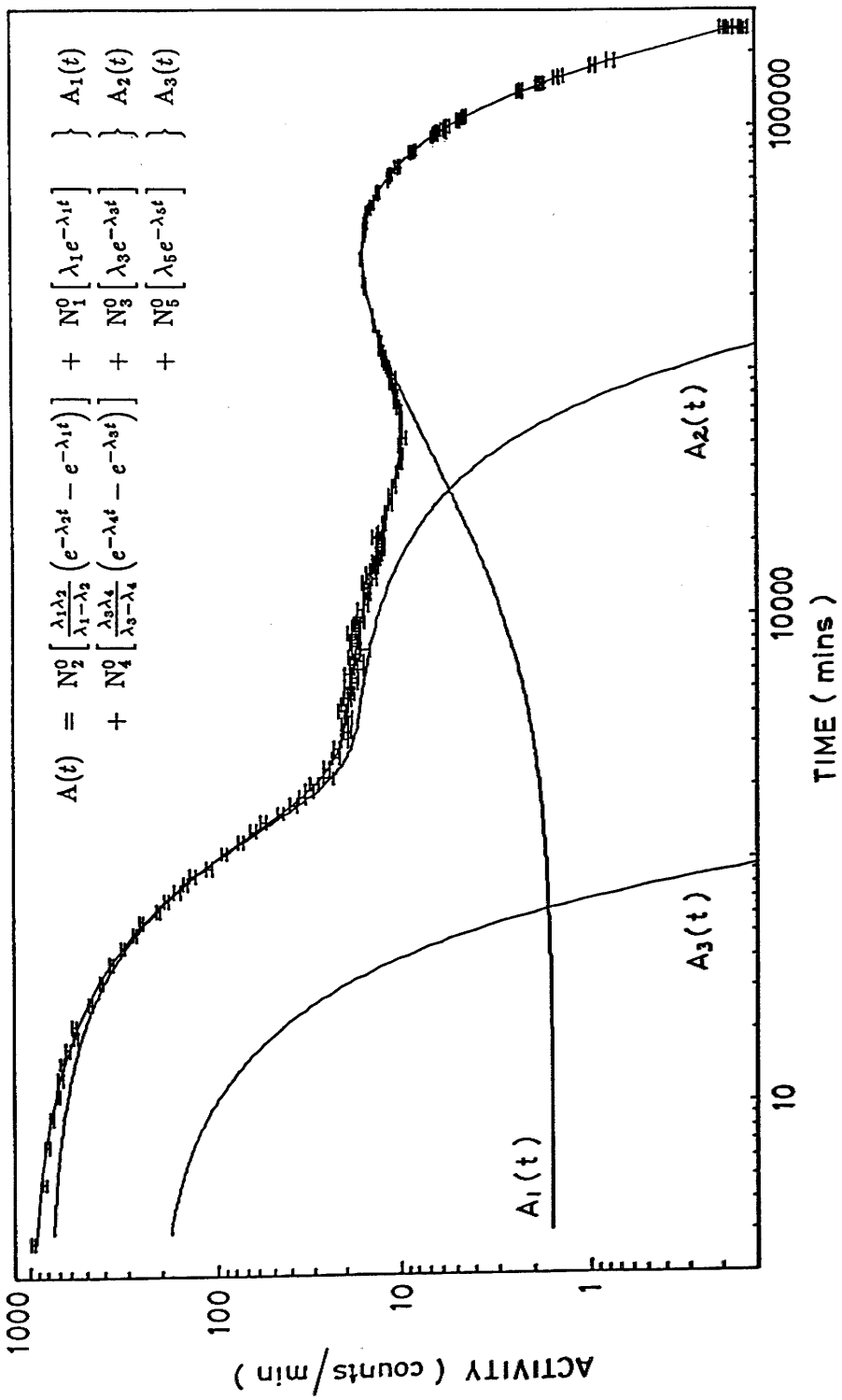

Figure 3.7: Composite decay curve for the peak triplet comprising ^{211}Bi, ^{222}Ra and ^{225}Th at 80 MeV with activities A_1, A_2 and A_3 respectively.
$A_1(t)$ reflects the parent activities N_2(^{227}Th, 18.7 days) $\longrightarrow$ N_1(^{223}Ra, 11.4 days).
$A_2(t)$ reflects the parent activities N_4(^{226}Ac, 29 hrs) $\longrightarrow$ N_3(^{226}Th, 30.6 min).
$A_3(t)$ shows the simple exponential decay of N_5(^{225}Th, 8.7 min).

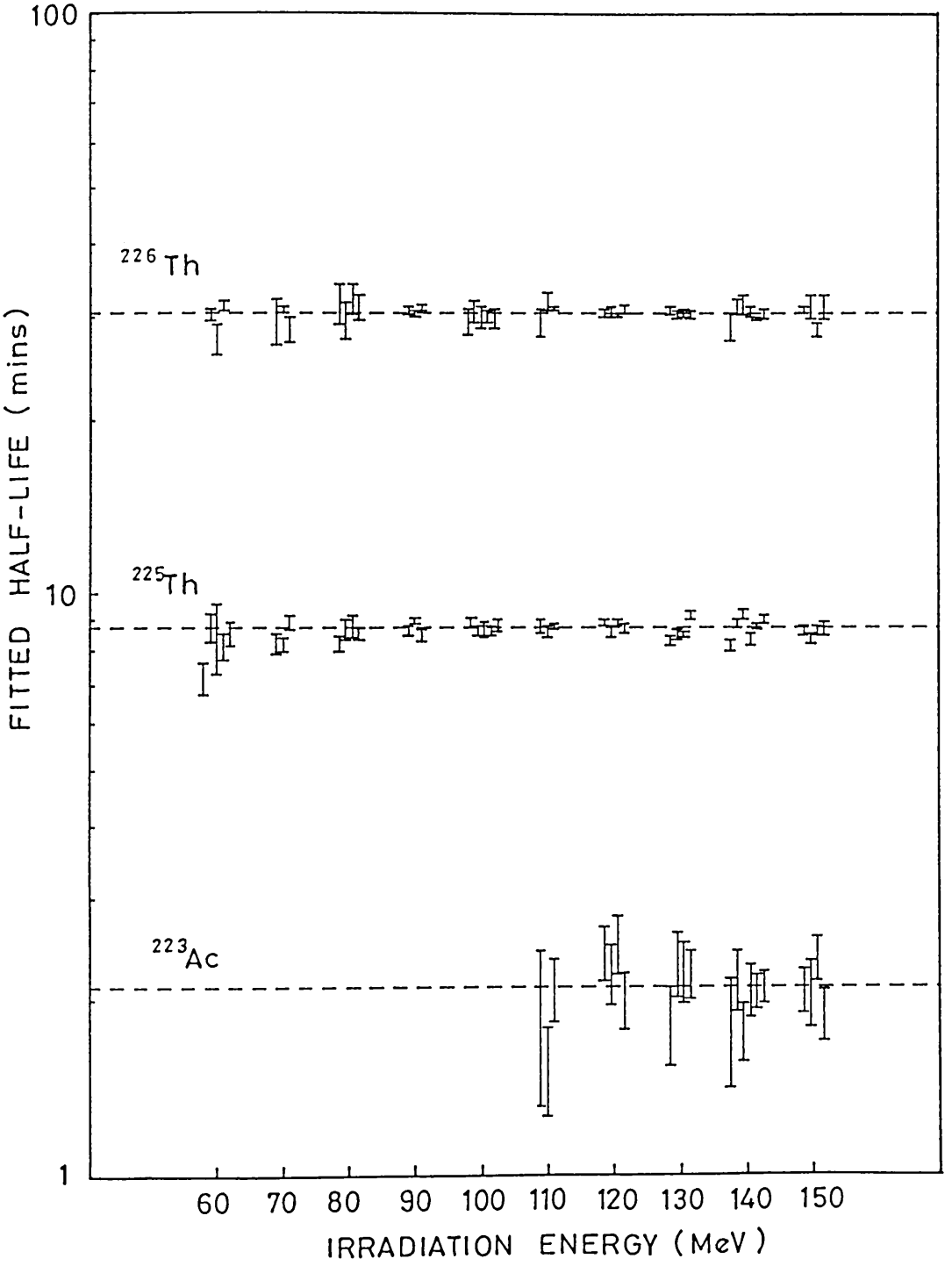

Figure 3.8: Dispersion of the half-lives obtained by non-linear fitting to the short-irradiation data. The individual fits are grouped by irradiation energy for clarity. Dashed lines depict the weighted means of plotted points.

3.4 Reduced Yield Calculation

This section describes the corrections applied to the measured data in the derivation of the reduced yield functions.

Decay Loss and Feeding Corrections

The decay curve fits of Section 3.3 enabled values to be determined for the isotopic contents of reaction products at a reference time $t = t_o$ just after the end of the irradiation. However, these values differ from the true reaction yields as a result of the following processes which occur during irradiation.

1. Due to the radio-active nature of the $(\gamma, xn\,yp)$ reaction products, some of their population is lost through decay prior to t_o.

2. The populations of some reaction products are enhanced by feeding from photoproduced parent nuclides lying higher in the same decay chain.

To determine the *true* reaction yield i.e. the total yield arising from photoproduction alone, the fitted contents were corrected for the above effects. The problem is summarised by the following decay scheme.

$$\boxed{N_1} \xrightarrow{\lambda_1} \boxed{N_2} \xrightarrow{\lambda_2}$$

The quantities N_1 and N_2 represent the contents of two photoproduced species which lie in the same decay chain and have decay constants λ_1 and λ_2 respectively. The first species is affected by decay losses only, while the second is subject to both decay loss and feeding from its photoproduced parent. The difference between the true and measured content is evaluated for each of the above cases in Appendix I. For an irradiation, at beam current, $I(\tau)$ spanning the period $\tau = o \rightarrow \tau_o$, the true yields Y_1, Y_2 are related to the measured yields

N_1, N_2 by the following expression

$$\begin{aligned} Y_1(\tau_o) &= N_1(\tau_o)\frac{Q_{tot}}{q_{11}} \\ Y_2(\tau_o) &= \left[N_2(\tau_o) - \frac{q_{12}}{q_{11}}N_1(\tau_o)\right]\frac{Q_{tot}}{q_{22}} \end{aligned} \tag{3.7}$$

where

$$\begin{aligned} q_{11} &= e^{-\lambda_1\tau_o}\int_o^{\tau_o} e^{\lambda_1\tau'} I(\tau')\,d\tau' \\ q_{22} &= e^{-\lambda_2\tau_o}\int_o^{\tau_o} e^{\lambda_2\tau'} I(\tau')\,d\tau' \\ q_{12} &= e^{-\lambda_2\tau_o}\int_o^{\tau_o} e^{(\lambda_2-\lambda_1)\tau'}\,d\tau' \int_o^{\tau'} e^{\lambda_1\tau''}\lambda_1 I(\tau'')\,d\tau'' \end{aligned} \tag{3.8}$$

The time dependence of the beam current was incorporated for each irradiation using the recorded beam profiles described in Section 2.3. The importance of correcting for the non-uniformity of the electron beam current was evident when the corresponding decay loss was calculated assuming a *constant* beam profile. For species with half-lives comparable to the length of the irradiation, the difference was found to be on average $\sim 3\%$ but could in some cases be as high as 6%.

Thorium Background Activity

To determine a true yield for the $(\gamma, 4n)$ reaction, the quantity of ^{228}Th known to exist in the natural decay chain of the target material had to be subtracted from the measured ^{228}Th content. Although the natural α–activity from ^{232}Th and its daughters was generally found to be very small ($< 1\%$ of the activity due to reaction products) such corrections proved important near reaction thresholds where the induced activity became very low. The natural content of ^{228}Th was evaluated by measuring the activity of ^{232}Th in each spectrum and multiplying by a known ratio for the activities ^{228}Th : ^{232}Th. This ratio was measured prior to irradiation for each individual target and monitored periodically, using a non-irradiated target from the same batch, over the entire

counting period of the experiment. Because the radio-active daughters in the target material were not quite in equilibrium, the above ratio was found to vary slowly over the counting period of the experiment. This fact was taken into account in the background subtraction.

Bremsstrahlung Yields

In addition to the electro-disintegration yields $y_e(E_j)$ determined at electron energies $E_j = 40, 50, \ldots, 150$ MeV, measurements were also made of the electron + bremsstrahlung induced reaction yields $y_{e+\gamma}(E_j)$ at end-point energies of 60, 100 and 140 MeV using the 'radiator sandwich' assembly described in Section 2.4.2. This method ensured that both targets were subject to the same irradiation conditions (beam current etc.) and, since the radiator was sufficiently thin, ensured that their yields differed only in the contribution from bremsstrahlung induced reaction products. Corrections to the electro-disintegration yield in the rear target, arising from electron energy losses in the radiator and multiple scattering, were discussed in Section 2.5 and shown to be small. It is sufficient therefore to approximate the reaction yield y_γ due to bremsstrahlung alone as

$$y_\gamma(E_j) = y_{e+\gamma}(E_j) - y_e(E_j) \tag{3.9}$$

Consistency Checks

In several cases yields were determined for the same $(\gamma, xnyp)$ reaction from the analysis of more than one decay curve or from repeated irradiations at the same end-point energy. The yields obtained from these different sources were found to show good overall agreement (Appendix J) and were consistent with the statistical uncertainties of the individual measurements. A weighted mean was calculated for the reaction yield when more than one independent

measurement was made. An overall systematic error of $\sim$ 5 % is estimated to remain in the yield measurements due to uncertainties in the current integrator calibration, the ^{232}Th half-life and the target area masked off for thickness determination.

3.5 Presentation of Results

The reduced yield functions for the 11 different xn,yp reaction channels measured in the present experiment are shown in Figures 3.9 to 3.13. The same data are listed in tabular form in Appendix J. The electron induced yields are measured in μb per incident electron. To remove the dependence of the bremsstrahlung yields upon the type and thickness of radiator used, these data are quoted as the yield 'per equivalent quantum' where the number of equivalent quanta Q in the bremsstrahlung spectrum N_{br} with end-point energy E_j is

$$Q = \frac{1}{E_j} \int_0^{E_j} N_{br}(E_j, E_\gamma)\, dE_\gamma \qquad (3.10)$$

In one case, only the combination of two channels, 4n and 3n1p, could be determined, since both resulted in the production of ^{228}Th. The (e,4n) reaction leads directly to the reaction product ^{228}Th, which decays with a half-life of nearly 2 years whereas the (e,3n1p) reaction produces ^{228}Ac which decays by β-emission with a relatively short half-life (6 hours) to produce ^{228}Th. This short half-life made it difficult to separate the two processes on the basis of the time dependence of the α-decay alone.

The (e, xn) yield functions, shown in the figures, rise rapidly from well defined energy thresholds which increase with the number of neutrons emitted. The magnitude of the yields on the other hand falls markedly with increasing x. Reaction thresholds for the (e, xn1p) functions again increase with x but are observed to lie higher than the corresponding (e, $(x+1)$n) thresholds for the same number of emitted particles. This is due to the large Coulomb barrier which has

to be overcome for proton emission. These yields rise less rapidly from threshold, have a distinctly different shape from those involving only neutron emission and diminish less rapidly with increasing x. The presence of charged particle decay channels with the strengths observed is not compatible with statistical particle evaporation from a heavy, excited nucleus in an equilibrated state and is indicative of pre-equilibrium 'fast' particle emission.

The activities measured for the (e, xn2p) reactions were low and had to be corrected, in all cases, for feeding from parent species much stronger in activity (Section 3.4). The resultant yields were therefore evaluated from the small difference between two much larger numbers and as such were determined with much less precision than the previous data, for which such effects gave rise to corrections of only a few per cent. While only the (e, 5n2p) measurement has any discerni ble structure, the other results provide an useful upper limit to reactions of this type and show the emission of two protons to be highly suppressed.

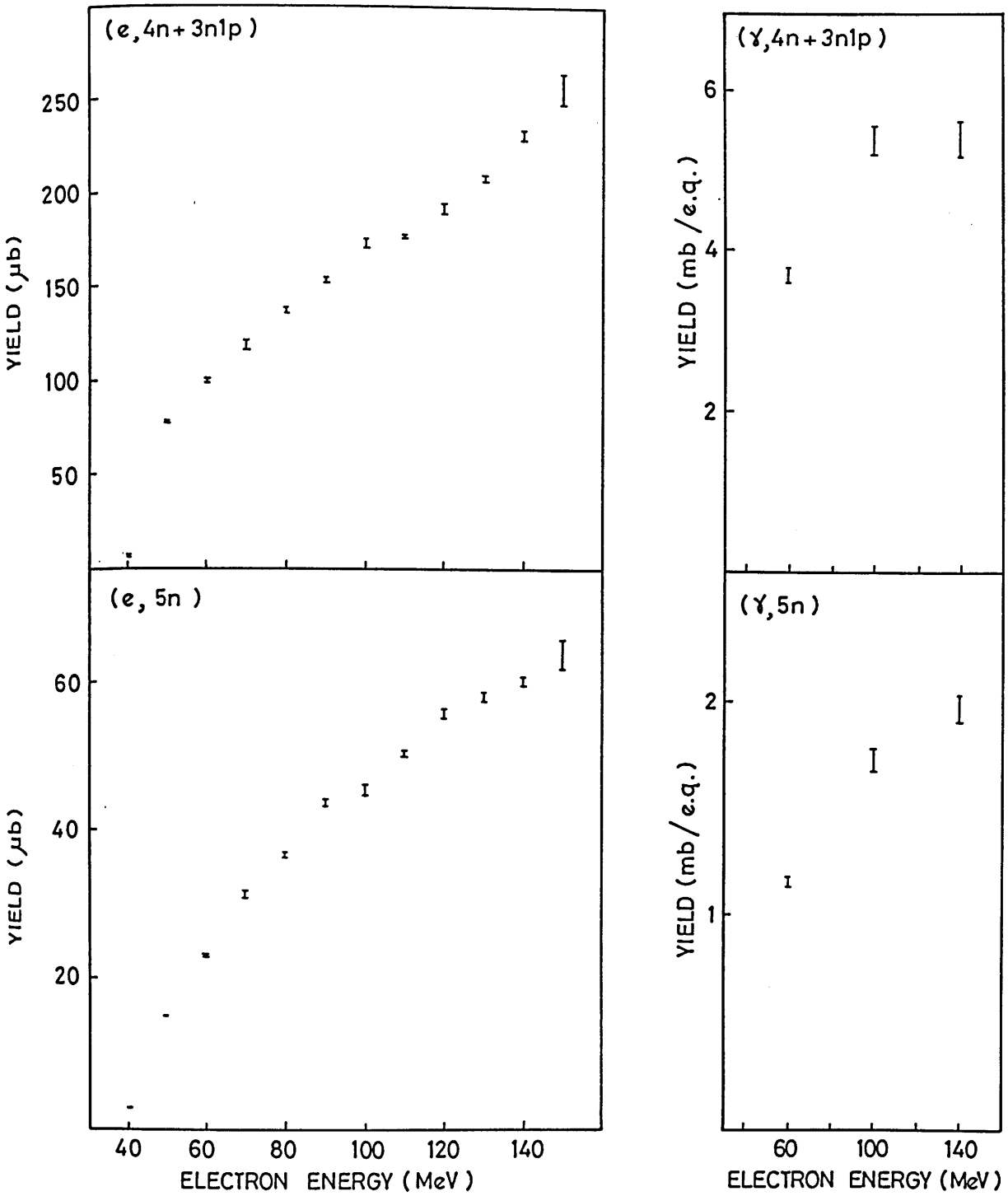

Figure 3.9: Reduced yield functions for the electron and bremsstrahlung photo-production of ^{228}Th and ^{227}Th. Bremsstrahlung yields are shown in mb per equivalent quantum.

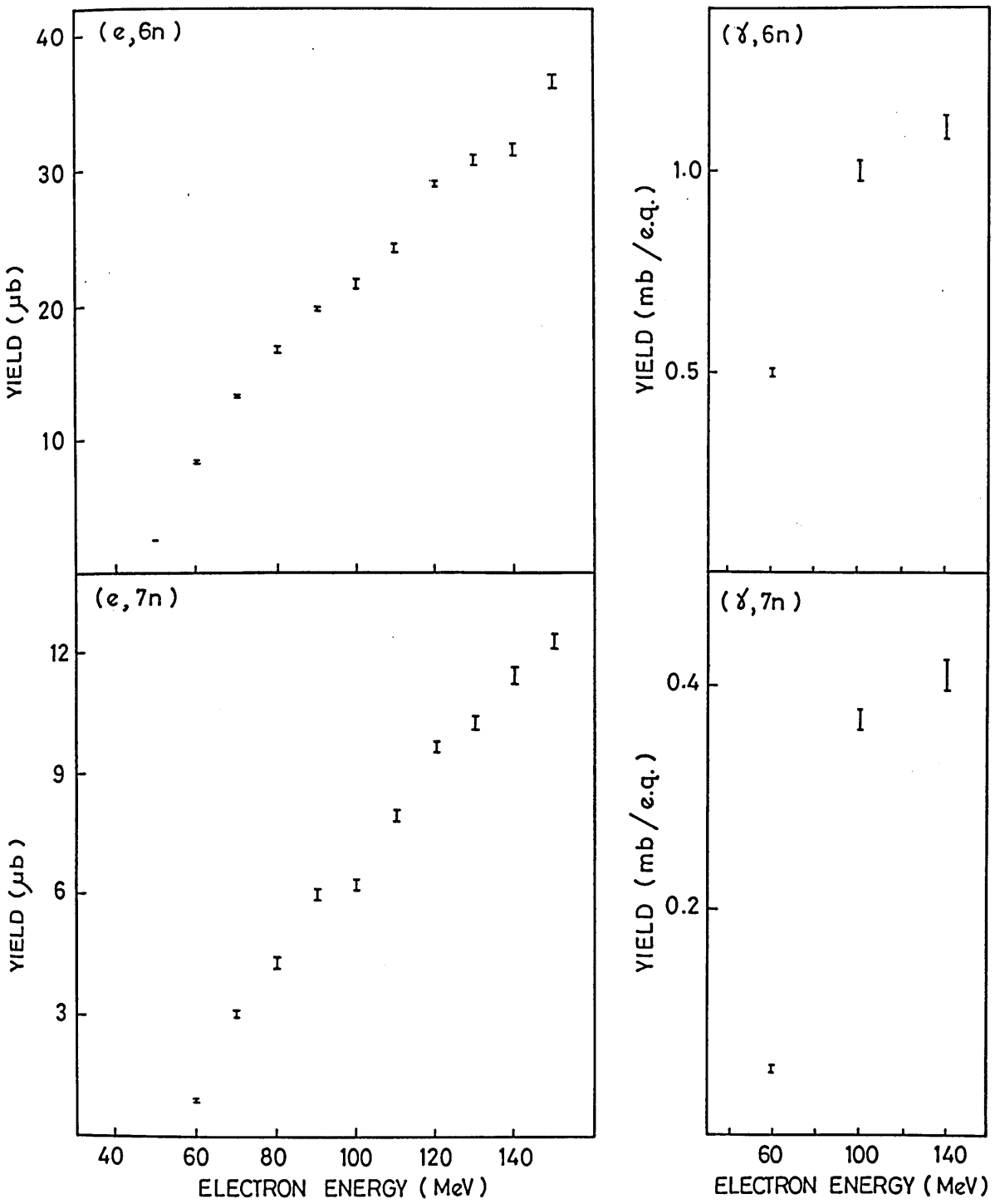

Figure 3.10: Reduced yield functions for the electron and bremsstrahlung photo-production of ^{226}Th and ^{225}Th. Bremsstrahlung yields are shown in mb per equivalent quantum.

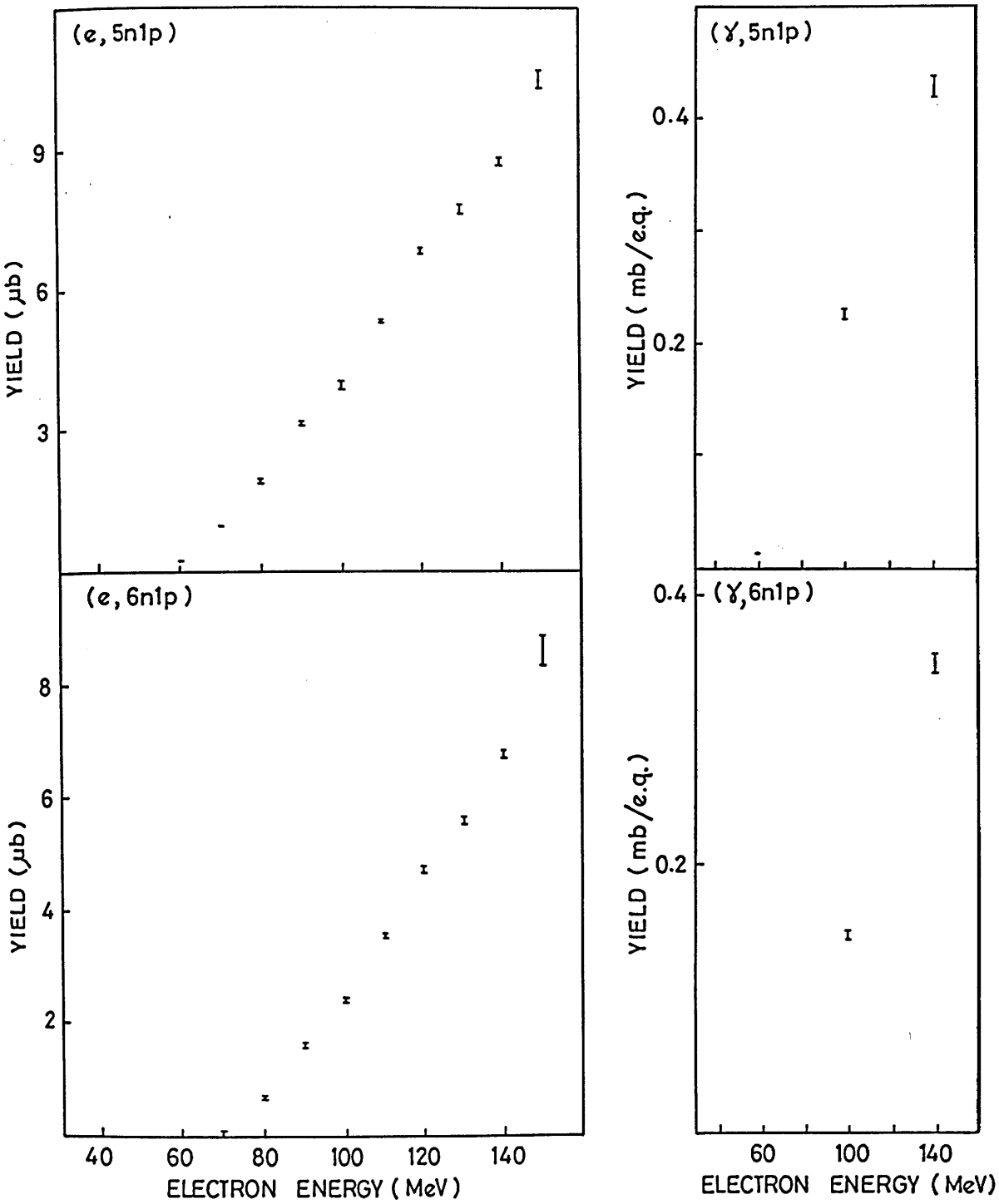

Figure 3.11: Reduced yield functions for the electron and bremsstrahlung photo-production of ^{226}Ac and ^{225}Ac. Bremsstrahlung yields are shown in mb per equivalent quantum.

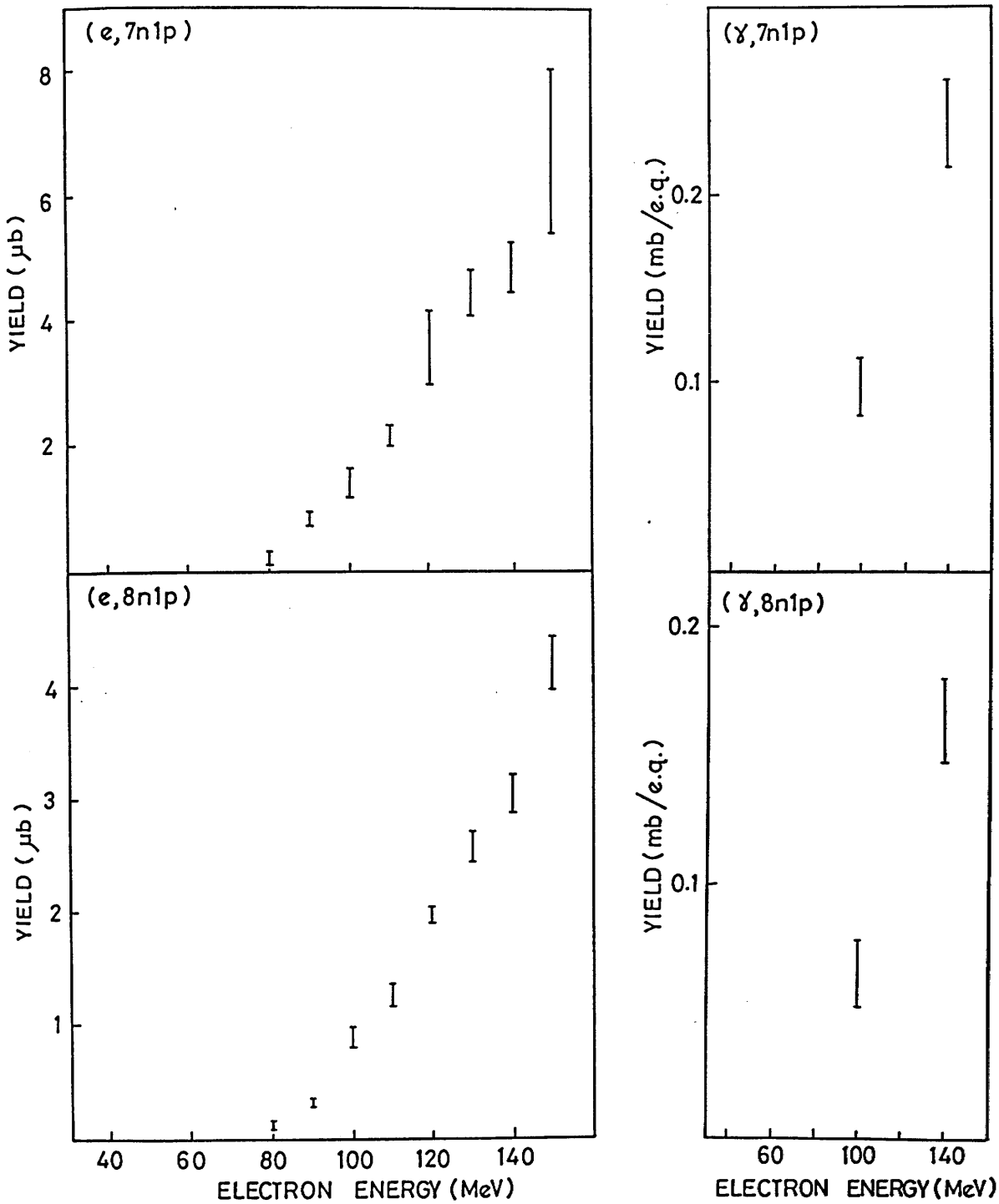

Figure 3.12: Reduced yield functions for the electron and bremsstrahlung photo-production of ^{224}Ac and ^{223}Ac. Bremsstrahlung yields are shown in mb per equivalent quantum.

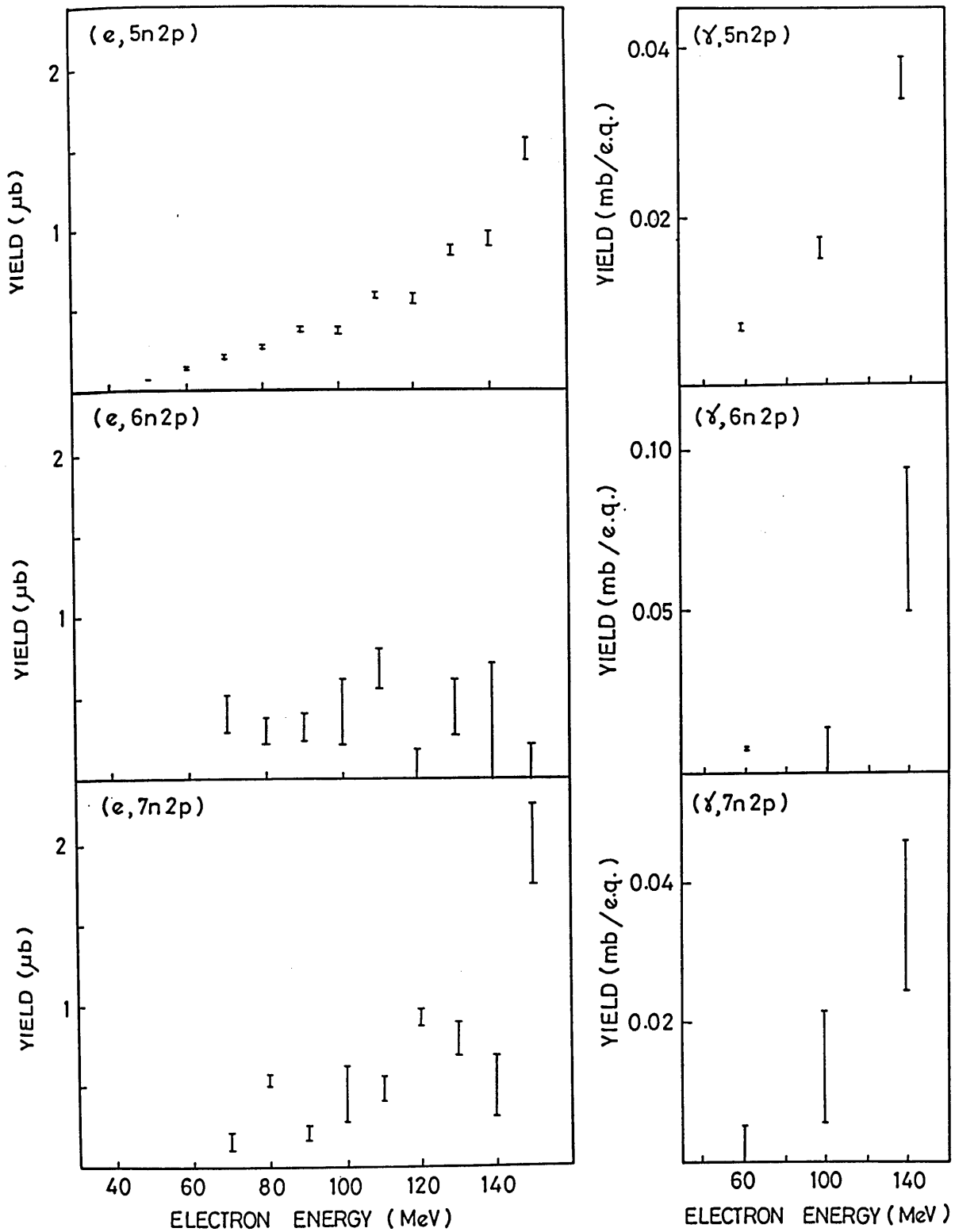

Figure 3.13: Reduced yield functions for the electron and bremsstrahlung photo-production of ^{225}Ra, ^{224}Ra and ^{223}Ra. Bremsstrahlung yields are shown in mb per equivalent quantum.

Chapter 4

Photodisintegration Models

4.1 Introduction

A comparison of measured cross-sections, for various nuclear decay channels, with those predicted by photodisintegration models should yield information on the photon absorption mechanism and test the ability of these models to correctly determine the effects of final state interactions in complex nuclei.

In this chapter, two of the precompound decay models which were introduced in Section 1.4 are discussed in more detail and a full description is given of the calculations performed. The first section describes the Intranuclear Cascade model in which the trajectories and collisions of all participating nucleons are followed in coordinate space using a Monte Carlo simulation method. In the second section, details are given of the Exciton Hybrid model and its recent application to photonuclear reactions [110]. In this model the nuclear state is characterised by the exciton number n which evolves as result of N-N collisions and particle emission. The formulation has a convenient closed form which allows for simpler computations than does the cascade model. It does however sacrifice the geometrical information which is inherent in the former model.

The theoretical distributions of photo-reaction products presented in this section were evaluated using the above models to describe the precompound components of the nuclear decay process and an evaporation model to describe

the subsequent de-excitation of the residual compound nucleus.

4.2 Intranuclear Cascade–Evaporation Model

The calculations described in this section, for high-energy photon-induced nuclear reactions, were made using the intranuclear cascade/evaporation code PICA [151]. This program adopts the intranuclear cascade concept [98]–[100] where it is assumed that, following an initial highly localised photon absorption, the resultant propagation of this excitation through the nucleus may be treated on the basis of quasi-free particle-particle collisions. Monte-Carlo methods are employed throughout to determine the types and positions of all collisions as well as the momenta and scattering angles of the struck particles. All such interactions are evaluated by statistical sampling, weighted by the appropriate free-particle differential cross-sections. Theoretical cross-sections are incorporated where no experimental values exist.

The initial photon absorption is assumed to occur on a correlated neutron-proton pair (the quasi-deuteron model of Levinger [9]) or, when energetically possible, through one of the four pion-nucleon states formed when a photon interacts with a quasi-free nucleon. The inclusion of secondary interactions (the intranuclear cascade) follows explicitly the formalism of Bertini [99]. All particles involved in the cascade process are traced through the nuclear volume until they either escape from the nucleus or are captured, at which stage their residual energy is shared with the remainder of the nucleus. This equilibration of energy results in a compound nuclear state which retains a large fraction of the original excitation energy. The compound nucleus is allowed to de-excite through the evaporation of particles using a modified version of Weisskopf's statistical evaporation model [96].

The key features of the code and associated parameter set, as well as de-

tails of the calculations performed, are given in the following sections. A full description of the PICA program has been given elsewhere by Gabriel *et al.* [151]–[153].

4.2.1 Nuclear Model

The effect, upon cascade calculations, of the particular nuclear model employed has been investigated by Bertini [99] who reports major improvements over the earlier work of Metropolis *et al.* [98,154]. Bertini's model of the nucleus has been incorporated, unchanged, in the present formulation and so only a brief description is given here.

Nuclear Density

Here a non-uniform nucleon density has replaced the constant value which was previously assumed [98,154]. The proton density distribution within the nucleus is obtained from a parameterised fit to the electron scattering data of Hofstadter [155]. Assuming an equivalent neutron density distribution, the overall nucleon density $\rho(r)$ at nuclear radius r may be written

$$\rho(r) = \frac{\rho_1}{1 + e^{\frac{(r-c)}{Z_1}}} \tag{4.1}$$

The parameters c and Z_1 are selected from fits to the electron scattering data and have values

$$c = 1.07\ \mathrm{A}^{\frac{1}{3}}\ \mathrm{fm} \qquad Z_1 = 0.545\ \mathrm{fm}$$

The normalisation factor ρ_1 ensures a total nucleon number equal to A. In the current model, the non-zero Fermi-type distribution of Equation (4.1) is approximated by dividing the nuclear volume into 3 concentric spheres (or shells) inside which the local density is assumed uniform. Following the recommended parameter set for this code [151], the outer radii of the 3 shells are set equal to the radii at which the nucleon density reaches 90 % , 20 % , and 1 % of its

central value. The density within each sphere is then set equal to the average value of $\rho(r)$ over that region (Figure 4.1).

Nucleon Momenta

In each of the 3 regions, the protons (and similarly the neutrons) are assumed to have momenta p described by a zero-temperature Fermi distribution

$$f_i(p) = \left[\frac{8\pi\omega_i}{h^3\rho_i} \right] p^2 \tag{4.2}$$

where

$$\begin{aligned} w_i &= \text{no. of protons in region } i \\ \rho_i &= \text{proton density in region } i \end{aligned}$$

The function is normalised to give the correct number of particles in each region when integrated up to the appropriate Fermi momentum p_i^F i.e.

$$\int_0^{p_i^F} f_i(p).dp = \omega_i \tag{4.3}$$

With this treatment however, the composite momentum distribution of the entire nucleus no longer appears as a true zero-temperature Fermi distribution but instead approximates a Maxwell-Boltzmann distribution with $kt \approx 15$ MeV.

Nuclear Potentials

In all regions, and for all nuclei, the least bound nucleons are assumed to have a binding energy of 7 MeV. The nuclear potential for protons in the i^{th} region, $\mathrm{V}_i^{\mathrm{p}}$, then has a depth equal to the relevent Fermi energy, $\epsilon_{\mathrm{F},i}^{\mathrm{p}}$, plus the binding energy

$$\mathrm{V}_i^{\mathrm{p}} = \epsilon_{\mathrm{F},i}^{\mathrm{p}} + 7 \quad \text{MeV} \tag{4.4}$$

A similar value is adopted for neutrons, while pions are assumed to experience the same nuclear potential as the nucleon with which they interact. Since this nuclear potential is clearly discontinuous, any particles which cross the regional boundaries have their kinetic energies suitably modified.

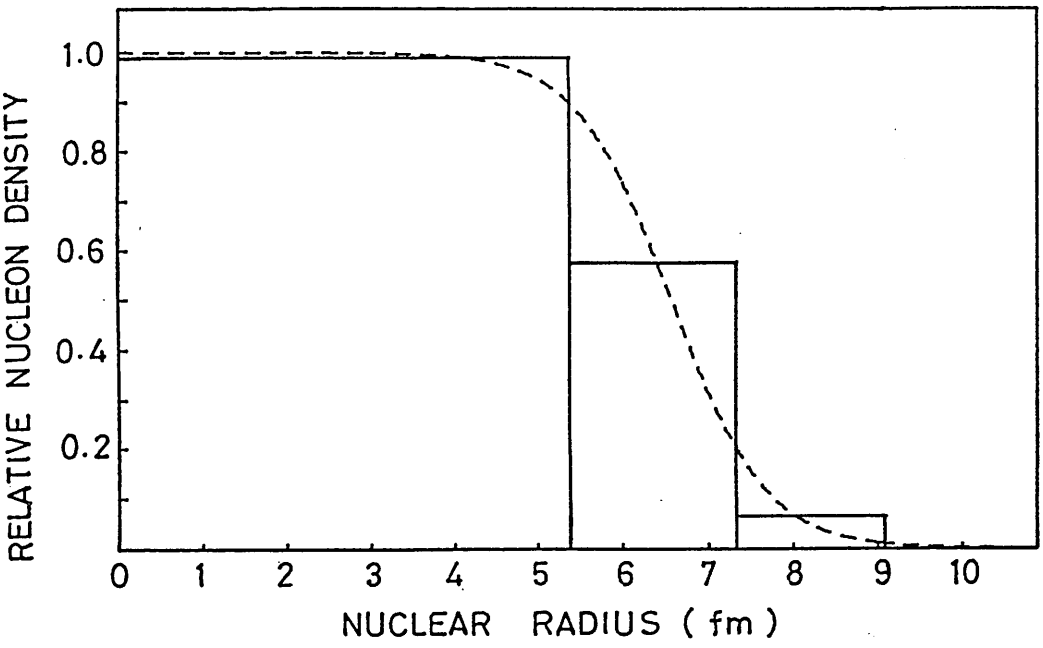

Figure 4.1: Nucleon density distributions. The dashed line depicts Hofdtadter's electron scattering data. The solid line describes the 3-shell configuration used in the PICA calculations.

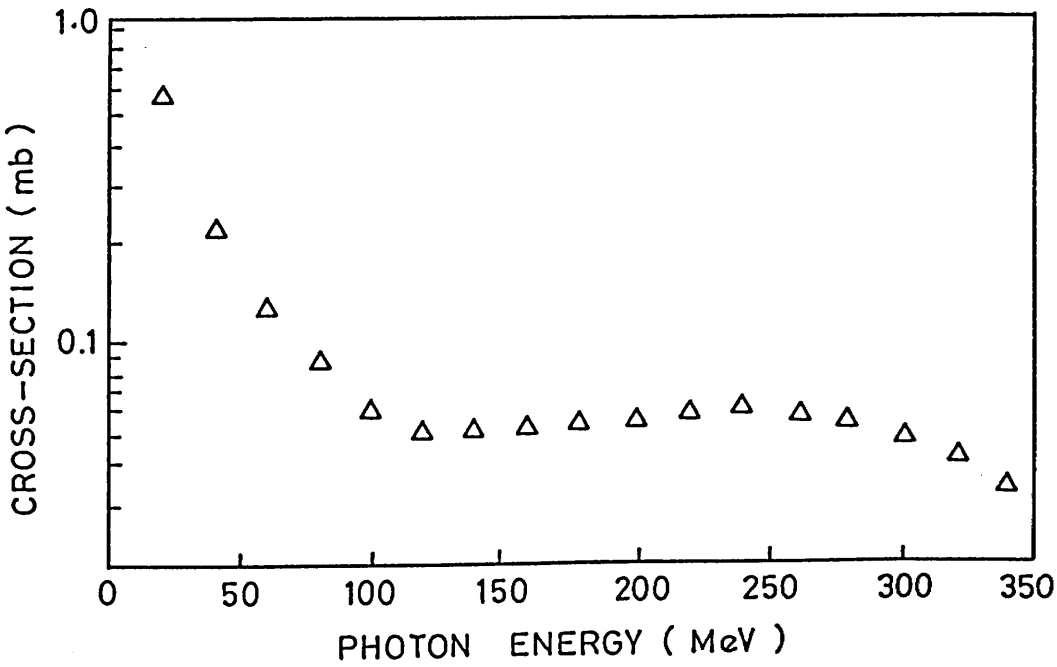

Figure 4.2: Photo-disintegration cross-section for the real deuteron, as employed in the PICA calculations.

4.2.2 Primary Interactions

At the photon energies of interest here (40–150 MeV), the principal mechanism governing the absorption of a photon is considered to be that of Levinger's quasi-deuteron model [9]. The PICA code is, in any case, inapplicable below $\sim$ 40 MeV since the formation of giant resonance states has not been included in its formulation. Above $\sim$ 140 MeV pion production is included as a possible initial interaction, but, having a marginal contribution to the absorption cross-section in the above energy range, will be discussed only briefly.

Quasi-deuteron Absorption

In the Levinger quasi-deuteron model [9] the absorption of a photon occurs on a correlated neutron-proton pair in a high relative momentum state and with a cross-section σ_{qd} proportional to that of the real deuteron σ_d

$$\sigma_{qd} = L \frac{NZ}{A} \sigma_d \tag{4.5}$$

In these calculations the Levinger parameter L, which is assumed independent of mass number, was given a value of 6.4 in order to reproduce the total absorption cross-section of $\sim$ 17 mb predicted by measurements made on other heavy nuclei at these energies (Section 1.2.2). The real deuteron photo-disintegration cross-section was taken as an average of experimentally measured values [156,157] (Figure 4.2). The relationship between real and quasi-deuteron absorption is, in fact, more complex than suggested by Equation (4.5) for it may be noted that the total energy in each process, for any given photon energy, is non-identical. In the rest frame of the quasi-deuteron the neutron and proton have positive relative energy whereas the binding energy of the real deuteron is negative. To maintain the analogy between the two processes, a pseudo-photon energy is defined which ensures that, in the centre-of-momentum system, these total en-

ergies are the same and most importantly that the proton and neutron emission angles are correctly determined.

The actual site of any photon—quasi-deuteron interaction within the nucleus depends upon the quasi-deuteron density, $\rho(\mathrm{qd})$, as well as the absorption cross-section, σ_{qd} (evaluated above), and is obtained by standard sampling techniques. The local quasi-deuteron densities are determined from the neutron-proton pairing in each region, which are assumed, for simplicity, to be independent. As no pairing is then considered between nucleons in different regions, the overall quasi-deuteron density $\rho(\mathrm{qd})$ must be renormalised to ensure that the total number of n-p pairs remains equal to NZ. The quasi-deuteron density in the i^{th} region is then

$$\rho_i(\mathrm{qd}) = \overbrace{\frac{(\mathrm{N}\rho_i\mathrm{V}_i)\,(\mathrm{Z}\rho_i\mathrm{V}_i)}{\mathrm{V}_i}}^{\text{no. of n's}\quad\text{no. of p's}}\ \overbrace{\left[\sum_{j=1}^{3}\rho_j^2\mathrm{V}_i^2\right]^{-1}}^{\text{normalisation}} \tag{4.6}$$

where

$$\begin{aligned}
\textstyle\sum_{i=1}^{3}(\rho_i\mathrm{V}_i) &= 1 \\
\rho_i &= \text{nucleon density in region } i \\
\mathrm{V}_i &= \text{volume of region } i \\
\textstyle\sum_{i=1}^{3}(\mathrm{NZ}\rho_i^2\mathrm{V}_i^2) &= \text{sum of all n-p pairs (equal to NZ)}
\end{aligned}$$

With the site of the photon—quasi-deuteron interaction specified, the initial momenta of the component nucleons are sampled from the Fermi distributions of Equation (4.2). It is assumed that their directions are isotropic. The emission angles of the neutron and proton are sampled from measured differential cross-sections [156] but using the pseudo-photon energies described above. To account for the effects of Pauli blocking on some of the final states reached by the emitted neutron and proton, Levinger proposed a modified quasi-deuteron model [48] which incorporates a phenomenological damping of the absorption cross-section at photon energies E_γ. This modified cross-section appears as

$$\sigma_{\mathrm{mqd}} = \mathrm{L}\,\frac{\mathrm{NZ}}{\mathrm{A}}\,\exp\left(-\frac{\mathrm{D}}{\mathrm{E}_\gamma}\right)\sigma_{\mathrm{d}} \tag{4.7}$$

Photon absorption cross-sections measured at Saclay [36,37] on ^{208}Pb yield a value of $\sim$ 60 MeV for the parameter D. In the PICA model the exclusion principle is taken into account by requiring the final neutron and proton kinetic energies to be above the appropriate Fermi energies. Any interactions leading to inaccessible states are simply discarded in the Monte-Carlo computations.

Pion Production Channels

Another absorption mechanism which becomes possible at the upper limit of our energy range ($>$ 140 MeV) is that of single pion photo-production on a quasi-free nucleon. The free γ–p cross-sections of various authors [158] are used to determine both the interaction probability and the energies and directions of the emergent pion and nucleon. Photon absorption on a neutron is assumed, through charge symmetry, to be equivalent to the γ–p interaction. Four pion–nucleon states are then possible

$$\left.\begin{array}{lcl} \gamma + p & \longrightarrow & p + \pi^{o} \\ \gamma + n & \longrightarrow & n + \pi^{o} \end{array}\right\} \text{charge symmetric}$$

$$\left.\begin{array}{lcl} \gamma + p & \longrightarrow & n + \pi^{+} \\ \gamma + n & \longrightarrow & p + \pi^{-} \end{array}\right\} \text{charge symmetric}$$

Again the site and type of interaction is evaluated by standard sampling and once again the Pauli Exclusion Principle is satisfied by ensuring the final nucleon energy to be above the Fermi level.

4.2.3 Secondary Interactions

The localised excitation, created by the primary interaction, is thought to propagate through the nucleus by an intranuclear cascade process. Since the wavelengths of the cascading nucleons are in general much smaller than the average internucleon distance ($\sim$ 1 fm) it is supposed that this process can be

treated in terms of free particle–particle collisions. Following the intranuclear cascade, a compound nucleus remains which is allowed to de-excite through nucleon evaporation.

The Intranuclear Cascade

The original cascade model developed by Serber [100] and used extensively by Metropolis *et al.* [98,154] was later combined with an improved nuclear model by Bertini [99]. It is Bertini's refined formulation that is incorporated in the present code.

On their passage through the nuclear volume, the high energy particles from the initial absorption may disturb the nuclear matter through interactions with the other nucleons. The secondary interactions which are considered here are

- nucleon—nucleon scattering
- nucleon—pion scattering
- charge exchange reactions
- pion absorption (on two-nucleon clusters)

The sites and types of interaction are again obtained by statistical sampling using measured free-particle cross-sections [99]. Struck particles may, in turn, cause further collisions, all of which are traced through the nucleus until the particles either escape from the nucleus (their energy must be above a certain threshold) or are captured (the energy having fallen below some pre-defined cut-off) at which stage they are assumed to share their energy with the remainder of the nucleus. The cut-off energies for cascade particles are generally set equal to half the emission thresholds, which in turn have the values

$$\begin{array}{ll} 0 & \text{for} \quad n, \pi^{\circ}, \pi^{-} \\ E_{CB} & \text{for} \quad p, \pi^{+} \end{array}$$

The Coulomb barrier for ^{232}Th is given approximately by the expression

$$E_{CB} \approx 0.9 \frac{Z}{A^{\frac{1}{3}}} \text{ MeV} \approx 13.2 \text{ MeV}$$

The exclusion principle forbids nucleon interactions which results in a final kinetic energy below the Fermi level. The cascade process is shown schematically in Figure 4.3. For each incident photon, the histories of all particles involved in the cascade are recorded. These can later be analysed to provide precompound emission spectra and angular distributions.

Evaporation from Compound Nucleus

When the precompound emission of particles has ceased (i.e. all cascade-particle energies have fallen below their appropriate emission thresholds), a compound nucleus remains which, in general, retains a large fraction of the original excitation energy. This contributes to the particle emission spectra through the evaporation of nucleons. The original theory of statistical evaporation due to Weisskopf [96] has been modified by Dostrovsky *et al.* [159,160] and, as implemented here, by Dresner [161].

Weisskopf [96] expresses the probability per unit time for the emission of a particle j with kinetic energy in the range $\epsilon \rightarrow \epsilon + \mathrm{d}\epsilon$ as

$$\mathrm{P}_j(\epsilon).\mathrm{d}\epsilon = \frac{g_j m_j}{\pi^2 \hbar^3}\, \sigma\, \epsilon\, \frac{\omega(f)}{\omega(i)}\, \mathrm{d}\epsilon \tag{4.8}$$

where

g_j = no. of spin states of particle j
m_j = mass of particle j
σ = cross-section for inverse reaction

$\omega(i)$ = level density of initial nucleus
$\omega(f)$ = level density of final nucleus
} at appropriate energy

For a completely degenerate Fermi gas, the nuclear level density, ω, at excitation energy E has the form [96]

$$\omega(\mathrm{E}) = \mathrm{C} \exp\left[2\mathrm{a}^{\frac{1}{2}}(\mathrm{E}-\delta)^{\frac{1}{2}}\right] \tag{4.9}$$

A pairing term, δ, has been included which corrects the excitation energy for

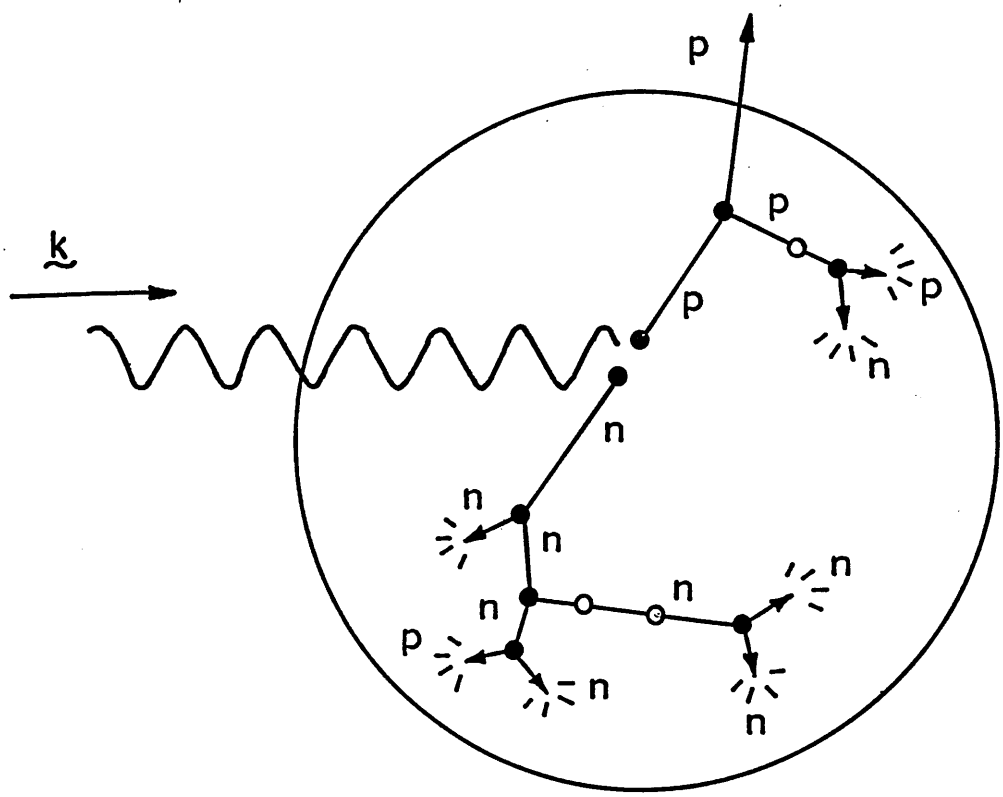

Figure 4.3: Schematic representation of the intranuclear cascade following photon absorption on a neutron-proton pair. The solid circles show the positions of N-N collisions. The open circles indicate collisions forbidden by the exclusion principle. In this case one proton reaches the nuclear surface with sufficient energy to escape. All other participating nucleons dissipate their energy through 2-body collisions and are eventually captured. The energy from captured particles is assumed to contribute to the overall nuclear excitation.

odd–even displacements in the ground-state energy.

$$\begin{aligned} \delta &= 0 \quad \text{for odd–odd nuclei} \\ \delta &\geq 0 \quad \text{otherwise} \end{aligned}$$

Magnitudes for the nucleon pairing terms are discussed elsewhere [162,163]. The parameter, C, being approximately constant need not be specified since only a ratio of level densities appears in Equation (4.8). (It is assumed that a slight A-dependence in C [162] will have negligible effect over the small A-range applicable to an evaporation process). The level density parameter, a, is essentially proportional to A and takes a value of a = A/8 in the standard parameter set for this code. Further irregularities in the level densities near closed shells [164] are unimportant in the case of ^{232}Th.

The total emission probability for a particle j is found through integration of Equation (4.8). Effects of the Coulomb barrier upon charged particle emission are incorporated in the derivation of the inverse cross-section, which is appropriately reduced [159]. The production cross-sections for all residual nuclides are obtained from knowledge of the total nucleon emission occuring at the cascade and evaporation stages. In this model γ–ray de-excitation is assumed to occur only when particle emission becomes energetically prohibited. It does not compete with particle emission above this limit. Competition due to fission is not included in this model.

4.2.4 Calculations and Results

In Monte-Carlo calculations of this nature, a large number of photons are considered incident upon the target nucleus at each of the required energies. Of these, only $\sim$ 2% lead to an inelastic event (i.e. an absorption) whose subsequent cascade can be traced through the nucleus in the manner described above. (This absorption rate corresponds to a nuclear transparency of $>$ 98 %). To generate results of reasonable statistical accuracy, especially where low cross-section

$(\gamma, x\text{n2p})$ reactions were involved, up to 10^7 incident photons were required per computation. For the results presented here, a total of more than 500 hours of c.p.u. time were utilised on the Kelvin Laboratory's VAX–11/780.

Figure 4.4 shows the average number of neutrons and protons which are emitted at the cascade and evaporation stages of the calculation. In these results the intranuclear cascade appears to be terminated relatively quickly, such that a majority of particles emerge from the evaporation process and with an energy spectrum dominated by low energy emissions. Very little evaporation is associated with proton emission due to the high potential barrier. In fact the average evaporation yield of protons is less than 0.07 % of that for neutrons at 100 MeV. Fast protons, which exist only during the cascade stage, are less inhibited by the Coulomb barrier but are still less likely to be emitted than fast neutrons which experience a much lower emission threshold.

Theoretical cross-sections for reactions of the type $(\gamma, x\text{n0p})$, $(\gamma, x\text{n1p})$ and $(\gamma, x\text{n2p})$ are shown in Figures 4.5, 4.6 and 4.7 respectively. The neutron-only channels show cross-sections which rise from well defined energy thresholds, peak rapidly and then diminish as new decay channels are opened. Sharply peaked cross-sections are characteristic of evaporation from a compound nucleus in thermal equilibrium, and this clearly dominates the emission mechanism for neutrons in the results shown. The high energy tails are a feature of pre-equilibrium emissions which, in general, remove a much larger fraction of the available excitation energy than an evaporated particle. The remaining compound nucleus can then evaporate fewer neutrons for the same incident photon energy. For this reason, individual reaction channels are not so rapidly suppressed when a higher decay channel become energetically possible, but instead retain a finite cross-section up to relatively high energies. In reactions where one or more protons are released the peaking becomes less pronounced

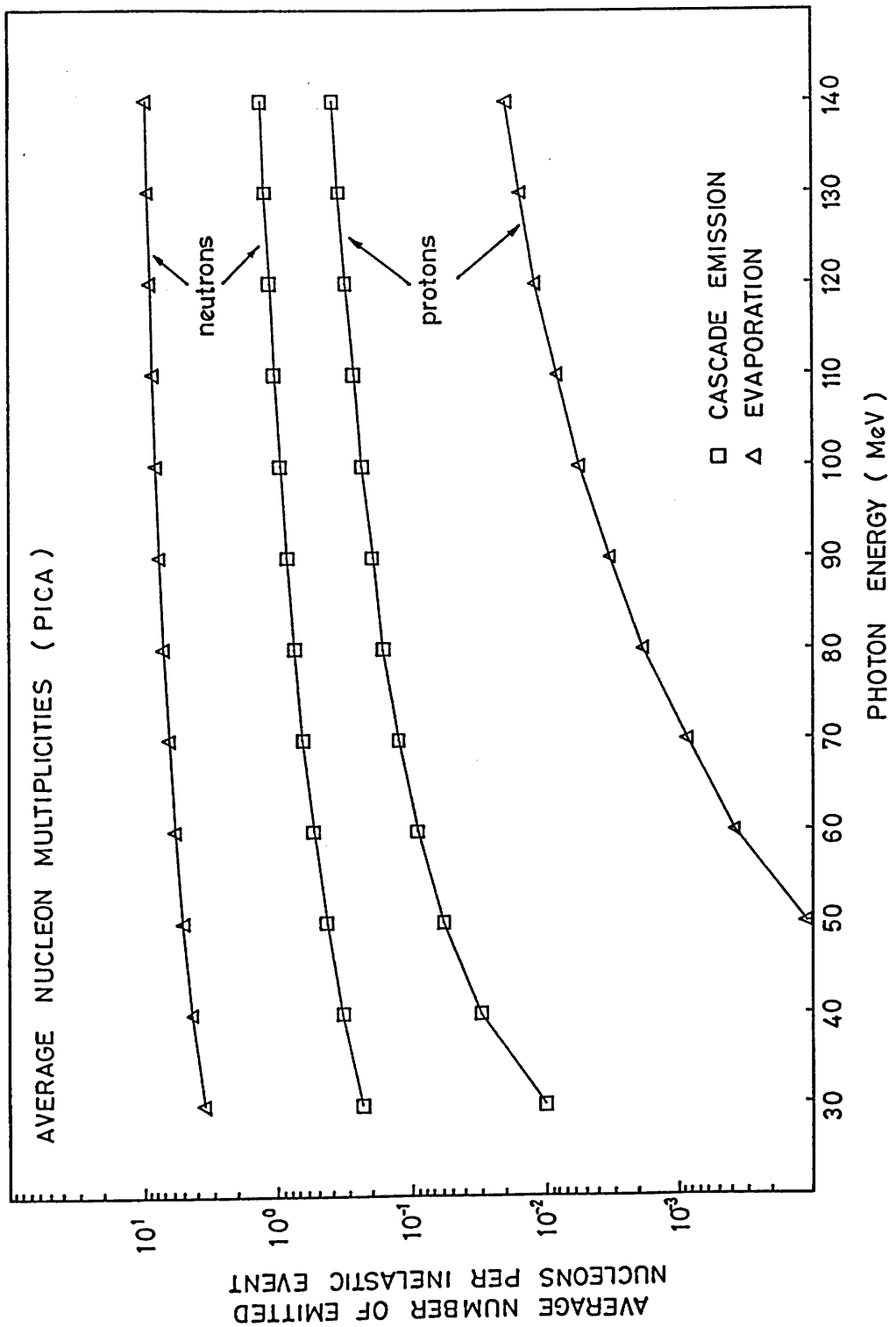

Figure 4.4: Average multiplicities of emitted nucleons at both the cascade and evaporation stages of the PICA calculations.

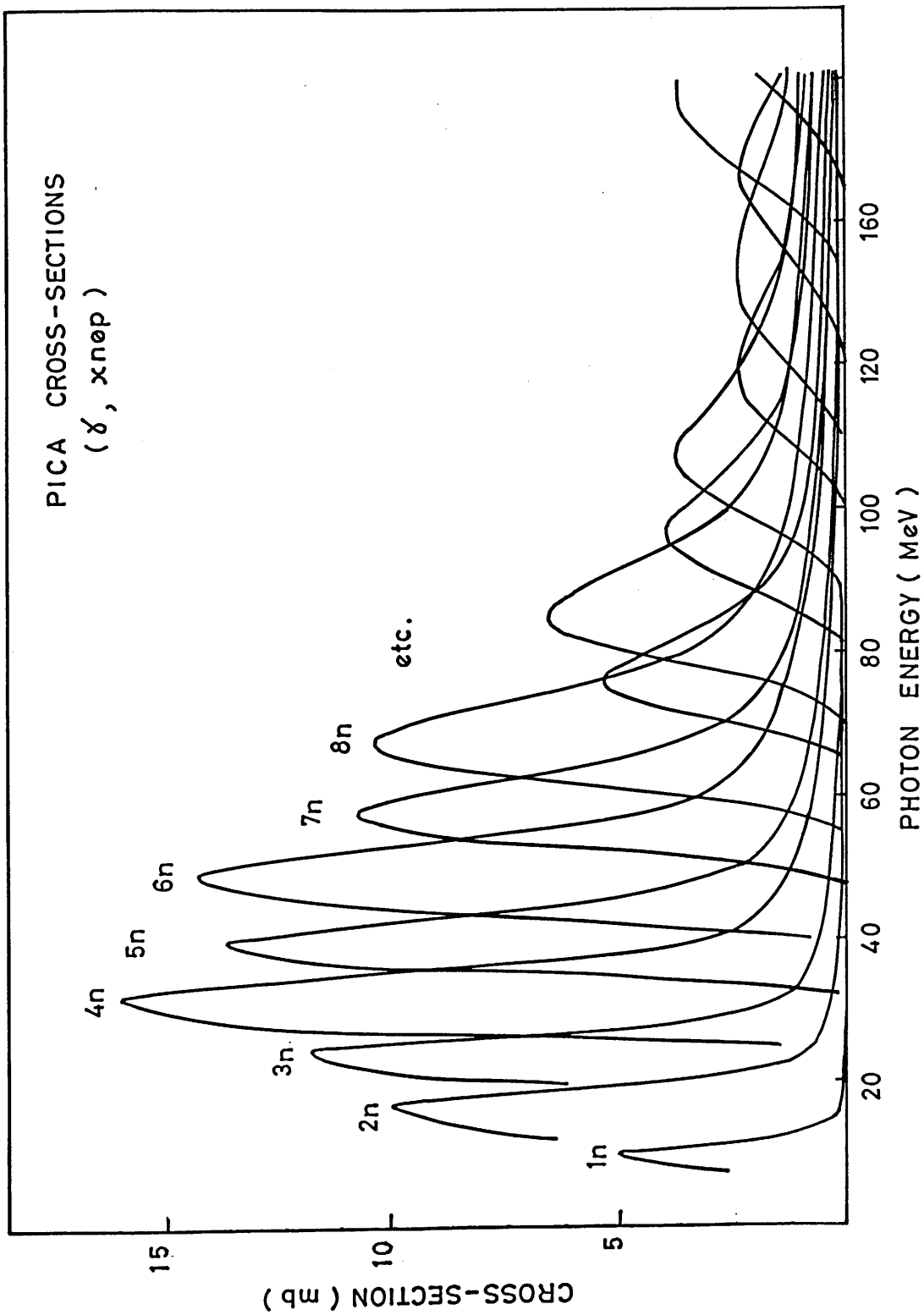

Figure 4.5: Predicted cross-sections for the reactions $(\gamma, xn0p)$ using the intranuclear cascade/evaporation model (PICA).

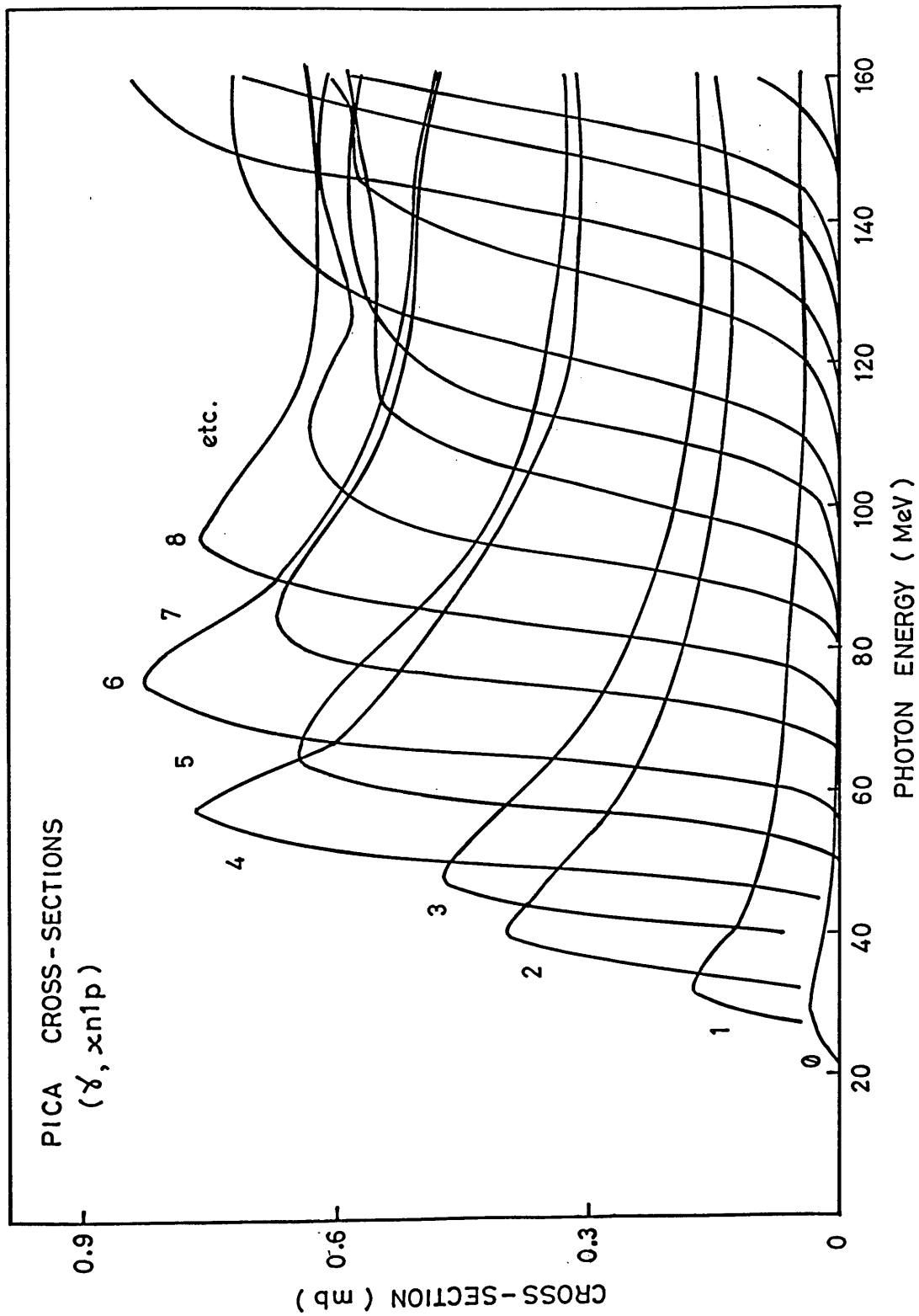

Figure 4.6: Predicted cross-sections for the reactions $(\gamma, x\text{n1p})$ using the intranuclear cascade/evaporation model (PICA).

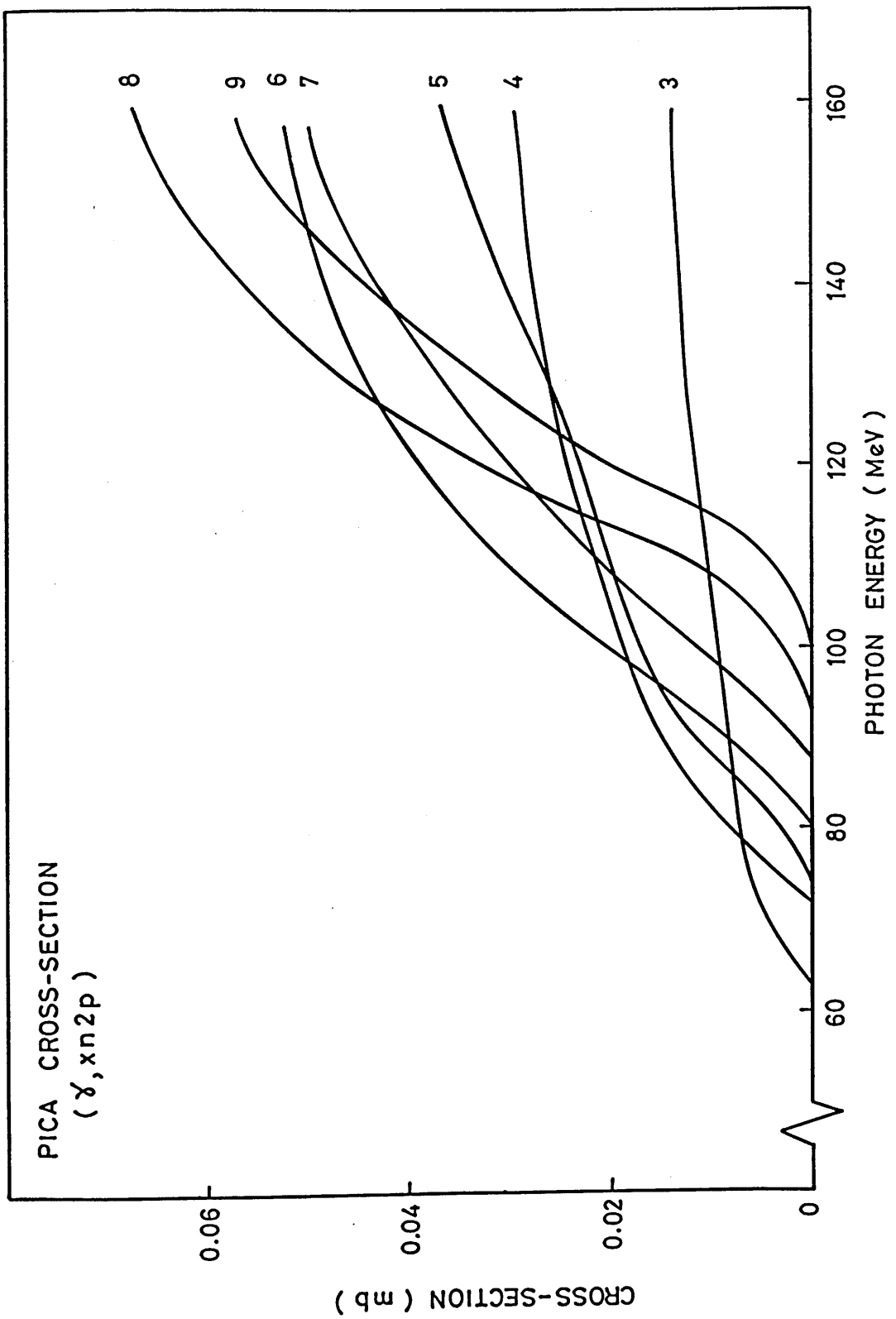

Figure 4.7: Predicted cross-sections for the reactions $(\gamma, xn2p)$ using the intranuclear cascade/evaporation model (PICA).

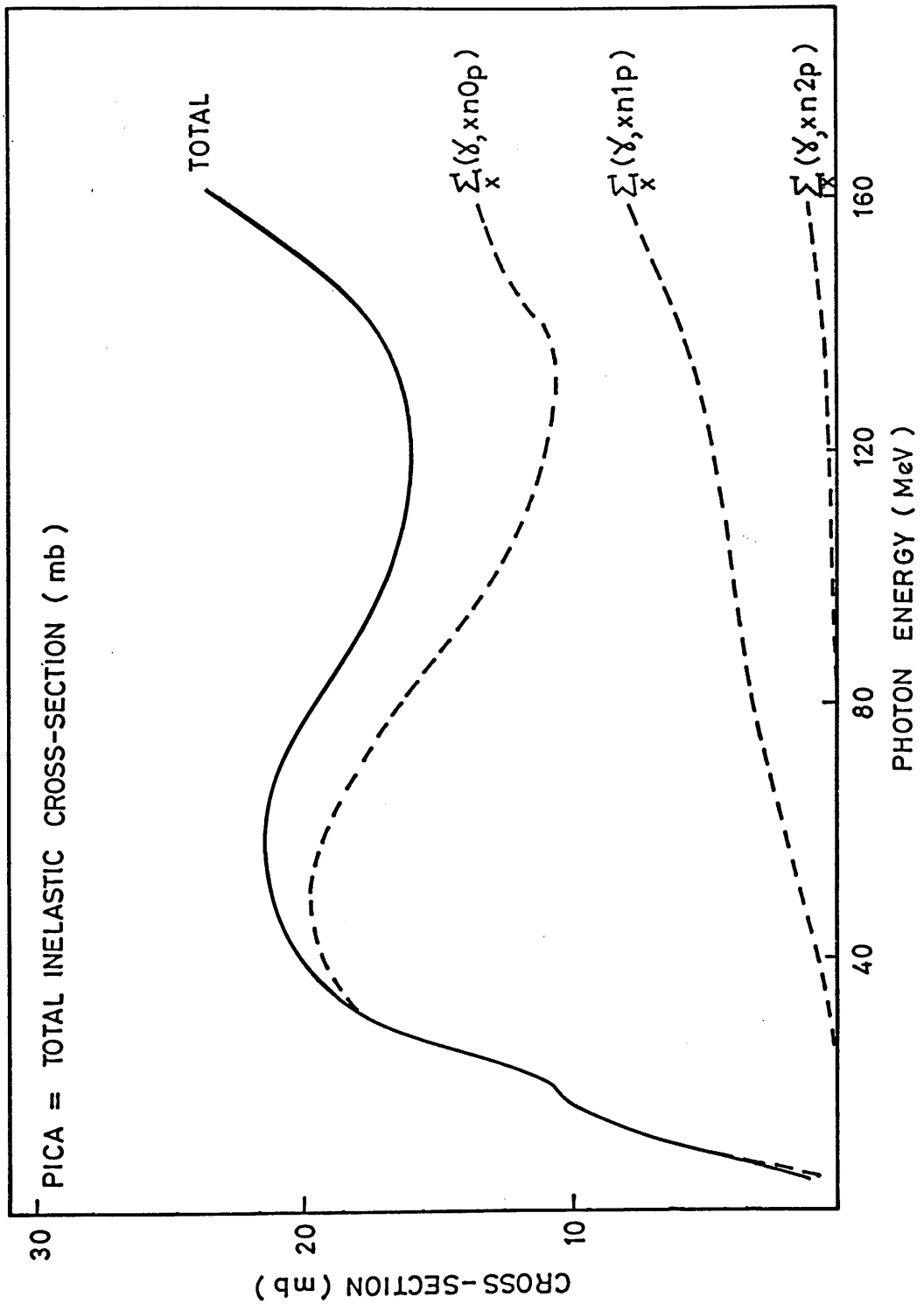

Figure 4.8: Total inelastic cross-section from intranuclear cascade/evaporation calculations (PICA) showing the relative contributions from charged particle channels.

and the high energy tailing more prominent. The charged particle emissions in these reaction channels are guaranteed to occur through a pre-equilibrium mechanism and therefore show less of the characteristics of a purely statistical evaporation. The total absorption cross-section, evaluated from the PICA model is shown in Figure 4.8.

4.3 Hybrid Plus Evaporation Model

The calculations reported in this section were made using a modified version of the hybrid precompound-decay code ALICE/LIVERMORE 82 [108]. In this code precompound particle emission is treated using Blann's hybrid model [106,107] with an initial exciton configuration appropriate to the photon absorption mechanism. The initial excitation is followed by an equilibration process which proceeds, via 2-body scattering events, through a series of so called intermediate exciton states. The exciton number n is an indication of the complexity of the excitation and increases (or decreases) by two for each successive state as an additional particle-hole pair is created (or destroyed). The precompound particle emission probability is evaluated at each of these states until an equilibrium situation is reached. Following this precompound stage a statistical evaporation calculation is performed using the formalism of Weisskopf and Ewing [96]. From this, the final distribution of $(\gamma, x\mathrm{n}\, y\mathrm{p})$ reaction products can be evaluated. Fission competition, which is also included at the equilibrium stage, is calculated according to the prescription of Bohr and Wheeler [165,58]. In these calculations, the fast precompound process is assumed to precede fission with no competition.

Details of the hybrid plus evaporation model and the calculations performed are given in the following sections. The symbols used are explained in Table 4.1.

4.3.1 Precompound Decay – the Hybrid Model

In the hybrid model [107] the result of the absorption of a photon is represented by the formation of some simple configuration of p particles and h holes (or $n = p + h$ excitons). Quasi-deuteron absorption for example, which involves the excitation of two nucleons, will lead to a (2p,2h) initial exciton state (Figure 4.9). Modifications to this (2p,2h) assumption are discussed later. The initial configuration may decay through the emission of up to p particles (from virtual levels) into the continuum or can undergo some internal transition, through a particle-particle or particle-hole interaction, to a new $n \pm 2$ exciton state. The reaction proceeds through a series of these p-p or p-h interactions which are observed, at least in the early stages of the equilibration process, to predominantly *increase* the total exciton number (Figure 4.10). It is assumed that every possible configuration of particles and holes within an n-exciton hierarchy, amongst which the excitation energy can be partitioned, may occur with equal *a priori* probability. An equilibrium situation is established for an ensemble of nuclei when all of the exciton configurations (for all n) are populated with equal *a priori* probability. The energy spectrum for particles emitted during the entire pre-equilibrium period is taken as a sum over the emissions from all intermediate exciton states i.e. from the initial exciton configuration $n = n_o$ to an equilibrium (or most probable) value $n = \overline{n}$ in increments of $+2$. The number of particles in this spectrum which have channel energy between ϵ and $\epsilon + d\epsilon$ has been shown by Blann [107] to be

$$\mathrm{N}_\nu(\epsilon)\,d\epsilon = \sum_{\substack{n=n_o \\ \Delta n=+2}}^{\overline{n}} \underbrace{\left[\frac{X_{n,\nu}\,\mathrm{N}_n(\mathrm{U},\epsilon)\,d\epsilon}{\mathrm{N}_n(\mathrm{E})}\right]}_{1} \underbrace{\left[\frac{\lambda_c(\epsilon)}{\lambda_c(\epsilon)+\lambda_+(\epsilon)}\right]}_{2} \underbrace{\mathrm{D}_n}_{3} \qquad (4.10)$$

The labelled terms within this summation are interpreted for each n-exciton configuration as follows :

1. The number of particles (of type ν) which are in the energy interval

$\epsilon \longrightarrow \epsilon + d\epsilon$ in the n-exciton hierarchy.

2. This represents the fraction of particles which will be emitted from the n-exciton hierarchy rather than undergoing a transition to an $(n+2)$-exciton hierarchy. It is simply the ratio of the transition rate into the continuum to the total transition rate for those particles at excitation ϵ.

3. D_n is a depletion factor. It denotes the fraction of the initial population of excited nuclei which has survived to the n-exciton hierarchy. That is to say, nuclei for which no particle has been emitted for exciton numbers lower than n.

All predictions made within the framework of the hybrid model are based on the solution of Equation 4.10. Its usage and important features are outlined in the remainder of this section.

Exciton State Densities

The exciton state densities $N_n(E)$ and $N_n(\epsilon, U)$ specify the number of possible configurations of n excitons which conform to the stated energy conditions. It is assumed that all of these configurations may occur with equal *a priori* probability, within the limits of the exclusion principle. For an infinitely deep well $N_n(E)$ has the form

$$N_n(E) = \frac{(g\,E)^{p+h-1}}{p!\,h!\,(p+h-1)!} \tag{4.11}$$

where g is the single particle level density. This expression assumes that the p and h excitons may each have between 0 and E of the available excitation energy shared in an equal *a priori* way between the $p + h - 1$ degrees of freedom. However, when the excitation energy E is significantly greater than the Fermi energy E_f this assumption no longer holds since it allows the holes to occupy energy levels below the bottom of the nuclear potential well. Clearly

ν	Particle type (neutron or proton)
ϵ	Channel energy in continuum i.e. measured with respect to outside of nucleus (Figure 4.9).
n	Exciton number for p-particle, h-hole state where $n = p + h$.
n_o	Initial exciton number
$\overline{n}$	Equilibrium (most probable) exciton number.
E	Total excitation energy of nucleus.
U	Total excitation energy of residual nucleus.
B_ν	Particle binding energy (type ν).
$N_\nu(\epsilon)\, d\epsilon$	Number of particles (type ν) emitted into range $\epsilon \longrightarrow \epsilon + d\epsilon$.
$X_{n,\nu}$	The number of particles in the n-exciton configuration which are of type ν.
$N_n(E)$	Number of ways in which n excitons can have a total energy of E partitioned between them.
$N_n(U,\epsilon)$	Number of ways of combining n excitons such that one, if emitted, would have energy ϵ, while the remaining $(n-1)$ excitons in the residual nucleus share the residual excitation $U = E - B_\nu - \epsilon$ (Figure 4.9).
$\lambda_c(\epsilon)$	Emission rate of particle with energy ϵ into the continuum.
$\lambda_+(\epsilon)$	Intranuclear transition rate of particle with energy ϵ.
D_n	Fraction of the initial population of excited nuclei surviving (i.e. without emitting a particle) to an n-exciton hierarchy.

Table 4.1: Summary of hybrid model symbols.

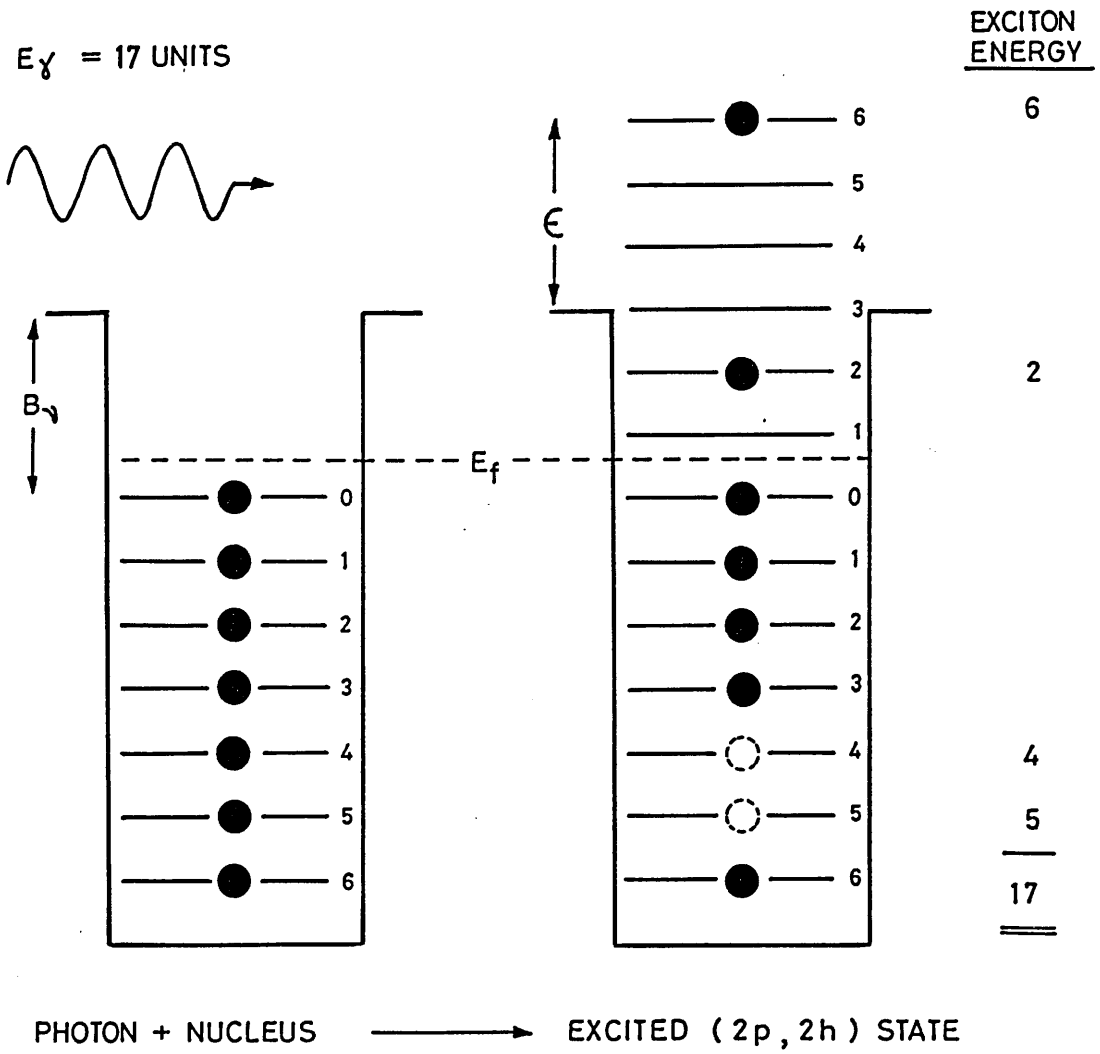

Figure 4.9: Quasi-deuteron photon absorption in the hybrid model leading to a (2p,2h) initial exciton state. A Fermi gas model with equidistant level spacing is assumed for the nucleus. This example shows one of many possible configurations for which 17 units of energy (E_γ) can be partitioned amongst 2 particles and 2 holes. If the particle (type ν) in virtual level ϵ is emitted into the continuum, a residual nucleus will remain with $(n-1)$ excitons and excitation energy $U = E - B_\nu - \epsilon$.

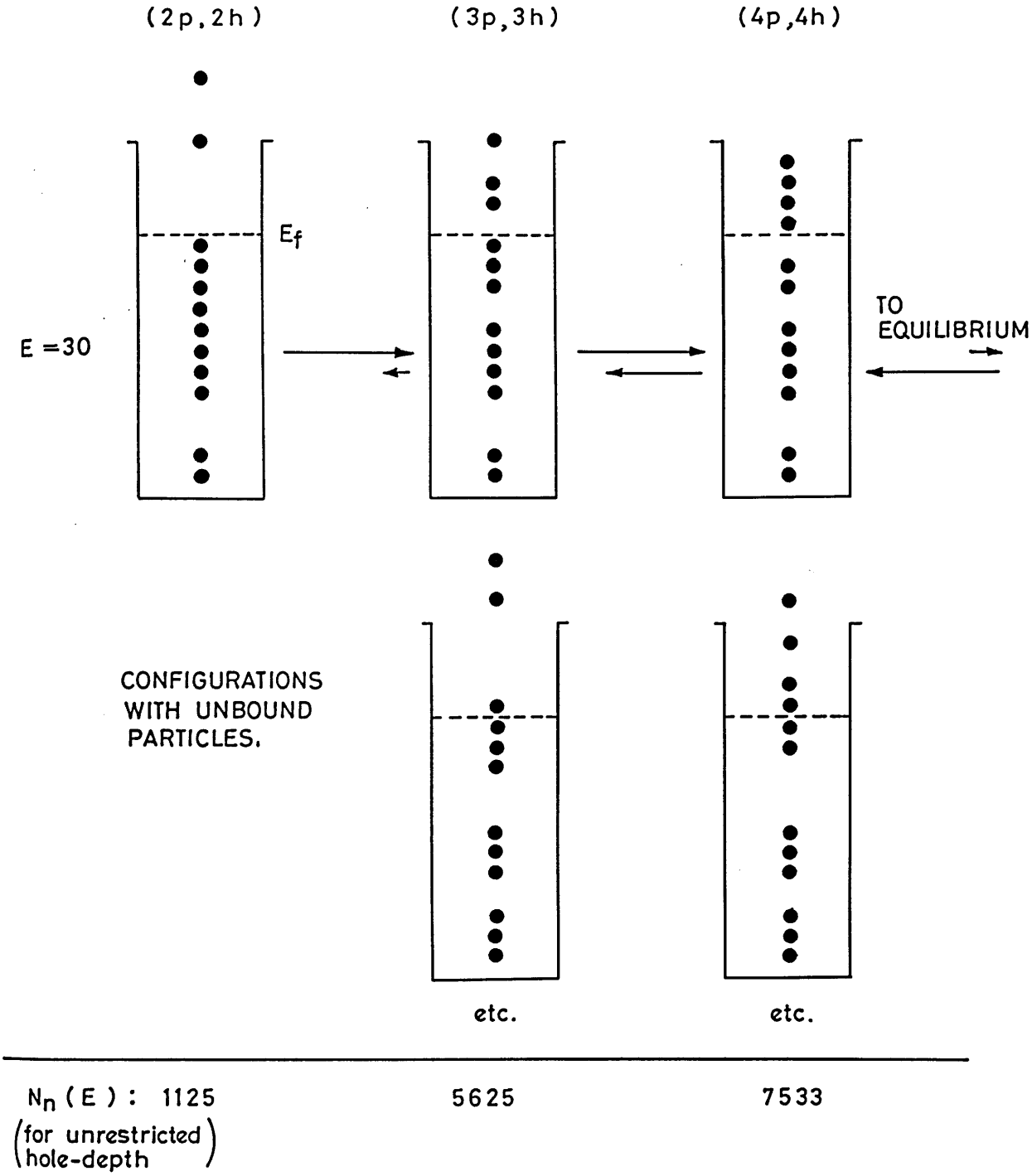

Figure 4.10: Evolution of exciton states through 2-body interactions in the hybrid model. Transitions which increase the exciton number by +2 are predominant in the early stages of the equilibration process due to an increasing phase space availability. Many configurations of the n excitons are possible within each n-exciton hierarchy, some of which will have particles in unbound virtual levels. From an initial $n = 4$ exciton state following photon absorption, the ensemble of nuclei approach an equilibrium distribution (as indicated by the arrows) when all configurations are populated with equal *a priori* probability.

the allowable hole depth should be constrained to be no greater than the well depth less the particle binding energy. Indeed, comparisons of hybrid model predictions with nucleon induced reaction data [166] have shown that such a consideration is important. Formulae which reduce the exciton state densities for "constrained" hole depths [109] have therefore been included in the present calculations.

Transition Rates

Whether a particle in a virtual level is emitted or undergoes a transition to a more complicated state depends upon the transition rates $\lambda_c(\epsilon)$ and $\lambda_+(\epsilon)$.

The internal transition rate $\lambda_+(\epsilon)$ for a particle at channel energy ϵ is based on the classical particle velocity divided by the average mean free path (m.f.p.) as calculated for nucleons in nuclear matter. In the calculations reported here, the Pauli corrected mean free paths obtained from nucleon-nucleon scattering cross-sections by Kikuchi and Kawai [167] have been doubled to compensate for the longer values which occur in the diffuse nuclear surface. Use of this averaged value, which will be referred to as the 'standard' m.f.p., follows from observations made in the original GDH formulation which explicitly includes these geometrical considerations.

Below about 100 MeV the internal transition rate can be approximated by the expression

$$\lambda_+(\epsilon) = \frac{1}{k}\left[1.4 \times 10^{21}(\epsilon + \mathrm{B}_\nu) - 6 \times 10^{18}(\epsilon + \mathrm{B}_\nu)^2\right] \qquad \mathrm{sec}^{-1} \qquad (4.12)$$

An effective m.f.p. can be specified by altering the parameter k and this may be used to incorporate local density effects into the calculation e.g. photon absorption in a diffuse nuclear surface region. Setting k equal to unity gives the original m.f.p.'s of Ref. [167].

The emission rate $\lambda_c(\epsilon)$ of a particle of energy ϵ into the continuum, is based

on the inverse reaction cross-section (through the law of detailed balance) and a phase space availabilty consideration. The transition rate used here is that employed by Harp and Miller [101] who write

$$\lambda_c(\epsilon) = \sigma_\nu(\epsilon) \left[\frac{2\epsilon}{\mathrm{m}}\right]^{\frac{1}{2}} \frac{\rho_c(\epsilon)}{\mathrm{g}_\nu \, \mathrm{V}} \tag{4.13}$$

where

$\sigma_\nu(\epsilon)$ = inverse reaction cross-section.
m = particle mass.
$\rho_c(\epsilon)$ = density of states for particle in continuum.
g_ν = single-particle density of states in excited nucleus (for a particle of type ν).
V = arbitrary volume cancelled by the same volume in ρ_c.

Multiple Precompound Decay

Early hybrid calculations arbitrarily restricted precompound emission to a total of one particle (or rather one particle of each type ν). The restriction was made simply for computational convenience but is clearly inadequate at excitations greater than $\sim$ 50 MeV. If an exciton configuration contains p particle excitons then it can, in principle, emit any number up to p of these; they would of course have to reside in virtual levels. Blann [111] has shown that *multiple* precompound emission becomes increasingly probable with increasing excitation energy. Two kinds of multiple precompound decay, labelled Types I and II, have been discussed in the literature with the differentiation made for reasons of computational convenience and efficiency.

- Type I [111] describes emission, from the nucleus, of more than one particle from a *single* exciton configuration.

- Type II [109] occurs when the first particle emission is followed by one or more 2-body transitions (now in the daughter nucleus) prior to the emission of a further particle. This differs from Type I decay only through

the existence of the intervening transitions. The first emission removes an amount of energy equivalent to the particle's kinetic energy plus its binding energy. The parent decay therefore populates a daughter product which has one exciton less and a residual excitation of $U = E - B_\nu - \epsilon$. The daughter ensemble is then treated by an equivalent version of Equation 4.10.

Since the first emission leaves a range of residual excitations and exciton numbers in the daughter nucleus, all of which must be followed, Type II calculations are substantially more complex and time consuming than Type I. Both types have however been included in the present calculations. Since the cross-section for precompound decay is greatest for $n = n_0$ and decreases rapidly with increasing exciton number, Type II decay has been shown [110] to be less important than Type I and to increase fast particle emission by at most $\sim$ 10 % at 140 MeV.

The treatment of multiple decay in the hybrid model is expected to have a major influence upon the predicted excitation functions for reactions in which one or more particles are emitted in the precompound mode.

Initial Exciton Number

If a quasi-deuteron mechanism is assumed for photon absorption then two particles, a neutron and a proton, are excited in the primary interaction. Two holes remain behind which also act as carriers of the available excitation energy. The holes may share in this energy in an equal *a priori* way unless restricted by the finite depth of the nuclear potential well (as described above). Since the nuclear density distribution, when averaged over the whole nucleus, corresponds to a Fermi energy of only $\sim$ 30 MeV and since excitation energies of up to 150 MeV are involved here, the hybrid model can realistically be applied only

if constraints are put upon the hole depths. The exciton state densities N_n, in both the initial and residual nucleus, have been appropriately modified [109] in the present formulation to include this effect. It has been suggested [110] for photon induced reactions, which require the excitation of a strongly correlated n-p pair, that the two holes will remain correlated in momentum and as such should be considered to provide only a single degree of freedom. In this case the "hole-pair" is restricted to an energy equivalent to twice that for a single hole. This idea that the two holes remain coupled is however open to question and will be discussed later. For the present calculations photon absorption was considered within the context of the following distinct initial exciton hierarchies.

(2p,2h) : This corresponds to quasi-deuteron absorption over a range of nuclear densities with no correlation between the final particle energies or the final hole energies. The holes may have energies up to E_f each.

(2p,1h) : This implies quasi-deuteron absorption in which the two holes remain strongly correlated in momentum so that jointly they provide only one degree of freedom (rather than two). In this case the hole-pair may have energy up to $2E_f$. In comparison with the (π^-, xn) results of Bassalleck [168], where pion absorption is also thought to proceed principally through a quasi-deuteron mechanism, this choice provides better agreement with the measured data.

(1p,1h) : This represents photon absorption on a single nucleon and was considered here simply to monitor the influence of the absorption mechanism upon the decay channels of the de-excitation process.

4.3.2 Decay of the Compound Nucleus

Following the precompound stage of the de-excitation process, particle evaporation from the remaining compound nucleus is calculated using the statistical evaporation model of Weisskopf and Ewing [96]. The treatment is similar to that discussed in Section 4.2 but now includes competition due to fission. The fission component is evaluated using the Bohr-Wheeler model [165,58] with fission parameters taken from experiment. The fission barriers B_f were taken from Reference [169] while the ratio of level densities a_f/a_n at the saddle-point and ground state was assumed to be 1.070 ± 0.01 for ^{232}Th. The validity of using this value, which was chosen to reproduce photo-fission probabilties measured by Caldwell *et al.* [56] in the giant resonance region (first and second chance fission), has yet to be checked for fission processes which follow multiple nucleon emission (multi-chance fission). Since the photon brings negligible angular momentum into the nuclear system, even at the highest energies considered here, all angular momentum effects have been ignored.

4.3.3 Calculations

Calculations have been performed for ^{232}Th using the hybrid + evaporation model at energies of $30, 40, \ldots, 150$ MeV. Initial exciton states of (2p,2h) and (2p,1h) have been considered for quasi-deuteron absorption as well as a (1p,1h) single particle exciton mode for comparison. Calculations were made using the standard mean free paths based on the Pauli corrected values of Kikuchi and Kawai [167]. One calculation was performed for (2p,1h) excitations using double this standard value to determine the extent to which the m.f.p. influences the precompound particle emission probability. An average Fermi energy of 32 MeV was assumed for thorium and was therefore the limiting energy that could be taken up by a single hole-exciton. Measurements made on other heavy nuclei

have shown the total photon absorption cross-section to remain approximately constant over the energy range 50 – 150 MeV and so in the present calculations a constant total cross-section has been assumed. The validity of this assumption is discussed later.

The fission probabilities calculated here, using a (2p1h) initial exciton state, have recently been compared [170] to others based on photo-fission measurements made at Saclay [54] (Figure 4.11). The hybrid model calculation is seen to be in reasonable agreement with the ratio of the Saclay $\sigma(\gamma, \mathrm{F})$ data and the predicted total cross-section $\sigma(\gamma, \mathrm{tot})$ discussed in Section 1.2.3.

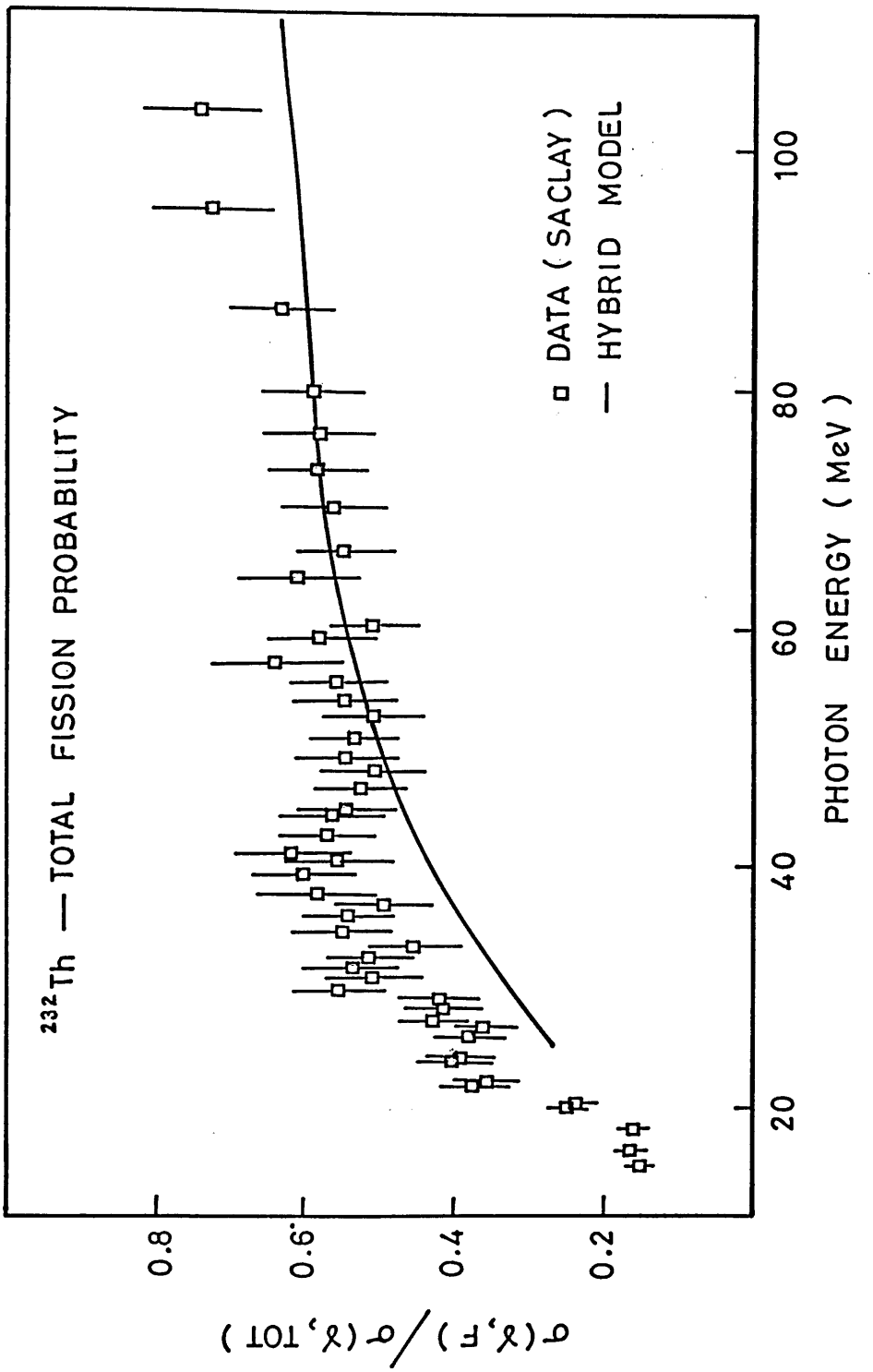

Figure 4.11: Total fission probability for ^{232}Th from ref. [170]. The 'data' corresponds to the photo-fission cross-section measured at Saclay [54] divided by a *predicted* total photo-absorption cross-section (Section 1.2.3). A reasonable fit is obtained using the Hybrid model and a (2p,1h) initial exciton configuration.

Chapter 5

Photoreaction Cross-Sections

5.1 Extraction of Photoreaction Cross-Sections

For comparison with the theoretical predictions of the photodisintegration models discussed in Chapter 4, it was necessary first of all to extract the energy dependent photoreaction cross-sections from the experimental yields y_e and y_{br}. The electron and bremsstrahlung induced yields can be related to the multipole decomposition of the photoreaction cross-sections by

$$y_e(E_e) = \sum_{\lambda L} \int_0^{E_e - m_n} \sigma_\gamma^{\lambda L}(E_\gamma)\, N_e^{\lambda L}(E_e, E_\gamma)\, \frac{dE_\gamma}{E_\gamma} \tag{5.1}$$

and

$$y_{br}(E_e) = \int_0^{E_e - m_n} \sigma_\gamma(E_\gamma)\, N_{br}(E_e, E_\gamma)\, \frac{dE_\gamma}{E_\gamma} \tag{5.2}$$

respectively, where the total photoreaction cross-section σ_γ at energy E_γ is just a sum of the multipole contributions $\sigma_\gamma^{\lambda L}$

$$\sigma_\gamma(E_\gamma) = \sum_{\lambda L} \sigma_\gamma^{\lambda L}(E_\gamma) \tag{5.3}$$

and the other symbols are as defined in Section 1.3.

The evaluation of this photoreaction cross-section as a function of E_γ thus requires a deconvolution of the radiation spectrum from the measured yield function. Bremsstrahlung yields were measured at too few end-point energies to allow σ_γ to be evaluated directly from Equation 5.2 and so the present results

are based primarily on an analysis of the electron induced yields, using the bremsstrahlung data as a check of the multipole strengths contributing to σ_γ and the correctness of the virtual photon spectrum.

The process by which the radiation spectrum is 'unfolded' from the activation yield curves has been a source of difficulty and uncertainty in previous experiments of this type and so more than one technique was employed in the present analysis to check for consistency in the unfolded solutions. A detailed description of the deconvolution procedure is given in Appendix K. The simplest process considered was a straight matrix transformation [171,172] but this led to excessive scatter in the unfolded cross-sections due to its failure to allow for the statistical nature of the experimental uncertainties. To remove this problem, a systematic smoothing (or "least structure") method was adopted. Using this approach [173] a search was made for solutions which passed most smoothly through the measured data, thereby minimising any false structure caused by their statistical distribution. Due, however, to the relatively large intervals (10 MeV) between the measured yield points, some residual oscillations were still evident in the unfolded cross-sections. The period of the oscillations showed an obvious correlation with the spacing of the data points and appeared to reflect some inadequacy in the unfolding procedure rather than any genuine structure in the photo-reaction cross-sections. To overcome this problem a "modified least structure" method [174] was tried and the corresponding solutions, whilst reproducing the same basic shapes for the reaction cross-sections, showed no such oscillations. This improvement was achieved by treating the integral of the cross-section, rather than the cross-section itself, as the unknown variable in the unfolding process. The smoother behaviour of this quantity as a function of end-point energy rendered the unfolded solutions less sensitive to uncertainties in the measured yields.

Using the modified least-structure method, sensible and consistent cross-section solutions have been obtained for most of the reactions investigated and only for the (e,6n2p) and (e,7n2p) reactions, where the statistical accuracy of the yields was poor, could no unambiguous solutions be determined.

A more fundamental uncertainty, which arises in the deduction of photonuclear cross-sections from electrodisintegration data, is the form of the virtual photon spectrum to be assumed in the unfolding process. As the relative multipole strengths which contribute to the photon absorption process are in principle unknown and since the virtual photon spectra are different for each of these multipole orders (Section 1.3), some assumptions have to be made as to the multipole composition of the photon absorption cross-section. Sum rules suggest that E1 transitions dominate the photon absorption process at these energies and so, as a first approximation, a purely E1 (SOBA) spectrum was used in the analysis of the electrodisintegration yields. The resultant cross-sections, referred to as $\sigma^{E1}_{100\%}$ here, are shown in Figures 5.1, 5.2 and 5.3.

The $(\gamma, x\text{n0p})$ cross-sections have a peak just above threshold which appears to diminish in size as the number of emitted neutrons, x, increases. In contrast to what would be expected if the evaporation process was dominant, the reaction cross-sections do not fall to zero as new decay channels become energetically possible but remain finite even to quite large energies above threshold. The $(\gamma, x\text{n1p})$ cross-sections are of similar magnitude at the high photon energies but rise less sharply from their reaction thresholds and show no sign of an initial peak. Although only a single $(\gamma, x\text{n2p})$ cross-section has been unfolded, there appears to be a trend that the cross-section rises less steeply from threshold as more charged particles are emitted. The smooth curves shown in the left hand columns of Figures 5.1, 5.2 and 5.3 are the least-structure solutions to the yield functions found by the unfolding procedure. These "smoothed yields"

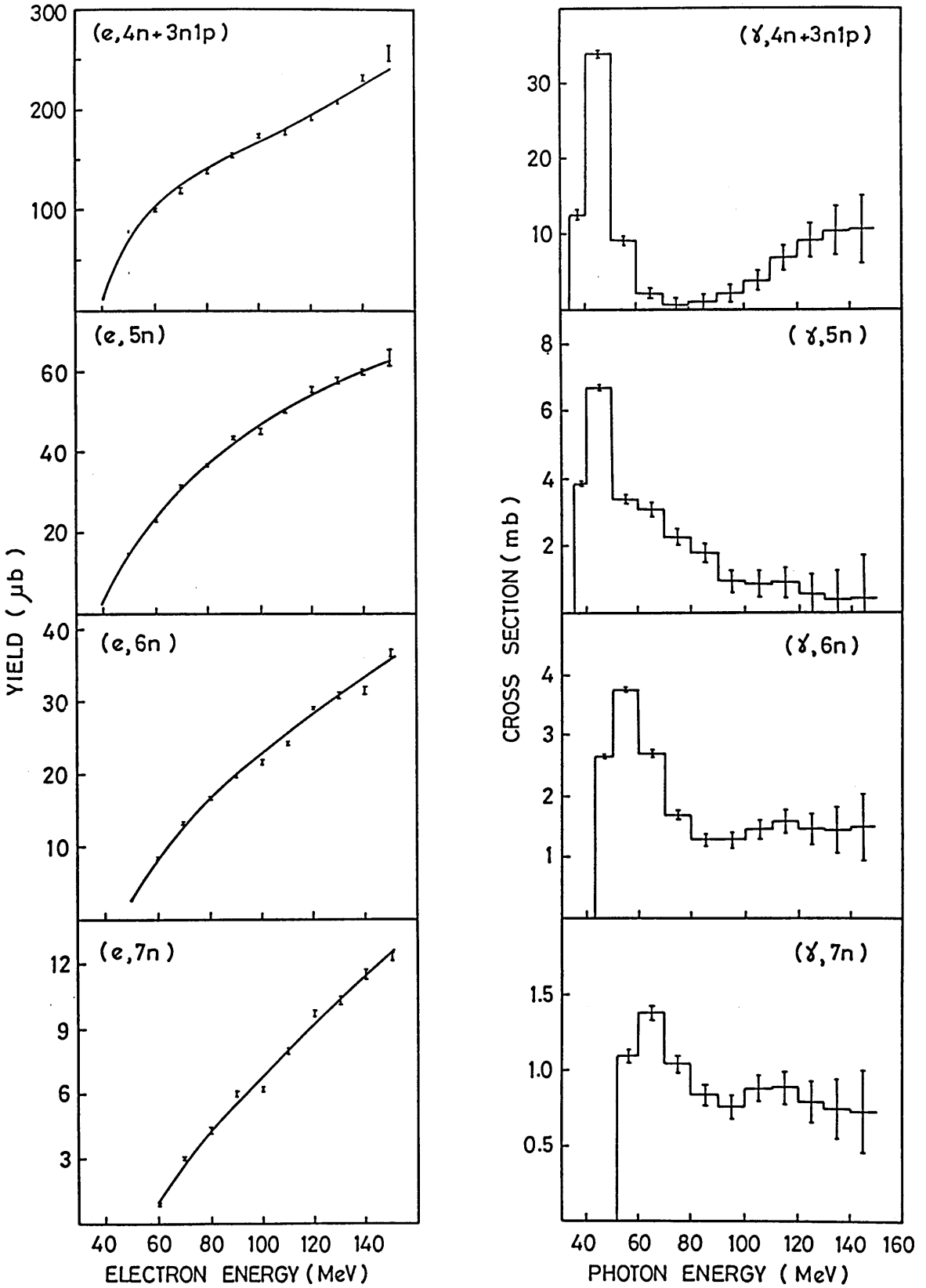

Figure 5.1: Smoothed yields and cross-sections obtained from the (e,xn0p) electrodisintegration yields using a modified least-structure method to unfold the E1 virtual photon spectrum (SOBA). The smoothed yields (left) correspond to the cross-section solutions (right) refolded with the radiation spectrum.

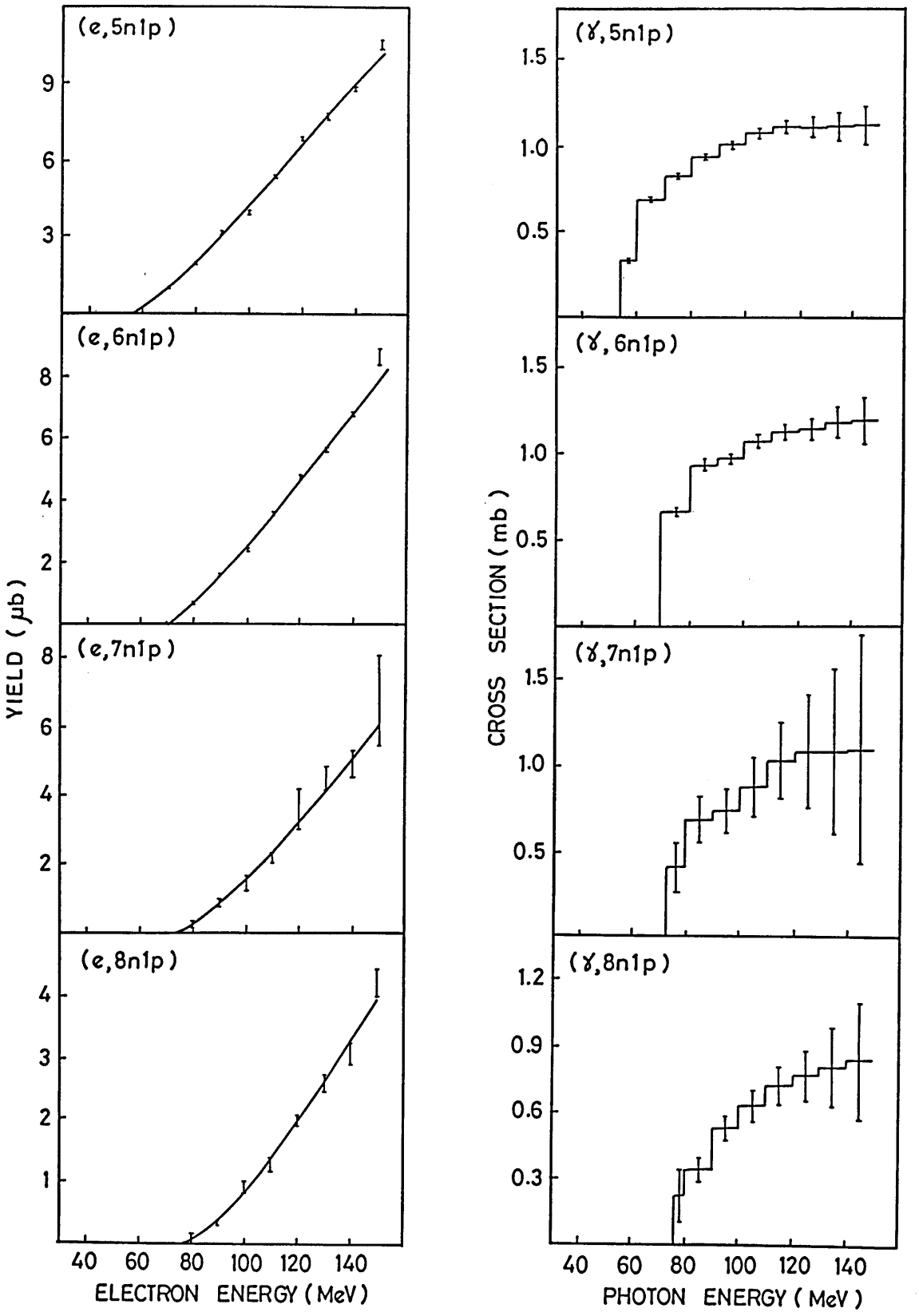

Figure 5.2: Smoothed yields and cross-sections obtained from the (e,xn1p) electrodisintegration yields using a modified least-structure method to unfold the E1 virtual photon spectrum (SOBA). The smoothed yields (left) correspond to the cross-section solutions (right) refolded with the radiation spectrum.

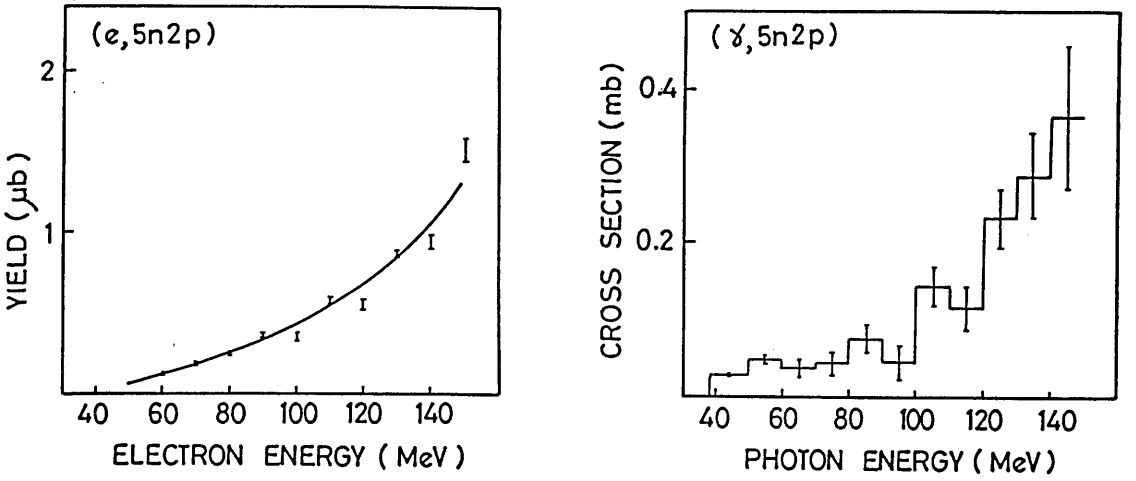

Figure 5.3: Smoothed yields and cross-sections obtained from the (e,xn2p) electrodisintegration yields using a modified least-structure method to unfold the E1 virtual photon spectrum (SOBA). The smoothed yield (left) corresponds to the cross-section solution (right) refolded with the radiation spectrum.

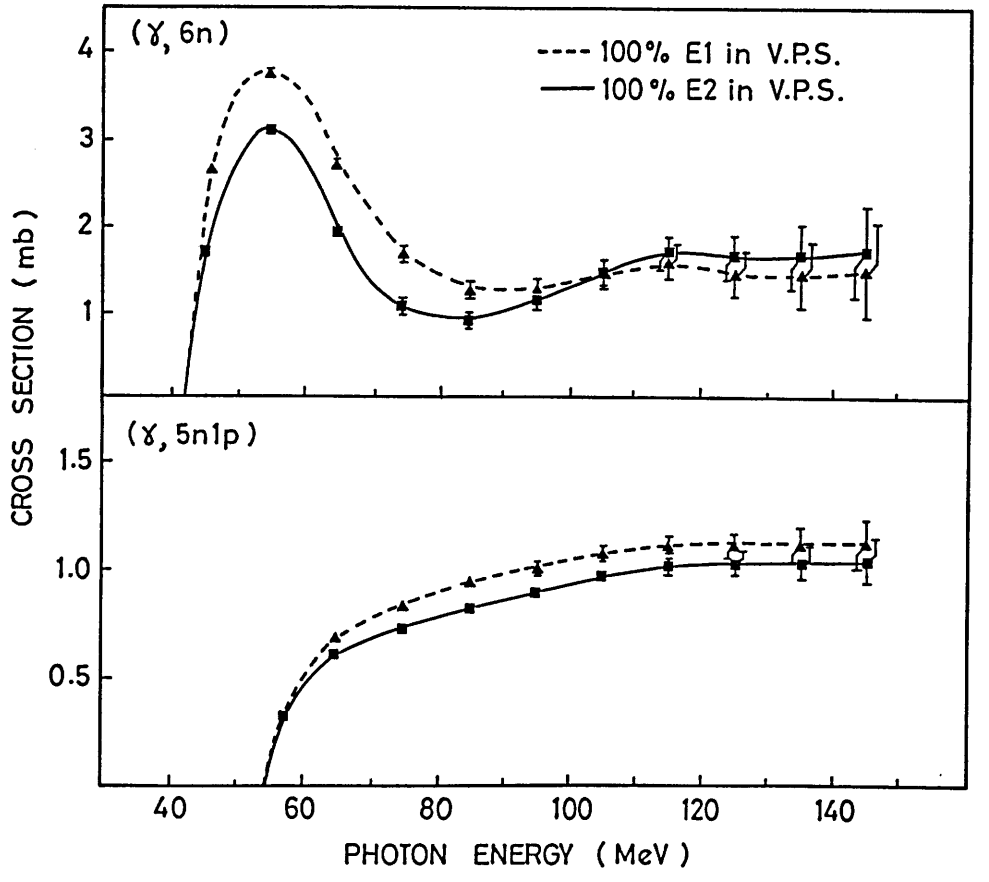

Figure 5.4: Cross-sections for the reactions $(\gamma, 6n)$ and $(\gamma, 5n1p)$ unfolded from their electrodisintegration yields. The two different solutions were obtained by assuming either 100 % E1 or 100 % E2 in the virtual photon spectrum (VPS). The similarity of the cross-section shapes implies that the E1 and E2 spectrum shapes are also rather similar.

correspond to the cross-section solutions refolded with the radiation spectrum.

To investigate the effects caused by other multipole components in the photo-absorption cross-section, the same yield curves were also analysed using a different radiation spectrum. The only other multipole expected to be important at these energies is E2 and it is informative to consider the extreme case of a virtual photon spectrum composed solely of this multipolarity. Figure 5.4 shows the cross-sections $\sigma^{E2}_{100\%}$ obtained from two of the measured yield curves by unfolding the E2 virtual photon spectrum. These examples are typical of the behaviour found in all of the unfolded reaction cross-sections. The corresponding E1 solutions are overlaid for comparison. While such a multipole composition (100% E2) is certainly unrealistic for photonuclear interactions at these energies, it can be seen that the shape of the unfolded cross-section appears relatively insensitive to the details of the radiation spectrum. There is weak evidence that the E2 solution produces a higher cross-section in the region well above threshold, but this is inconclusive due to the large statistical errors associated with the unfolded cross-sections in that area. In fact the only significant difference between the E1 and E2 solutions is in their magnitudes and this stems from the differing intensities of the two virtual photon spectra. Even so, the difference is only of the order of 20% even between these extreme assumptions.

Additional information does however exist, in the form of the bremsstrahlung induced yields, which in principle allows the relative strengths of E1 and E2 transitions in the photonuclear cross-section to be more accurately determined. Since the bremsstrahlung spectrum has equal intensity for all multipoles, this data was used to check the correctness of the multipolarity assigned to the photon absorption process. As bremsstrahlung measurements were made at only a few selected energies, it was impossible to unfold the photonuclear reac-

tion cross-section σ_γ from those yield curves directly. Instead the cross-sections obtained from the electron induced yields, in the pure E1 and pure E2 approximations, were refolded with the bremsstrahlung spectrum to simulate the 'expected' bremsstrahlung yields in these extreme cases. The consistency between the real and virtual photon data was assessed by a comparison of the measured and 'reconstructed' bremsstrahlung yield curves (Figures 5.5 and 5.6).

It is clear from this comparison that the refolded E1 (SOBA) bremsstrahlung yields lie above the measured points in most cases. Overall sytematic errors between the electrodisintegration and bremsstrahlung data are not thought to be responsible for this discrepancy since the electron and photon activation yields were determined under the same experimental conditions. Nor can the disagreement be attributed to uncertainties in the bremsstrahlung photon flux since the radiator thickness was determined to a much greater accuracy (Section 2.5) than would allow for such a discrepancy. It is possible however that the theoretical bremsstrahlung spectrum is itself inaccurate. Koch and Motz [133] suggest that the Bethe-Heitler formula used in the present analysis, although an apparently well understood formalism, could in fact be in error by as much as 10% at energies near the electron end-point. However, no experimental evidence has been found to confirm this and, with some reservation, it is assumed for the present that no such gross error exists in the bremsstrahlung spectrum. The above comparison then implies that the quantity $\sigma^{E1}_{100\%}$ is an overestimate of the total reaction cross-sections σ_γ. Such a result might arise if some other multipole, for which the virtual photon intensity was greater, also contributed to σ_γ. It is known that the E2 virtual photon spectrum is indeed more intense than the E1 spectrum and the corresponding yields generated from the $\sigma^{E2}_{100\%}$ cross-sections, while giving rise to curves similar in form to the E1 versions, are seen to fall below the real photon yields in most cases. Clearly then $\sigma^{E2}_{100\%}$

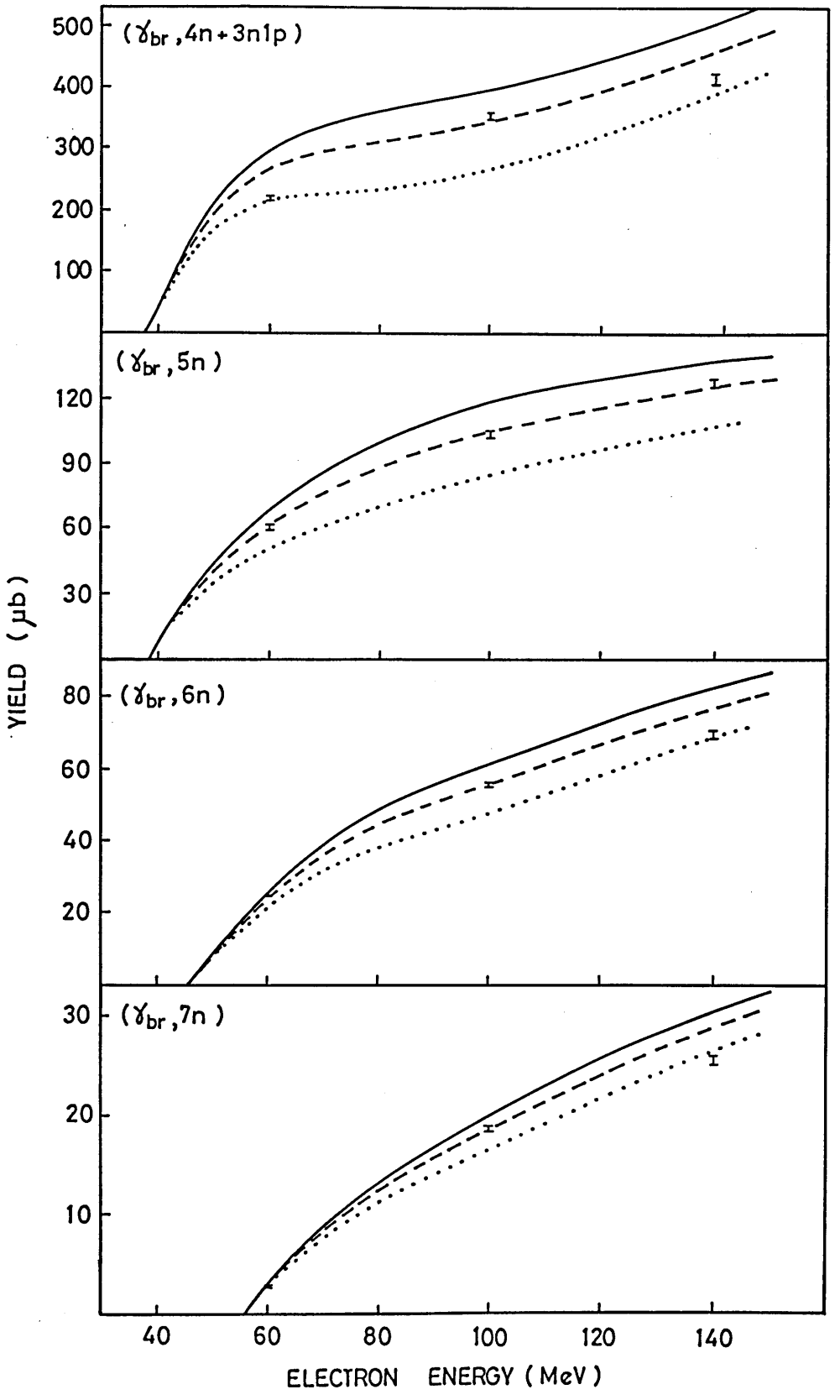

Figure 5.5: A comparison of the measured bremsstrahlung yields (γ_{br}, xn0p) with those obtained by folding the bremsstrahlung spectrum with the cross-section obtained from the electrodisintegration yields. The solid line results from cross-sections obtained using a pure E1 virtual photon spectrum while the dotted line corresponds to pure E2. An improved fit (dashed line) is obtained in some cases when the reaction cross-section is taken to be approximately 60% E1 + 40% E2.

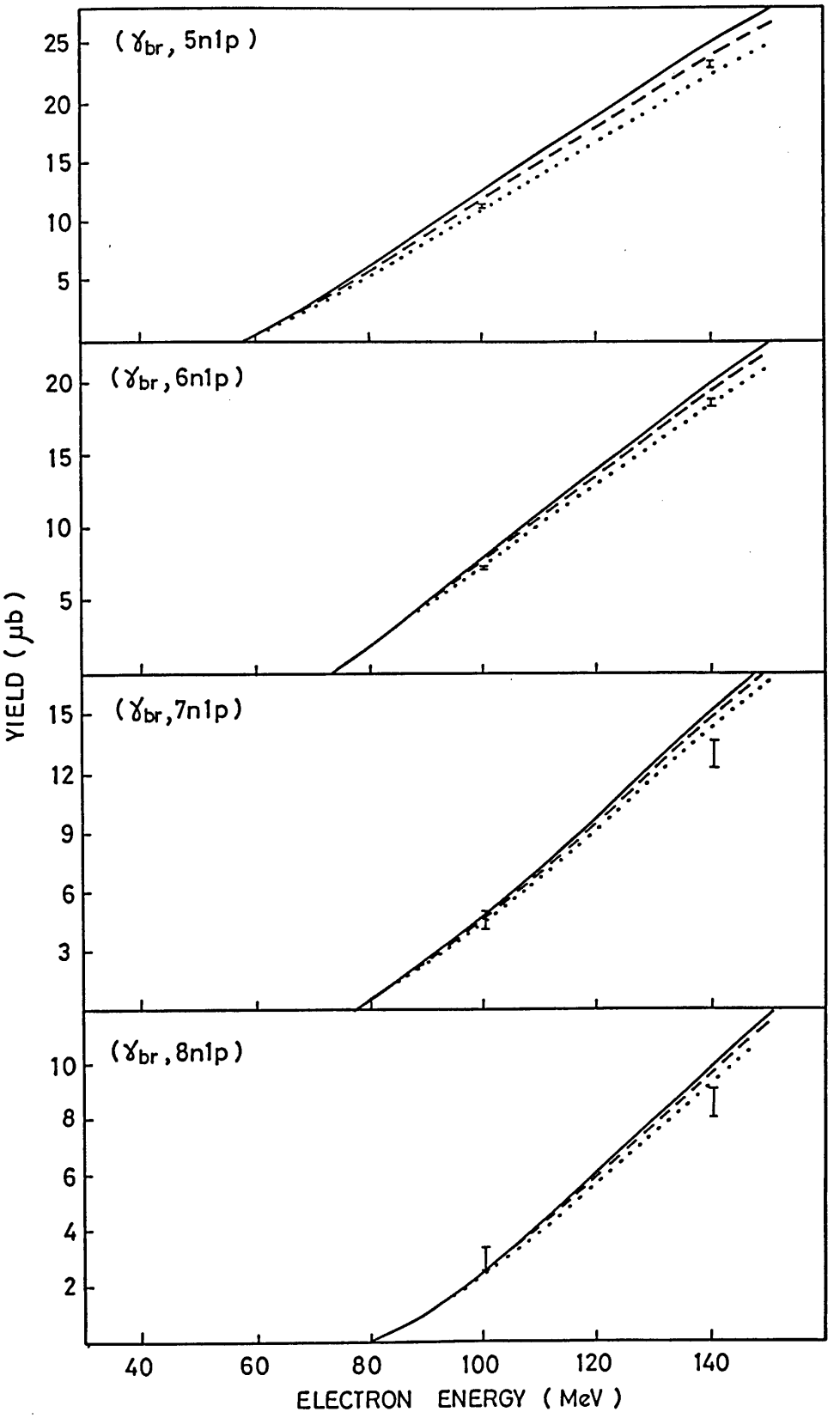

Figure 5.6: A comparison of the measured bremsstrahlung yields (γ_{br}, xn1p) with those obtained by folding the bremsstrahlung spectrum with the cross-section obtained from the electrodisintegration yields. The solid line results from cross-sections obtained using a pure E1 virtual photon spectrum while the dotted line corresponds to pure E2. An improved fit (dashed line) is obtained in some cases when the reaction cross-section is taken to be approximately 60% E1 + 40% E2.

is an underestimate of σ_γ. An improved fit can be achieved with a mixture of these multipoles, if the E2 contribution to the total reaction cross-section is assumed to be of the order of 40%. Such a contribution is however well in excess of any sum rule prediction of the E2 strength in photonuclear interactions at these energies. It is also greater than the E2 strengths suggested by other measurements of this type, although different and probably less reliable formalisms were used to derive the virtual photon intensities in the earlier investigations. Unlike the present virtual photon calculations, the E2 intensity in the previously used formalisms was greatly enhanced over that for E1 and so disparities between the real and virtual photon yields could be explained by a much smaller fraction of E2 transitions. It is necessary therefore to consider whether the present disagreement results from a remaining deficiency in the virtual photon calculation. As discussed in Section 1.3, the manner by which nuclear size and charge effects are incorporated into the virtual photon formalism can lead to quite large variations in the calculated intensities and it is possible that the SOBA approximation, as applied to this energy and nuclear mass region, is insufficient. Indeed as nuclear charge effects are included to first order only in the SOBA calculations, it is clear that the approximations involved in this formalism become less valid when applied to a nucleus as heavy as thorium. As seen in Section 1.3 the incorporation of charge effects tends to enhance the virtual photon spectra and in fact an increase of only about 10% in the E1 intensity would be sufficient to explain the present measurements, reasonably well, on the basis of E1 transitions only (Figures 5.7 and 5.8).

Other evidence that the E1 (SOBA) virtual photon intensity might be an underestimate of the true intensity, has arisen in a recent ^{181}Ta(e, π^+) measurement made by Anthony *et al.* [175]. They found that the pion electroproduction data, measured between 140 and 360 MeV, could be explained within the SOBA

framework only by increasing the E1 intensity by some 20% . Their data could not be fitted by increasing the strength of any other relevant multipoles due to the very similar magnitudes of those virtual photon spectra when calculated in SOBA.

Conclusions

The systematic smoothing techniques employed here in the deconvolution process have allowed cross-sections, without spurious structure, to be unfolded from the measured electrodisintegration yield curves. However those cross-sections obtained on the basis of E1 transitions only were found to be in slight disagreement with the real photon bremsstrahlung measurements. The inclusion of a finite E2 strength into the absorption cross-section improved the agreement somewhat, but due to a close similarity between the E1 and E2 virtual photon intensities an anomolously large contribution was required. It is unlikely that the E2 contribution of some 40% predicted here is a genuine reflection of the importance of such processes. It is more likely that in the present virtual photon formalism, the E1 intensity is underestimated and indeed an enhancement of only $\sim$ 10% provides a substantial improvement to the fit. This may be due to an incomplete treatment of the nuclear charge effects which are included to first order only in the present SOBA calculations and suggests that a full treatment of the nuclear size and charge effects, such as that being developed by Onley [88,89], is required for an accurate virtual photon analysis in nuclei as heavy as thorium. Only then will the importance of E2 transitions in this mass region be properly assessed.

Despite this it was shown that, as far as the cross-section shapes are concerned, it is non-critical whether the virtual photon spectrum is purely E1 or not. In terms of absolute magnitude, the range of uncertainty is only of the

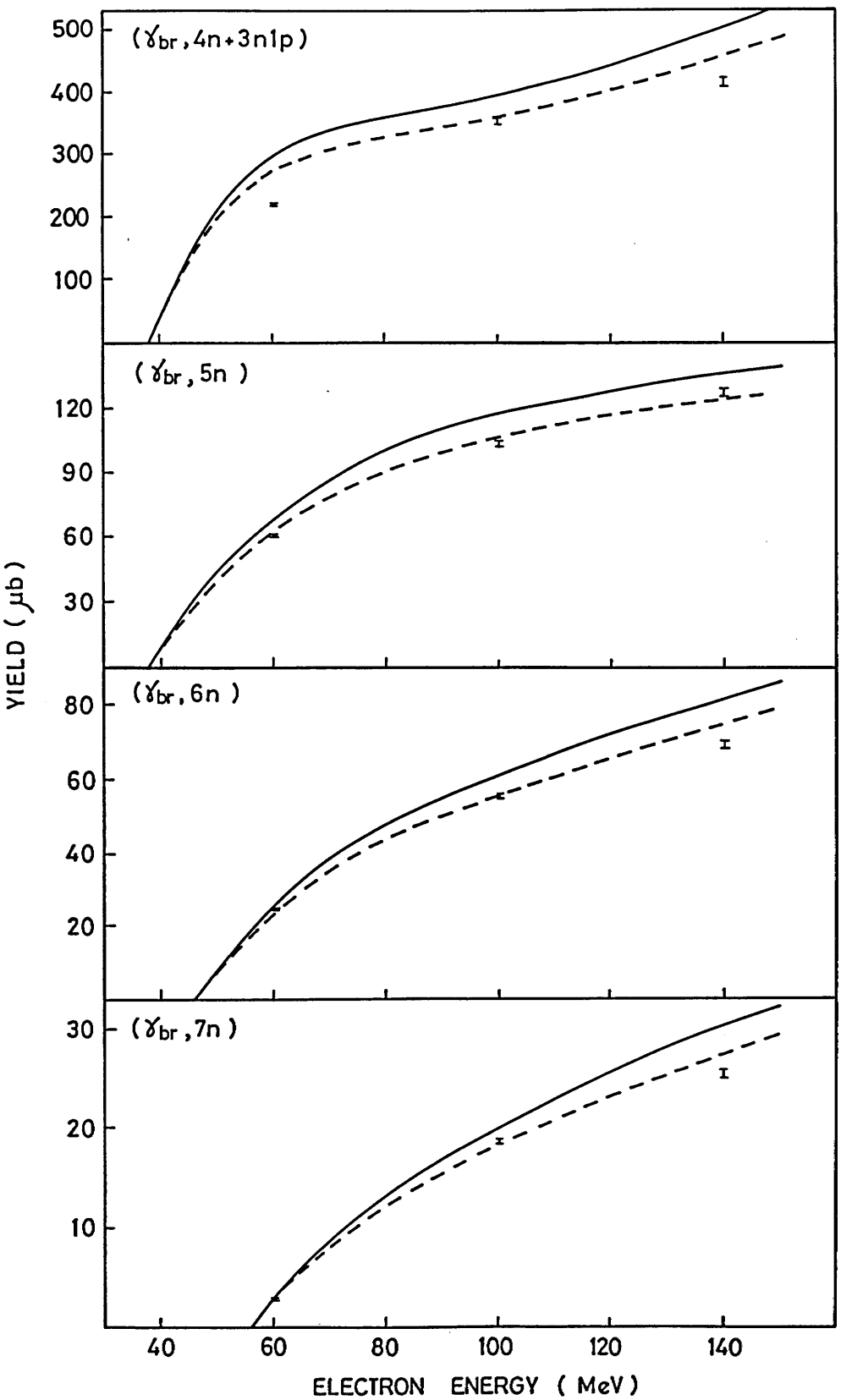

Figure 5.7: A comparison of the measured bremsstrahlung yields (γ_{br}, xn0p) with those obtained by folding the bremsstrahlung spectrum with the cross-section obtained from the electrodisintegration yields. The solid line results from those cross-sections obtained using a pure E1 (SOBA) virtual photon spectrum while the dashed line was obtained using the E1 (SOBA) spectrum enhanced by 10% .

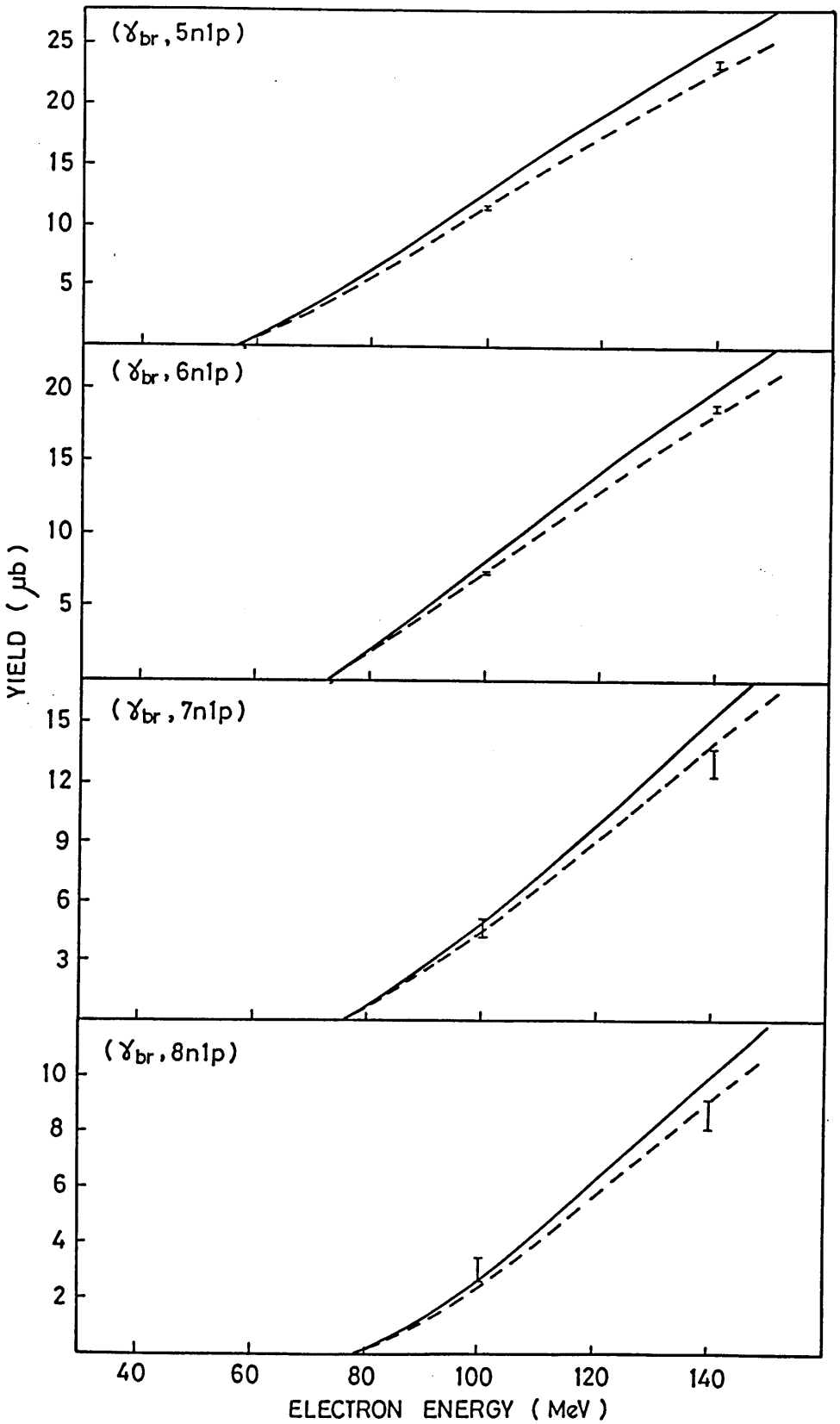

Figure 5.8: A comparison of the measured bremsstrahlung yields (γ_{br}, xn1p) with those obtained by folding the bremsstrahlung spectrum with the cross-section obtained from the electrodisintegration yields. The solid line results from those cross-sections obtained using a pure E1 (SOBA) virtual photon spectrum while the dashed line was obtained using the E1 (SOBA) spectrum enhanced by 10% .

order of 20% even when the most extreme contributions of E1 and E2 are assumed in the virtual photon spectrum and this uncertainty is reduced somewhat when a comparison is made between the real and virtual photon measurements. Overall, a systematic uncertainty of $\sim$ 10% remains in the magnitudes of the reaction cross-sections due to errors in either the virtual photon and/or the bremsstrahlung calculations.

5.2 Comparison with the Cascade Model

In this section the photoreaction cross-sections predicted by the cascade model are compared, in two separate ways, with the measured data. Firstly, a direct comparison is made between the theoretical and experimental excitation functions and secondly the calculated cross-sections, folded with the virtual photon spectrum, are compared with the measured yield curves. It is known, following the discussion of the previous section, that the photoreaction cross-sections, obtained by a deconvolution of the E1 (SOBA) virtual photon spectrum from the experimental yields, are reasonable representations of the true reaction cross-sections. The systematic uncertainty of about 10% affects only the relative magnitude of the measured and calculated quantities. For the present purposes a total photon absorption cross-section of 17 mb has been assumed in the calculations in accordance with measurements made on other heavy nuclei at these energies (Section 1.2.2). This corresponds to a Levinger parameter of $\sim$ 6.4 as discussed in Section 4.2. The yield curves and excitation functions predicted by the cascade model are compared with the experimental data in Figures 5.9, 5.10 and 5.11. The cascade results were found to poorly predict the overall strengths of the individual decay channels and for ease of comparison an arbitrary normalisation has been applied to the theoretical curves in each of these figures. Reasons for this disparity are suggested later.

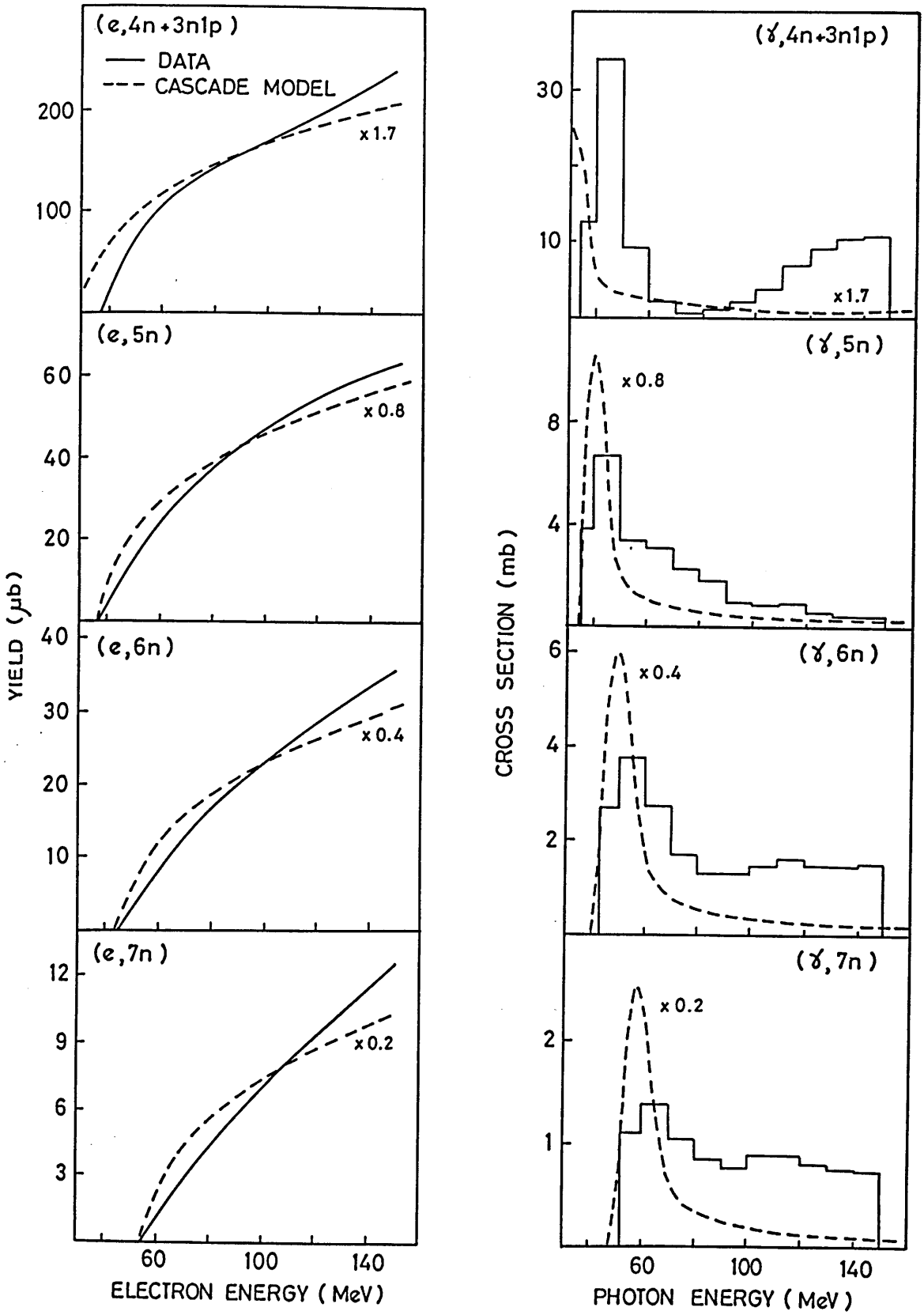

Figure 5.9: Comparison of the measured (γ,xn0p) yields (left) and excitation functions (right) with those predicted by the intranuclear cascade model. The cascade results have been multiplied by an arbitrary normalisation factor to allow clearer comparison.

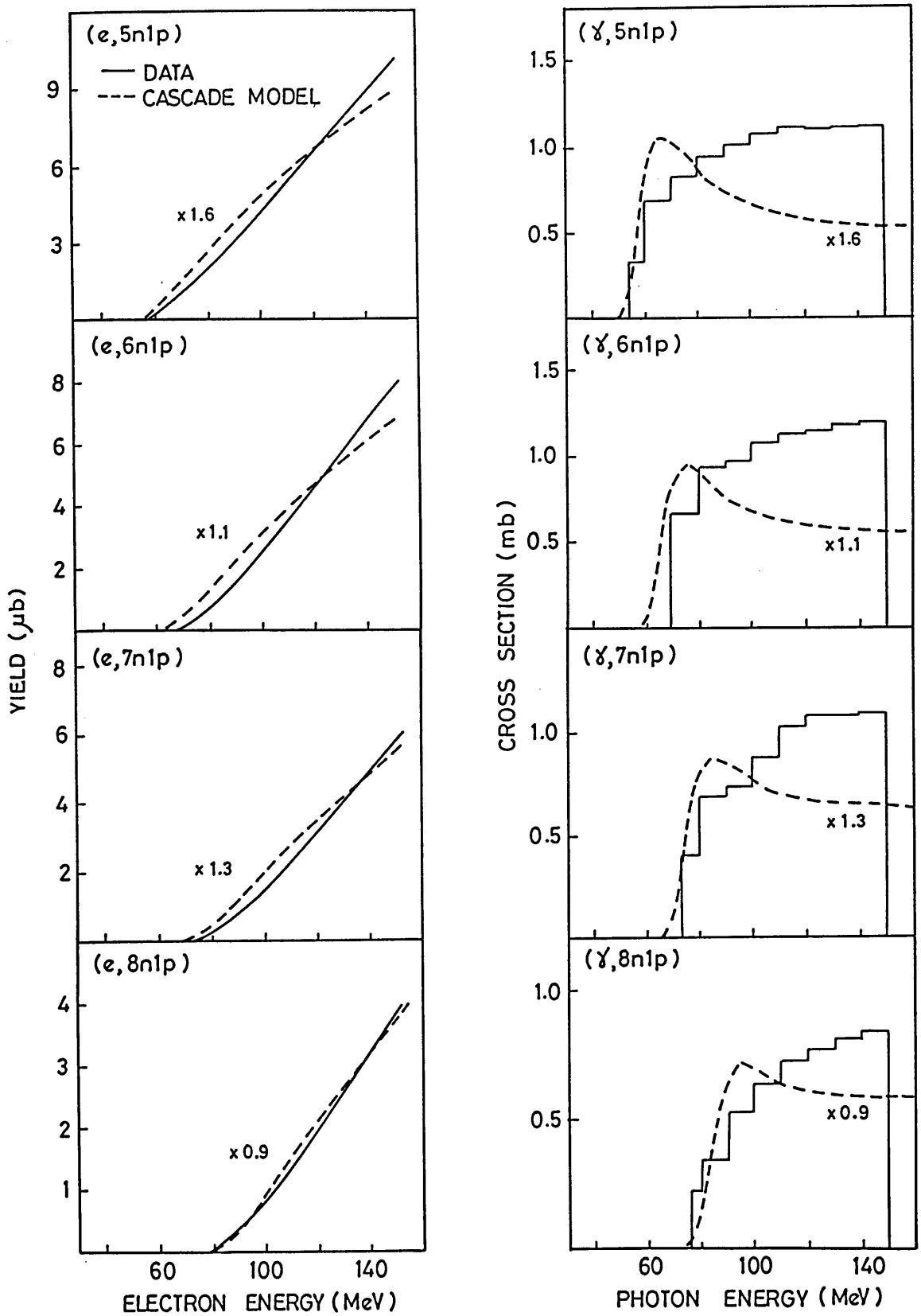

Figure 5.10: Comparison of the measured (γ,xn1p) yields (left) and excitation functions (right) with those predicted by the intranuclear cascade model. The cascade results have been multiplied by an arbitrary normalisation factor to allow clearer comparison.

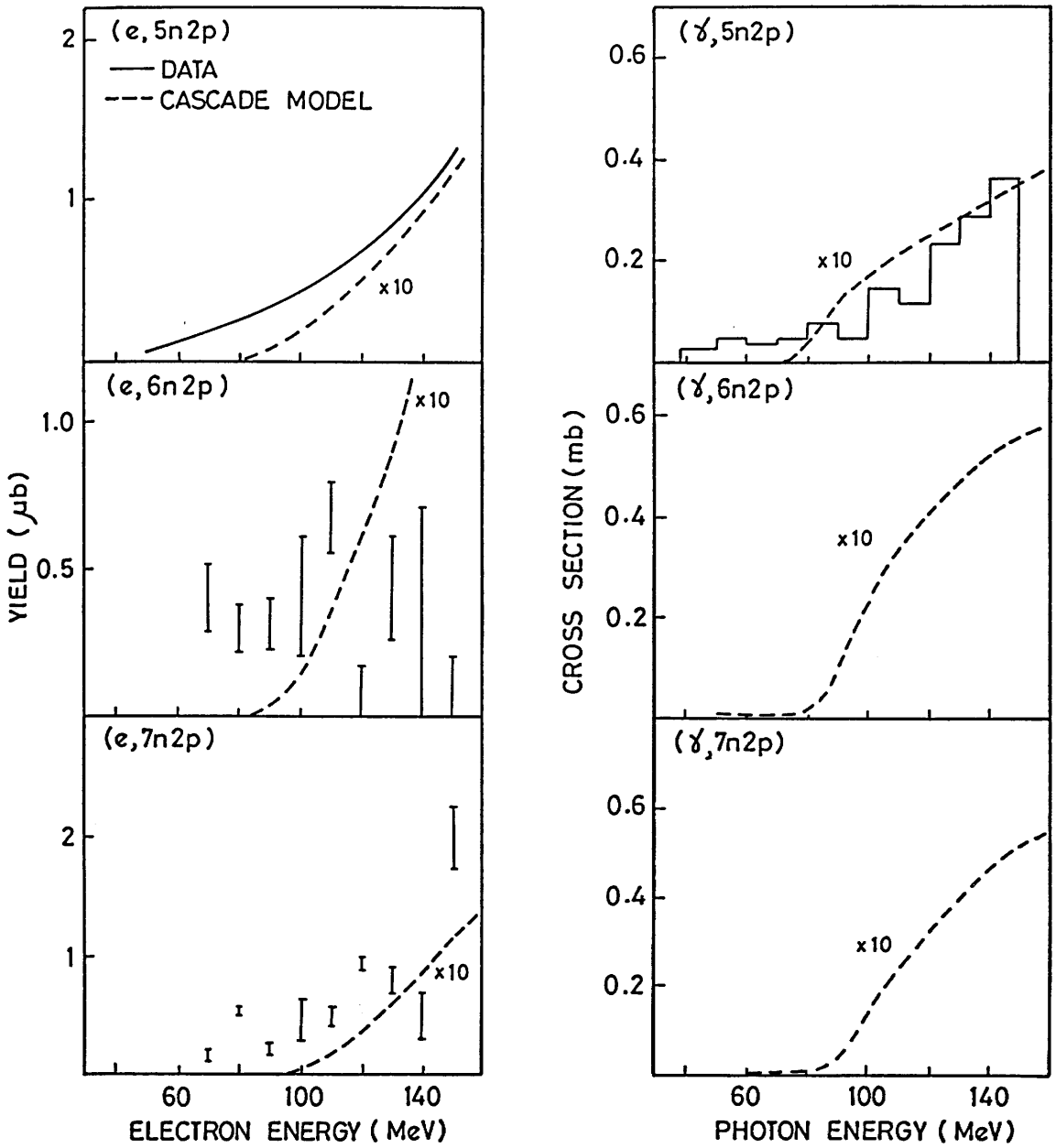

Figure 5.11: Comparison of the measured (γ,xn2p) yields (left) and excitation functions (right) with those predicted by the intranuclear cascade model. The cascade results have been multiplied by an arbitrary normalisation factor to allow clearer comparison.

In the case of the $(\gamma, 4n + 3n1p)$ reaction, the peak in the theoretical cross-section lies at a different energy than the measured peak and unlike the other decay channels the calculated and apparent reaction thresholds are in substantial disagreement. The low threshold value associated with the theoretical yield curve may be due to an incorrect treatment of shell effects (pairing terms etc.) in the PICA calculation. However as this was the only reaction investigated where the natural thorium background had to be subtracted from the photon induced activity, some suspicions must arise regarding the accuracy of this correction. While the background contribution to the measured yield was negligible at most of the end-point energies considered (Section 3.4), it was precisely at those energies near the reaction threshold that such corrections became important. Although none has been found, a systematic error in the subtraction process might conceivably be responsible for the observed discrepancy in the reaction thresholds. It would be useful to obtain measurements below 40 MeV to verify the position of this reaction threshold and to test for the large strength predicted there by the cascade model. Unfortunately this was the only reaction investigated which had an energy threshold below the lowest electron energy available from the LINAC and so at present it remains uncertain whether the model prediction of the $(\gamma, 4n)$ reaction threshold is too low or whether the experimental value, based on the trend of the lowest energy yield points, is erroneously high. No such doubts surround the other measurements, however.

The threshold related peaks in the remaining $(\gamma, xn0p)$ excitation functions are smaller and much broader than those predicted by the cascade model and appear to diminish with increasing x. Their high energy tails are also more prominent. It is these effects which also cause the cascade-model yield curves to rise too rapidly from threshold and to level off more quickly than the corresponding experimental values. The large peak in the theoretical cross-section, which

is generally the signature of a statistical evaporation process, suggests that particle emission from the compound nucleus stage of the nuclear de-excitation process is overestimated. In reality, a smaller and broader 'evaporation' peak is observed, probably due to the enhanced emission of fast particles from the precompound stage of the nuclear decay each of which remove, on average, more excitation energy than would a statistically evaporated neutron. If this is so and if only a moderately excited nucleus remains behind (from which fewer neutrons can be evaporated), it is reasonable to expect that the $(\gamma, x\mathrm{n})$ reaction cross-sections will indeed have strength over a much wider range of excitation energies. In addition, statistical evaporation alone can not account for the high energy tails observed in these reaction cross-sections where at least one of the emitted particles must remove a large amount of the available energy. It is clear that a substantial increase in the precompound particle emission probability is required in the cascade code if this model is to account for the measured $(\gamma, x\mathrm{n})$ cross-sections, which remain finite even to quite large photon energies.

In the $(\gamma, x\mathrm{n1p})$ channels, the cascade calculations still show signs of a peak just above threshold which is clearly absent in the measured data and once again underestimate the strength of the cross-section at high energies. Since proton emissions occur only at the precompound stage of the cascade calculation (Section 4.2) and with a large range of kinetic energies, the theoretical cross-sections do in fact have broader peaks and larger high energy tails than before but it still appears that the low energy evaporation contributions to the nuclear de-excitation process are overemphasised.

Despite the large uncertainties associated with the $(\gamma, x\mathrm{n2p})$ reaction channels it appears that two proton emission is significantly greater than the low value predicted by the cascade model. Once again this points to an underestimation of fast particle emission and to an overemphasis of compound nucleus

production.

For the $(\gamma, x\mathrm{n0p})$ channels in particular, a large discrepancy was observed between the magnitudes of the calculated and measured reaction cross-sections neccessitating some arbritrary normalisation in order to make a visual comparison of their shapes. The behaviour of this normalisation factor indicates that the cascade model increasingly overestimates the strength of each decay channel as the number of emitted neutrons becomes larger. This can almost certainly be attributed to a neglect of fission competition (Section 1.2.3), the probability of which is known to increase with successive neutron evaporations (multi-chance fission). Since the fraction of particle emission chains which end in fission $(\gamma, x\mathrm{n}y\mathrm{p}f)$ becomes larger with x, the number of residual nuclides produced by the corresponding non-fission channel $(\gamma, x\mathrm{n}y\mathrm{p})$ is depleted. The effects of fission competition appear to be less severe for the $(\gamma, x\mathrm{n1p})$ decay channels, probably due to the reduced Coulomb energy [165] associated with the nucleus after precompound proton emission which renders it less fissile.

Limitations of the Cascade Model

In addition to the confinements imposed by the omission of fission competition, the cascade-evaporation model of the photonuclear interaction has been shown to have some serious limitations regarding the criteria by which precompound fast particle emission is governed. This may be due to an oversimplified treatment of the nuclear transmission probabilities which are assumed, in the present formulation, to be energy-dependent step-functions. In reality these functions vary smoothly with energy and are highly angular momentum dependent [19].

It is also possible, due to the neglect of angular momentum considerations, that the multiplicity of neutrons released from the compound nucleus stage is

overestimated. Although the initial interaction will generally populate states of low angular momentum **J** (E1 transitions tending to dominate the photon absorption process), with successive particle emissions the value of **J** will spread out. A large angular momentum barrier for neutron emission can be built up when states of high **J** are populated and at this stage γ and α emission (as well as fission) become competitive modes of decay [176]. If a significant amount of the nuclear excitation energy is removed via γ-ray emission then this might also contribute to the broadened peaks and high energy tails observed in the measured cross-sections.

5.3 Comparison with the Exciton Model

A comparison is made here between the measured photoreaction cross-sections and those predicted by the hybrid exciton model. The yield curves and excitation functions are compared in Figures 5.12 and 5.13 for those channels where theoretical results are presently available. The theoretical values were obtained using a two-particle,one-hole initial exciton configuration to represent quasi-deuteron photon absorption after which the two holes remain strongly correlated in momentum (Section 4.3). The mean free paths used here were based on the Pauli corrected values derived for nucleons in nuclear matter by Kikuchi and Kawai [167], but doubled to compensate for the longer mean free paths experienced by nucleons in the diffuse nuclear surface. This averaged value, referred to here as the 'standard mean free path', forms part of the standard parameter set for this code and is an attempt to simulate some of the geometrical properties of the nucleus which are not included explicitly in the hybrid formulation. Once more the total photon absorption cross-section has been taken to be 17 mb over the energy range of interest but this value requires experimental verification before any useful comment can be made regarding

relative magnitudes of the measured and calculated reaction cross-sections.

Although the peaks in the calculated excitation functions do appear to be marginally broader than in the previous calculation and the high energy cross-sections slightly larger, it appears that the exciton model, with this basic parameter set, is not much more successful at reproducing the individual cross-section shapes than the intranuclear cascade model. However there is no longer any need to normalise each channel individually and this rather important improvement over the cascade model can almost certainly be attributed to the inclusion of fission competition in the evaporation chain of the compound nucleus. The fission parameters used in the present calculations (Section 4.3) were assumed, in absence of better information, to be equal to those obtained from photofission measurements in the giant resonance region. The variation with x of the individual $(\gamma, xnyp\overline{f})$ reaction cross-sections is reproduced well by the present model and suggests that the extrapolation of low-energy fission parameters to the present range of nuclear excitations is reasonably valid.

Calculations performed with 2p-2h (normal quasi-deuteron) or 1p-1h (single particle absorption) initial configurations give rise to results which are not substantially different from those shown. This is basically due to the fact that, for the reactions measured, the features of the calculated cross-sections are dominated by compound evaporation decay rather than pre-equilibrium particle emission. However the measured cross-sections imply that precompound effects have a much greater influence upon the decay mechanism than is suggested by current models and an improved treatment of the final-state interactions might still yield valuable information regarding the initial absorption process.

Limitations of the Exciton Model

The most obvious limitation of the exciton model is that it does not allow for

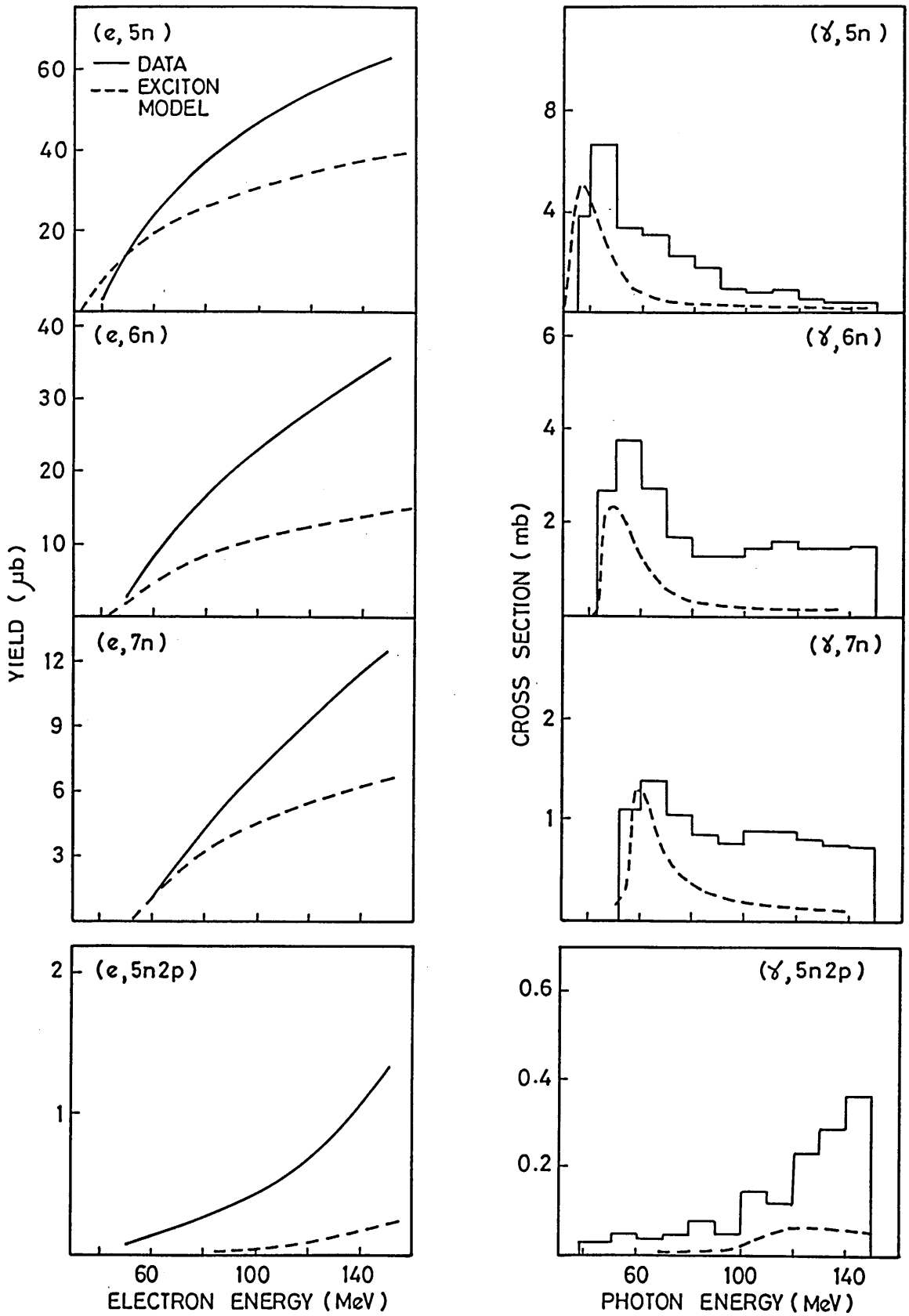

Figure 5.12: Comparison of the measured yields (left) and excitation functions (right) with those predicted by the hybrid exciton model. An initial exciton configuration of (2p,1h) has been assumed here with a standard value for the mean free path of nucleons in nuclear matter (1 × standard m.f.p.). A constant total absorption cross-section of 17 mb was used in the calculation.

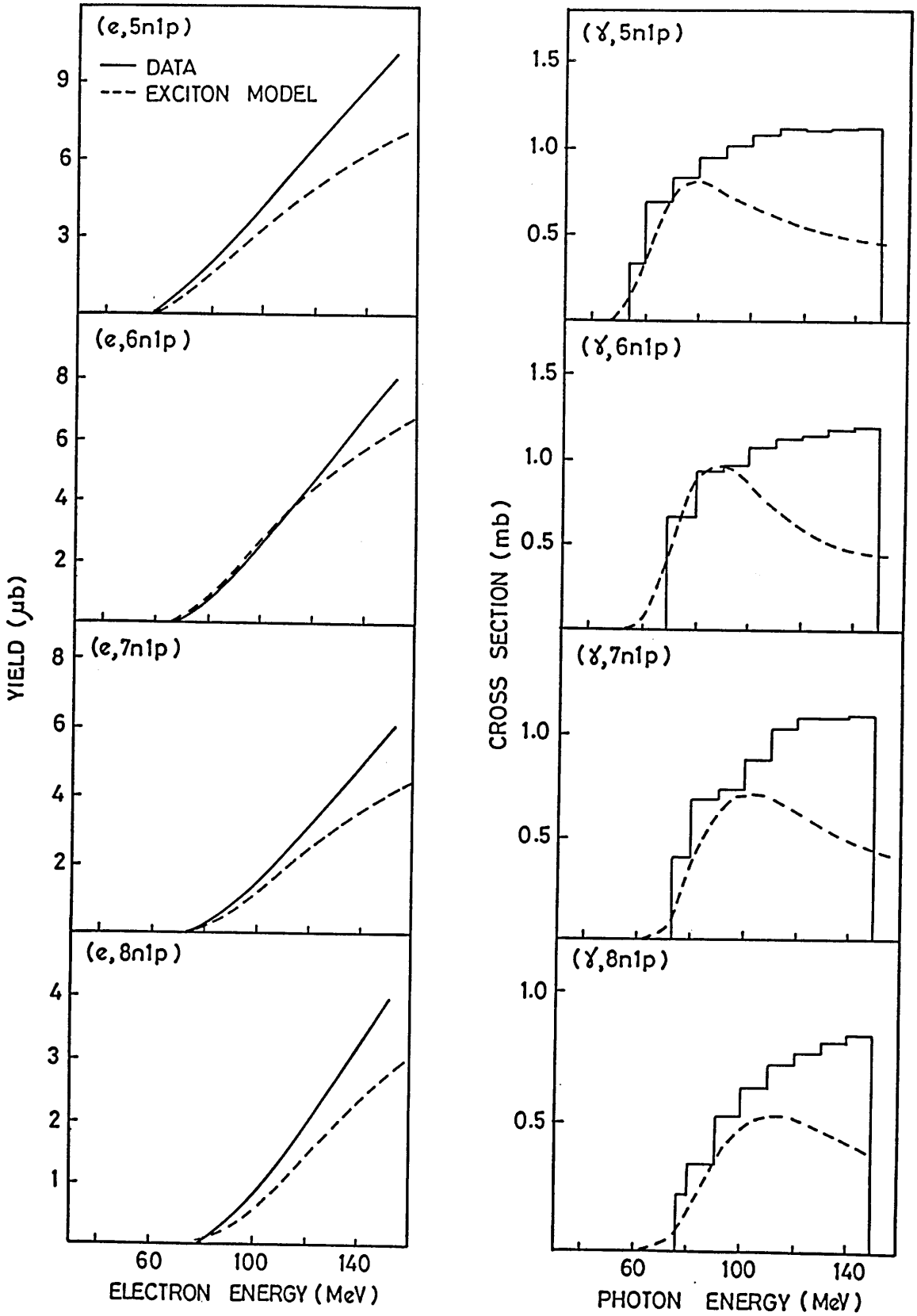

Figure 5.13: Comparison of the measured yields (left) and excitation functions (right) with those predicted by the hybrid exciton model. An initial exciton configuration of (2p,1h) has been assumed here with a standard value for the mean free path of nucleons in nuclear matter (1 × standard m.f.p.). A constant total absorption cross-section of 17 mb was used in the calculation.

the clear dependence of the outcome of the intranuclear de-excitation process upon the location of the initial interaction within the nucleus. Only average parameters, describing the mean behaviour of nucleons at all positions in the nucleus, are introduced. By adjusting the model parameters (m.f.p.'s etc.) to obtain the correct averaging, the exciton model has proved very successful in reproducing the experimental data for nucleon induced reactions (Section 1.4). Although the nuclear excitation mechanism is intrinsically different, the same basic parameter set has been used in the few cases (including the present one) where this model has been applied to the problem of photonuclear interactions. It is clear however, that there are some important differences between the two processes and these should be incorporated, if possible, into the hybrid model if it is to provide a physically well founded fit to the photoreaction data. The remainder of this section explores some of the possible reasons why the hybrid model, with its present parameterisation, tends to underestimate precompound particle emission in photon induced reactions.

For example, the first interaction of a nucleon projectile is likely to occur near the nuclear surface whereas the high transparency of nuclear matter to γ-rays suggests that photon absorption will occur homogeneously throughout the nuclear volume. Unless the effects of Pauli blocking lead to an enhancement of surface interactions, it would appear at first as if the precompound particle emission probabilty associated with photonuclear interactions should actually be *lower* than that for nucleon induced reactions. However in the latter case the excited nucleon pair from the primary interaction are scattered, on average, towards the nuclear centre owing to the large linear momentum carried by the projectile. This forward focussing of the two fast particles into a region of high nuclear density does in fact favour additional two-body scattering rather than emission into the continuum. The same mean free paths which reproduce the

nucleon induced reaction data may therefore be inappropriate to the photon absorption process if the average directions of the initially excited nucleons are significantly different from this. Indeed that is precisely the case, since the low momentum introduced by the photon implies that no such forward peaking should occur. In fact to conserve momentum, the initially excited particles will move in almost opposite directions and, in general, at least one of the particles will have a trajectory which actually favours emission. A longer mean free path might therefore be considered to simulate, to some degree, the lower average collision rate experienced by these nucleons following photon absorption.

Figures 5.14 and 5.15 show the yields and cross-sections obtained from the hybrid model when the mean free path is set to twice its standard value. By doubling the mean free path, some strength is indeed shifted towards the higher photon energies as precompound emission is increased, but this rather simple method of incorporating, into the phase space calculation, some geometrical properties of the intranuclear cascade is clearly insufficient to remove the large disparity between theory and experiment. The larger mean free path serves mainly to alter the strengths of the individual reaction cross-sections and changes their overall shapes very little. This points perhaps to an inaccuracy in the energy dependence of the intranuclear transition rate $\lambda_+(\epsilon)$ (Equation 4.12) rather than in its magnitude, which is merely scaled by altering the mean free path. The energy dependence of this important parameter should clearly be the subject of further investigation.

Another part of the nuclear excitation process where nucleon and photon induced reactions are expected to differ is the way in which the available energy is partitioned between the initially excited nucleons. In the present exciton model description of quasi-deuteron photon absorption, the initial (2p-1h) exciton configuration is essentially the same as that used for nucleon induced

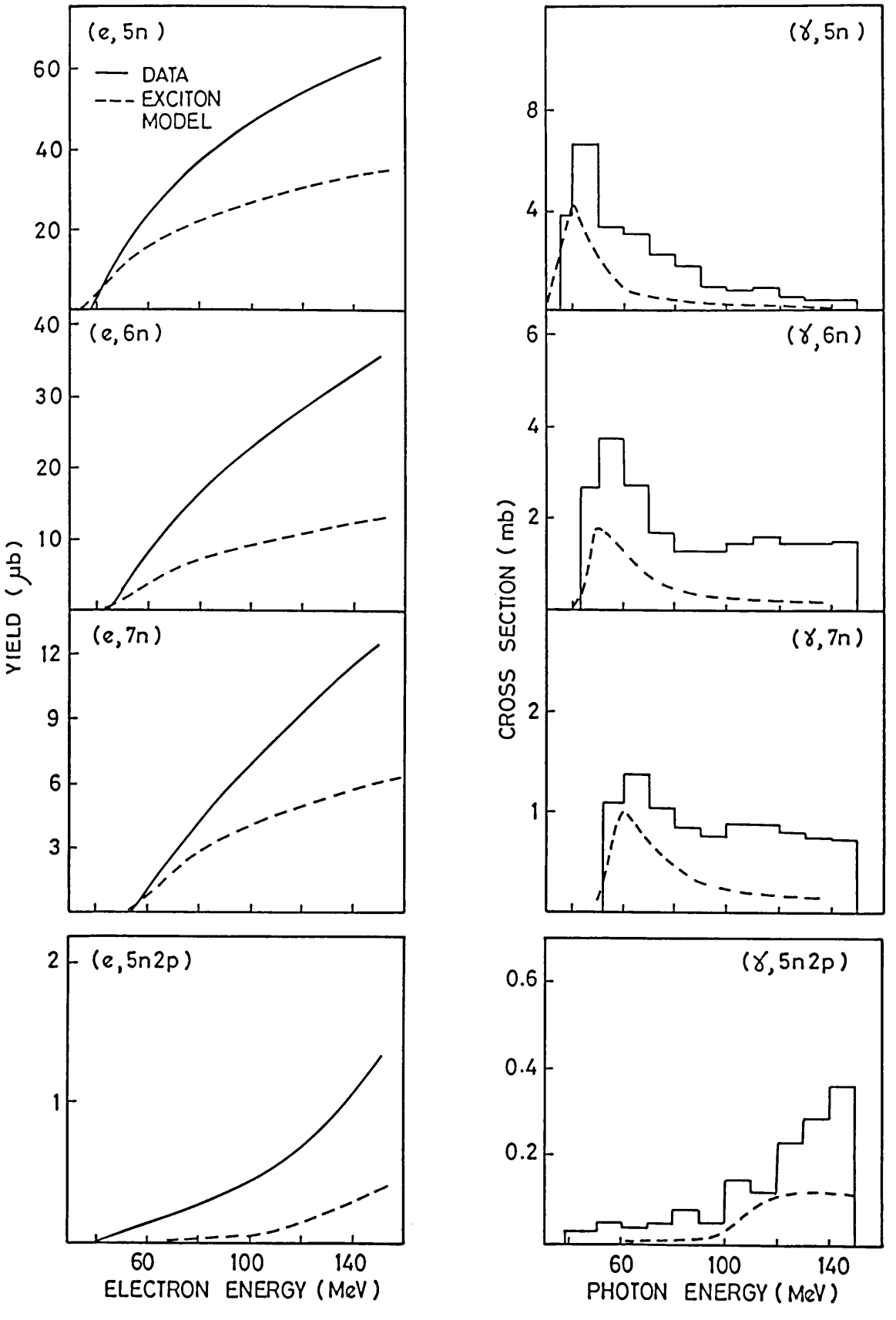

Figure 5.14: Comparison of the measured yields (left) and excitation functions (right) with those predicted by the hybrid exciton model. A mean free path equal to *twice* the standard value for nucleons in nuclear matter is used here.

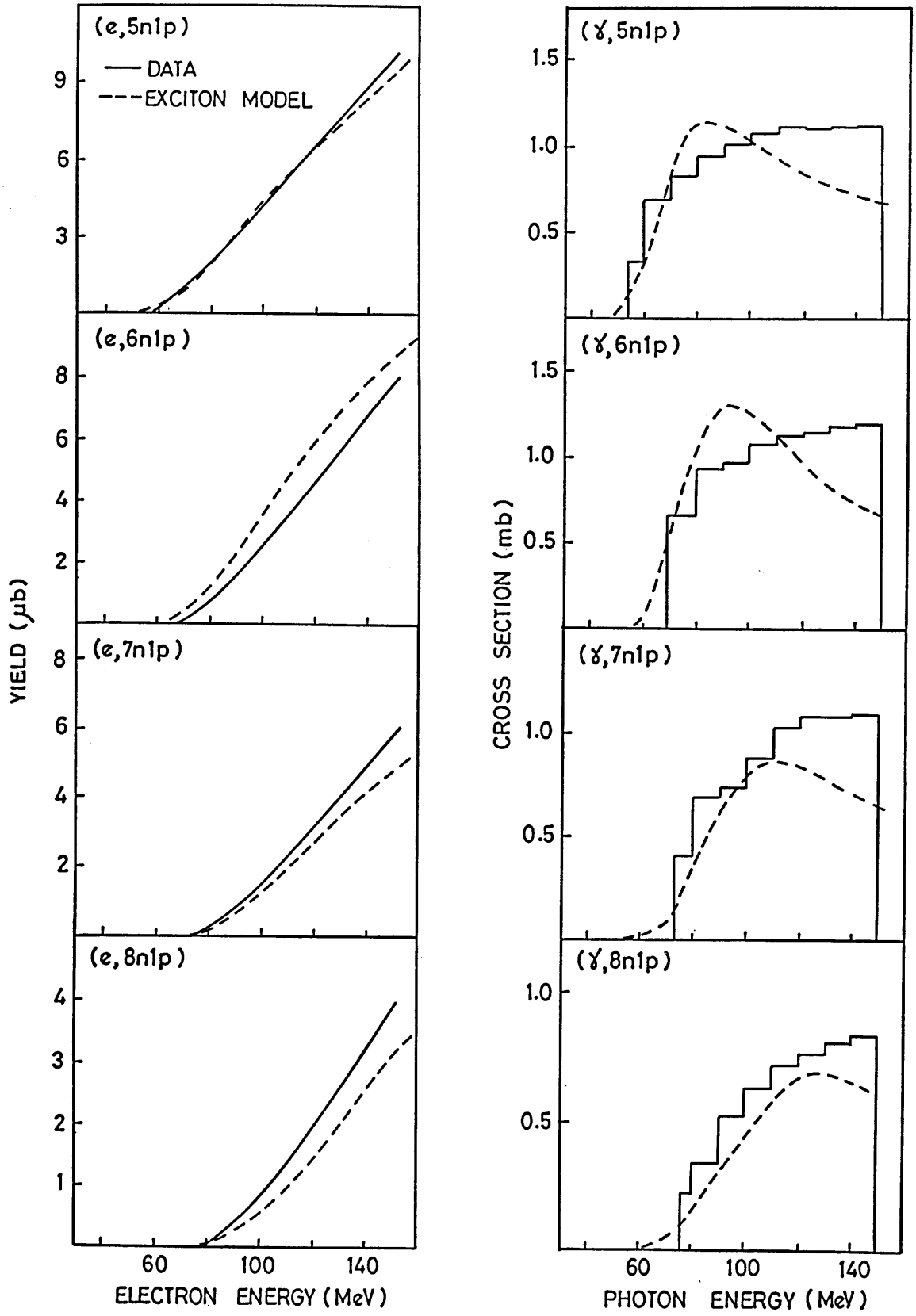

Figure 5.15: Comparison of the measured yields (left) and excitation functions (right) with those predicted by the hybrid exciton model. A mean free path equal to *twice* the standard value for nucleons in nuclear matter is used here.

reactions. However, for reasons of momentum conservation, the absorption of a photon on a quasi-deuteron might be expected to lead to the preferential excitation of particle-hole pairs which share the available excitation energy in an approximately equal fashion. This rather fundamental departure from the continuous energy distribution expected for nucleon induced reactions may produce a large alteration in the precompound emission of fast particles. Unfortunately it is not incorporated into any of the presently used hybrid model formulations.

Any suggestion, that the dissimilarity of the experimental and theoretical cross-section shapes might be attributed to an incorrect virtual photon spectrum, is dispelled by a comparison of the model calculations to the real photon bremsstrahlung data. The cascade and exciton model cross-sections have of course firstly to be folded with the bremsstrahlung photon spectrum. Figure 5.16 shows that a disparity, identical to that observed with the electrodisintegration data, arises between the experimental bremsstrahlung yields and their calculated equivalents. The structure of the original cross-sections therefore appears to be quite genuine and this points to some serious failings in the present photodisintegration models.

5.4 Conclusions

It was described in this chapter how the quasi-monoenergetic photoreaction cross-sections were unfolded from the measured electrodisintegration yield functions. Uncertainties in the virtual photon intensity did not affect, to any great extent, the shapes of these excitation functions but led only to a systematic error of $\sim$ 10 % in their overall magnitudes. Current photodisintegration models were shown to predict, with only modest accuracy, the form of the measured cross-sections and to underestimate the emission probability of those fast particles which arise in the early stages of the photo-excitation process. The

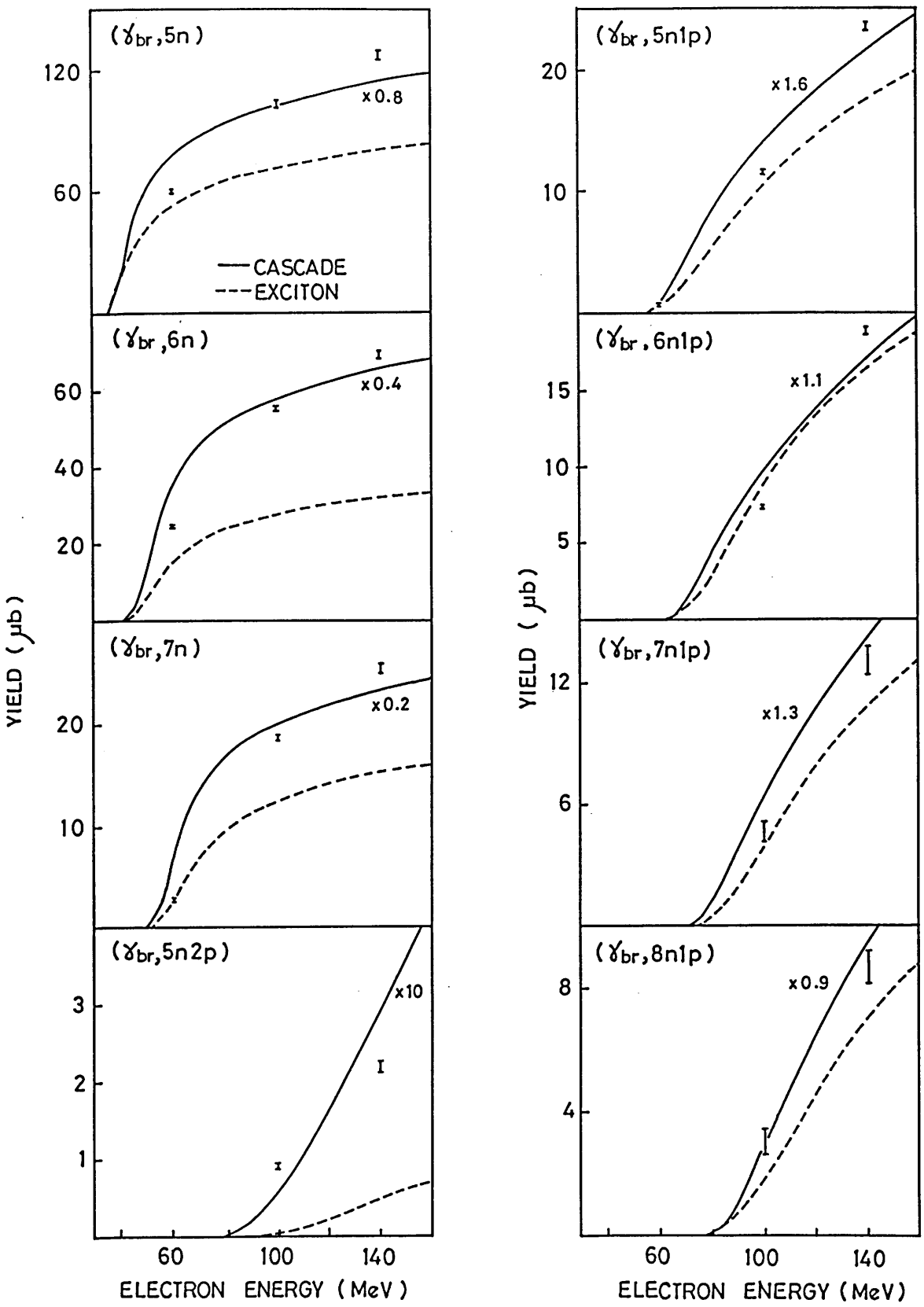

Figure 5.16: Comparison of the measured bremsstrahlung yields with those predicted by the cascade and exciton models. A disparity, similar to that observed for the electrodisintegration yields, exists here between the experimental and theoretical values. The calculated curves rise too rapidly from threshold and level off more quickly than the measured data. The exciton results shown here were obtained using the standard value for the mean free path.

consequent overemphasis of compound nuclear evaporation predicts too large a peak in the (γ, xn) excitation functions near threshold and leads to a general underestimation of the cross-section strengths at high energies. The assumption made in current calculations, that the nuclear de-excitation process can be divided into precompound and compound stages, where one (or only a few) *fast* particles are released followed by a larger number of statistically evaporated neutrons, may not be realistic. It would therefore be useful to measure the total energy spectra of particles emitted from heavy nuclei as a check of this distribution.

In a comparison of the experimental and theoretical excitation functions, it was clearly shown that present photodisintegration models have some serious failings. In the cascade model for example, a very primitive treatment is given to nuclear transmission coefficients and all competition due to fission is ignored. To include realistic transmission functions, a description of the intranuclear cascade will be required which incorporates the angular momentum of the evaporated particles and the residual nuclear system. Fission competition, which was shown to be of great importance for ^{232}Th is, on the other hand, treated well in the hybrid exciton model. However, this model does not include important geometrical features of the intranuclear cascade which affect the emission probabilties of nucleons at the precompound stage of the calculation, and neglects others which are specific to the case of photonuclear interactions. These include, for example, the energy distribution and opening angle of the initially excited particles. In order to obtain information about the photon absorption mechanism in heavy nuclei, which is in principle possible from the present results, a much more sophisticated treatment of the cascade process will have to be introduced into the theoretical models.

Since some of the reactions investigated here involve charged particle emis-

sion, and are not therefore strictly evaporative, the current data set should be particularly useful for assessing any improvements made to the theoretical treatment of the intranuclear cascade. Where comparison is possible, the main difference between the $(\gamma, x\mathrm{n})$ and $(\gamma, (x-1)\mathrm{n1p})$ excitation functions does in fact appear to be the existence (or not) of an evaporation-type peak. The high energy behaviour in the two sets of cross-sections appears to be very similar. The simplest interpretation of this would be that the de-excitation of a heavy nucleus proceeds in a small fraction of cases by the emission of a fast particle (either a neutron or a proton) followed by the evaporation of a few low energy particles (neutrons only) while in most cases, all of the fast particles are captured and a compound nucleus formed without prior emission. Only the former process contributes to the $(\gamma, x\mathrm{n1p})$ channels since the Coulomb barrier acts as a filter of low energy protons. The results for these channels are therefore sensitive to the precompound part of the model calculations and are not 'swamped' by compound nucleus effects.

The present results indicate that the total absorption cross-section for ^{232}Th might perhaps be larger than the projected value of 17 mb used in the calculations. However with such a poor correlation observed between the measured and calculated reaction cross-sections, it is impossible at this stage to extrapolate the small number of channels investigated here to a total summed value. Clearly it will be possible to extract more precise information from the present data, regarding the distribution of strength among the various decay channels, when measurements become available of the total photon absorption cross-section for thorium. It must also be verified that there is no strongly rising trend in the total cross-section which might be responsible for the large photoreaction strengths found at the higher energies.

The reaction cross-sections measured in the present experiment, in conjunc-

tion with improved nuclear cascade models, will provide a useful test of our understanding of both the nucleon-nucleon interactions which occur during the intranuclear cascade process and the initial interaction mechanism which governs photonuclear absorption at high energies.

Chapter 6

Summary

6.1 Summary and Future Work

This study of the electro- and photodisintegration of ^{232}Th, at energies between the giant resonance and the pion threshold, has provided new data on the cross-sections for multiple nucleon emission in heavy nuclei following high energy photo-excitation. In addition to the $^{232}\mathrm{Th}(\gamma, x\mathrm{n})$ decay channels it has also been possible to measure cross-sections for reactions of the type $(\gamma, x\mathrm{n}y\mathrm{p})$ which involve the emission of one or more charged particles. This improvement over previous activation experiments, where only the photoneutron channels could be measured, was achieved by monitoring the residual activity of those reaction products which decayed by α-emission. By using the natural radio-activity of the thorium to determine the density of target nuclei, the usual uncertainties surrounding the target thicknesses and detector solid angle have also been much reduced.

In the course of this experiment, improved half-life values were obtained for several of the actinide nuclides investigated. The results of this work have since been published in Reference [177].

Current precompound plus evaporation models were found to predict poorly the shapes of the measured photoreaction cross-sections and to reproduce only the most general features of the photodisintegration process. This has been

attributed mainly to an underestimation of fast particle emission at the precompound stage of the nuclear de-excitation. In the intranuclear cascade model this is principally due to a poor treatment of the interactions of the initially excited nucleons and an improved formulation, with realistic angular-momentum dependent transmission functions, has been suggested. The value and energy dependence of the mean free path of nucleons in nuclear matter, which determines the average collision rate for high energy particles within the nucleus and their emission rate from the early stages of the intranuclear cascade, is also uncertain and further experimental and theoretical investigations of this parameter are needed. It is also possible that the computational treatment of the precompound stage of the intranuclear cascade is arrested too quickly in this model; a measurement of the particle energy spectra from photo-excited heavy nuclei would be useful in assessing the relative importance of the compound and precompound particle emission processes. The available version of the model also fails to account for the effects of multi-chance fission, which was seen to be an important and competitive mode of decay in the evaporation chain of the excited compound nuclei. Fission competition was found to affect principally the $(\gamma, x\mathrm{n})$ photoneutron decay channels, probably due to the reduced Coulomb energy and hence lower fissionability associated with the proton deficient nuclei which follow precompound charged particle emission. The exciton hybrid model on the other hand, by incorporating a Bohr-Wheeler prescription for the fission competition, was found to account well for the depletion in strength of these channels. Although the fission parameters assumed in this model were evaluated from giant resonance data, their extrapolation to the present range of photon energies appears to be of reasonable validity. However, the exciton model suffers from the same uncertainties surrounding the nuclear mean free path as the cascade model and once again appears to

underestimate the emission probability for fast particles. A simple reduction of the intranuclear collision rate did not substantially improve the calculation and this concentrates suspicion on some important geometrical features of the intranuclear cascade and nuclear model which are not incorporated explicitly in the phase-space formulation. For instance, little or no allowance is made in the present exciton model for the directions of the initially participating nucleons, at least one of which will have a trajectory which favours emission. Nor has the possibility been investigated that the photon might be preferentially absorbed in a region of less than saturation density (i.e. nearer the nuclear surface) and therefore lead to the enhanced emission of nucleons excited early in the intranuclear cascade. It is hoped that such features can be incorporated in some way into the exciton formulation, perhaps by developing a 'geometry dependent hybrid' model analagous to that used for nucleon induced reactions. This would allow the physics surrounding the photon-nucleus interaction and many of the ideas outlined above to be more rigorously tested. A cascade model with realistic transmission functions and fission competition might also furnish such an investigation since it would contain most of these geometrical features intrinsically. However, since angular momentum information must then be retained, the present code is totally unsuitable for such a modification. Due to the Monte Carlo nature of the computations, such calculations may anyway prove to be too expensive in terms of computer time.

In a comparison of the electron and bremsstrahlung induced yield curves, it was noted that either an anomolously large contribution of E2 transitions or a reduction in the E1 virtual photon intensity was required to explain both the real and the virtual photon data. It is most likely that the virtual photon spectra used in the present investigation are slightly in error, although still much improved over previous calculations. These spectra, which were calculated in

second order Born approximation and therefore include an incomplete treatment of nuclear charge effects, may underestimate the true virtual photon intensity in nuclei as heavy as thorium. It is hoped that a full distorted wave treatment of the virtual photon spectrum, which incorporates both nuclear size and charge effects to all orders, will be available in the near future. It should then be possible to assess properly the importance of multipole contributions other than E1 in photonuclear processes above the GDR.

With the present rather unsatisfactory correlation between experimental and theoretical cross-sections, it has not been possible to extrapolate from the small number of photoreaction channels investigated here to obtain an overall value for the total photo-absorption cross-section. It would be useful therefore to gather excitation functions for some of the missing ^{232}Th$(\gamma, xnyp)$ reaction channels, perhaps by measuring the residual γ-ray activity of β-decaying reaction products. In the meantime it is hoped that the ^{232}Th total absorption cross-section can be measured independently, perhaps as part of the systematic study of actinide nuclides currently being performed at Saclay, so adding a further constraint into the photodisintegration calculations. The validity of the constant cross-section assumed in the hybrid model would also be checked by such a measurement. In addition it would be a reliable check of the present results if some of the individual excitation functions could also be measured with mono-energetic photons, thereby avoiding the deconvolution of the photon spectrum necessary in the present analysis.

In conclusion, it is hoped that the reaction cross-sections measured in the present experiment can be used in conjunction with modified photodisintegration models to test some of the important physics of the photon-nucleus interaction.

Appendix A

Toroid Calibration

The toroid charge monitor was calibrated against an evacuated Faraday Cup which was placed in the beam-line near the exit of scattering chamber. The Faraday cup has a known efficiency [122] of 99.6 % and this allowed the 'true' electron beam charge to be determined. It could not itself be used as a charge monitor in the present experimental situation since sustained use at the beam currents involved would have led to melting.

Two identical Brookhaven integrators were employed in the calibration procedure, each of which outputs a single logic pulse for every 2×10^{-8} Coulombs of charge [1] received at its input. This conversion rate has been verified to ± 0.2 % using a Weston standard cell and precision resistor as an accurate current source. The output pulses were electronically scaled to determine the total charge collected by each integrator.

Using one integrator to accumulate signals from the Faraday cup and the other to monitor the toroid response (Section 2.3), the ratio of toroid to Faraday cup integrated charge ($Q_T : Q_{FC}$) was measured over a wide range of beam currents (0—20 μA). In terms of the *true* charge carried by the electron beam,

[1] The intrinsic conversion rate is in fact range dependent. The quoted value is for the current-meter range (2×10^{-6} full scale deflection) used in this experiment.

the absolute efficiency of the toroid system $\mathcal{E}_T$ becomes :

$$\mathcal{E}_T = \frac{0.996\ Q_T}{Q_{FC}}$$

The toroid efficiency was found to remain constant up to 20 μA (Figure A.1) with a mean value of

$$\mathcal{E}_T = 0.09252 \pm 0.00018$$

In practice, currents greater than 20 μA were never exceeded and a linear toroid response was always ensured.

Knowledge of the toroid efficiency allows a calibration constant C_B to be defined relating the *true* beam current to the digital output rate of the Brookhaven integrator. Combining $\mathcal{E}_T$ with the intrinsic conversion rate of the integrator yields a value for C_B of

$$C_B = (2.1617 \pm .0042) \times 10^{-7} \quad \text{Coulombs per logic pulse}$$

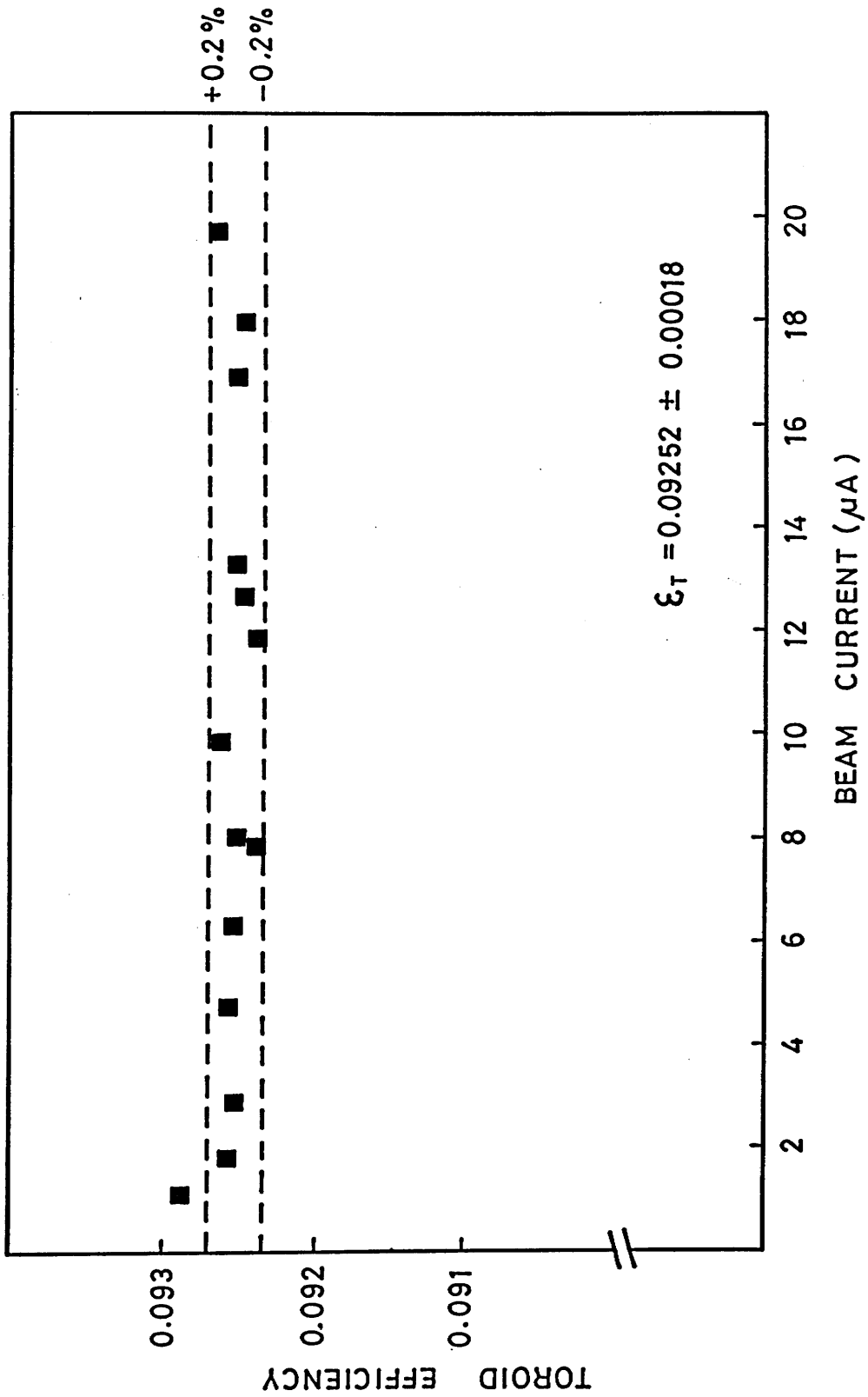

Figure A.1: Toroid Charge Monitor Efficiency

Appendix B

Contribution of Energy Losses in the Thorium Targets to Total Alpha Resolution

The large ionisation losses of α–particles in the target material (Table B.1) can easily dominate the energy resolution of the measured α–spectra. The reaction yield however, varies directly with the target thickness and must be large enough to provide statistically valid data. The relationship between target density and resolution was therefore examined in order to define an optimum target thickness.

When α–particles traverse an absorbing material, a 'straggling' width is introduced into the final energy distribution due to the statistical nature of the energy loss process [178]–[180]. The FWHM of this energy spread is $\sim$ 20% of the mean energy loss. However a more significant dispersion occurs when the absorber itself is the source of activity, as in the present case of an irradiated target, and the α–particles originate throughout the target volume. Each emergent particle suffers an energy loss which is proportional to its path-length in the absorber. If the maximum half-angle from source to detector (Section 2.6) is θ_m then the FWHM, ΔE, for the distribution of energy losses is

$$\Delta \mathrm{E} = \mathrm{E_T}\left[\frac{2}{1+\cos^2\theta_m}\right]^{\frac{1}{2}} \qquad (B.1)$$

α–Energy (MeV)	Stopping Power (keV/μg cm^{-2})
4	0.264
5	0.228
6	0.210
7	0.193
8	0.177
9	0.167
10	0.156

Table B.1: Stopping Powers of α–particles in Thorium [181].

where E_T is the energy lost crossing the full target thickness. The width of this function at $\theta_m = 45°$ is approximately $1.15 \times E_T$, and it is further broadened due to straggling. To maintain the resolution of 35 keV required in this experiment an upper limit of ~ 150 μg cm^{-2} was placed on the deposit thickness. In practice other factors were found to dominate the resolution and targets, very much thinner than this, were required.

Appendix C

Radiator Uniformity

The thickness uniformity of the tantalum radiator was verified using the apparatus of Figure C.1.a. The absorption-rate of low energy x–rays was monitored at several areas of the foil surface to examine local variations in the sample density. The transmitted photon flux, $I(d)$, through a sample of thickness d (mg.cm^{-2}) is given by :

$$I(d) = I_o \, e^{-\mu_m d} \qquad (C.1)$$

where I_o = incident photon flux
μ_m = mass absorption coefficient (cm^2.mg^{-1})

A 3.2 mm thick iron collimator with a 2 mm diameter aperture was used in conjunction with a 10 μCi ^{241}Am point source to produce a narrow beam of low energy photons (13.9 keV, k_α x–rays). The transmitted flux through the tantalum foil, in the region of the collimator aperture, was measured using a solid state germanium detector. (The incident flux I_o is the value measured with no absorber in position.) The foil was scanned in 2 mm steps along two adjacent diameters which were assumed to exhibit typical cross-sectional behaviour.

The quantity $\ln(I_o/I)$, which is proportional to sample thickness (Eqn. C.1), is shown as a function of surface position in Figure C.1.b. No serious irregularities in the sample thickness are evident above the statistical uncertainties of the measurement.

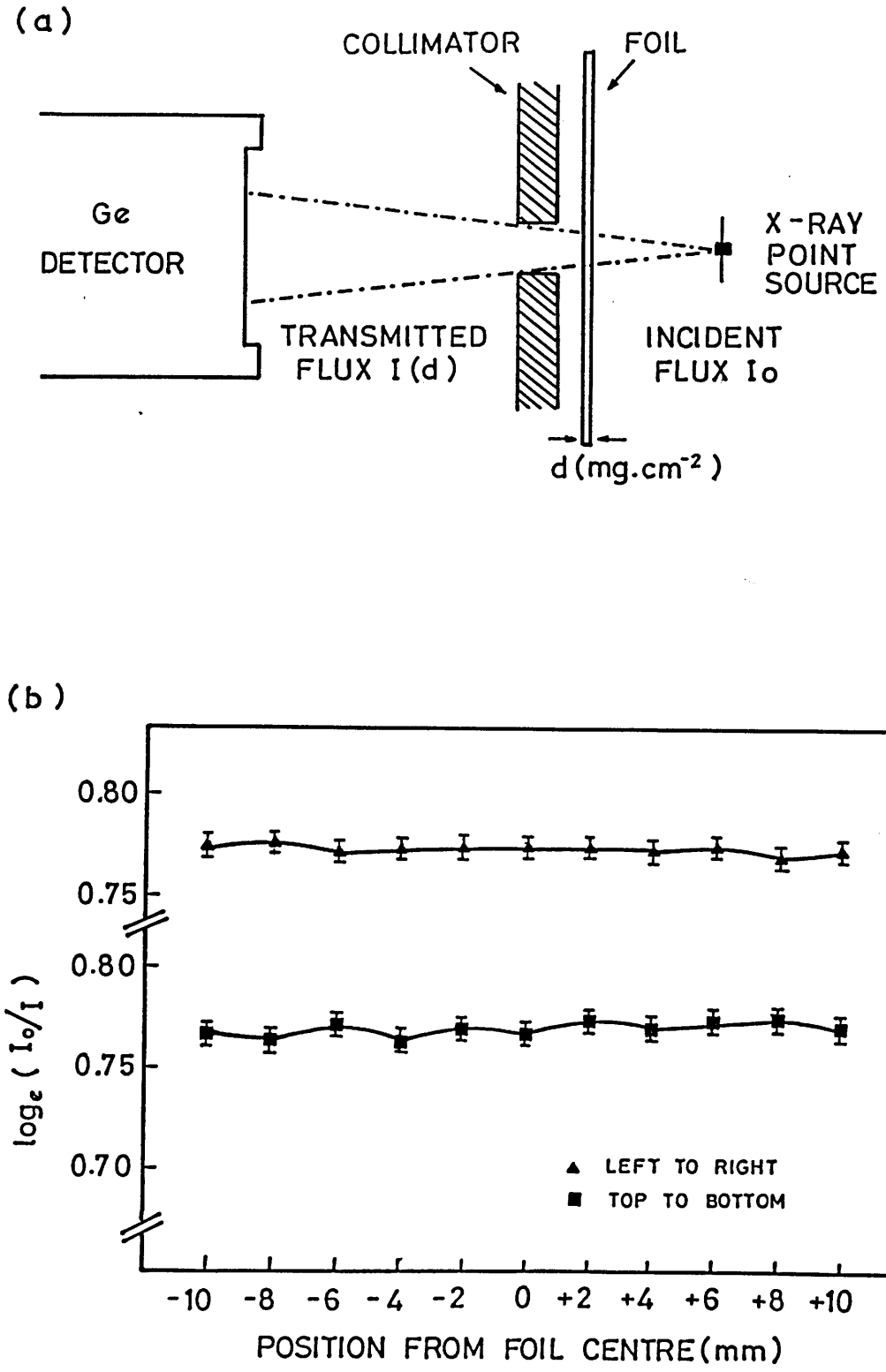

Figure C.1: (a) Schematic diagram of x–ray absorption apparatus. (b) Variation of $\ln(I_o/I)$, which is proportional to foil thickness, along two adjacent diameters of the tantalum radiator.

Appendix D

Effective Solid Angle

An 'effective' solid angle is defined for an extended source subtended by a circular detector. The total activity from a finite area may then be considered to emanate from a central point-source but with a reduced effective solid angle.

Figure D.1.a shows the geometry considered here, with positions expressed in cylindrical coordinates and all dimensions normalised to the detector radius. The solid angle subtended by a surface S (the detector's acceptance area) from a point P at (ρ, z) in the source plane, may be expressed [182] as :

$$\Omega_p(\rho, z) = 2\pi - 2z \int_0^{\pi} \frac{\mathrm{d}\phi}{\sqrt{z^2 + S_1^2}} \qquad \text{for} \quad \rho < 1 \tag{D.1}$$

where

$$S_1 = \rho \cos\phi + \sqrt{1 - \rho^2 \sin^2\phi} \tag{D.2}$$

For numerical intergration eqn. (D.1) is rewritten as :

$$\Omega_p(\rho, z) = 2 \int_0^{\pi} \left(\frac{S_1}{z}\right)^2 \left[1 + \left(\frac{S_1}{z}\right)^2 + \sqrt{1 + \left(\frac{S_1}{z}\right)^2}\right]^{-1} \mathrm{d}\phi \tag{D.3}$$

Thus, if N_T decays occur at a point (ρ, z) in the source plane, $N_T \Omega_p(\rho, z)/4\pi$ will be detected.

When the activity is spread over a finite area πa^2, the acceptance towards the edges is reduced. The solid angle contribution from an element $2\pi\rho.\mathrm{d}\rho$ in the source plane (Figure D.1.b) is :

$$\mathrm{d}\Omega = \frac{\Omega_p(\rho, z) 2\pi\rho.\mathrm{d}\rho}{\pi a^2} \tag{D.4}$$

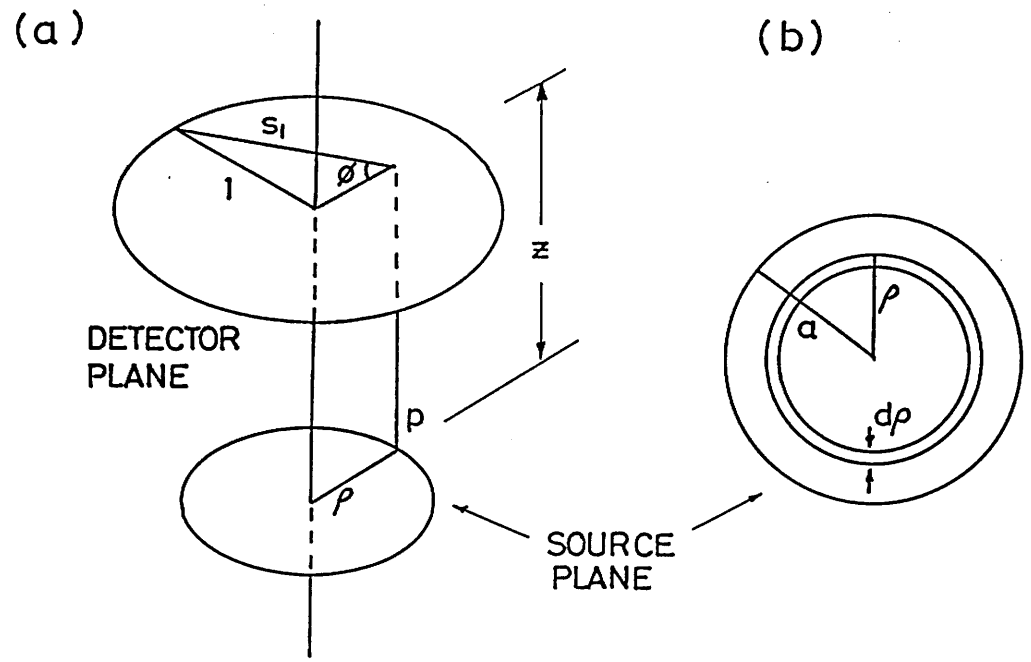

Figure D.1: Effective solid-angle formulation — all dimensions are normalised with respect to the detector radius. (a) Circular source and detector in parallel planes with a common central axis. (b) Source plane.

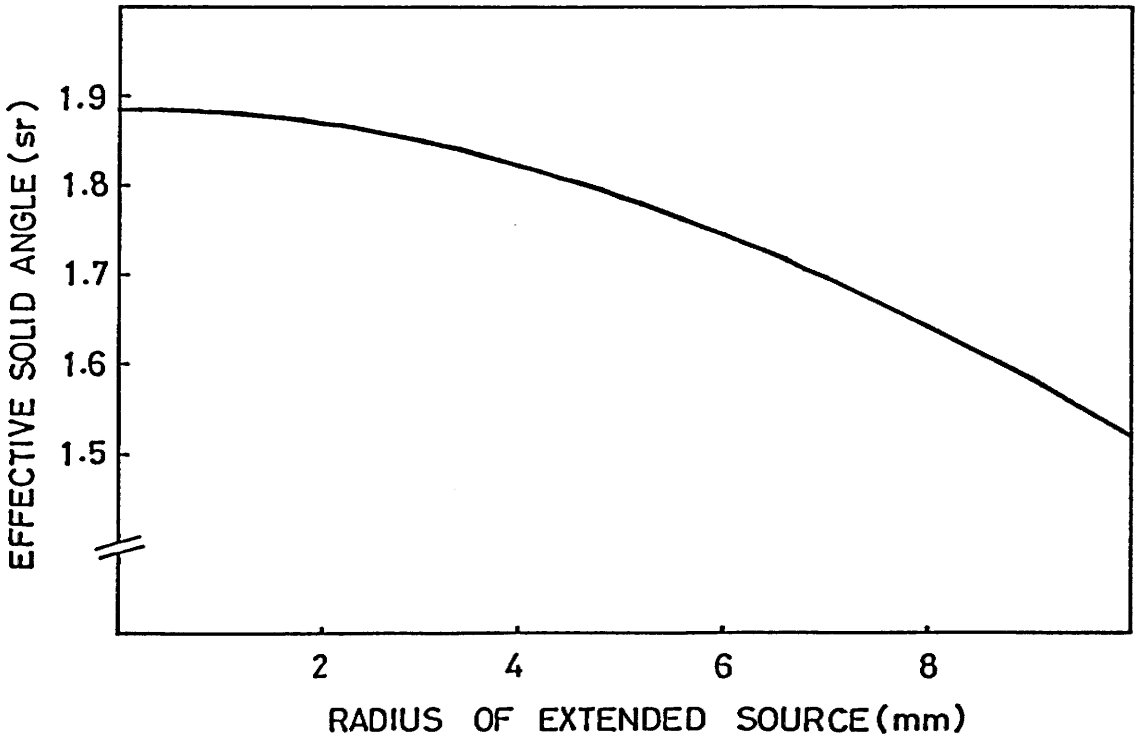

Figure D.2: Variation of Ω_{eff} with source radius.

For a source of radius a at distance z, the effective solid angle for the total surface activity is given by :

$$\Omega_{\text{eff}}(a,z) = \frac{\int_0^a \Omega_p(\rho,z)\rho\,\mathrm{d}\rho}{\int_0^a \rho\,\mathrm{d}\rho} \qquad (D.5)$$

If N_T total decays occur over the area πa^2, the detected fraction would be $N_T\Omega_{\text{eff}}(a,z)/4\pi$.

The above formulation holds only while the source radius a remains smaller than that of the detector (set to unity here). It is also assumed that the total source activity is distributed evenly over the extended area. Figure D.2 shows this effective solid angle as a function of extended-source radius in the geometry of the current experiment.

Appendix E

Least-Squares Fitting

This appendix describes the method used for the least-squares fitting of theoretical functions to the experimental data. The linear and non-linear cases are treated seperately.

Linear Functions

A matrix formulation was employed to determine the best fit of a linear function $f(x)$ to a measured data set (x_i, y_i) where $i = 1, 2, \ldots, n$ and δy_i is the experimental uncertainty in the i^{th} point. In this work $f(x)$ took the general form

$$\begin{aligned} f(x_i) &= a_1\phi_1(x_i) + a_2\phi_2(x_i) + \cdots + a_M\phi_M(x_i) \\ &= \sum_{l=1}^{M} a_l.\phi_l(x_i) \end{aligned} \qquad (E.1)$$

where each ϕ_l is a linearly independent function of x. The χ^2 parameter, describing the quality of such a fit, is defined as

$$\chi^2 = \sum_{i=1}^{n} \left[\frac{y_i - f(x_i)}{\delta y_i} \right]^2 \qquad (E.2)$$

A 'best fit' is obtained by minimising χ^2 with respect to each coefficient of the function such that

$$\left(\frac{\partial \chi^2}{\partial a_1}\right) = \left(\frac{\partial \chi^2}{\partial a_2}\right) = \cdots = \left(\frac{\partial \chi^2}{\partial a_M}\right) = 0 \qquad (E.3)$$

Simultaneous solution of these M equations yields the values for the coefficients, a_l , at which χ^2 is minimal. The problem is best expressed in matrix notation such that

$$\mathbf{HA} = \mathbf{G} \qquad (E.4)$$

where $\mathbf{H}$ is symmetric and

$$h_{kl} = \sum_{i=1}^{n} \frac{\phi_k(x_i).\phi_l(x_i)}{\delta y_i^2} \qquad \text{and} \qquad g_l = \sum_{i=1}^{n} \frac{y_i.\phi_l(x_i)}{\delta y_i^2} \qquad (E.5)$$

The optimised coefficients

$$a_k = \sum_{l=1}^{N} (h^{-1})_{kl}.g_l \qquad (E.6)$$

are then terms of the 1–dimensional solution matrix $\mathbf{A}$. This can be found by rearrangement of equation (E.4).

$$\mathbf{H'HA} = \mathbf{A} = \mathbf{H'G} \qquad (E.7)$$

The inverse matrix $\mathbf{H'}$ was calculated using Cholesky's method [183]. The error in each coefficients [184] was obtained from the diagonal elements of $\mathbf{H'}$ and can be written as

$$(\Delta a_k)^2 = \frac{\chi^2}{(n - M - 1)} (h^{-1})_{kk} \qquad (E.8)$$

Non-linear Functions

When the mathematical function to be fitted is non-linear in one or more of its parameters, as in the measurement of radio-active half-lives, the elegant fitting method described above is no longer applicable. A possible solution is to linearize the function (e.g. by Taylor expansion) and drop the highest order terms but this neccessarily perturbs the original functional form. The method followed here, for functions containing N non-linear parameters b_j where $j = 1, 2, \ldots, N$ (as well as any number of linear parameters), involved a search of

N–dimensional space for an overall minimum in the χ^2. The best fit criteria of equation (E.3) still held in addition to the following

$$\left(\frac{\partial\chi^2}{\partial b_1}\right) = \left(\frac{\partial\chi^2}{\partial b_2}\right) = \cdots = \left(\frac{\partial\chi^2}{\partial b_N}\right) = 0 \qquad (E.9)$$

Successive approximations were made to the b_j best fit values by repeated calculation. Each time, a normal determination was made of the linear parameters while the non-linear parameters were incremented in such a way that a minimum in the χ^2 value was eventually reached. The best fit parameters, $\bar{b}_j$, and their uncertainties, $\sigma(\bar{b}_j)$, were derived from the function $\chi^2(b_1, b_2, \ldots, b_N)$ which was assumed to be roughly parabolic in the vicinity of the minimum. In the case where $N = 1$, the χ^2 function is in fact a simple parabola of the form

$$(\chi^2 - \overline{\chi}^2) = \frac{(b_j - \bar{b}_j)^2}{c_{jj}} \qquad (E.10)$$

where $\overline{\chi}^2$ and $\bar{b}_j$ denote values at the χ^2 minimum and c_{jj}, the variance in parameter b_j, reflects the curvature. These quantities were found exactly by fitting a parabola to values computed near the minimum. An example is shown in Figure E.1. The standard deviation in $\bar{b}_j$ is given [185] by

$$\sigma^2(\bar{b}_j) = \frac{\overline{\chi}^2}{(n - M - N)} c_{jj} \qquad (E.11)$$

The functional relationship between χ^2, b_j and $\sigma(b_j)$ is discussed by Archer et al [186] who have shown that the parabolic behaviour of the χ^2 hypersurface yields precise values for the standard deviations of non-linear parameters when $N \leq 2$ but only approximate values otherwise. No calculations in the present work involved more than two non-linear parameters.

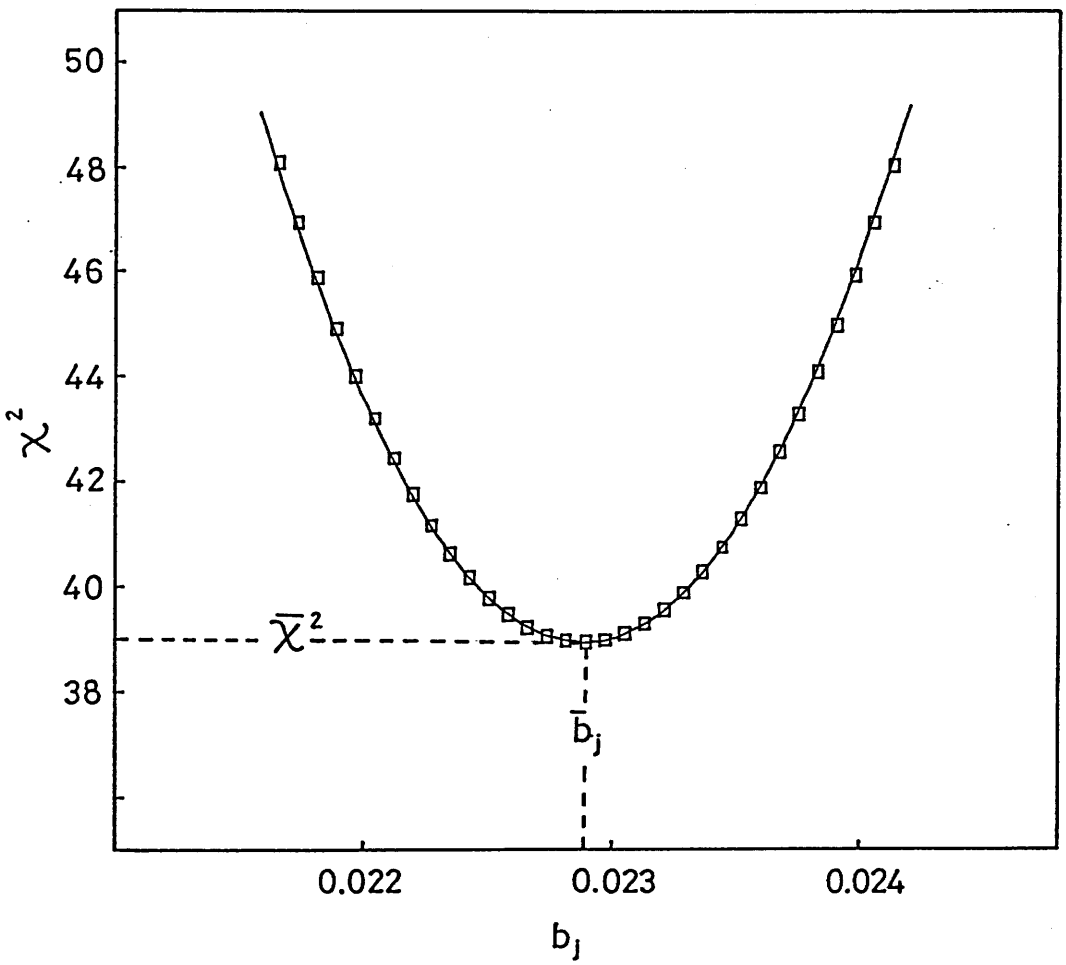

Figure E.1: Half-life determination for ^{226}Th using a parabolic method to fit one non-linear parameter, b_j. The parabola takes the form $\chi^2(b_j) = c_{jj}^{-1}(b_j - \overline{b_j})^2 + \overline{\chi}^2$ with curvature c_{jj}. In this case b_j represents the nuclide decay constant λ and is equal to 0.0229 ± 0.0004 min^{-1}. Total degrees of freedom $(n - M - N) = 39$.

Appendix F

Line Shape Fitting

A modified version of the γ–ray analysis code SAMPO [139,140,141] is discussed here for the line-shape fitting of α–peaks in spectra from thin targets. An assymetric Gaussian, with different widths below and above the centroid, was used to simulate the low energy broadening observed in real alpha peaks due to energy losses and straggling. Low and high energy exponential tailing, as well as a linear background option, were retained from the original formulation. A full description of the fitting algorithms used in this code are given by Routti & Prussin [139,140] and so only the modifications are outlined here.

A set of generalised shape parameters were defined by fitting the functional form of Equation (F.1) to several strong and isolated lines, well separated in energy.

$$\begin{aligned}
f_i &= p_1 + p_2(i - p_4) + p_3 \exp\left[\frac{p_7^2(2i - 2p_4 + p_7^2)}{2p_5^2}\right] && \text{for} \quad i < p_4 - p_7^2 \\
f_i &= p_1 + p_2(i - p_4) + p_3 \exp\left[\frac{-(i-p_4)^2}{2p_5^2}\right] && \text{for} \quad p_4 - p_7^2 \leq i \leq p_4 \\
f_i &= p_1 + p_2(i - p_4) + p_3 \exp\left[\frac{-(i-p_4)^2}{2p_6^2}\right] && \text{for} \quad p_4 \leq i \leq p_4 + p_8^2 \\
f_i &= p_1 + p_2(i - p_4) + p_3 \exp\left[\frac{p_8^2(2p_4 - 2i + p_8^2)}{2p_6^2}\right] && \text{for} \quad i > p_4 + p_8^2
\end{aligned} \qquad (F.1)$$

i = channel number
p_1, p_2 = constant and slope in linear background
p_3, p_4 = height and centroid of Gaussian
p_5 = Gaussian width parameter below centroid (FWHM = 2.355 p_5)
p_6 = Gaussian width parameter above centroid (FWHM = 2.355 p_6)
p_7^2, p_8^2 = distance from centroid to lower and upper tailing junctions.

A list of approximate peak positions were then specified for each spectrum under examination and a general fit was obtained through interpolation of the parameters $p_4, p_5, \ldots, p_8$ which were assumed to vary smoothly over the entire energy range of the spectrum. Up to six overlapping peaks could be fitted within a single multiplet over which the peak heights, peak positions and, to a lesser extent, the local background were varied until a minimum was reached in the χ^2 value of Equation (F.2). The decay constants of the tailing functions were determined from the peak heights, peak widths and distance from the peak centroid to the junction point. Fits were accepted or rejected by visual inspection using an interactive graphics routine.

$$\chi^2 = \sum_{i=k-l}^{k+m} \left(c_i - b_i - \sum_{j=1}^{n_p} f_{ij} \right) \frac{1}{c_i} \qquad (F.2)$$

$$f_{ij} = p_{2+2j} \exp\left[\frac{l_j(2i - 2p_{3+2j} + l_j)}{2w_j^2}\right] \quad \text{for} \quad i < p_{3+2j} - l_j$$

$$f_{ij} = p_{2+2j} \exp\left[\frac{-(i - p_{3+2j})^2}{2w_j^2}\right] \quad \text{for} \quad p_{3+2j} - l_j \leq i \leq p_{3+2j}$$

$$f_{ij} = p_{2+2j} \exp\left[\frac{-(i - p_{3+2j})^2}{2v_j^2}\right] \quad \text{for} \quad p_{3+2j} \leq i \leq p_{3+2j} + h_j$$

$$f_{ij} = p_{2+2j} \exp\left[\frac{h_j(2p_{3+2j} - 2i + h_j)}{2v_j^2}\right] \quad \text{for} \quad i > p_{3+2j} + h_j$$

c_i = number of counts in i^{th} channel
b_i = background function for multiplet with reference channel k
l, m = extent of fitted region
n_p = number of peaks in multiplet
p_{2+2j} = height of j^{th} peak in multiplet
p_{3+2j} = centroid of j^{th} peak in multiplet
l_j, h_j = interpolated lower and upper tailing parameters
w_j, v_j = interpolated lower and upper width parameters

For the α–spectra encountered in this experiment, where low-energy tailing remained short range, the simple function described above provided a satisfactory description of the general peak shape. The average peak width showed no strong variation over the energy range of the alpha spectrum and the fitted backgrounds were always close to zero.

Appendix G

Decay Functions

The functions which describe the activities of radioactive nuclei in a sequential decay chain follow the traditional formulation of Bateman [187]. A 4–stage decay chain is evaluated here which may be represented by :

$$\boxed{N_4} \longrightarrow \boxed{N_3} \longrightarrow \boxed{N_2} \longrightarrow \boxed{N_1} \longrightarrow$$

If N_i^0 represents the content of the i^{th} element at $t = 0$ and λ_i is its decay constant then the activity $A_1(t)$ of the final nuclide in the chain may be written as :

$$\begin{aligned} A_1(t) &= N_4^0 \left[G_{44}\lambda_4 e^{-\lambda_4 t} + G_{43}\lambda_3 e^{-\lambda_3 t} + G_{42}\lambda_2 e^{-\lambda_2 t} + G_{41}\lambda_1 e^{-\lambda_1 t} \right] \\ &+ N_3^0 \left[G_{33}\lambda_3 e^{-\lambda_3 t} + G_{32}\lambda_2 e^{-\lambda_2 t} + G_{31}\lambda_1 e^{-\lambda_1 t} \right] \\ &+ N_2^0 \left[G_{22}\lambda_2 e^{-\lambda_2 t} + G_{21}\lambda_1 e^{-\lambda_1 t} \right] \\ &+ N_1^0 \left[\lambda_1 e^{-\lambda_1 t} \right] \end{aligned} \qquad (G.1)$$

where

$$G_{44} = \frac{(\lambda_3\lambda_2\lambda_1)}{(\lambda_3-\lambda_4)(\lambda_2-\lambda_4)(\lambda_1-\lambda_4)} \qquad G_{43} = \frac{(\lambda_4\lambda_2\lambda_1)}{(\lambda_4-\lambda_3)(\lambda_2-\lambda_3)(\lambda_1-\lambda_3)}$$

$$G_{42} = \frac{(\lambda_4\lambda_3\lambda_1)}{(\lambda_4-\lambda_2)(\lambda_3-\lambda_2)(\lambda_1-\lambda_2)} \qquad G_{41} = \frac{(\lambda_4\lambda_3\lambda_2)}{(\lambda_4-\lambda_1)(\lambda_3-\lambda_1)(\lambda_2-\lambda_1)}$$

$$G_{33} = \frac{(\lambda_2\lambda_1)}{(\lambda_2-\lambda_3)(\lambda_1-\lambda_3)} \qquad G_{32} = \frac{(\lambda_3\lambda_1)}{(\lambda_3-\lambda_2)(\lambda_1-\lambda_2)} \qquad G_{31} = \frac{(\lambda_3\lambda_2)}{(\lambda_3-\lambda_1)(\lambda_2-\lambda_1)}$$

$$G_{22} = \frac{(\lambda_1)}{(\lambda_1-\lambda_2)} \qquad G_{21} = \frac{(\lambda_2)}{(\lambda_2-\lambda_1)}$$

Equation (G.1) is abbreviated in an obvious fashion when fewer parents feed into the lower members of the chain.

Since $A(t)$ represents the instantaneous activity at time t, it differs slightly from any *measured* activity $\overline{A}(t)$ which is averaged over an interval $[t - \delta t, t + \delta t]$. In fact

$$\overline{A}(t_j) = \frac{\int_{t_j-\delta t_j}^{t_j+\delta t_j} A(t)dt}{\int_{t_j-\delta t_j}^{t_j+\delta t_j} dt}$$

In practice, a correction to the decay function of Equation (G.1) was made for finite count intervals by replacing each of the

$$\lambda_i e^{-\lambda_i t} \quad \text{with} \quad \left[\frac{\sinh(\lambda_i \delta t)}{\delta t}\right] e^{-\lambda_i t}$$

However, such corrections were found to be significant only when the count interval was comparable to the half-life $\ln 2/\lambda$.

Appendix H

Radioactive Decay Schemes

Figures H.1 to H.4 show the various radioactive decay schemes which follow $(\gamma, x\mathrm{n}\, y\mathrm{p})$ reactions on ^{232}Th. Nuclides resulting from the emission of more than 14 nucleons or from the release of more than 3 protons are expected to be highly suppressed or energetically forbidden at the nuclear excitations involved here. Most of these have been excluded from the diagrams.

Although a great many chains are initiated, a large number of reaction products are so short lived that their activities are exhausted well before the start of data collection. Unless there exists a long lived daughter within the decay chain, the yields of such reaction products can never be determined by the present method of remote counting. Species lost from the cascades in this way are shown within broken boxes. Residual nuclides from reactions with relatively high energy thresholds (e.g. $\geq$ 10 n or $\geq$ 3 p), for which little activity has been measured, make negligible contribution to the content of species lower in the decay chain and are similarly represented.

Several decay schemes are 'blocked' by the presence of exceptionally long lived daughters which halt the radioactive cascade. Transitions supressed in this way are depicted by broken arrows.

The α–particle energies and branching ratios pertinent to each decay series are given in the accompanying tables.

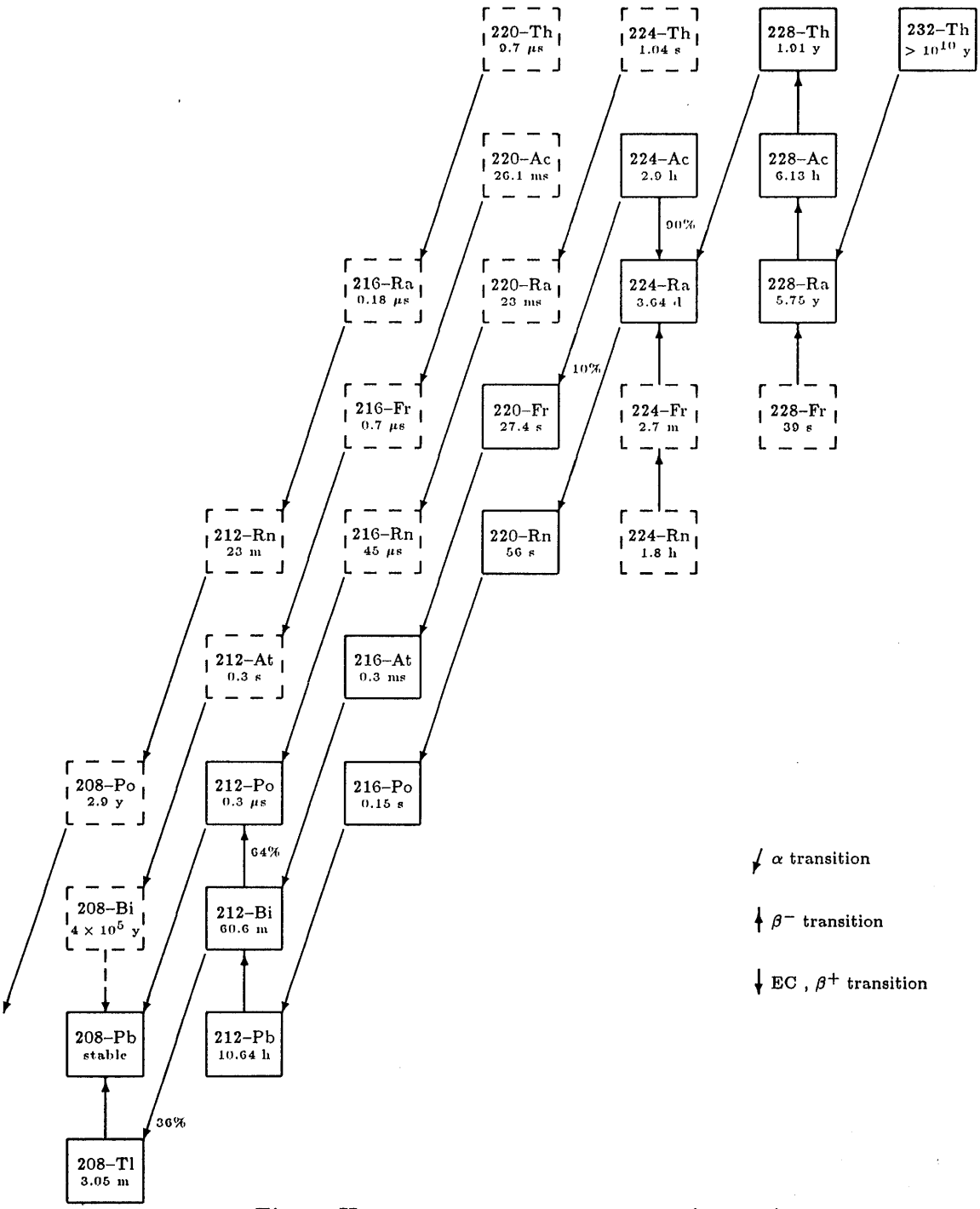

Figure H.1: Radioactive decay schemes (A = 4*n*).

Nuclide	Half-life	Decay Mode	Branch	α–Energy (MeV)
232–Th	1.41×10^{10} y	α	77 %	4.016
		α	23 %	3.957
228–Th	1.91 y	α	72.7 %	5.42333
		α	26.7 %	5.34054
228–Ac	6.13 h	β^-	100 %	
228–Ra	5.75 y	β^-	100 %	
228–Fr	39 s	β^-	100 %	
224–Th	1.05 s	α	81 %	7.17
		α	19 %	7.00
224–Ac	2.9 h	EC	90 %	
		α	2.04 %	6.2106
		α	1.19 %	6.2038
		α	2.56 %	6.1385
		α	2.19 %	6.0566
		α	small	5.6 → 6.1
224–Ra	3.665 d	α	95.1 %	5.6857
		α	4.9 %	5.4489
224–Fr	2.67 m	β^-	100 %	
224–Rn	1.78 h	β^-	100 %	
220–Th	9.7 μs	α	100 %	8.79
220–Ac	26.1 ms	α	3 %	8.196
		α	6 %	8.061
		α	5 %	8.006
		α	4 %	7.986
		α	24 %	7.851
		α	13 %	7.791
		α	21 %	7.68
		α	23 %	7.61
220–Ra	23 ms	α	100 %	7.457
220–Fr	27.4 s	α	61.1 %	6.686
		α	12.2 %	6.642
		α	6.5 %	6.630
		α	9.8 %	6.582
		α	small	6.3 → 6.5
220–Rn	55.61 s	α	99.93 %	6.288
216–Ra	0.182 μs	α	100 %	9.349
216–Fr	0.70 μs	α	100 %	9.006
216–Rn	45 μs	α	100 %	8.047
216–At	0.30 ms	α	97 %	7.800
		α	2.1 %	7.697
		α	small	7.2 → 7.6
216–Po	0.145 s	α	100 %	6.7785
212–Rn	23 m	α	99.95 %	6.264
212–At	0.315 s	α	83.5 %	7.679
		α	15.1 %	7.618
		α	small	6.6 → 7.2
212–Po	0.296 μs	α	100 %	8.78437
212–Bi	60.600 m	β^-	64.00 %	
		α	9.79 %	6.090087
		α	25.1 %	6.050985
		α	0.612 %	5.769
212–Pb	10.643 h	β^-	100 %	
208–Po	2.8976 y	α	100 %	5.110
208–Bi	3.68×10^5 y	EC	100 %	
208–Pb	stable			
208–Tl	3.0527 m	β^-	100 %	

Table H.1: Decay characteristics of $(4n)$–scheme.

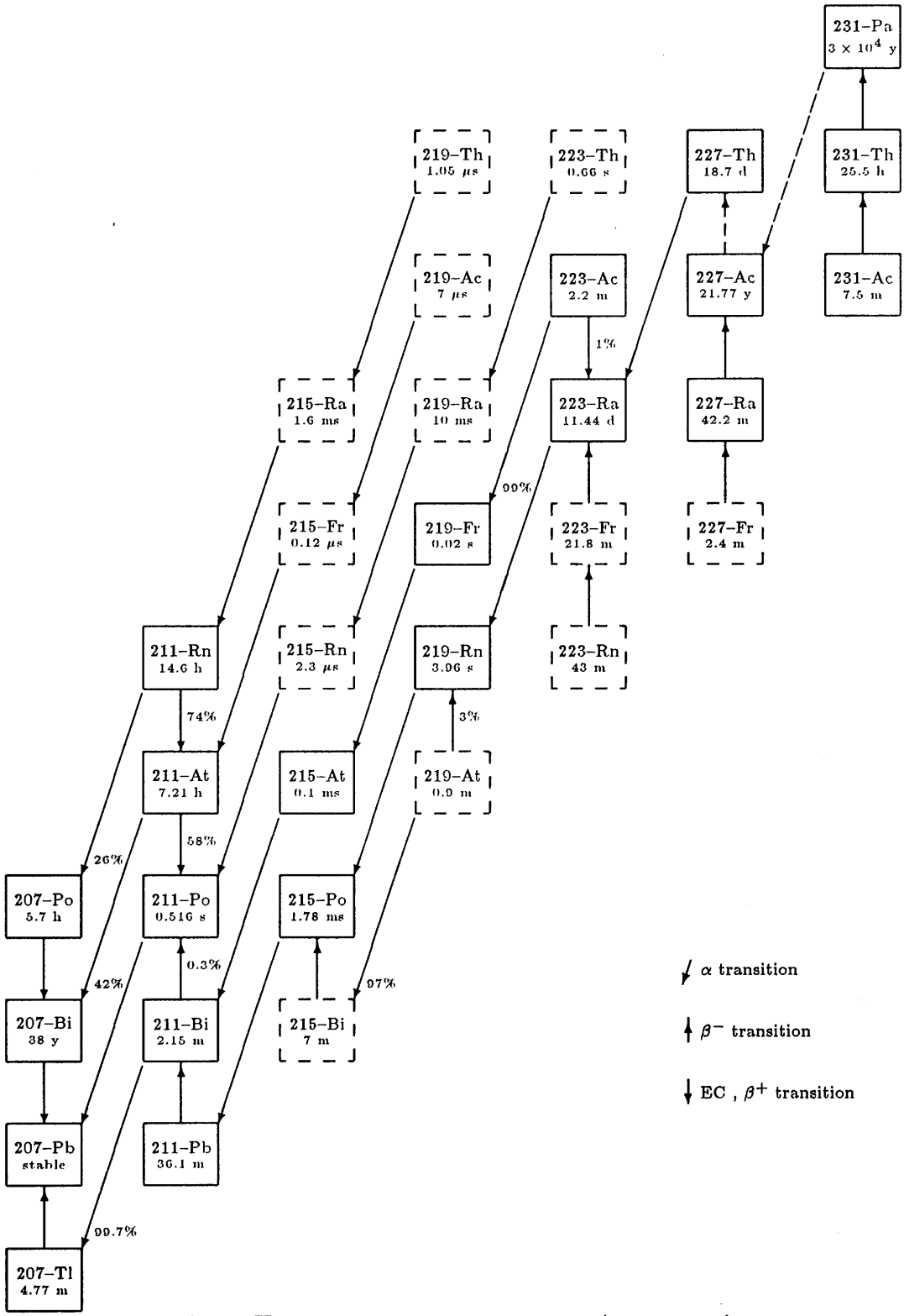

Figure H.2: Radioactive decay schemes (A = $4n + 3$).

Nuclide	Half-life	Decay Mode	Branch	α–Energy (MeV)
231–Pa	3.276×10^4 y	α	11 %	5.058
		α	20 %	5.029
		α	25.4 %	5.012
		α	22.8 %	4.951
		α	8.4 %	4.737
		α	small	4.6 → 5.0
231–Th	25.52 h	β^-	100 %	
231–Ac	7.5 m	β^-	100 %	
227–Th	18.7176 d	α	24.5 %	6.0383
		α	23.4 %	5.9780
		α	20.3 %	5.7569
		α	8.2 %	5.7090
		α	4.89 %	5.7132
		α	small	5.0 → 5.9
227–Ac	21.7728 y	β^-	100 %	
227–Ra	42.2 m	β^-	100 %	
227–Fr	2.4 m	β^-	100 %	
223–Th	0.66 s	α	40 %	7.317
		α	60 %	7.287
223–Ac	2.2 m	EC	1 %	
		α	31.5 %	6.6621
		α	44.2 %	6.6472
		α	13.6 %	6.5642
		α	small	6.0 → 6.6
223–Ra	11.4346 d	α	9.1 %	5.7478
		α	53.7 %	5.7165
		α	26.0 %	5.6075
		α	9.1 %	5.5400
		α	small	5.0 → 5.9
223–Fr	21.8 m	β^-	100 %	
223–Rn	43 m	β^-	100 %	
219–Th	1.05 μs	α	100 %	9.34
219–Ac	7 μs	α	100 %	8.664
219–Ra	10 ms	α	35 %	7.980
		α	65 %	7.675
219–Fr	0.02 s	α	98.8 %	7.3132
219–Rn	3.96 s	α	81 %	6.8189
		α	11.5 %	6.5527
		α	7.5 %	6.4246
219–At	0.9 m	β^-	3 %	
		α	97 %	6.28
215–Ra	1.56 ms	α	95.7 %	8.697
		α	1.3 %	8.167
		α	3.0 %	7.879
215–Fr	0.12 μs	α	100 %	9.364
215–Rn	2.30 μs	α	100 %	8.674
215–At	0.10 ms	α	100 %	8.026
215–Po	1.778 ms	α	100 %	7.3864
215–Bi	7.4 m	β^-	100 %	
211–Rn	14.6 h	EC,β^+	74 %	
		α	8.8 %	5.850
		α	16.4 %	5.783
		α	0.7 %	5.616
211–At	7.214 h	EC	58.06 %	
		α	41.94 %	5.866
211–Po	0.516 s	α	98.86 %	7.450
		α	0.56 %	6.8925
		α	0.58 %	6.5700
211–Bi	2.15 m	β^-	0.274 %	
		α	83.8 %	6.6231
		α	15.9 %	6.2788

Table H.2: Decay characteristics of $(4n + 3)$–scheme.

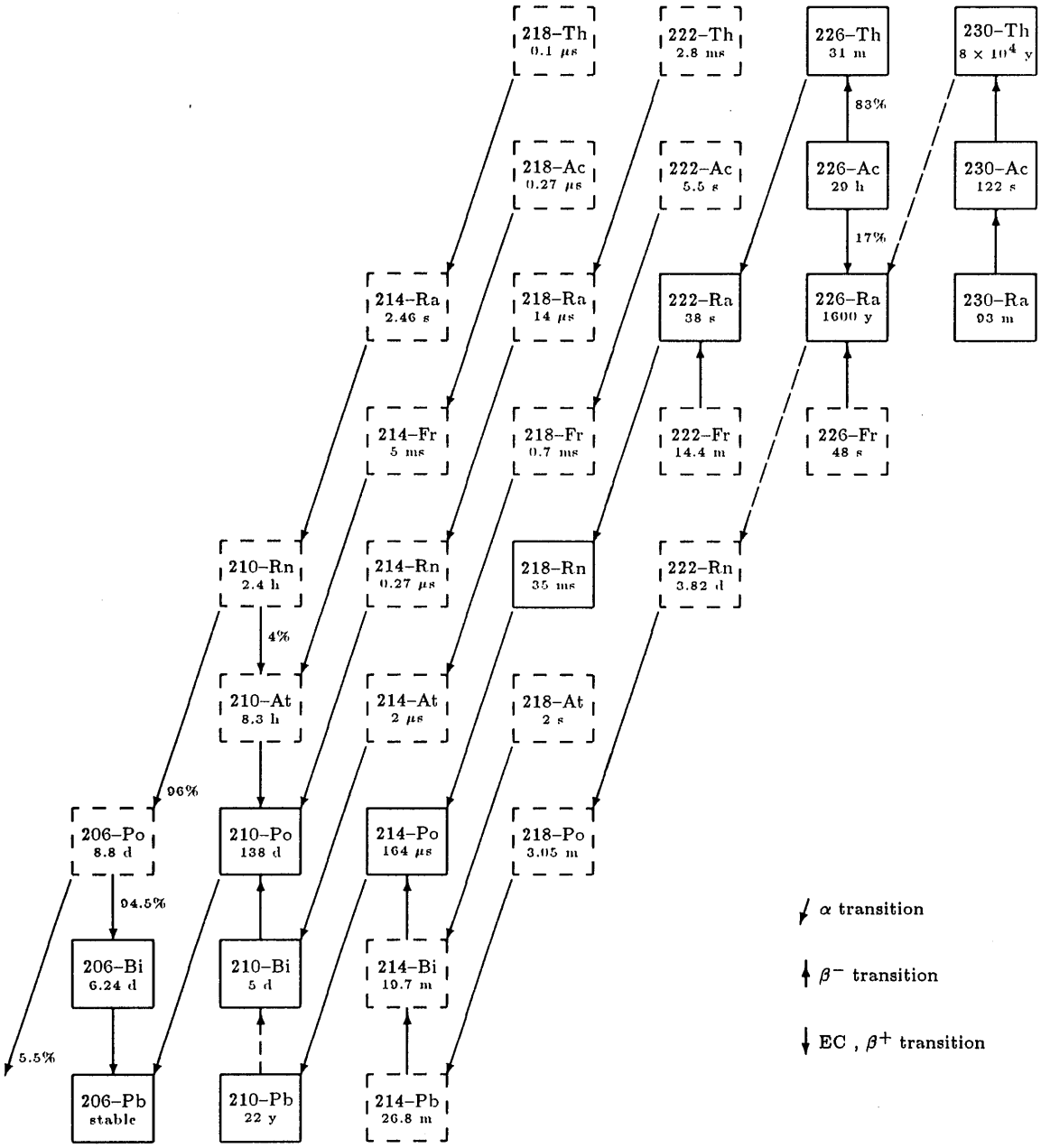

Figure H.3: Radioactive decay schemes (A = $4n + 2$).

Nuclide	Half-life	Decay Mode	Branch	α–Energy (MeV)
230–Th	8.0×10^4 y	α	76.3 %	4.6875
		α	23.4 %	4.6210
230–Ac	122 s	β^-	100 %	
230–Ra	93 m	β^-	100 %	
226–Th	30.9 m	α	79 %	6.335
		α	19 %	6.225
		α	1.7 %	6.100
		α	0.58 %	6.034
226–Ac	29 h	β^-	83 %	
		EC	17 %	
226–Ra	1599 y	α	94.45 %	4.7845
		α	5.55 %	4.6015
226–Fr	2.4 m	β^-	100 %	
222–Th	2.8 ms	α	100 %	7.984
222–Ac	5.5 s	α	100 %	7.013
222–Ra	38 s	α	96.9 %	6.556
		α	3.1 %	6.232
222–Fr	14.4 m	β^-	100 %	
222–Rn	3.82351 d	α	100 %	5.48966
218–Th	96 ns	α	100 %	9.664
218–Ac	7 μs	α	100 %	9.204
218–Ra	14 μs	α	100 %	8.392
218–Fr	0.7 ms	α	93 %	7.851
		α	5 %	7.556
218–Rn	35 ms	α	100 %	7.133
218–At	1.5 s	α	3.6 %	6.757
		α	90 %	6.694
		α	6.4 %	6.654
218–Po	3.05 m	α	100 %	6.00255
214–Ra	2.46 s	α	100 %	7.138
214–Fr	5.0 ms	α	93 %	8.426
		α	4.7 %	8.358
214–Rn	0.27 μs	α	100 %	9.035
214–At	2 μs	α	100 %	8.819
214–Po	163.7 μs	α	100 %	7.687090
214–Bi	19.7 m	β^-	100 %	
214–Pb	26.8 m	β^-	100 %	
210–Rn	2.42 h	EC	4 %	
		α	96 %	6.040
210–At	8.3 h	EC,β^+	100 %	
210–Po	138.3763 d	α	100 %	5.30451
210–Bi	5.013 d	β^-	100	
210–Pb	22.26 y	β^-	100 %	
206–Po	8.83 d	EC	94.55 %	
		α	5.45 %	5.224
206–Bi	6.243 d	EC	100 %	
206–Pb	stable			

Table H.3: Decay characteristics of $(4n + 2)$–scheme.

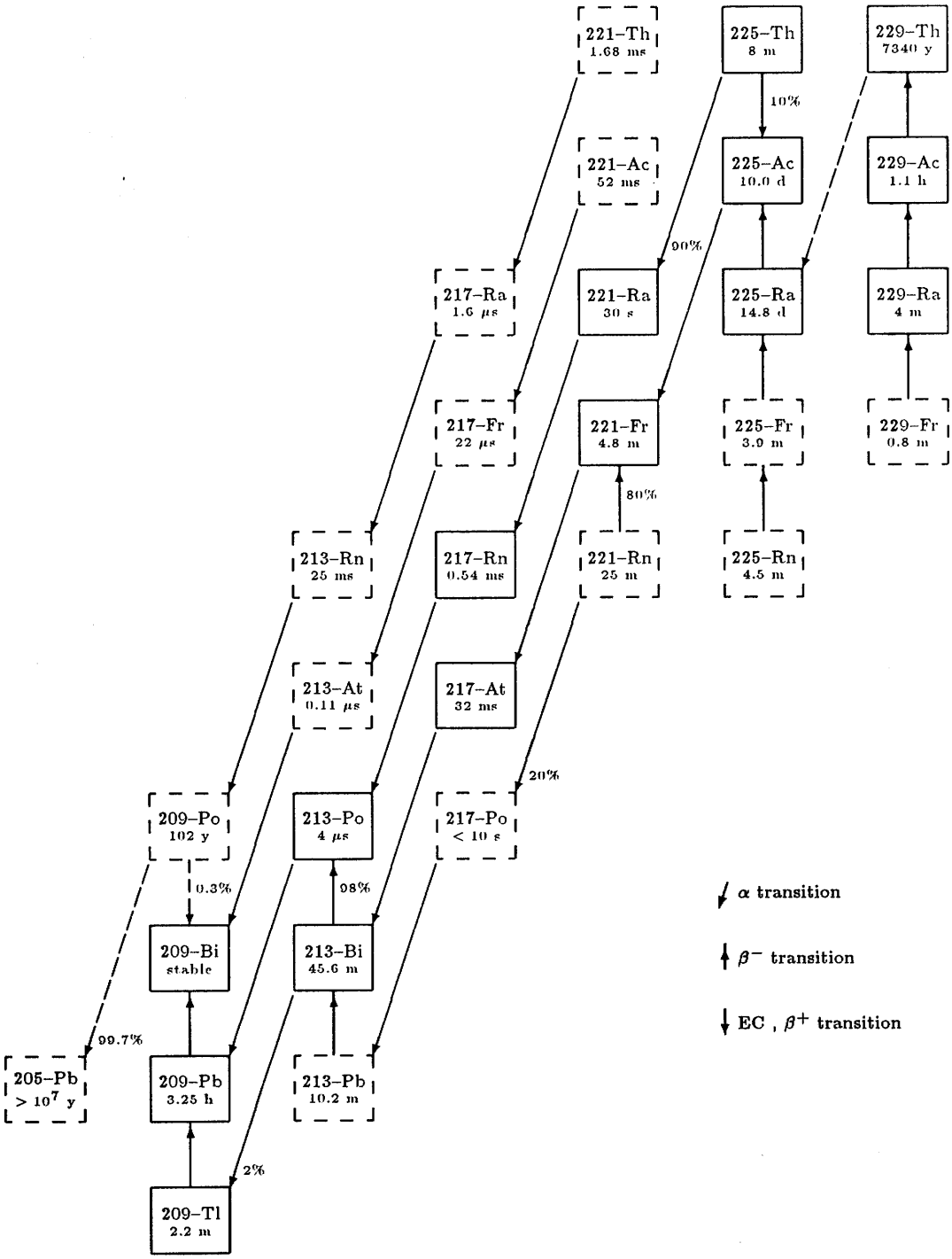

Figure H.4: Radioactive decay schemes (A = $4n + 1$).

Nuclide	Half-life	Decay Mode	Branch	α–Energy (MeV)
229–Th	7340 y	α	5.2 %	5.051
		α	3.2 %	4.9785
		α	6.4 %	4.9675
		α	10.8 %	4.9010
		α	56.2 %	4.8453
		α	4.8 %	4.838
		α	8.4 %	4.8146
		α	small	4.4 → 5.1
229–Ac	62.7 m s	β^-	100 %	
229–Ra	4.0 m	β^-	100 %	
229–Fr	50 s m	β^-	100 %	
225–Th	8.0 m	EC	10 %	
		α	8.1 %	6.798
		α	6.3 %	6.744
		α	12.6 %	6.501
		α	38.7 %	6.478
		α	13.5 %	6.441
		α	small	6.3 → 6.7
225–Ac	10.0 d	α	50.65 %	5.8300
		α	24.3 %	5.7940
		α	10.1 %	5.7320
		α	4.35 %	5.6372
		α	small	4.9 → 5.8
225–Ra	14.8 d	β^-	100 %	
225–Fr	3.9 m	β^-	100 %	
225–Rn	4.5 m	β^-	100 %	
221–Th	1.68 ms	α	39 %	8.471
		α	56 %	8.146
		α	6 %	7.726
221–Ac	52 ms	α	70 %	7.647
		α	20 %	7.442
		α	10 %	7.377
221–Ra	30 s	α	30 %	6.758
		α	20 %	6.665
		α	34 %	6.610
		α	8 %	6.588
		α	3 %	6.578
		α	small	6.1 → 6.5
221–Fr	4.8 m	α	83.4 %	6.3410
		α	15.1 %	6.1264
		α	small	5.6 → 6.3
221–Rn	25 m	β^-	80 %	
		α	20 %	6
217–Ra	1.6 μs	α	100 %	8.990
217–Fr	22 μs	α	100 %	8.315
217–Rn	0.54 ms	α	100 %	7.739
217–At	32.3 ms	α	100 %	7.067
217–Po	< 10 s	α	100 %	6.54
213–Rn	25.0 ms	α	99 %	8.085
		α	1 %	7.550
213–At	0.11 μs	α	100 %	9.080
213–Po	4.2 μs	α	100 %	8.375
213–Bi	45.59 m	β^-	97.84 %	
		α	2 %	5.869
213–Pb	10.2 m	β^-	100 %	
209–Po	102 y	EC	0.26 %	
		α	99.26 %	4.877
209–Bi	stable			
209–Pb	3.253 h	β^-	100 %	
209–Tl	2.20 m	β^-	100 %	
205–Pb	$> 10^7$ y			

Table H.4: Decay characteristics of $(4n + 1)$–scheme.

Appendix I

Corrections to the Measured Yields for Decay Loss and Feeding during Irradiation

One of the problems associated with the evaluation of reaction yields by a residual activity method, is that some of the reaction products are lost through decay during the irradiation period. Corrections must be made to the measured yields to allow for these losses. A further correction is required when the reaction product under investigation is also populated by the decay of some parent species lying higher in the same decay chain. The problem is formulated as follows :

$$\boxed{N_1} \xrightarrow{\lambda_1} \boxed{N_2} \xrightarrow{\lambda_2}$$

Here, N_1 and N_2 represent the populations of two nuclides in the same decay chain, each of which are produced through photoreactions in the target. The parameters λ_1 and λ_2 denote their respective decay constants. During an irradiation, the content of the first species N_1 is subject to decay losses only. The N_2 population is affected by a similar decay loss, but is additionally contaminated by the products of the N_1 decay. At time τ during the irradiation, the photoproduction rate R of each species is proportional to the instantaneous beam

current $I(\tau)$

$$\begin{aligned} R_1(\tau) &= k_1\, I(\tau) \\ R_2(\tau) &= k_2\, I(\tau) \end{aligned} \qquad (I.1)$$

The net rates of production, inclusive of decay loss and feeding, may then be written as

$$\begin{aligned} \frac{dN_1}{d\tau} &= R_1(\tau) - \lambda_1 N_1 \\ \frac{dN_2}{d\tau} &= R_2(\tau) - \lambda_2 N_2 + \lambda_1 N_1 \end{aligned} \qquad (I.2)$$

The contents of each species, at time τ during the irradiation, are therefore

$$\begin{aligned} N_1(\tau) &= e^{-\lambda_1\tau} \int_o^{\tau} e^{\lambda_1\tau'} R_1(\tau')\, d\tau' \\ N_2(\tau) &= e^{-\lambda_2\tau} \int_o^{\tau} e^{\lambda_2\tau'} R_2(\tau')\, d\tau' \\ &+ e^{-\lambda_2\tau} \int_o^{\tau} e^{(\lambda_2-\lambda_1)\tau'}\, d\tau' \int_o^{\tau'} e^{\lambda_1\tau''} \lambda_1 R_1(\tau'')\, d\tau'' \end{aligned} \qquad (I.3)$$

The contents measured at the end of irradiation period ($\tau = \tau_o$) are then

$$\begin{aligned} N_1(\tau_o) &= k_1\, q_{11} \\ N_2(\tau_o) &= k_2\, q_{22} + k_1\, q_{12} \end{aligned} \qquad (I.4)$$

where

$$\begin{aligned} q_{11} &= e^{-\lambda_1\tau_o} \int_o^{\tau_o} e^{\lambda_1\tau'} I(\tau')\, d\tau' \\ q_{22} &= e^{-\lambda_2\tau_o} \int_o^{\tau_o} e^{\lambda_2\tau'} I(\tau')\, d\tau' \\ q_{12} &= e^{-\lambda_2\tau_o} \int_o^{\tau_o} e^{(\lambda_2-\lambda_1)\tau'}\, d\tau' \int_o^{\tau'} e^{\lambda_1\tau''} \lambda_1 I(\tau'')\, d\tau'' \end{aligned} \qquad (I.5)$$

The *true* yields Y_1, Y_2 for the same irradiation period are

$$\begin{aligned} Y_1(\tau_o) &= \int_o^{\tau_o} R_1(\tau) d\tau = k_1 \int_o^{\tau_o} I(\tau) d\tau = k_1\, Q_{tot} \\ Y_2(\tau_o) &= \int_o^{\tau_o} R_2(\tau) d\tau = k_2 \int_o^{\tau_o} I(\tau) d\tau = k_2\, Q_{tot} \end{aligned} \qquad (I.6)$$

where Q_{tot} is the total beam charge. A combination of Equations (I.4) and (I.6) relates the true yield Y to the observed value N

$$\begin{aligned} Y_1 &= N_1 \frac{Q_{tot}}{q_{11}} \\ Y_2 &= \left[N_2 - \frac{q_{12}}{q_{11}} N_1 \right] \frac{Q_{tot}}{q_{22}} \end{aligned} \qquad (I.7)$$

A proper evaluation of these corrections requires a knowledge of the electron beam current $I(\tau)$, which was shown in Section 2.3 to be far from constant over a typical irradiation period. To correct for this non-uniformity, the beam current profiles, which were recorded graphically for each of the 61 irradiations, were used to incorporate the time dependence of the beam current during each irradiation period. Each profile was divided into n intervals (generally more

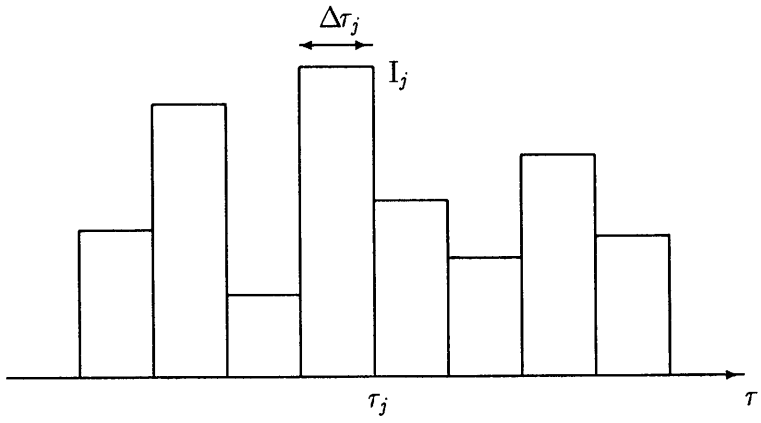

Figure I.1: Schematic representation of the subdivided beam profile $I(\tau)$ showing the j^{th} interval over which the beam current I_j is assumed constant.

than 100) of length $\Delta\tau_j$, over each of which a constant beam current I_j could be assumed (Figure I.1). The values of n were chosen such that further subdivision made negligible difference to the calculated correction. In this case the integral expressions of Equation I.5 were substituted by the following summations :

$$\begin{aligned} q_{11} &= \sum_j I_j \, e^{\lambda_1(\tau_n-\tau_j)} \, \lambda_1^{-1} \left(1 - e^{-\lambda_1 \Delta\tau_j}\right) \\ q_{22} &= \sum_j I_j \, e^{\lambda_2(\tau_n-\tau_j)} \, \lambda_2^{-1} \left(1 - e^{-\lambda_2 \Delta\tau_j}\right) \\ q_{12} &= \sum_k e^{-\lambda_2(\tau_n-\tau_k)} \sum_{j \le k} I_j \, e^{\lambda_1(\tau_k-\tau_j)} \, \lambda_1^{-1} \left(1 - e^{-\lambda_1 \Delta\tau_j}\right) \end{aligned} \qquad (I.8)$$

Appendix J

Tabulated Results

This appendix contains a tabulation of the reduced yields, as defined in Section 3.1, for all of the photo-reactions investigated. Where a particular reaction yield has been extracted in several different ways (i.e. from the analysis of more than one decay curve), individual results are given for each of the measured nuclide activities as well as the final weighted mean and error in the mean. Results obtained from the 'short' irradiation data set are marked with an (s) and are themselves the averaged values from up to four separate measurements at each electron end-point energy. All other values are derived from the analysis of the 'long' irradiaton data.

The upper part of each table shows the electro-disintegration yields at $40, 50, \ldots, 150$ MeV while in the lower part, the yields for electron + bremsstrahlung are given at 60, 100 & 140 MeV. The separated bremsstrahlung yields are also given, quoted in μb per equivalent quantum.

Electron Energy		Reduced Yield (μb) measured per decay curve 228–Th
40 MeV	e	6.66 ± 0.63
50 MeV	e	77.90 ± 0.63
60 MeV	e	100.0 ± 1.0
70 MeV	e	118.7 ± 2.2
80 MeV	e	137.8 ± 1.4
90 MeV	e	153.7 ± 1.5
100 MeV	e	173.3 ± 2.6
110 MeV	e	176.9 ± 1.3
120 MeV	e	192.3 ± 2.4
130 MeV	e	208.1 ± 1.7
140 MeV	e	231.6 ± 3.0
150 MeV	e	256.4 ± 8.0
60 MeV	$e + \gamma$	219.6 ± 2.6
	γ	$^{\dagger}3962 \pm 85$
100 MeV	$e + \gamma$	354.3 ± 5.5
	γ	$^{\dagger}5386 \pm 181$
140 MeV	$e + \gamma$	416.6 ± 7.1
	γ	$^{\dagger}5404 \pm 226$

Table J.1: Reduced yields for the reactions $^{232}\mathrm{Th}(\gamma, 4\mathrm{n} + 3\mathrm{n1p})^{228}\mathrm{Th}, ^{228}\mathrm{Ac}$ and $^{232}\mathrm{Th}(e, 4\mathrm{n} + 3\mathrm{n1p})^{228}\mathrm{Th}, ^{228}\mathrm{Ac}$. † Bremsstrahlung yields in μb per equivalent quantum.

Electron Energy		Reduced Yield (μb) measured per decay curve 215–Po
40 MeV	e	2.840 ± 0.073
50 MeV	e	15.107 ± 0.111
60 MeV	e	22.999 ± 0.204
70 MeV	e	31.334 ± 0.324
80 MeV	e	36.643 ± 0.336
90 MeV	e	43.623 ± 0.416
100 MeV	e	45.250 ± 0.726
110 MeV	e	50.264 ± 0.366
120 MeV	e	55.623 ± 0.617
130 MeV	e	57.789 ± 0.640
140 MeV	e	59.996 ± 0.564
150 MeV	e	63.543 ± 1.906
60 MeV	$e + \gamma$	60.339 ± 0.657
	γ	$^{\dagger}1153 \pm 21$
100 MeV	$e + \gamma$	103.112 ± 1.489
	γ	$^{\dagger}1722 \pm 49$
140 MeV	$e + \gamma$	127.091 ± 2.060
	γ	$^{\dagger}1959 \pm 62$

Table J.2: Reduced yields for the reactions $^{232}\mathrm{Th}(\gamma, 5\mathrm{n})^{227}\mathrm{Th}$ and $^{232}\mathrm{Th}(e, 5\mathrm{n})^{227}\mathrm{Th}$. † Bremsstrahlung yields in μb per equivalent quantum.

Electron Energy		Reduced Yield (μb) measured per decay curve 214–Po	218–Rn	222–Ra	214–Po (s)	Weighted Mean (μb)
40 MeV	e	$.00121 \pm .00001$	$.00121 \pm .00001$	$.00121 \pm .00001$	$-.005 \pm .013$	$.00121 \pm .00001$
50 MeV	e	2.512 ± 0.041	2.467 ± 0.039	2.432 ± 0.044	2.437 ± 0.134	2.471 ± 0.023
60 MeV	e	8.231 ± 0.115	8.486 ± 0.099	8.268 ± 0.137	8.053 ± 0.242	8.332 ± 0.080
70 MeV	e	13.102 ± 0.185	13.530 ± 0.183	13.271 ± 0.200	13.150 ± 0.224	13.275 ± 0.100
80 MeV	e	17.072 ± 0.235	16.760 ± 0.186	16.709 ± 0.234	16.151 ± 0.297	16.732 ± 0.161
90 MeV	e	19.991 ± 0.260	19.790 ± 0.212	19.689 ± 0.266	19.673 ± 0.159	19.756 ± 0.105
100 MeV	e	22.824 ± 0.457	22.226 ± 0.384	21.983 ± 0.430	21.109 ± 0.233	21.688 ± 0.373
110 MeV	e	24.706 ± 0.248	23.803 ± 0.195	24.679 ± 0.259	24.954 ± 0.587	24.318 ± 0.263
120 MeV	e	28.925 ± 0.475	29.024 ± 0.349	28.680 ± 0.457	29.277 ± 0.281	29.061 ± 0.182
130 MeV	e	31.552 ± 0.430	31.252 ± 0.371	30.010 ± 0.419	30.540 ± 0.446	30.866 ± 0.345
140 MeV	e	31.933 ± 0.430	31.377 ± 0.343	30.730 ± 0.411	33.173 ± 0.533	31.612 ± 0.450
150 MeV	e	35.058 ± 1.174	35.610 ± 1.085	35.858 ± 1.136	37.203 ± 0.452	36.658 ± 0.467
60 MeV	$e + \gamma$	24.567 ± 0.328	23.971 ± 0.303	24.543 ± 0.326	25.427 ± 0.405	24.526 ± 0.279
	γ					$^{\dagger}500 \pm 9$
100 MeV	$e + \gamma$	56.823 ± 0.934	53.904 ± 0.807	56.719 ± 0.954	55.111 ± 0.593	55.394 ± 0.631
	γ					$^{\dagger}1003 \pm 22$
140 MeV	$e + \gamma$	72.113 ± 1.273	69.637 ± 1.164	68.196 ± 1.324	68.631 ± 1.024	69.549 ± 0.827
	γ					$^{\dagger}1108 \pm 28$

Table J.3: Reduced yields for the reactions $^{232}\mathrm{Th}(\gamma, 6\mathrm{n})^{226}\mathrm{Th}$ and $^{232}\mathrm{Th}(e, 6\mathrm{n})^{226}\mathrm{Th}$. † Bremsstrahlung yields in μb per equivalent quantum.

Electron Energy		Reduced Yield (μb) measured per decay curve 213–Po
50 MeV	e	0.019 ± 0.015
60 MeV	e	0.883 ± 0.046
70 MeV	e	3.029 ± 0.071
80 MeV	e	4.304 ± 0.149
90 MeV	e	6.029 ± 0.122
100 MeV	e	6.244 ± 0.105
110 MeV	e	7.989 ± 0.144
120 MeV	e	9.716 ± 0.124
130 MeV	e	10.301 ± 0.177
140 MeV	e	11.483 ± 0.224
150 MeV	e	12.339 ± 0.181
60 MeV	$e + \gamma$	2.778 ± 0.102
	γ	$^{\dagger}58 \pm 3$
100 MeV	$e + \gamma$	18.644 ± 0.293
	γ	$^{\dagger}369 \pm 9$
140 MeV	$e + \gamma$	25.491 ± 0.419
	γ	$^{\dagger}409 \pm 14$

Table J.4: Reduced yields for the reactions $^{232}\mathrm{Th}(\gamma, 7\mathrm{n})^{225}\mathrm{Th}$ and $^{232}\mathrm{Th}(e, 7\mathrm{n})^{225}\mathrm{Th}$. † Bremsstrahlung yields in μb per equivalent quantum.

Electron Energy		Reduced Yield (μb) measured per decay curve 214–Po	218–Rn	222–Ra	Weighted Mean (μb)
50 MeV	e	0.0222 ± 0.0007	0.0140 ± 0.0014	0.0192 ± 0.0044	0.0206 ± 0.0022
60 MeV	e	0.2163 ± 0.0038	0.2264 ± 0.0052	0.266 ± 0.012	0.2226 ± 0.0083
70 MeV	e	0.956 ± 0.013	0.989 ± 0.019	0.942 ± 0.022	0.963 ± 0.012
80 MeV	e	1.956 ± 0.021	1.942 ± 0.022	1.817 ± 0.026	1.917 ± 0.041
90 MeV	e	3.133 ± 0.034	3.186 ± 0.035	3.070 ± 0.040	3.135 ± 0.032
100 MeV	e	4.008 ± 0.067	4.047 ± 0.069	3.774 ± 0.068	3.943 ± 0.085
110 MeV	e	5.298 ± 0.043	5.330 ± 0.045	5.358 ± 0.052	5.325 ± 0.027
120 MeV	e	6.861 ± 0.078	6.870 ± 0.079	6.754 ± 0.082	6.830 ± 0.046
130 MeV	e	7.781 ± 0.090	7.838 ± 0.092	7.543 ± 0.093	7.723 ± 0.089
140 MeV	e	8.789 ± 0.085	8.875 ± 0.090	8.616 ± 0.090	8.761 ± 0.075
150 MeV	e	10.429 ± 0.314	10.665 ± 0.321	10.428 ± 0.315	10.505 ± 0.183
60 MeV	$e+\gamma$	0.654 ± 0.010	0.662 ± 0.013	0.662 ± 0.019	0.658 ± 0.007
	γ				$^{\dagger}13.4 \pm 0.3$
100 MeV	$e+\gamma$	11.723 ± 0.171	11.685 ± 0.172	11.319 ± 0.174	11.578 ± 0.128
	γ				$^{\dagger}227 \pm 5$
140 MeV	$e+\gamma$	23.352 ± 0.379	24.067 ± 0.393	23.122 ± 0.388	23.506 ± 0.281
	γ				$^{\dagger}431 \pm 9$

Table J.5: Reduced yields for the reactions ^{232}Th$(\gamma, 5n1p)^{226}$Ac and ^{232}Th$(e, 5n1p)^{226}$Ac. † Bremsstrahlung yields in μb per equivalent quantum.

Electron Energy		Reduced Yield (μb) measured per decay curve 213–Po	217–At	Weighted Mean (μb)
70 MeV	e	0.022 ± 0.017	0.159 ± 0.048	0.037 ± 0.043
80 MeV	e	0.664 ± 0.018	0.762 ± 0.056	0.673 ± 0.028
90 MeV	e	1.605 ± 0.026	1.517 ± 0.055	1.589 ± 0.034
100 MeV	e	2.405 ± 0.046	2.336 ± 0.099	2.393 ± 0.042
110 MeV	e	3.534 ± 0.035	3.568 ± 0.056	3.544 ± 0.029
120 MeV	e	4.766 ± 0.064	4.638 ± 0.106	4.732 ± 0.056
130 MeV	e	5.604 ± 0.070	5.582 ± 0.100	5.597 ± 0.057
140 MeV	e	6.761 ± 0.078	6.860 ± 0.128	6.788 ± 0.067
150 MeV	e	8.663 ± 0.284	8.336 ± 0.688	8.615 ± 0.263
100 MeV	$e+\gamma$	7.381 ± 0.114	7.208 ± 0.183	7.332 ± 0.097
	γ			$^{\dagger}147 \pm 3$
140 MeV	$e+\gamma$	18.763 ± 0.312	18.845 ± 0.355	18.80 ± 0.23
	γ			$^{\dagger}351 \pm 7$

Table J.6: Reduced yields for the reactions ^{232}Th$(\gamma, 6n1p)^{225}$Ac and ^{232}Th$(e, 6n1p)^{225}$Ac. † Bremsstrahlung yields in μb per equivalent quantum.

Electron Energy		Reduced Yield (μb) measured per decay curve 216–At	212–Po	Weighted Mean (μb)
80 MeV	e	0.164 ± 0.204	0.263 ± 0.119	0.238 ± 0.103
90 MeV	e	0.835 ± 0.242	0.866 ± 0.130	0.859 ± 0.114
100 MeV	e	1.234 ± 0.361	1.544 ± 0.312	1.412 ± 0.236
110 MeV	e	2.411 ± 0.295	2.064 ± 0.190	2.165 ± 0.160
120 MeV	e	2.659 ± 0.499	3.966 ± 0.317	3.590 ± 0.592
130 MeV	e	4.014 ± 0.356	4.771 ± 0.274	4.490 ± 0.366
140 MeV	e	4.488 ± 0.525	5.300 ± 0.531	4.890 ± 0.406
150 MeV	e	4.777 ± 0.587	7.615 ± 0.389	6.749 ± 1.307
100 MeV	$e + \gamma$	3.843 ± 0.631	4.941 ± 0.360	4.671 ± 0.473
	γ			$^{\dagger}97 \pm 16$
140 MeV	$e + \gamma$	12.921 ± 0.922	13.197 ± 1.011	13.046 ± 0.681
	γ			$^{\dagger}238 \pm 23$

Table J.7: Reduced yields for the reactions ^{232}Th$(\gamma, 7n1p)^{224}$Ac and ^{232}Th$(e, 7n1p)^{224}$Ac. † Bremsstrahlung yields in μb per equivalent quantum.

Electron Energy		Reduced Yield (μb) measured per decay curve 215–At (s)
80 MeV	e	0.118 ± 0.042
90 MeV	e	0.319 ± 0.032
100 MeV	e	0.890 ± 0.097
110 MeV	e	1.264 ± 0.101
120 MeV	e	1.971 ± 0.075
130 MeV	e	2.583 ± 0.134
140 MeV	e	3.054 ± 0.171
150 MeV	e	4.200 ± 0.227
100 MeV	$e + \gamma$	3.042 ± 0.427
	γ	$^{\dagger}64 \pm 13$
140 MeV	$e + \gamma$	8.663 ± 0.529
	γ	$^{\dagger}164 \pm 16$

Table J.8: Reduced yields for the reactions ^{232}Th$(\gamma, 8n1p)^{223}$Ac and ^{232}Th$(e, 8n1p)^{223}$Ac. † Bremsstrahlung yields in μb per equivalent quantum.

Electron Energy		Reduced Yield (μb) measured per decay curve 213–Po
50 MeV	e	0.052 ± 0.002
60 MeV	e	0.127 ± 0.006
70 MeV	e	0.193 ± 0.013
80 MeV	e	0.254 ± 0.012
90 MeV	e	0.372 ± 0.015
100 MeV	e	0.363 ± 0.023
110 MeV	e	0.590 ± 0.017
120 MeV	e	0.567 ± 0.033
130 MeV	e	0.883 ± 0.025
140 MeV	e	0.956 ± 0.043
150 MeV	e	1.517 ± 0.071
60 MeV	$e + \gamma$	0.358 ± 0.010
	γ	$^{\dagger}7.1 \pm 0.4$
100 MeV	$e + \gamma$	0.917 ± 0.037
	γ	$^{\dagger}16.4 \pm 1.3$
140 MeV	$e + \gamma$	2.202 ± 0.072
	γ	$^{\dagger}36.4 \pm 2.4$

Table J.9: Reduced yields for the reactions ^{232}Th$(\gamma, 5n2p)^{225}$Ra and ^{232}Th$(e, 5n2p)^{225}$Ra. † Bremsstrahlung yields in μb per equivalent quantum.

Electron Energy		Reduced Yield (μb) measured per decay curve 215–Po
60 MeV	e	0.066 ± 0.009
70 MeV	e	0.40 ± 0.12
80 MeV	e	0.30 ± 0.08
90 MeV	e	0.31 ± 0.09
100 MeV	e	0.41 ± 0.20
110 MeV	e	0.68 ± 0.12
120 MeV	e	-0.02 ± 0.20
130 MeV	e	0.44 ± 0.18
140 MeV	e	0.35 ± 0.37
150 MeV	e	0.004 ± 0.204
60 MeV	$e + \gamma$	0.22 ± 0.01
	γ	$^{\dagger}6.9 \pm 0.4$
100 MeV	$e + \gamma$	0.53 ± 0.24
	γ	$^{\dagger}3.8 \pm 9.4$
140 MeV	$e + \gamma$	2.8 ± 0.7
	γ	$^{\dagger}71 \pm 22$

Table J.10: Reduced yields for the reactions ^{232}Th$(\gamma, 6n2p)^{224}$Ra and ^{232}Th$(e, 6n2p)^{224}$Ra. † Bremsstrahlung yields in μb per equivalent quantum.

Electron Energy		Reduced Yield (μb) measured per decay curve 215–Po	211–Bi	Weighted Mean (μb)
70 MeV	e	0.13 ± 0.03	0.26 ± 0.07	0.16 ± 0.05
80 MeV	e	0.49 ± 0.05	0.57 ± 0.05	0.53 ± 0.04
90 MeV	e	0.18 ± 0.06	0.24 ± 0.07	0.21 ± 0.04
100 MeV	e	0.32 ± 0.05	0.67 ± 0.07	0.45 ± 0.17
110 MeV	e	0.41 ± 0.06	0.57 ± 0.07	0.48 ± 0.08
120 MeV	e	0.90 ± 0.07	0.95 ± 0.08	0.92 ± 0.05
130 MeV	e	0.69 ± 0.06	0.91 ± 0.07	0.78 ± 0.11
140 MeV	e	0.33 ± 0.07	0.70 ± 0.08	0.49 ± 0.19
150 MeV	e	1.78 ± 0.09	2.30 ± 0.11	2.00 ± 0.25
100 MeV	$e + \gamma$	0.72 ± 0.13	1.14 ± 0.14	0.91 ± 0.21
	γ			$^{\dagger}13.5 \pm 8.0$
140 MeV	$e + \gamma$	1.45 ± 0.16	2.11 ± 0.21	1.69 ± 0.32
	γ			$^{\dagger}35 \pm 11$

Table J.11: Reduced yields for the reactions ^{232}Th$(\gamma, 7n2p)^{223}$Ra and ^{232}Th$(e, 7n2p)^{223}$Ra. † Bremsstrahlung yields in μb per equivalent quantum.

Appendix K

Yield Function Analysis

When photonuclear reactions are investigated using photon sources with a continuous spectrum (bremsstrahlung or virtual photons), the mono-energetic reaction cross-sections are not measured directly but must instead be extracted from some measured integral quantity. In this case they must be unfolded from the reduced yield functions of Section 3.1. Various techniques have been used for such analysis, several of which are reviewed by Bramanis *et al* [188]. Penfold and Leiss [171,172] employ a basic matrix approximation, but their method fails to give proper treatment to the statistical uncertainties in the measured data and can generate spurious structure in the unfolded cross-sections. To overcome this difficulty Cook [173] enforced a 'least structure' condition upon the unfolded cross-sections by fitting a 'smoothed' yield function to the measured data, subject to some χ^2 condition. Another method similar to Cook's and employing the same least structure criterion, has been developed by Grosswendt *et al* [174]. In this 'modified least structure' method a solution is sought for the *integrated* cross-sections, which vary more smoothly with end-point energy than do the cross-sections themselves. Details are given here of the latter two methods, due to Cook and Grosswendt, which have been employed explicitly in the present analysis.

Solution of Yield Equation

The reduced yield, $y(E_i)$, measured at an electron energy E_i, is related to the mono-energetic reaction cross-section $\sigma(E_\gamma)$ as follows

$$y(E_i) = \int_{E_o}^{E_i} \sigma(E_\gamma)\, N(E_i, E_\gamma)\, dE_\gamma \qquad (K.1)$$

Here $N(E_i, E_\gamma)dE_\gamma$ represents the number of photons between E_γ and $E_\gamma + dE_\gamma$ in the radiation spectrum and E_o denotes the reaction threshold. In practice, $y(E_i)$ cannot be measured continuously but is determined at a series of discrete end-points E_i where i = $1, 2, \ldots, n$. Equation K.1 must then be approximated by a set of n linear equations of the form

$$y(E_i) = \sum_{j=1}^{i} \int_{E_{j-1}}^{E_j} \sigma(E_\gamma)\, N(E_i, E_\gamma)\, dE_\gamma \quad , \quad i = 1, 2, \ldots, n \qquad (K.2)$$

It is assumed that the radiation spectrum $N(E_i, E_\gamma)$ varies sufficiently slowly over each interval $[E_{j-1}, E_j]$ that it may be replaced by a constant value N_{ij} evaluated at the mean photon energy $\frac{1}{2}(E_{j-1}+E_j)$ of that interval. Equation K.2 then becomes

$$y(E_i) = \sum_{j=1}^{i} N_{ij} \int_{E_{j-1}}^{E_j} \sigma(E_\gamma)\, dE_\gamma \qquad (K.3)$$

Solution of this 'non-continuous' yield function may now follow several paths. Cook [173], using a matrix transformation to extract the *mean* cross-sections $\overline{\sigma_j}$ over each energy interval, considers Equation K.3 in the form

$$\underbrace{y(E_i)}_{y_i} = \sum_{j=1}^{i} \underbrace{N_{ij}\,[E_j - E_{j-1}]}_{N^*_{ij}}\; \underbrace{[E_j - E_{j-1}]^{-1} \int_{E_{j-1}}^{E_j} \sigma(E_\gamma)\, dE_\gamma}_{\overline{\sigma_j}} \qquad (K.4)$$

which in matrix notation can be written as

$$\mathbf{Y} = \mathbf{N}^* \cdot \mathbf{\Sigma} \qquad (K.5)$$

$\mathbf{Y}$ and $\mathbf{\Sigma}$ are 1-dimensional column matrices containing the y_i and $\overline{\sigma_j}$ respectively and $\mathbf{N}^*$ is an $n \times n$ triangular matrix with elements $N^*_{ij} = 0$ for $j > i$.

The solution matrix Σ is found through inversion of $\mathbf{N}^*$ such that

$$\Sigma = (\mathbf{N}^*)^{-1} \cdot \mathbf{Y} \qquad (K.6)$$

An alternative approach, used by Grosswendt *et al* [174], to the solution of Equation K.3, makes use of the observation [189] that the integral of the cross-section $s(E_i)$ up to the end-point E_i has a smoother dependence upon energy than does the cross-section itself. An unfolding procedure based on these integral values may then be expected to show less sensitivity to statistical fluctuations in the experimentally measured yields. Firstly an expression is derived relating the measured data y_i to the required integrals. In this case Equation K.3 takes the form

$$y(E_i) = \sum_{j=1}^{i} N_{ij}\, \tau_j \qquad (K.7)$$

where

$$\tau_j = \int_{E_{j-1}}^{E_j} \sigma(E_\gamma)\, dE_\gamma \quad \text{and} \quad i = 1, 2, \ldots, n$$

In an obvious matrix notation Equation K.7 is represented by

$$\mathbf{Y} = \mathbf{N} \cdot \mathbf{T} \qquad (K.8)$$

The entire integrated cross-section up to E_i is simply a sum over all intervals

$$s(E_i) = \sum_{j=1}^{i} \tau_j \quad \text{or} \quad \mathbf{S} = \mathbf{M} \cdot \mathbf{T} \qquad (K.9)$$

where $\mathbf{M}$ is chosen to have elements appropriate to the above transformation

$$M_{ij} = \begin{cases} 1 & \text{for} \quad j \leq i \\ 0 & \text{for} \quad j > i \end{cases}$$

Combining Equations K.8 and K.9 we obtain the required relation between the measured quantities $y(E_i)$ (matrix $\mathbf{Y}$) and the integrated cross-sections $s(E_i)$ (matrix $\mathbf{S}$)

$$\mathbf{S} = (\mathbf{M} \cdot \mathbf{N}^{-1}) \cdot \mathbf{Y} = \mathbf{Q} \cdot \mathbf{Y} \qquad (K.10)$$

Solving the right hand side of Equation K.10, where $\mathbf{Q} \equiv \mathbf{M} \cdot \mathbf{N}^{-1}$, yields a solution set for the s_j from which the mean cross-sections within each energy bin can be calculated

$$\overline{\sigma_j} = \frac{s_j - s_{j-1}}{E_j - E_{j-1}} \quad , \quad j = 1, 2, \ldots, n \qquad (K.11)$$

Since the measured yield points are relatively widely spaced and are known only to moderate precision, this latter method due to Grosswendt in general provides a more satisfactory solution than does the Cook technique. In their basic form however, both unfolding procedures still lead to strong oscillations in **S** and **T** which can result in physically unacceptable solutions. To overcome such problems, Cook's method of 'least structure' is employed to provide some degree of smoothing upon $s(E_\gamma)$. The smoothing procedure applied to $\sigma(E_\gamma)$, when unfolding is performed on the cross-sections themselves, is analagous to this approach and will not be discussed here.

Least Structure Concept

Although the functional form of the 'true' yield is unknown, any unfolded solution (or *smoothed* yield y_i^*), which might be considered as a satisfactory representation of this true value, must satisfy the basic χ^2 condition

$$\chi^2 = \sum_{i=1}^{n} \left[\frac{y_i^* - y_i}{\delta y_i} \right]^2 \approx n \qquad (K.12)$$

This, of course, only holds if the δy_i are truly representative of statistical uncertainties in the measured data points. When this condition is in doubt, perhaps due to some undefined systematic error, the χ^2 constraint may be suitably relaxed. The smoothed yields y_i^* quoted above, correspond to the refolded solutions of Equation K.10 i.e.

$$y_i^* = \sum_{j=1}^{n} \left(\mathbf{Q}^{-1} \right)_{ij} s_j \qquad (K.13)$$

There are, however, an infinite number of curves which satisfy the χ^2 condition and for this reason the further condition of least structure is assumed to apply. The least structure solution is taken to be that which minimises the structure function

$$\Phi(s_j) = \sum_{j=1}^{n} \left[\frac{s_j - s_{j-1}}{E_j - E_{j-1}} \right]^2 \qquad (K.14)$$

where Φ is large when $\mathbf{S}$ contains much structure and small when $\mathbf{S}$ is smooth. In this manner fluctuations in the integrated cross-sections are controlled, but with no assumption as to the 'true' shape of the solution. Minimisation of Φ, while satisfying the χ^2 constraint, is a standard problem of variational calculus, and requires that

$$d\chi^2(s_j) + \lambda \, d\Phi(s_j) = 0 \qquad (K.15)$$

where λ is an undetermined Lagrange multiplier. Evaluation of the partial derivatives with respect to the s_j leads to the following matrix relation

$$\left(\mathbf{Q}^{-1} + \lambda \, \mathbf{W}^{-1} \cdot \mathbf{Q}^{\mathrm{T}} \cdot \mathbf{\Phi} \right) \cdot \mathbf{S} = \mathbf{Y} \qquad (K.16)$$

$\mathbf{W}$ is a diagonal weighting matrix with elements $w_{ii} = \left(\frac{1}{\delta y_i}\right)^2$. The superscript T denotes a transposed matrix. The smoothing matrix $\mathbf{\Phi}$ can be shown to have elements

$$\begin{aligned}
\Phi_{i\,i-1} &= -(E_i - E_{i-1})^{-2} \\
\Phi_{i\,i} &= (E_i - E_{i-1})^{-2} + (E_{i+1} - E_i)^{-2} \\
\Phi_{i\,i+1} &= -(E_{i+1} - E_i)^{-2} \\
\Phi_{i\,j} &= 0 \quad \text{otherwise}
\end{aligned}$$

The Lagrange multiplier, λ, is adjusted through an iterative procedure until the χ^2 parameter falls within the desired limits. The solution set $\mathbf{S}$ is then obtained from Equation K.16 by matrix inversion. If $\mathbf{H}$ represents $\left(\mathbf{Q}^{-1} + \lambda \, \mathbf{W}^{-1} \cdot \mathbf{Q}^{\mathrm{T}} \cdot \mathbf{\Phi} \right)$ this is merely

$$\mathbf{S} = \mathbf{H}^{-1} \cdot \mathbf{Y} \qquad (K.17)$$

The uncertainties in $s(E_j)$ are

$$\delta s(E_j) = \left[\sum_{k=1}^{n} \left(H^{-1}\right)_{jk}^2 (\delta y_k)^2 \right]^{\frac{1}{2}} \qquad (K.18)$$

The mean cross-section $\overline{\sigma_j}$ within each interval $[E_{j-1}, E_j]$ is given by Equation K.11 with an uncertainty

$$[\delta\overline{\sigma_j}]^2 = \frac{[\delta s_j]^2 + [\delta s_{j-1}]^2}{[E_j - E_{j-1}]^2} \qquad (K.19)$$

Bibliography

[1] B.L.Berman and S.C.Fultz, Rev. Mod. Phys. **47** (1975) 713.

[2] M.Goldhaber and E.Teller, Phys. Rev. **74** (1948) 1048.

[3] D.H.Wilkinson, Physica **22** (1956) 1039.

[4] N.de Botton, "Proceedings of the International Conference on Nuclear Physics with Electromagnetic Interactions", edited by H.Arenhövel and D.Drechsel, Lecture Notes in Physics **108** (1979) 339.

[5] S.Costa, "Proceedings of the International Conference on Photonuclear Reactions and Applications, Vol. 2", edited by B.L.Berman, Lawrence Livermore Laboratory, Univ. of California (1973) 1319.

[6] J.S.Levinger, "Proceedings of the International Conference on Low and Intermediate Energy Electromagnetic Interactions, Vol. 3", Dubna (1967) 411.

[7] G.Ricco, "Photonuclear Reactions", Lecture Notes in Physics, Vol 61 (Springer, 1977) 223.

[8] W.Weise and M.G.Huber, Nucl. Phys. **A162** (1971) 330.

[9] J.S.Levinger, Phys. Rev. **84** (1951) 43.

[10] H.G.Miller, W.Buss and J.A.Rawlins, Nucl. Phys. **A163** (1971) 637.

[11] J.A.Rawlins, C.Glavina, S.H.Ku and Y.M.Shin, Nucl. Phys. **A122** (1968) 128.

[12] J.Chadwick and M.Goldhaber, Nature **134** (1934) 237.

[13] L.Szilard and T.A.Chalmers, Nature **134** (1934) 494.

[14] G.B.Collins, B.Waldman and E.Guth, Phys. Rev. **56** (1939) 876.

[15] D.W.Kerst, Phys. Rev. **58** (1940) 841.

[16] G.C.Baldwin and G.S.Klaiber, Phys. Rev. **71** (1947) 3.
G.C.Baldwin and G.S.Klaiber, Phys. Rev. **73** (1948) 1156.

[17] G.A.Price and D.W.Kerst, Phys. Rev. **77** (1950) 806.
J.Halpern, A.K.Mann and R.Nathans, Rev. Sci. Instr. **23** (1952) 678.
R.Montalbetti, L.Katz and J.Goldemberg, Phys. Rev. **91** (1953) 659.
R.Nathans and J.Halpern, Phys. Rev. **92** (1953) 940.
R.Nathans and J.Halpern, Phys. Rev. **93** (1953) 437.
R.Nathans and J.Halpern, Phys. Rev. **98** (1955) 1296.
and references therein.

[18] A.I.Berman and K.L.Brown, Phys. Rev. **96** (1954) 83.
and references therein.

[19] J.M.Blatt and V.F.Weisskopf, "Theoretical Nuclear Physics", J.Wiley & Sons, Inc., New York (1952).

[20] L.W.Jones and K.M.Terwilliger, Phys. Rev. **91** (1953) 699.

[21] N.Sugarman and R.Peters, Phys. Rev. **81** (1950) 951.

[22] L.B.Aull, G.C.Reinhardt and W.D.Whitehead, Nucl. Phys. **13** (1959) 292.

M.L.Perlman and G.Friedlander, Phys. Rev. **74** (1948) 442.

B.C.Diven and G.M.Almy, Phys. Rev. **80** (1950) 407.

O.Hirzel and H.Wäffler, Helv. Phys. Acta, **20** (1947) 373.

[23] J.Moffat and D.Reitmann, Nucl. Phys. **65** (1965) 130.

[24] G.G.Jonsson and B.Forkman, Nucl. Phys. **A107** (1968) 52.

[25] K.Lindgren and G.G.Jonsson, Nucl. Phys. **A166** (1971) 643.

[26] J.S.Pringle, A.G.Flowers, D.Branford, J.C.McGeorge, C.H.Zimmerman, Nucl. Phys. **A325** (1979) 63.

[27] J.M.Wyckoff, B.Ziegler, H.W.Koch and R.Uhling, Phys. Rev. **137** (1965) B756.

[28] I.Anthony, D.Branford, A.G.Flowers, J.C.McGeorge, M.R.Sené, A.C.Shotter, P.J.Thorley, C.H.Zimmerman, J.Friedrich, N.Voegler, K.Bangert and U.E.P.Berg, Phys. Lett. **141B** (1984) 309.

[29] G.G.Jonsson and K.Lindgren, Nucl. Phys. **A141** (1970) 355.
G.G.Jonsson and B.Persson, Nucl. Phys. **A153** (1970) 32.
B.Bülow, M.Eriksson, G.G.Jonsson and E.Hagebø, Z. Physik **A275** (1975) 261.

[30] C.Schuhl and C.Tzara, Nucl. Instr. and Meth. **10** (1961) 217.
H.Beil, R.Bergère, and A.Veyssière, Nucl. Instr. and Meth. **67** (1969) 293.

[31] C.P.Jupiter, N.E.Hanson, R.E.Shafer and S.C.Fultz, Phys. Rev. **121** (1961) 886.
S.C.Fultz, R.L.Bramblett, J.T.Caldwell and C.P.Jupiter, Phys. Rev. **128** (1962) 2345.

[32] E.Wolynec, A.R.V.Martinez, P.Gouffon, Y.Miyao, V.A.Serão and M.N.Martins, Phys. Rev. **C29** (1984) 1137.

[33] P.Carlos, H.Beil, R.Bergère, B.L.Berman, A.Leprêtre and A.Veyssière, Nucl. Phys. **A378** (1982) 317.

[34] A.Leprêtre, H.Beil, R.Bergère, P.Carlos, J.Fagot and A.Veyssière, Nucl. Phys. **A390** (1982) 221.

[35] A.Leprêtre, H.Beil, R.Bergère, P.Carlos, J.Fagot and A.Veyssière, Nucl. Phys. **A390** (1982) 240.

[36] A.Leprêtre, H.Beil, R.Bergère, P.Carlos, J.Fagot, A.de Miniac and A.Veyssière, Nucl. Phys. **A367** (1981) 237.

[37] A.Leprêtre, H.Beil, R.Bergère, P.Carlos, J.Fagot, A.Veyssière, J.Ahrens, P.Axel and U.Kneissl, Phys. Lett. **79B** (1978) 43.

[38] J.Ahrens, H.Borchert, K.H.Czock, H.B.Eppler, H.Gimm, H.Gundrum, M.Kröning, P.Riehn, G.Sita Ram, A.Zieger and B.Ziegler, Nucl. Phys. **A251** (1975) 479.
B.Ziegler, "Nuclear Physics with Electromagnetic Interactions," (Mainz, 1979) Lecture Notes in Physics, Vol. **108** (Springer, Berlin).

[39] R.Bergère, Nuclear Physics with Electromagnetic Interactions, (Mainz, 1979) Lecture Notes in Physics, Vol. **108** (Springer, Berlin).

[40] J.D.T.Arruda Neto, M.Sugawara, T.Tamae, O.Sasaki, H.Ogino, H.Miyase and K.Abe, Phys. Rev. **C34** (1986) 935.

[41] M.Danos, Nucl. Phys. **5** (1958) 23.
E.G.Fuller and M.S.Weiss, Phys. Rev. **112** (1958) 560.

[42] R.Pitthan and T.Walcher, Phys. Lett. **36B** (1971) 563.
S.Fukuda and Y.Torizuka, Phys. Rev. Lett. **29** (1972) 1109.
M.B.Lewis and F.E.Bertrand, Nucl. Phys. **A196** (1972) 337.

[43] R.Pitthan, H.Hass, D.H.Meyer, J.N.Dyer and F.R.Buskirk, Phys. Rev. Lett. **41** (1978) 1276.

[44] J.H.Carver and W.Turhinetz, Proc. Phys. Soc. (London) **71** (1957) 613.

[45] J.T.Caldwell, E.J.Dowdy, B.L.Berman, R.A.Alvarez and P.Meyer, Phys. Rev. **C21** (1980) 1215.

[46] G.Taran and A.N.Gorbunov, Sov. Phys. JETP **19** (1964) 1010.

[47] M.Anghinolfi, V.Lucherini, N.Bianchi, G.P.Capitani, P.Corvisiero, E.De Sanctis, P.Di Giacomo, C.Guaraldo, P.Levi-Sandri, E.Polli, A.Reolon, G.Ricco, M.Sanzone and M.Taiuti, Nucl. Phys. **A457** (1986) 645.

[48] J.S.Levinger, Phys. Lett. **82B** (1979) 181.

[49] J.D.T.Arruda Neto, S.B.Herdade, B.S.Bhandari and I.C.Nascimento, Phys. Rev. **C18** (1978) 863.
J.D.T.Arruda Neto, B.L.Berman, S.B.Herdade, and I.C.Nascimento, Lett. Nuovo Cimento **26** (1979) 487.

[50] B.Ziegler, "Proceedings of the Workshop on Few Body Systems and Electromagnetic Interactions" (Frascati,1978), Lecture Notes in Physics, **86** (1978) 101.

[51] W.Kuhn, Z. Phys. **33** (1925) 408.
W.Reiche and W.Thomas, Z. Phys. **34** (1925) 510.

[52] S.B.Gerasimov, Phys. Let. **13** (1964) 240.

[53] J.S.Levinger and H.A.Bethe, Phys. Rev. **78** (1950) 115.

[54] A.Lepreêtre, R.Bergère, P.Bourgeois, J.Fagot, J.L.Fallou, P.Garganne, A.Veyssière, R.Göbel, H.Ries, U.Kneissl, G.Mank, H.Ströher, W.Wilke, D.Ryckbosch and J.Jury, (1987) submitted to Nucl. Phys.

[55] A.Veyssière, H.Beil, R.Bergère, P.Carlos, A.Leprêtre and K.Kernbath, Nucl. Phys. **A199** (1973) 45.

[56] J.T.Caldwell, E.J.Dowdy, B.L.Berman, R.A.Alvarez and P.Meyer, Phys. Rev. **C21** (1980) 1215.

[57] J.D.T.Arruda Neto, W.Rigolon, S.B.Herdade and H.L.Riette, Phys. Rev. **C29** (1984) 2399.

[58] R.Vandenbosch and J.R.Huizenga, "Nuclear Fission", Academic Press, New York & London (1973).

[59] K.F.von Weizsäcker, Z. Phys. **88** (1934) 612.

[60] E.J.Williams, Mat. Fys. Medd. Dan. Vid. Selsk. **13** (1935) 4.

[61] R.H.Dalitz and D.R.Yennie, Phys. Rev. **105** (1957) 1598.
G.C.Wick, Ricerca Sci. **11** (1940) 49.
B.Peters and C.Rickman, Phys. Rev. **59** (1941) 804.
J.S.Blair, Phys. Rev. **75** (1949) 907.
E.Guth and C.J.Mullin, Phys. Rev. **76** (1949) 234.
C.J.Mullin and E.Guth, Phys. Rev. **82** (1951) 141.
J.A.Thie, C.J.Mullin and E.Guth, Phys. Rev. **87** (1952) 962.

[62] D.Reagan, Phys. Rev. **100** (1955) 113.

[63] K.L.Brown and R.Wilson, Phys. Rev. **93** (1954) 443.

[64] D.W.Scott, A.O.Hansen and D.W.Kerst, Phys. Rev. **100** (1955) 209.

[65] R.L.Hines, Phys. Rev. **105** (1957) 1534.

[66] W.C.Barber, Phys. Rev. **111** (1958) 1642.

[67] W.C.Barber and T.Wiedling, Nucl. Phys. **18** (1960) 575.

[68] W.R.Dodge and W.C.Barber, Phys. Rev. **127** (1962) 1746.

[69] V.L.Telegdi and M.Gell-Man, Phys. Rev. **91** (1953) 169.

[70] J.S.O'Connell, Proceedings of the International Conference on Photonuclear Reactions and Applications, Asilomar (1973), edited by B.L.Berman, Lawrence Livermore Laboratory, Univ. of California. Vol.1 **A71** CONF–730301.

[71] E.Wolynec, G.Moscati, O.D.Goncalves and M.N.Martins, Nucl. Phys. **A244** (1975) 205.

[72] E.Wolynec, G.Moscati, O.D.Goncalves and M.N.Martins, Univ. de São Paulo, Report No. IFUSP/P–38.

[73] L.Tiator and L.E.Wright, Comp. Phys. Comm. **28** (1983) 265.

[74] L.Tiator and L.E.Wright, Nucl. Phys. **A379** (1982) 407.

[75] L.E.Wright and L.Tiator, Phys. Rev. **C26** (1982) 2349.

[76] D.F.Herring, I.C.Nascimento, R.B.Walton and R.E.Sund, Phys. Rev. **139** (1965) B562.

[77] W.W.Gargaro and D.S.Onley, Phys. Rev. **C4** (1971) 1032.

[78] I.C.Nascimento, E.Wolynec and D.S.Onley, Nucl. Phys. **A246** (1975) 210.

[79] M.N.Martins, E.Wolynec and G.Moscati, Phys. Rev. **C16** (1977) 613.

[80] E.Wolynec, G.Moscati, J.R.Moreira, O.D.Goncalves and M.N.Martins, Phys. Rev. **C11** (1975) 1083.

[81] C.W.Soto Vargas, D.S.Onley and L.E.Wright, Nucl. Phys. **A288** (1977) 45.

[82] L.E.Wright and C.W.Soto Vargas, Comp. Phys. Comm. **20** (1980) 337.

[83] L.E.Wright, D.S.Onley and C.W.Soto Vargas, J. Phys. **A10** (1977) 153.

[84] K.Sud, L.E.Wright and D.S.Onley, J. Math. Phys. **17** (1976) 2175.

[85] D.B.Isabelle and G.R.Bishop, Nucl. Phys. **45** (1963) 209.

[86] A.C.Shotter, J. Phys. **G5** (1979) 371.

[87] R.H.Helm, Phys. Rev. **104** (1956) 1466.

[88] D.S.Onley, Bull. Am. Phys. Soc. **26** (1981) 1129.

[89] F.Zamani-Noor and D.S.Onley, Phys. Rev. **C33** (1986) 1354.

[90] P.Durgapal and D.S.Onley, Phys. Rev. **C27** (1983) 523.

[91] P.Durgapal and D.S.Onley, Comp. Phys. Comm. **32** (1984) 291.

[92] P.Durgapal and D.S.Onley, Bull. Am. Phys. Soc. **26** (1981) 1130.

[93] L.S.Cutler, Phys. Rev. **157** (1967) 885.

[94] J.C.Bergstrom, Phys. Rev. **C11** (1975) 1514.

[95] D.S.Onley, Private Communication (1986).

[96] V.F.Weisskopf, Phys. Rev. **52** (1937) 295.
V.F.Weisskopf and D.H.Ewing, Phys. Rev. **57** (1940) 472.

[97] M.Goldberger, Phys. Rev. **74** (1948) 1269.

[98] N.Metropolis, R.Bivins, M.Storm, A.Turkevich, J.M.Miller and G.Friedlander, Phys. Rev. **110** (1958) 185.

[99] H.W.Bertini, Phys. Rev. **131** (1965) 1801.

[100] R.Serber, Phys. Rev. **72** (1947) 1114.

[101] G.D.Harp and J.M.Miller, Phys. Rev. **C3** (1971) 1847.

[102] G.D.Harp, J.M.Miller and B.J.Berne, Phys. Rev. **165** (1968) 1166.

[103] J.J.Griffin, Phys. Rev. Lett. **17** (1966) 478.

[104] J.J.Griffin, Phys. Rev. Lett. **B24** (1967) 5.

[105] J.R.Wu and C.C.Chang, Phys. Rev. C16 (1977) 1812.
J.R.Wu and C.C.Chang, Phys. Rev. C17 (1978) 1540.

[106] M.Blann, Annu. Rev. Nucl. Sci. **25** (1975) 123.

[107] M.Blann, Phys. Rev. Lett. **27** (1971) 337, **27** (1971) 700E, **27** (1971) 1550E.

[108] M.Blann and J.Bisplinghoff, University of California Report UCID–19614 (1982), unpublished.

[109] M.Blann, Phys. Rev. **C28** (1983) 1648.

[110] M.Blann, B.L.Berman and T.T.Komoto, Phys. Rev. **C28** (1983) 2286.

[111] M.Blann, Phys. Rev. **C28** (1983) 1475.

[112] E.Gadioli, E.Gadioli-Erba and P.G.Sona, Nucl. Phys. **A217** (1973) 589.

[113] J.M.Miller, Proceedings of the International Conference on Nuclear Physics, Munich 1973, Edited by J.de Boer and H.J.Mang, (Amsterdam : North Holland).

[114] F.E.Bertrand and R.W.Peele, Phys. Rev. **C8** (1973) 1045.

[115] M.Blann, Phys. Rev. Lett. **28** (1972) 757.

[116] G.R.Hogg, A.G.Slight, T.E.Drake, A.Johnston and G.R.Bishop, Nucl. Instr. and Meth. **101** (1972) 203.

[117] W.A.Gillespie and M.G.Kelliher, Nucl. Instr. and Meth. **184** (1981) 285.

[118] S.Penner, Rev. Sci. Instr. **32** (1961) 150.

[119] D.Gibson, Ph.D. Thesis, University of Glasgow (1979), unpublished.

[120] A.G.Flowers, Ph.D. Thesis, University of Edinburgh (1980), unpublished.

[121] S.N.Gardiner, J.L.Mathews and R.O.Owens, Nucl. Instr. and Meth. **87** (1970) 285.

[122] A.G.Slight, Ph.D. Thesis, University of Glasgow (1971), unpublished.

[123] L.Yaffe, Ann. Rev. Nucl. Sci. **12** (1962) 153.

[124] R.B.Belser and W.H.Hicklin, Rev. Sci. Instr. **27** (1956) 293.

[125] T.Novakov and M.Mladjenovic, Rev. Sci. Instr. **27** (1956) 415.

[126] R.P.Wiltshire, Chemistry Division, AERE, UKAEA, Harwell (Private Communication).

[127] F.Asaro, F.L.Reynolds and I.Perlman, Phys. Rev. **87** (1952) 277.

[128] W.Parker, M. de Croëss and K.Sevier Jr., Nucl. Instr. and Meth. **7** (1960) 22.

[129] Goodfellow Metals, Cambridge Science Park, Cambridge.

[130] Physics Data, W.Westmeier and A.Merklin, **29 – 1** (1985).

[131] C.N.Yang, Phys. Rev. **84** (1951) 599.

[132] H.A.Bethe and W.Heitler, Proc. Roy. Soc. (London) **a146** (1934) 83.

[133] H.W.Koch and J.W.Motz, Rev. Mod. Phys. **31** (1959) 920.

[134] M.J.Berger and S.M.Seltzer, Phys. Rev. **C2** (1970) 621.

[135] J.L.Mathews and R.O.Owens, Nucl. Instr. and Meth. **111** (1973) 157.

[136] ENERTEC, Branche Instrumentation Nucleaire, Lingolsheim (France).

[137] C.M.Lederer and V.S.Shirley, "Table of Isotopes", 7^{th} edition, J.Wiley and Sons (1978).

[138] IAEA Report INDC(NDS)–149/NE (1983).

[139] J.T.Routti and S.G.Prussin, Nucl. Instr. and Meth. **72** (1969) 125.

[140] J.T.Routti, University of California, Lawrence Berkeley Laboratory Report, UCRL–19452 (1969).

[141] M.J.Koskelo, P.A.Aarnio and J.T.Routti, Comp. Phys. Comm. **24** (1981) 11.

[142] M.H.Studier and E.K.Hyde, Phys. Rev. **74** (1948) 591.

[143] W.W.Meinke, A.Ghiorso and G.T.Seaborg, Phys. Rev. **81** (1951) 782.

[144] J.F.Eichelberger, G.R.Grove, L.V.Jones and E.A.Rembold, Mound Laboratory, Miamisburg, Ohio, Report–1155 (1963), Report–1364 (1967).

[145] G.R.Hagee, M.L.Curtis and G.R.Grove, Phys. Rev. **96** (1954) 817.

[146] S.Peterson, Nat. Nuclear Energy Series **14B** (1949) 1424.

[147] H.W.Kirby, K.C.Jordan, J.Z.Braun, M.L.Curtis and M.L.Salutsky, J. Inorg. Nuc. Chem. **27** (1965) 1881.

[148] J.Robert, Ann. Phys. **4** (1959) 89.

[149] W.W.Meinke and G.T.Seaborg, Phys. Rev. **78** (1950) 475.

[150] F.Hagemann, L.I.Katzin, M.H.Studier, G.T.Seaborg and A.Ghiorso, Phys. Rev. **79** (1950) 435.

[151] T.A.Gabriel, M.P.Guthrie and O.W.Hermann, Oak Ridge National Laboratory Report, ORNL–4687 (1971).

[152] T.A.Gabriel and R.G.Alsmiller, Jr., Phys. Rev. **182** (1969) 1035.

[153] T.A.Gabriel, Phys. Rev. **C13** (1976) 240.

[154] N.Metropolis, R.Bivins, M.Storm, J.M.Miller, G.Friedlander and A.Turkevich, Phys. Rev. **110** (1958) 204.

[155] R.Hofstadter, Rev. Mod. Phys. 28 (1956) 214.

[156] J.L.Mathews, dissertation, Massachusetts Institute of Technology (1967), unpublished.
F.Partovi, Ann. Phys. (N.Y.) **27** (1964) 79.
A.V.Tollestrup and J.C.Keck, Phys. Rev. **101** (1956) 360.

[157] R.Ching and C.Schaerf, Phys. Rev. **141** (1966) 1320.

[158] D.H.White *et al.*, Phys. Rev. **120** (1960) 614.
V.L.Highland and J.W.de Wire, Phys. Rev. **137** (1963) 1293.
K.Berkelman and J.A.Waggoner, Phys. Rev. **117** (1960) 1364.
J.I.Vette, Phys. Rev. **111** (1958) 622.

M.Beneventano *et al.*, Nuovo Cimento **4** (1956) 333.

A.V.Tollestrup, J.C.Keck and R.M.Worlock, Phys. Rev. **99** (1955) 220.

R.L.Walker, J.G.Teasdale, V.Z.Peterson and J.J.Vette, Phys. Rev. **99** (1955) 210.

C.Freitag *et al.*, Z. Physik **175** (1963) 1.

[159] I.Dostrovsky, Rabinowitz and R.Bivins, Phys. Rev. **111** (1958) 1659.

[160] I.Dostrovsky, Z.Fraenkel and G.Friedlander, Phys. Rev. **116** (1959) 683.

[161] L.Dresner, Oak Ridge National Laboratory Report, ORNL–CF-61-12-30 (1961).

[162] A.G.W.Cameron, Can. J. Phys. **34** (1958) 1040.

[163] M.El-Nadi and M.Wafik, Nucl. Phys. **9** (1958) 22.

[164] C.Block, Phys. Rev. **93** (1954) 1094.

[165] N.Bohr and J.A.Wheeler, Phys. Rev. **56** (1939) 426.

[166] M.Blann, A.Mignerey and W.Scobel, Nukleonika **21** (1976) 335.

[167] K.Kikuchi and M.Kawai, "Nuclear Matter and Nuclear Reactions", North Holland Publishing Co. (1968).

[168] B.Bassalleck, W.D.Klotz, F.Takeutchi and H.Ullrich, Phys. Rev. **C16** (1977) 1526.

[169] S.Bjornholm and J.E.Lynn, Rev. Mod. Phys. **52** (1980) 725.

[170] D.Ryckbosch, P.Carlos and A.Leprêtre, (1987) to be published.

[171] A.S.Penfold and J.E.Leiss, Phys. Rev. **95** (1954) 637A.

[172] A.S.Penfold and J.E.Leiss, Phys. Rev. **114** (1959) 1332.

[173] B.C.Cook, Nucl. Instr. and Meth. **24** (1963) 256.

[174] B.Grosswendt, W.Collin and U.Schneider, Nucl. Instr. and Meth. **144** (1977) 271.

[175] I.Anthony, J.C.McGeorge and D.Branford, submitted to J. Phys. G (1987).

[176] J.R.Grover and J.Gilat, Phys. Rev. **157** (1966) 802.

[177] G.J.Miller, J.C.McGeorge, I.Anthony and R.O.Owens, Phys. Rev. (Brief Reports), accepted for publication (1987).

[178] L.Landau, J. Phys. (USSR) **8** (1944) 201

[179] B. Rossi, "High Energy Particles" (Prentice Hall, New York) (1952) p32.

[180] H.D.Maccabee and D.G.Papworth, Phys. Lett. **30A** (1969) 241.

[181] J.F.Ziegler "The Stopping and Ranges of Ions in Matter, Vol. 4", Pergamon Press (1977).

[182] A.V.H.Masket, R.L.Macklin and H.W.Schmitt, "Tables of Solid Angles and Activations", (ORNL–2170, Oak Ridge National Laboratory).

[183] J.H.Wilkinson and C.Reinsch, "Handbook for Automatic Computation", Vol. II, Springer-Verlag, (1971).

[184] P.Cziffra and M.J.Moravcsik, "A Practical Guide to the Method of Least Squares", (UCRL–8523 Rev., University of California).

[185] Y.V.Linnik, "Method of Least Squares and Principles of the Theory of Observations", Pergamon Press (1961).

[186] N.P.Archer, W.V.Prestwich and G.L.Keech, Nucl. Instr. and Meth. **44** (1966) 114.

[187] H.Bateman, Proc. Camb. Phil. Soc. **15** (1910) 423.

[188] E.Bramanis, T.K.Deague, R.S.Hicks, R.J.Hughes, E.G.Muirhead, R.H.Sambell and R.J.J.Stewart, Nucl. Instr. and Meth. **100** (1972) 59.

[189] B.C.Cook, Phys. Rev. **106** (1957) 300.